

MAPs

115

NMR-based Structural Biology of Dynamic Biomolecular Complexes

Agnes Adler

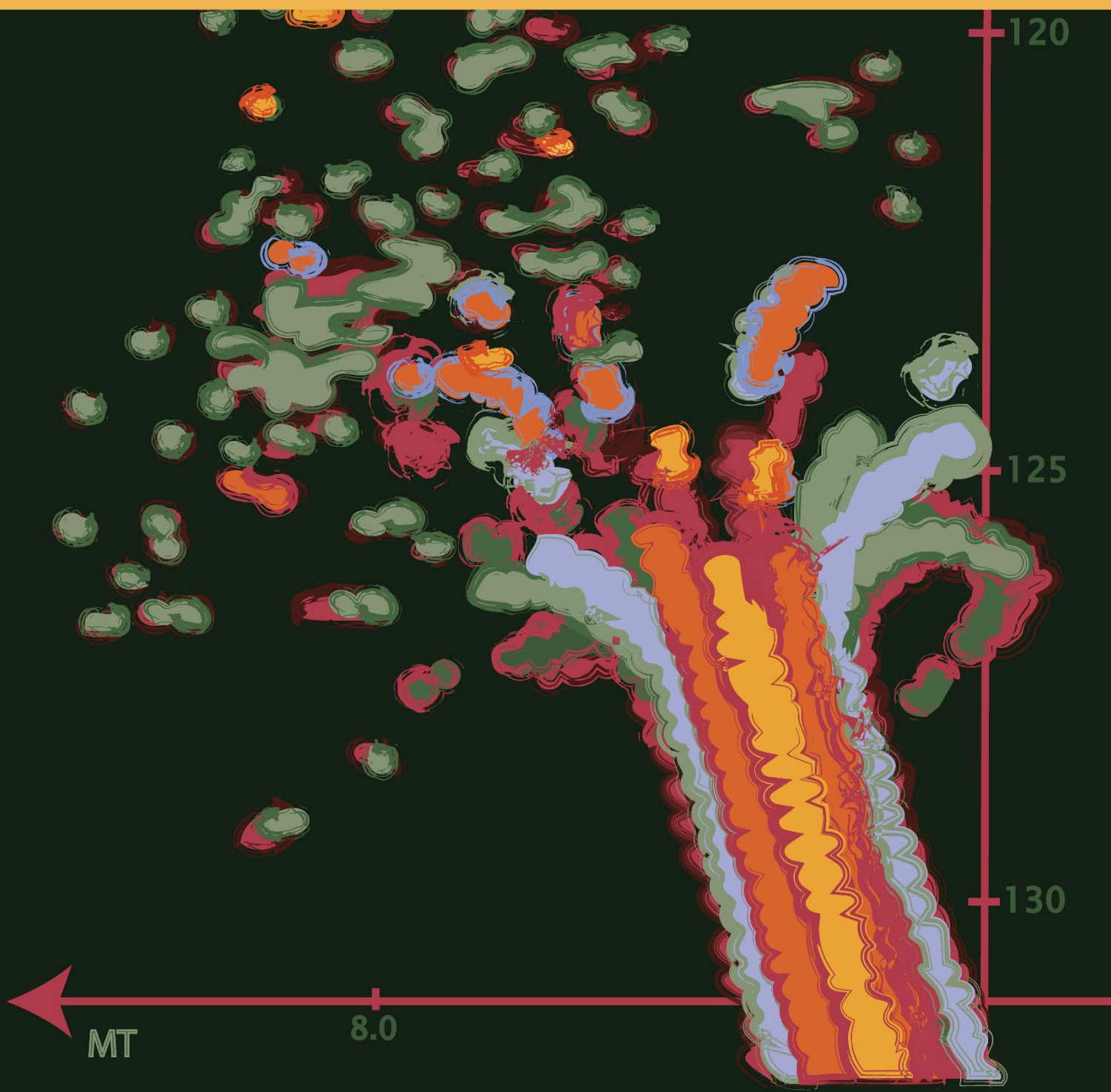
120

125

130

MT

8.0



NMR-based Structural Biology of Dynamic Biomolecular Complexes

Agnes Hildegard Adler

ISBN 978-94-6469-535-9

Doctoral Thesis

NMR-based Structural Biology of Dynamic Biomolecular Complexes

Agnes Adler

NMR Spectroscopy

Bijvoet Center of Biomolecular Research, Faculty of Chemistry, Utrecht University,
the Netherlands

September 2023

Cover and lay-out design: Agnes Adler Printed in the Netherlands by

Copyright © 2023 Agnes Adler

NMR-based Structural Biology of Dynamic Biomolecular complexes

NMR gebaseerde Structurele Biologie van Dynamische Biomoleculaire complexen

(met een samenvatting in het Nederlands)

Proefschrift

ter verkrijging van de graad van doctor aan de
Universiteit Utrecht
op gezag van de
rector magnificus, prof.dr. H.R.B.M. Kummeling,
ingevolge het besluit van het college voor promoties
in het openbaar te verdedigen op

woensdag 20 september 2023 des middags te 2.15 uur

door

Agnes Hildegard Adler

geboren op 23 april 1995
te Pirna, Duitsland

Promotor:

Prof. dr. M. Baldus

Copromotor:

Dr. H. van Ingen

Beoordelingscommissie:

Prof. dr. A.S. Akhmanova

Prof. dr. F.G. Förster

Prof. dr. A. Perrakis

Prof. dr. S.G.D. Rüdiger

Prof. dr. R. Sprangers

Da steh' ich nun, ich armer Tor,
Und bin so klug als wie zuvor!
Heiße Magister, heiße Doktor gar,
Und ziehe schon an die zehn Jahr'
Herauf, herab und quer und krumm
Meine Schüler an der Nase herum -
Und sehe, dass wir nichts wissen können!
Das will mir schier das Herz verbrennen.
Zwar bin ich gescheiter als alle die
Laffen, Doktoren, Magister, Schreiber und Pfaffen;
Mich plagen keine Skrupel noch Zweifel,
Fürchte mich weder vor Hölle noch Teufel –
Dafür ist mir auch alle Freud' entrissen,
Bilde mir nicht ein, was Rechts zu wissen,
Bilde mir nicht ein, ich könnte was lehren,
Die Menschen zu bessern und zu bekehren.
Auch hab' ich weder Gut noch Geld,
Noch Ehr' und Herrlichkeit der Welt;
Es möchte kein Hund so länger leben!

Johann Wolfgang von Goethe (1749-1832)

This thesis is dedicated to my siblings and all the other people that I love with all of my heart and without whom I would be a completely different being.

Contents

List of Abbreviations	10
Chapter 1	
Introduction	13
Chapter 2	
Resonance assignments of the microtubule-binding domain of the microtubule-associated protein 7 (MAP7).....	43
Chapter 3	
Solid-State NMR Spectroscopy for Studying Microtubules and Microtubule-Associated Proteins.....	57
Chapter 4	
¹ H-detected characterization of carbon-carbon networks in highly flexible protonated biomolecules using MAS NMR	71
Chapter 5	
A structural and dynamic visualization of the interaction between the Microtubule-associated protein 7 (MAP7) and microtubules .	97
Chapter 6	
Analysis of the dynamic interaction of Tau and microtubules	143
Chapter 7	
Utilizing solid-state NMR to investigate mRNA processing bodies	185
Chapter 8	
Discussion and future perspectives.....	205
Appendices	
English Summary	216
Nederlandse Samenvatting	219
Acknowledgments.....	222
Curriculum Vitae	229
List of Publications	230

List of Abbreviations

2-ME	β -mercaptoethanol
ALS	Amyotrophic Lateral Sclerosis
CAMSAP	CAIModulin-regulated Spectrin-Associated Protein
CEX	Cation EXchange
CP	Cross-Polarisation
Cryo-EM	Cryogenic Electron Microscopy
CSA	Chemical Shift Anisotropy
CTT	Carboxy-Terminal Tail
Dcp	Decapping protein
DIPSI	Decoupling In the Presence of Scalar Interactions
DMEM	Dulbecco's Modified Eagle Medium
DMSO	DiMethyl SulfOxide
DNA	DeoxyriboNucleic Acid
DNP	Dynamic Nuclear Polarization
DQ-SQ	Double-Quantum Single- Quantum
DTT	DiThioThreitol
<i>E.coli</i>	<i>Escherichia coli</i>
Edc	Enhancer of decapping
EGTA	Ethylene Glycol-bis(β -aminoethyl ether)-N,N,N',N'-Tetraacetic Acid
EMMI	Metainference for <i>cryo-EM</i>
FBS	Fetal Bovine Serum
FID	Free Induction Decay
FUS	FUsed in Sarcoma
GDP	Guanosine-5'-DiPhosphate
GTP	Guanosine-5'-TriPhosphate
HR	High-Resolution
HSQC	Heteronuclear Single-Quantum Correlation
INEPT	Insensitive Nuclei Enhancement by Polarization Transfer
IMAC	Immobilized Metal Affinity Chromatography
IPTG	Isopropyl- β -D-thiogalactoside
LB	Lysogeny Broth
LLPS	Liquid-Liquid Phase Separation
MAP	Microtubule-Associated Protein
MAS	Magic Angle Spinning
MBP	Maltose Binding Protein
mRNA	messenger RiboNucleic Acid
MTs	MicroTubule
MTBD	MicroTubule-Binding Domain

NMR	Nuclear Magnetic Resonance
PAGE	PolyAcrylamide Gel Electrophoresis
PDB	Protein Data Bank
PDSF	Proton-Driven Spin Diffusion
PIPES	piperazine-N,N'-bis (2-ethanesulfonic acid)
PMSF	PhenylMethylSulfonyl Fluoride
PTM	Post-Translational Modification
ppm	parts per million
RCI-S ²	Random-Coil-Index-derived generalized order-parameter squared
RF	Radio Frequency
RFDR	Radio Frequency Driven Recoupling
RI	Refraction Index
RNA	RiboNucleic Acid
S.commune	<i>Schizophyllum commune</i>
SAH	Single Alpha-Helix
SDS	Sodium Dodecyl Sulfate
SEC	Size Exclusion Chromatography
Sec-MALLS	Size-exclusion chromatography coupled with Multi-Angle Light Scattering
ssNMR	solid-state Nuclear Magnetic Resonance
TOCSY	Total Correlation Spectroscopy
TROSY	Transverse Relaxation Optimised Spectroscopy

Chapter 1

General Introduction



1.1 General Introduction

Macromolecular complexes are an essential aspect of all cellular processes, including metabolism, cell signalling, gene expression, trafficking, cell cycle regulation and the formation of sub-cellular structures. Their malfunction can lead to all kinds of diseases. Therefore understanding these systems, their formation and the protein- protein interactions that are their building blocks is of great interest. Combined efforts of scientific disciplines are needed to obtain a detailed picture and to place the complex in the big biological picture of cells. For a detailed understanding of biomolecules and their interactions, structural biology is applied. There are three major disciplines. Cryo-electron microscopy (cryo-EM) is electron microscopy performed on cryogenically cooled samples which allows imaging of the average structure of a molecular assembly. X-ray crystallography relies on the scattering of X-rays due to the passage of the rays through a biomolecular crystal to solve structures. Finally, nuclear magnetic resonance (NMR) relies on the behaviour of nuclear spins in relation to their environment to study biomolecular structure and dynamics. With solid-state NMR (ssNMR), very large molecular assemblies may be studied, such as Microtubules (MTs) and Liquid-liquid phase separates (LLPS).

MTs are biopolymers that play an essential role in mitosis, cell migration and polarization. Many of these functions critically rely on microtubule-associated proteins (MAPs) and their association with MTs. However, so far, little is known about the interaction of MAPs and their intrinsically disordered regions with the dynamic MTs surface. In particular, the role of the unstructured C-terminal tails of tubulin, critical for many MAP interactions, has remained elusive. Considering the importance of protein dynamics for MTs function, and especially the role of the highly flexible tubulin tails in cellular processes and human disorders such as ciliopathies, cancer and neurodegeneration ¹, it is of high significance to unravel the molecular mechanisms and structures underlying these processes. NMR now offers the

possibility to further elucidate the interaction of whole MTs with MAPs without neglecting the dynamics experienced by the proteins ²⁻⁴.

In contrast to MTs, LLPS are biomolecule-built compartments. They exhibit dynamic structures that can condense or dissolve under specific conditions to regulate molecular functions. These biomolecular condensates can play key roles in cellular processes like DNA repair, stress response or processing of RNA. The combination of solution and solid-state NMR in allows the study of these systems as interacting complexes. A first insight into simplified mRNA processing bodies shows the potential of this approach ⁵. Nonetheless, a deeper understanding of enzyme behaviour in the LLPS is still missing.

Considering the importance of MTs and LLPS for cell function and the potential power of NMR, and especially ssNMR, I present here my research utilising this method for these macromolecular complexes.

1.2 Nuclear Magnetic Resonance

Nuclear magnetic resonance (NMR) spectroscopy is based on the principle that every atomic nucleus possesses a spin. If this spin is non-zero, it will align in an external magnetic field. Nuclei with an even number of protons and neutrons are therefore NMR inactive.

The interaction of a spin 1/2 nucleus (e.g. ¹H, ¹³C, ¹⁵N, ³¹P) leads to two spin states, one of high energy where the spin is aligned against the external magnetic field and one of low energy where the alignment is with the external magnetic field. More nuclei occupy the low energy state N_{lower} than the higher one N_{upper} . The Boltzmann equation gives the distribution of the two states:

$$\frac{N_{upper}}{N_{lower}} = e^{\frac{-\Delta E}{kT}} \quad (1.1)$$

In the equation ΔE is the energy difference of these two Zeeman energy states, which can be calculated using:



$$\Delta E = \gamma \hbar B_0 = \hbar \omega_0 \quad (1.2)$$

Where B_0 is the magnetic field strength, γ is the gyromagnetic ratio (the ratio of a nucleus magnetic moment to its angular momentum), \hbar is the reduced Planck constant and ω_0 is the Larmor frequency (**Fig. 1.1**). This radio wave frequency denotes the precession rate of the nuclei in the magnetic field. The energy gap between the two Zeeman energy states is relatively small, making NMR a low sensitivity spectroscopy.

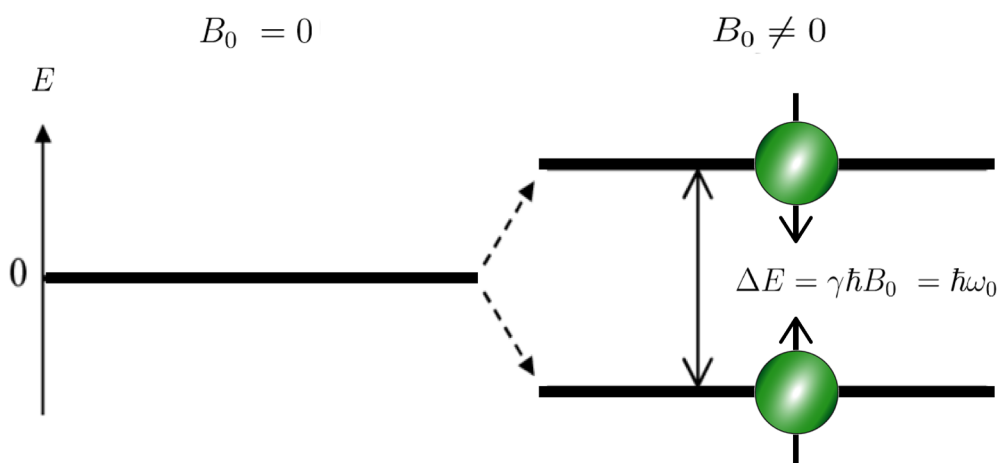


Fig. 1.1: Zeeman energy levels for a spin 1/2 nucleus. With an external magnetic field along the Z-direction the spin will align against or with the field.

To record an NMR signal, a sample placed in a magnetic field is excited by a pulse matching the Larmor frequency, leading to the reorientation of the atomic spins so that their precession around the magnetic field axis can be detected by detection coils in which they induce an electric current (**Fig. 1.2**). This is depicted as a 90° flip of magnetisation into the transverse plane. In the absence of further pulses, the magnetisation returns to its initial state, giving rise to a free induction decay (FID) signal. The NMR spectrum hence contains the detected resonance frequencies after Fourier Transformation of the FID.

The field-independent chemical shift units δ in parts per million (ppm) are used to normalize the frequency values (in Hz), which are dependent on the external magnetic field. Since this has an arbitrary value a standard reference point is needed (eq. (1.3)).

$$\delta_{(ppm)} = \frac{\nu_{sample} - \nu_{standard}}{\nu_{spectrometer} (MHz)} \quad (1.3)$$

The process leading to the return of the signal to its initial position is called relaxation. A realignment along the external magnetic field is called T_1 -relaxation or spin-lattice relaxation, and a dephasing of the spins in the transversal xy-plane is called T_2 -relaxation or spin-spin relaxation (Fig. 1.2).

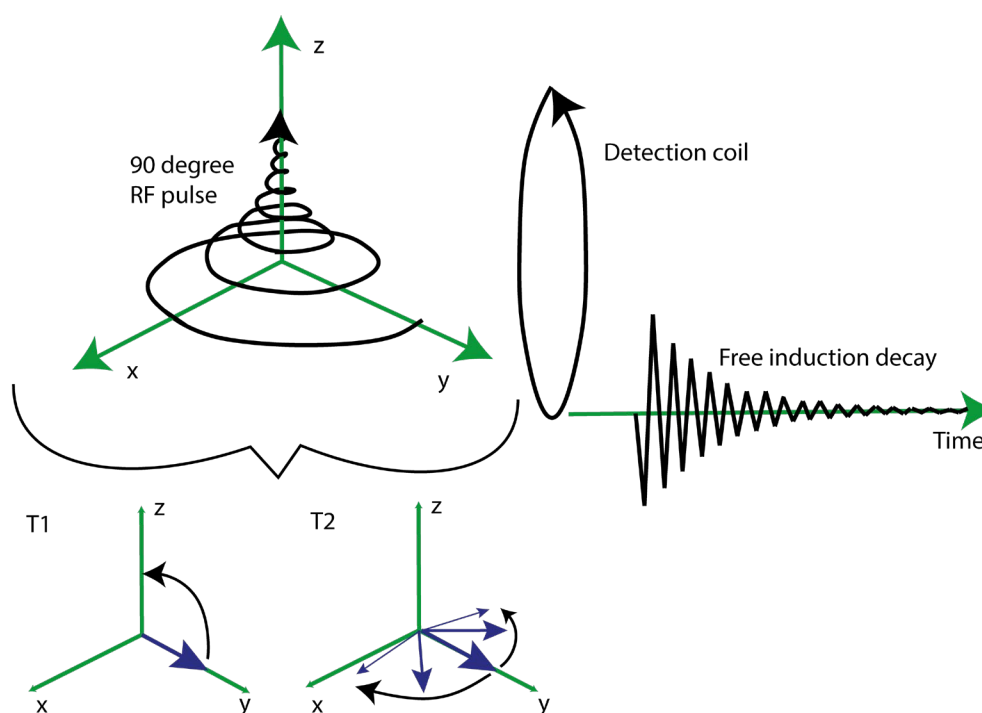


Fig. 1.2: Signal detection in NMR. To detect a signal in NMR a radio frequency pulse is applied and the precession of the magnetisation around the main magnetic field is detected in the detection coils. The result is a free induction decay signal. T_1 (spin-lattice)-relaxation is the exponential relaxation from a higher energy. T_2 (spin-spin)-relaxation is the decay

of the magnetization within the xy-plane. This leads to an exponential decay in the received NMR signal.

Chemical Shift

Electrons, which form a current in a magnetic field, can shield a nucleus and change its precession frequency, leading to a modified signal in the detector coils. Depending on the local surrounding of a nucleus, its Larmor frequency is modified because, as seen before, the Larmor frequency depends on the local magnetic field that a spin experiences. The environmental effect leads to the characteristic shift in frequency in the NMR spectrum and is defined as the chemical shift. This shift depends on the nucleus orientation, giving rise to the chemical shift anisotropy (CSA). In a solid sample, a molecule can adopt different orientations, each with a different chemical shift associated with it. This results in a broadening of the line shape resulting in the so-called “powder pattern”. In solution, however, molecules tumble rapidly. Therefore different orientations are populated equally, causing the averaging of the anisotropy.

Spin Interactions

The nature of magnetic interaction of a spin with another spin results in specific chemical shifts and gives rise to spin-spin interactions (**Fig. 1.3**).

J-coupling

J-coupling (also often referred to as scalar coupling) are indirect interactions between two nuclear spins mediated by the bonding electrons. A nucleus is not only influenced by its surrounding, but it also interacts with its surrounding electrons depending on the spin orientation. A change in the polarization of a neighbouring electron spin might, therefore, through the connecting bond leads to a change in an electron spin in the proximity of another nuclear spin, which changes subtly the

Larmor frequency of this second spin. Therefore scalar couplings are a great tool to study the through-bond connectivity of molecules.

Dipolar coupling

In contrast to scalar coupling, dipolar couplings are mediated through space. They arise through their magnetic moment, leading to a spin generating its own magnetic field, which, like a bar magnet, influences nearby magnets. In the same way as bar magnets, dipolar interactions are orientation-dependent, just like the CSA.

Dipolar couplings usually are bigger than J-couplings and depend on the distance and orientation of the two spins to each other and the gyromagnetic ratio. This spin-spin interaction can be homonuclear (between the same kind of spins) or heteronuclear (between different types of nuclei).

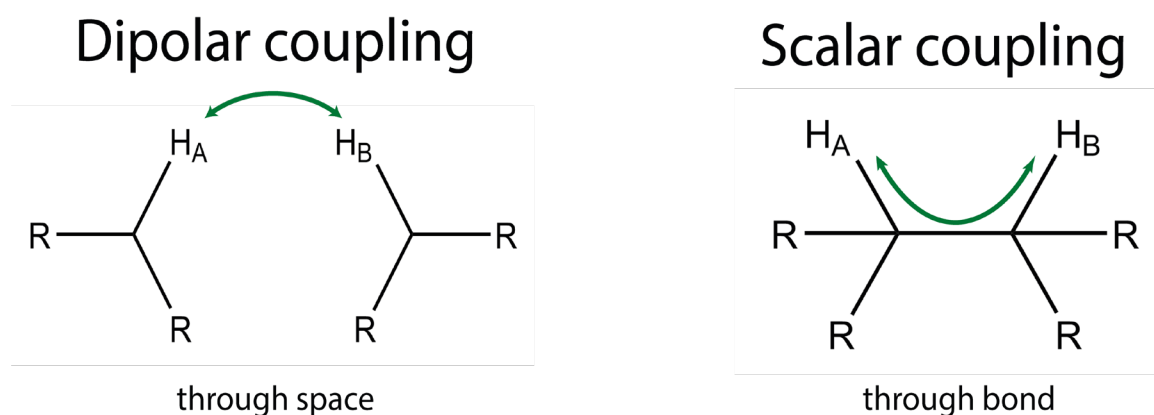


Fig. 1.3: Schematic representation of dipolar and scalar coupling between two proton spins H_A and H_B . Dipolar couplings are through space (**left**), while scalar ones are transmitted through bond (**right**).

Magic-Angle Spinning

In solution-state NMR molecules are free to tumble, which leads to averaging of the orientation dependence of dipolar couplings and the CSA. Unfortunately, if the molecule to be measured has an increased molecular mass, as seen for

Chapter 1

microtubules, the tumbling becomes slower and the signal broadens. Within solids, the molecules are found in many random orientations, leading to strong anisotropic interactions that dominate the NMR spectrum. The result is a so-called powder spectrum.

To overcome this issue and increase the spectral resolution, Magic-Angle Spinning (MAS) of the NMR sample in an NMR rotor is performed. The magical angle is at 54.74° with respect to the external magnetic field ⁶. This technique attenuates the anisotropy by averaging it out. However, to effectively average out an interaction, the sample must spin at a frequency higher than the interaction strength. For example, spinning around 5 kHz will already remove most ^{13}C - ^{13}C and ^{13}C - ^1H couplings. While 30 kHz is required to remove one bond ^{13}C - ^1H couplings, higher MAS rates (> 40 kHz) are needed to also suppress ^1H - ^1H couplings and to conduct proton-detected ssNMR experiments. At MAS rates up to 30 kHz, detection is often on ^{13}C or ^{15}N and interactions to proton spins are decoupled. The general idea of decoupling is to irradiate the spins of a type of nucleus by transmitting a continuous radio frequency (RF) pulse at their Larmor frequency thereby removing couplings to other spins. Notably and unlike MAS, RF decoupling can be used to remove both dipolar and scalar couplings. Other techniques to overcome the signal broadening and spectral overlap are using specific labelling schemes, deuterating the sample, or spinning even faster. Ultra-fast MAS with spinning rates up to 125 kHz are available today (**Fig. 1.4**). In general, to achieve high spinning speeds small MAS rotors are used, getting down in size to 1.3 or even 0.7 mm radii with samples volumes in the order of one microliter.

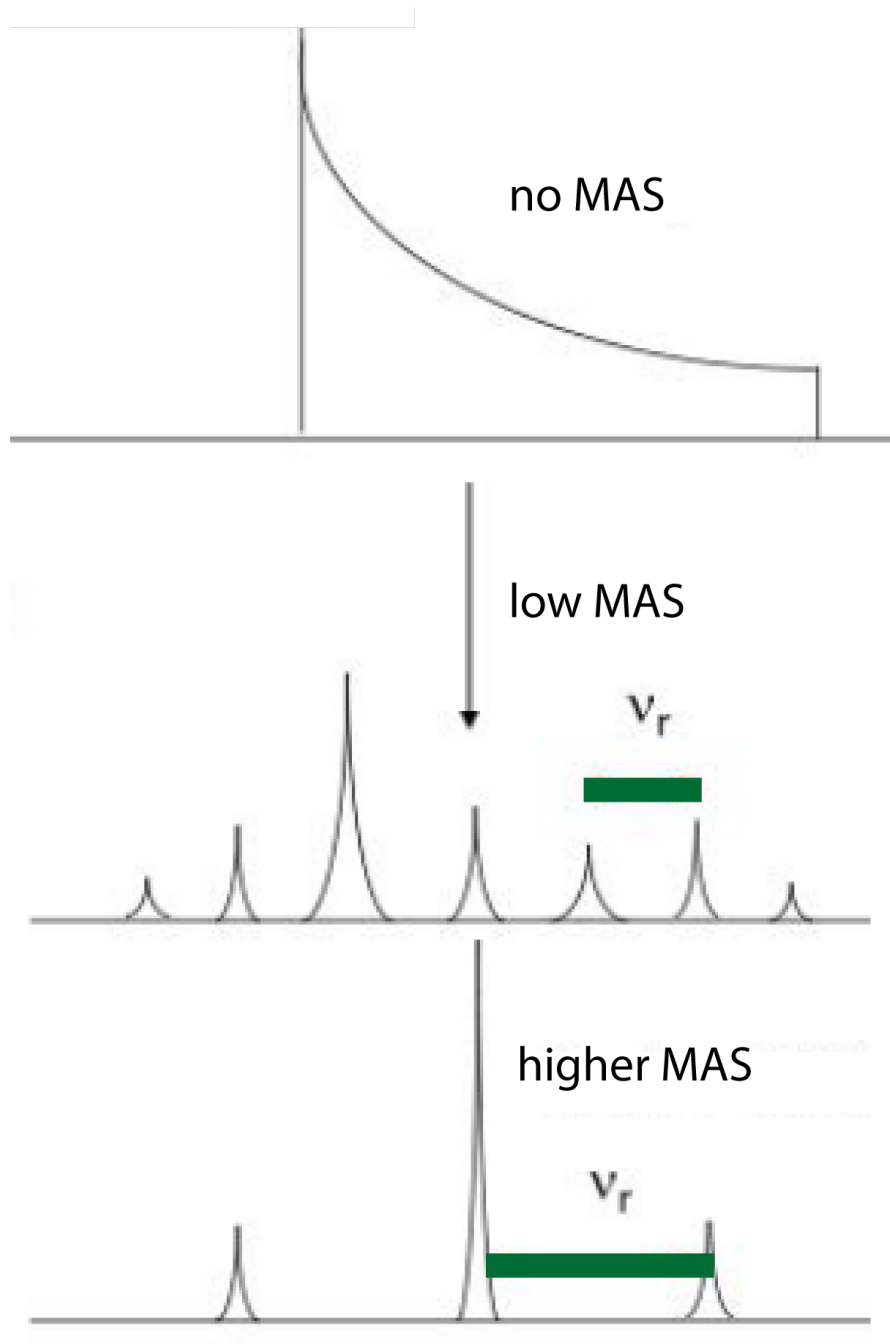


Fig. 1.4: Schematic representation of the removal of anisotropic interactions by magic-angle spinning at the “magic” angle of 54.74° in respect to the static magnetic field. At the **top** a powder pattern, that results from chemical shift interactions is displayed. At a low spinning frequency this pattern is split into a series of spinning side bands (**middle**), which are averaged out by a MAS frequency above the magnitude of the anisotropic interactions (**bottom**).

Proton detection

Combining high-speed MAS with proton detection allows recording high sensitivity ssNMR spectra. The higher sensitivity arises not only through the high natural abundance but also through the bigger gyromagnetic ratio of ^1H . Compared to other common atoms in biological samples, the proton's gyromagnetic ratio is four times greater than that of ^{13}C and even ten times larger than that of ^{15}N . As mentioned earlier, high spinning speeds are needed to average out the dipolar interactions between the ^1H spins.

NMR experiments used in this thesis

Structural biology is a branch of biology that deals with the structure of biological macromolecules. Specifically, X-ray crystallography, cryo-electron microscopy and NMR are commonly used to study protein structures and interactions. NMR is especially well suited to look at protein dynamics, and therefore the study of intrinsically disordered proteins and coiled-coil regions. Additionally, by means of ssNMR, the atomic-level analysis of large complexes like microtubules ⁷, fibrils ⁸ or nucleosomes ⁹ becomes possible.

Solution-state NMR experiments

A variety of solution- and solid-state NMR experiments were employed for the investigation of the interaction of microtubule-associated proteins (MAPs) with microtubule (MTs).

In solution-state NMR, experiments are mostly recorded utilising the through-bond J-couplings between spins. By recording a two-dimensional heteronuclear single-quantum correlation (HSQC) experiment ¹⁰, a spectrum with a ^1H dimension and an X nucleus in the second dimension can be recorded. The HSQC is connecting either ^{13}C or ^{15}N with ^1H , which allows the study of single bond correlations in a protein ¹¹.

Each residue, except proline in ^{15}N -HSQC, will produce an observable peak in the spectrum. Especially the ^{15}N -HSQC experiment enables the observation of slight changes in the environment of residues. The transverse relaxation optimised spectroscopy (TROSY) experiment ¹² deals with the issue that the NMR signal from larger molecules decays faster and therefore leads to a broader signals ¹³. In the pulse sequence of this experiment, only the slowest decaying multiplet signals of J-coupled nuclei are selected, while in an HSQC, these signals are collapsed. This significantly increases the resolution and extends the mass range of molecules that can be studied by solution NMR, while providing a spectrum of almost identical appearance to the HSQC. To know which residue gives rise to which peak in an HSQC spectrum, an array of three-dimensional solution-state experiments can be used to assign the chemical shifts. Experiments like HNCACB (**Fig. 1.5**), HNCACO, CBCA(CO)NH, HNCO, HNCA or HBHACONH ^{14–17} provide information about the chemical shifts of the backbone residues and the side chains of the protein. These three-dimensional NMR experiments resolve overlapping regions and give the sequential connection of residues/atoms employing heteronuclear through-bond couplings of ^1H , ^{13}C and ^{15}N nuclei.

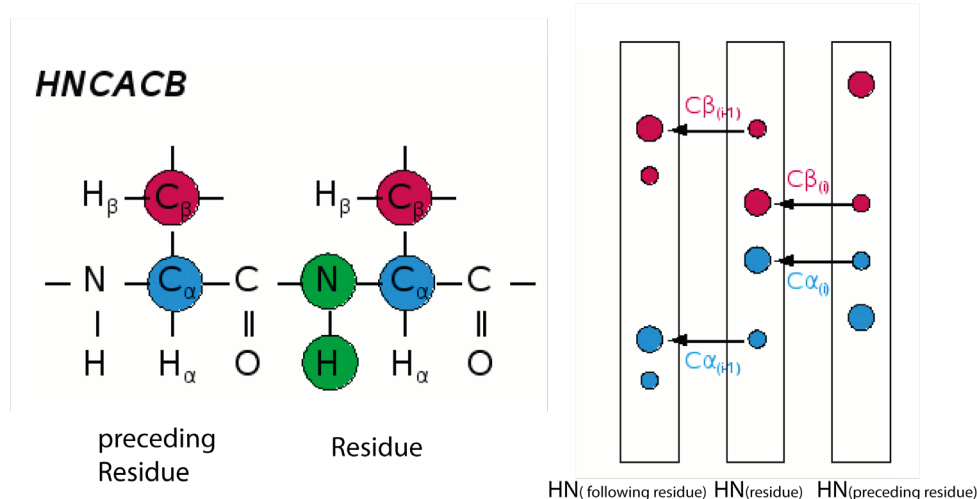


Fig. 1.5: HNCACB. The HNCACB spectrum provides H, N, CB and CA resonances of residues and CB and CA resonances of its preceding residue. Adapted from the CCPNMR website ¹⁸ (<https://protein-nmr.org.uk/solution-nmr/>).

Solid-state NMR experiments

As mentioned before, both scalar and dipolar-based spin-spin interactions can be exploited in the context of ssNMR experiments ^{19,20}. By utilising the spins that exchange magnetisation through space via dipolar couplings, ssNMR allows studying a molecule's rigid/folded parts. Since the two spins are changing their orientation too fast for the magnetization to be transferred between them, the flexible components of the sample are averaged out. Several dipolar-based ssNMR experiments have been used in this thesis. The focus was especially on heteronuclear proton detected ¹H-¹³C correlation and ¹H-¹⁵N correlation experiments. To increase the sensitivity of these experiments based on dipolar couplings, cross-polarisation (CP) is utilised ²¹. During CP, a spin with a high gyromagnetic ratio (normally proton spins) transfers magnetisation to a heteronucleus close in space (**Fig. 1.6**). This process increases the magnetisation of spins with a lower gyromagnetic ratio. Moreover, proton relaxation times are usually shorter and thus their transferred magnetisation will faster return to the equilibrium value via T₁ relaxation. Consequently, experiments utilising CP can use a shorter delay time between measurements and will obtain stronger signals (typically 2-4 times for ¹³C and for ¹⁵N, respectively).

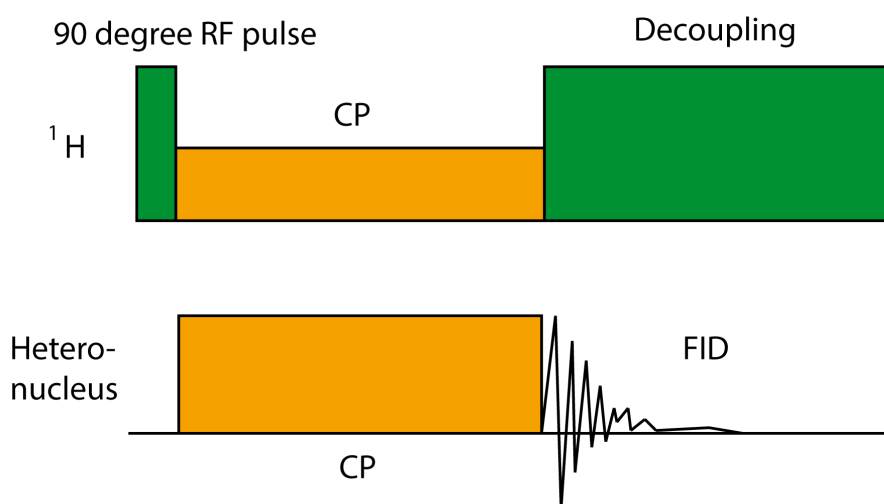


Fig. 1.6: Schematic representation of a cross polarization pulse sequence. During the CP step the magnetization is transferred from the ¹H to the heteronucleus and subsequently measured during the FID in the presence of ¹H decoupling.

In contrast to experiments based on dipolar couplings, a J-based experiment allows measuring the flexible parts of a protein (or other biomolecules) in ssNMR. The reason for this is that rigid elements usually exhibit a shorter T_2 relaxation time. By having longer delays in J-based NMR experiments, these signals are therefore filtered out. When performing heteronuclear proton detected ^1H - ^{13}C and ^1H - ^{15}N experiments and comparing dipolar experiments with solution-state NMR experiments probing the same nuclei, it becomes possible to elucidate residues that become rigid or remain flexible upon binding to an unlabelled interaction partner or undergo other modifications. Together and demonstrated in this thesis, such experiments can contribute to obtaining a more comprehensive picture of the structural and dynamics changes that accompany formation of a large protein complex by NMR.

1.3 Microtubule

Microtubules (MTs) are next to actin and intermediate filament one of the three cytoskeletal structures in eukaryotic cells (**Fig. 1.7**). For example, they are essential in intracellular organization, organelle trafficking and mitosis. MTs are highly dynamic structures that undergo continuous assembly and disassembly within the cell. They grow by appending α/β -tubulin dimers. These dimers contain guanosine-5'-triphosphate (GTP) at the nucleotide-binding sites of α -tubulin and β -tubulin ²². In the MT complex, GTP of the β -tubulin site is eventually hydrolyzed into guanosine-5'-diphosphate (GDP). Interestingly, GDP makes MT more prone to depolymerization and therefore explains the polymer's dynamic instability. The GTP bound to α -tubulin is buried by the β -tubulin rendering it non-hydrolysable.



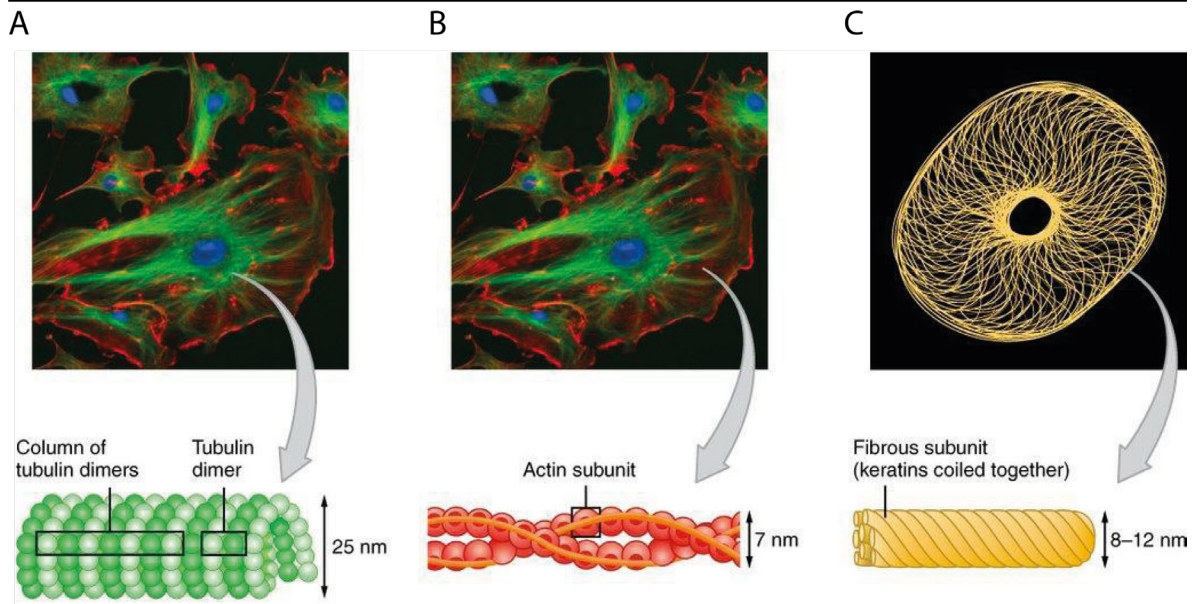


Fig. 1.7: The three cytoskeletons. The images are showing the filaments location within cells by fluorescence imaging (**top**) and their schematic structure (**bottom**). **(A)** microtubules (green in the fluorescent image), **(B)** actin (red in the fluorescent image) and, **(C)** intermediate filaments ²³.

Polymerization of MTs leads to the formation of a hollow tube out of 13 protofilaments with a fast-growing plus end and a slow-growing minus end (**Fig. 1.8**).

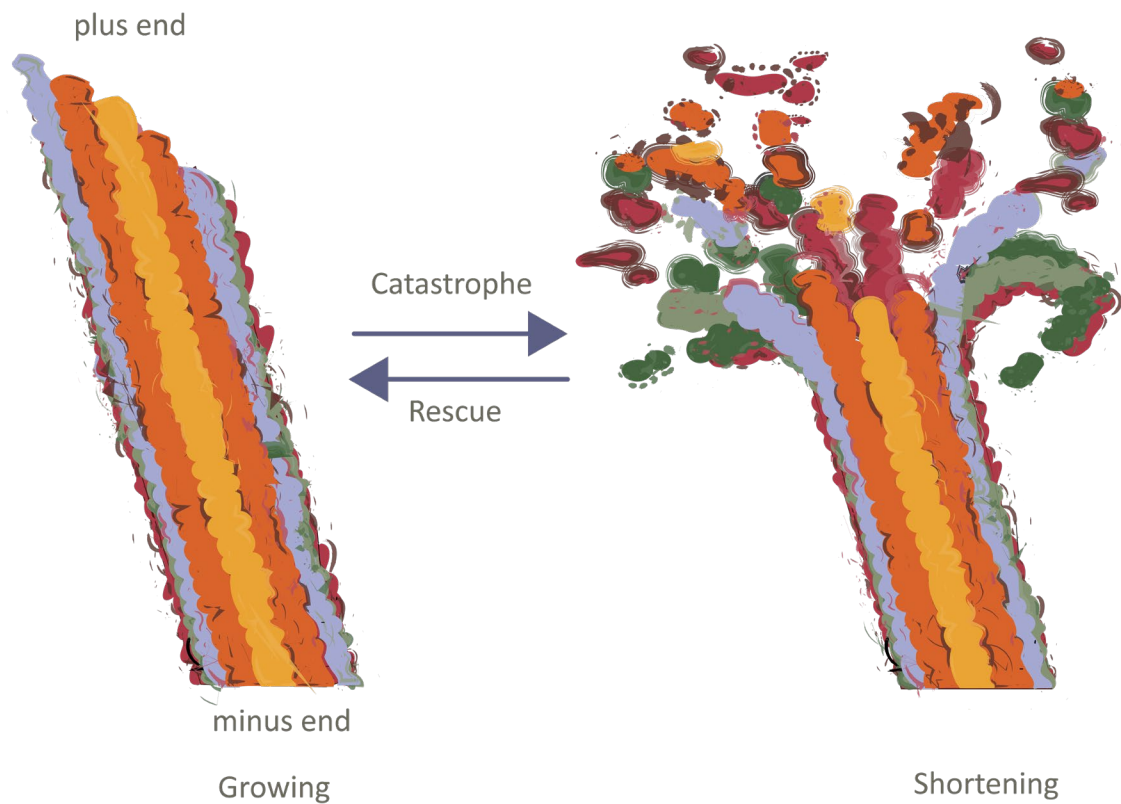


Fig. 1.8: Left: Representation of the dynamic polymerisation. **Right:** depolymerisation cycle of Microtubules. The biopolymers are composed of tubulin heterodimers that assemble in a head to tail fashion giving the Microtubules an unstable plus and a more stable minus end.

Chapter 1

Tubulin dimers consist of two closely related 55-kDa proteins, α -tubulin and β -tubulin (**Fig. 1.9**). There are several tubulin isotypes showing specificity for tissue types ²⁴. Even among the animal kingdoms, the fold of the tubulin core is highly conserved. The main differences between the different isotypes are their carboxy-terminal tails (CTT) ^{25,26}. The CTTs of the tubulin extend outwards of the microtubule tube structure. In contrast to the rigid and well-folded tubulin core, those tails are highly dynamic. Additionally, CTTs are also highly negatively charged, consisting primarily of glutamates ²⁷. The surface exposure makes CTTs a likely target of many post-translational modifications (PTMs) ²⁸⁻³¹. This molecular and chemical diversity via the combination of different tubulin isotypes and PTMs even led to the term 'tubulin code' to explain the fine-tuning observed in MT function ³².

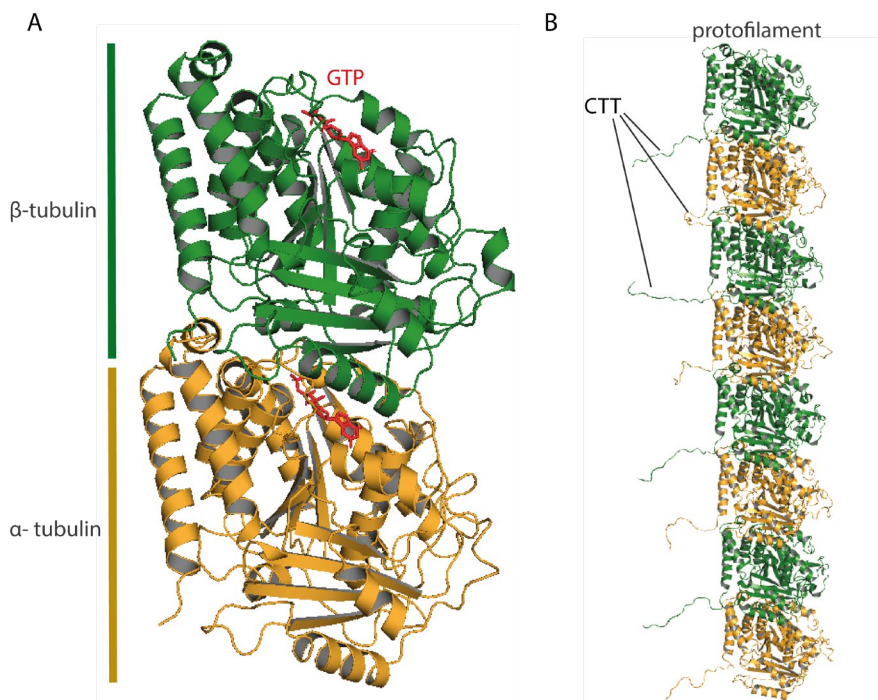


Fig. 1.9: Tubulin organization in MTs (A) Representation of a tubulin dimer with GTP (red) bound in the α -tubulin (orange) and GDP (red) in the β -tubulin (green) (PDBid: 1TUB). In **(B)** the protofilament is shown, including the CTTs (adapted from PDBid: 7PQC).

MTs are subject to almost all known PTMs ³³. While the tails seem to be a major modification site, several PTMs like acetylation occur at the lumen of the tubulin tube ^{34,35}. The tail modifications are associated with changing the interaction of the MTs

with its surrounding. Common modifications include polyglutamylation, polyglycylation and detyrosination ³². For several psychological processes, significant progress has been made in studying the importance of the tubulin code. A particularly noteworthy example is the importance of glutamylation, which controls sperm development and function, as deregulation leads to male infertility in mice ³⁶.



Microtubule-Associated Proteins

The execution of the incredible variety of MTs functions needs the binding and interaction with microtubule-associated proteins (MAPs). These MAPs play an essential role in regulating the MTs structure, stability, and length and perform other functions such as the transport inside the cell or localization of the MTs by attaching them to other cell structures ³⁷.

Intuitively, the tubulin code is a perfect regulator of these MAPs-MTs interactions, allowing pattern and isotype-specific regulations, also considering the importance of the flexible CTTs. For example, the mitotic spindle assembly depends on the binding of Dam1 to the CTTs ³⁸ and the stabilization of MTs is linked to the greater binding of MAP2 ³⁹ or Tau ⁴⁰ due to their interactions with the CTTs.

The Tau protein is one of the first discovered MAPs ⁴¹ and it is primarily found in neurons where it seems to play a role in microtubule assembly ^{42,43}. However, Tau also appears to disrupt kinesin-1 binding to MTs ⁴⁴. As a result, it affects cargo transport along the cytoskeleton, as kinesins are motor proteins. Because of its hydrophilic character, Tau is an intrinsically disordered protein, not adapting any specific fold ^{45,46}. The flexibility of the Tau protein makes it difficult to study by cryo-EM and crystallography. The probably most complete description of the soluble Tau is therefore found in a paper by Mukrasch *et al.* (2009) who used NMR for their investigations ⁴⁷. For the MTs-bound Tau several studies were performed giving rise to a fuzzy binding mechanism ^{48–50} also discussed in the context of cryo-EM data incorporated into molecular dynamics simulations (**Fig. 1.10**) ⁵¹. A latest model was suggested by solid-state nuclear magnetic resonance ⁵².

Chapter 1

Tau is a highly-studied MAP because of its association with neurodegenerative diseases called tauopathies ⁵³. One example is Alzheimer's disease. There the protein is found to be hyperphosphorylated ^{54,55} in a manner that its MTs binding capacity is impaired, the results are Tau aggregates and destabilized MTs ^{56,57}. The destabilization of the MTs might lead to neuron death and, hence, the disease's progression. Intriguingly, Tau shares many characteristics of proteins known to induce liquid-liquid phase separation and found in membrane-less organelles ^{58,59}. A growing body of studies has found evidence of additional physiological roles of Tau in phase separates, including importance in messenger ribonucleic acid (mRNA) procession ⁶⁰ and the nucleation of MTs polymerization ⁶¹. To this end, several research groups confirmed that through a prolonged existence of the phase separate aggregation-prone Tau species can form. This eventually might lead to toxic Tau filaments present in diseases like Alzheimer's ⁶².

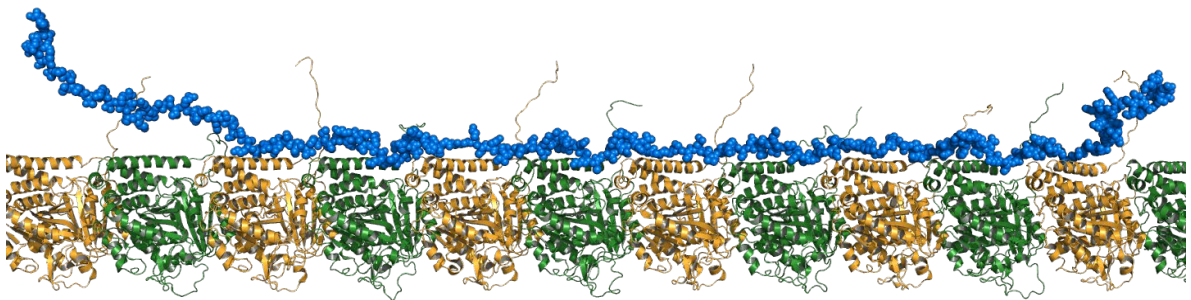


Fig. 1.10: Computational structural ensemble of the extended microtubule binding region of Tau (202-395) with Microtubule (PDBid: 7PQP), as determined by EMMI, which is a method of metainference able to incorporate cryo-EM data into molecular dynamics simulations. Tau is displayed in blue, α -tubulin orange, β -tubulin green.

Unlike Tau, the microtubule-associated protein 7 (MAP7) is far less studied and shows an alpha helix fold for its microtubule-binding region (**Fig. 1.11**). Moreover and unlike Tau, MAP7 is required for kinesin-driven transport in the cell ⁶³.

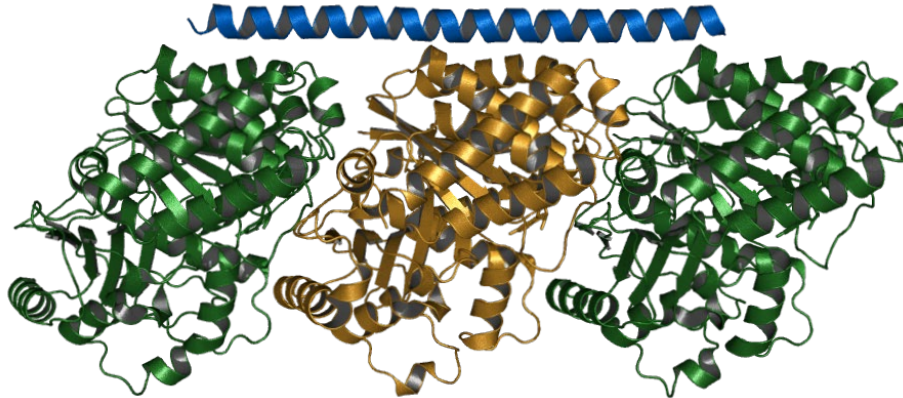


Fig. 1.11: The structural ensemble of a 53 long stretch of MAP7 interacting with Microtubule based on cryo-EM (PDBid: 7SGS). MAP7 is displayed in blue, while α -tubulin is orange and β -tubulin green.

Studying the Microtubule structure and interaction with Microtubule-Associated Proteins

Microtubules (MTs) and their binding to Microtubule-Associated Proteins (MAPs) have been studied by structural biology techniques since the development of these methods. In spite of inherent challenges ⁶⁴, cryo-electron microscopy (cryo-EM) has been extensively used for such studies. Pseudo symmetries induced by the presence of the MTs seam and variability of the lattice are complicating the analysis, particularly if more than a tubulin dimer needs to be analysed ⁶⁵.

Additionally, X-ray crystallography provided several structures of tubulin in complex with MTs polymerisation inhibitors or smaller molecules ⁶⁶⁻⁶⁸. An example is stathmin ⁶⁹ which prevents MTs assembly and plays an important role in cellular processes like mitosis ⁷⁰. However, X-ray crystallography cannot be used study intact polymerized MTs.



Eventually, nuclear magnetic resonance (NMR) spectroscopy has given insights into MAP behaviour in solution, but also into their binding mechanism ⁷¹. For example, the binding of Tau was studied with solution-state NMR. These studies discuss the binding of the MTs binding repeats and part of the proline-rich region ⁷²⁻⁷⁴.

Recent advances were also accomplished in our group, allowing the isotopic labelling of MTs and therefore the study of whole MTs, including their flexible carboxy-terminal tails with solid-state NMR ^{4,7}.

1.4 Processing Bodie's assembly and Liquid-Liquid Phase Separation

A similarity observed in many protein aggregation diseases is that the associated protein can undergo liquid-liquid phase separation (LLPS) and interacts in this state with RNA or DNA ⁷⁵. As previously mentioned the Alzheimer's associated protein Tau is considered to be a notable example ⁶², but also proteins like FUsed in Sarcoma (FUS) are found aggregated in amyotrophic lateral sclerosis (ALS) ⁷⁶ or the prion protein, infamous for inducing transmissible spongiform encephalopathies ⁷⁷ shows this pattern.

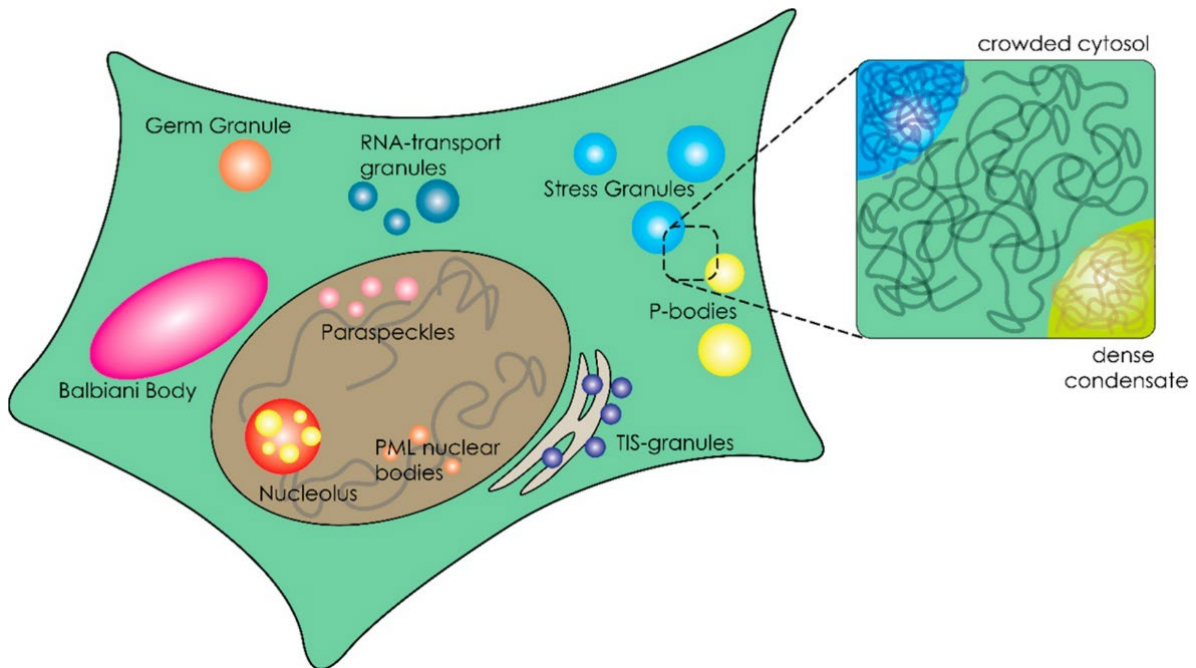


Fig. 1.12: Organelle organization in an eukaryotic cell. The figure gives a schematic overview of the membranous and membrane-less organelles in an eukaryotic cell. The concept of membrane-less organelles is highlighted with a box ⁷⁸.

Condensates can form cellular membrane-less organelles of higher protein density and a gel-like viscosity, which, for example, allow for increased rate and catalytic turnover of biochemical reactions ^{79,80}. Examples include nuclear condensates mediating transcription ⁸¹, chromatin condensates ⁸² or the control of mRNA degradation in so-called processing bodies (**Fig. 1.12**) ⁸³. To regulate such processes, the involved proteins in LLPS exhibit weak and dynamic interactions ⁸⁴ and a constant exchange with the environment is observed. Interactions between the involved proteins might strengthen over time leading to a more mature state and eventually to a solid phase. Proteins that initiate phase separation often contain intrinsically disordered regions that interact with the condensed matter molecules and more well-folded regions that adapt their folds to oligomerise the structuralising proteins. The review of Wang et al. describes in greater detail how these processes in relation to the physiological function of these condensates can be understood ⁸⁰.

Chapter 1

Several techniques are used to study LLPS. Nonetheless, the study of the processes leading to condensation on an atomic level has proven challenging due to the dynamic nature and divergence of the involved molecules. Cryo-electron microscopy and X-ray crystallography are vital tools to shed light on the matured state and the fibrillated proteins, but give little insight into the physiological present form. Solution-state NMR can partly overcome this issue and was therefore extensively employed to gain information on the components of LLPS^{85–87}. Finally, solid-state NMR allows for studying the gel-like phase separation by probing both the ensemble's rigid and flexible parts. Therefore, ssNMR can provide the essential link to understanding the importance of the intrinsically disordered regions and the oligomerisation process which have been proven necessary for LLPS.

For example, significant advances in the LLPS and maturation mechanism of mRNA processing bodies have been made showing the specific conformation of the gels central hub enhancer of decapping 3 (Edc3) in its phase-separated state⁵ (**Fig. 1.13**). On the other hand, the state of enzymatic components including the decapping protein 2 (Dcp2) in the LLPS remains unclear. Dcp2 is a key protein involved in the regulation of mRNA decay. It is responsible for removing the cap structure from mRNAs, which triggers their degradation⁸⁸.

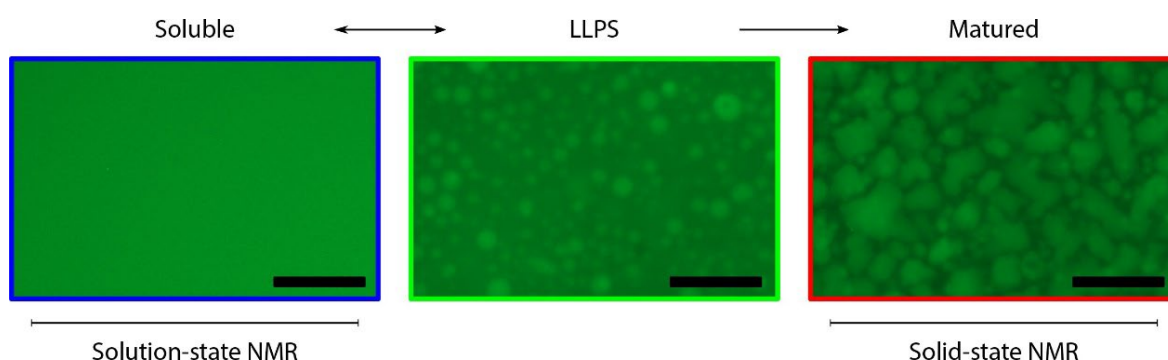


Fig. 1.13: Fluorescence microscopy images of the three states of the processing bodies central-hub Edc3 showing that the process of phase separation can be studied by solution and solid-state NMR. On the left soluble Edc3-dLsm, in the middle panel Edc3 is undergoing liquid-liquid phase separation. The right panel shows the matured phase of Edc3 that can be studied by solid-state NMR. The scale bar has a length of 50 μm . The figure is adapted from Damman et al⁵.

1.5 Scope of this thesis

This thesis aims to contribute to our knowledge of the interaction of microtubule-associated proteins (MAPs) with microtubules (MTs), which is fundamental to understanding the complex interplay leading to MTs performing their multiplex of essential functions. We used a combination of state-of-the-art solid-state nuclear magnetic resonance (NMR), solution-state NMR, and biophysical and biochemical methods to archive this. Moreover, the phase-separation of processing bodies was studied with the aim of understanding the complex ensemble of proteins and mRNA in the phase-separated state.

Chapter 1 gives a general introduction to the mechanisms underlying NMR and how to implement them to obtain information about complex systems. Also, the biological background and importance of MTs and MAPs are discussed in this chapter and a general overview of processing bodies is given.

Chapter 2 presents the assignment of the microtubule binding domain of the protein MAP7 in solution. This chapter additionally investigates the MAPs secondary structure and its behaviour in a free, unbound form.

Chapter 3 provides a protocol to prepare isotopically labelled MTs from HeLa S3 cells. The functional MTs enable the analysis of the biopolymers by ssNMR.

Chapter 4 discusses a novel hCCH through-bond sequence to measure mobile side-chains of complex biomolecules with High-resolution Magic-Angle Spinning via proton detection. The approach involves an additional broadband through-bond CC transfer.

Chapter 5 examines the interaction of MAP7s microtubule-binding domain (MTBD) with MTs. By using the previously obtained solution-state NMR assignment, we were able to study MAP7s MTBDs binding to MTs by high-resolution proton- and carbon-detected solid-state NMR, as well as by solution-state NMR. In addition we studied the binding of MAP7 to MTs by cryo-EM and we present an approach to study the



Chapter 1

interaction of the carboxy-terminal tails of MTs and their interaction with MAPs. We designed peptides comprising the carboxy-terminal tails and studied their interactions with the MAPs. In this chapter we report a comprehensive view of the MAP7-MT binding mode with particular focus on the interaction between MAP7 and the MTs tails.

In the **Chapter 6**, we use a combination of solution- and solid-state NMR to probe the binding of the MAP Tau to MTs. By comparing the spectra of free Tau with the spectra of Tau bound to MT, binding and flexible regions could be specified. Moreover, this chapter studies the interaction of MTs carboxy-terminal tails with Tau by titrating peptides comprising the tails to their interaction partners in solution-state NMR. In this case, the focus was on the change in the MAP. In order to validate the binding fluorescence anisotropy experiments were performed. Also, we cleaved off the carboxy-terminal tails of the biopolymer with subtilisin. Moreover, solid-state NMR experiments served to look at the changes from the side of the tails. To gain this information the MAPs were bound to labelled MTs and scalar-based NMR spectra were recorded.

Chapter 7 discusses the LLPS of mRNA processing bodies studied by solution- and solid-state NMR, elucidating not only the full-length structure and interaction of proteins in phase separates, but also giving structural and dynamics insights into the enzymatic activity of the mRNA decapping protein 2 in this state.

Finally, **Chapter 8** summarizes this thesis's findings, sets them in context with the greater picture and discusses possible future work. This chapter emphasizes how NMR can be used in the future for probing MAP-MTs interactions and studying LLPS.

References

1. Gadadhar, S., Bodakuntla, S., Natarajan, K. & Janke, C. The tubulin code at a glance. *Journal of cell science* **130**, 1347–1353 (2017).
2. Atherton, J. *et al.* Structural determinants of microtubule minus end preference in CAMSAP CKK domains. *Nature communications* **10**, 1–16 (2019).
3. Atherton, J. *et al.* A structural model for microtubule minus-end recognition and protection by CAMSAP proteins. *Nature structural & molecular biology* **24**, 931–943 (2017).
4. Luo, Y. *et al.* Solid-State NMR Spectroscopy for Studying Microtubules and Microtubule-Associated Proteins. in *Structural Proteomics* 193–201 (Springer, 2021).
5. Damman, R. *et al.* Atomic-level insight into mRNA processing bodies by combining solid and solution-state NMR spectroscopy. *Nature communications* **10**, 1–11 (2019).
6. Andrew, E., Bradbury, A. & Eades, R. Nuclear magnetic resonance spectra from a crystal rotated at high speed. *Nature* **182**, 1659–1659 (1958).
7. Pines, A. *et al.* Direct observation of dynamic protein interactions involving human microtubules using solid-state NMR spectroscopy. *Nature communications* **11**, 1–10 (2020).
8. Bertini, I., Gonnelli, L., Luchinat, C., Mao, J. & Nesi, A. A new structural model of A β 40 fibrils. *Journal of the American Chemical Society* **133**, 16013–16022 (2011).
9. le Paige, U. B. *et al.* Characterization of nucleosome sediments for protein interaction studies by solid-state NMR spectroscopy. *Magnetic Resonance* **2**, 187–202 (2021).
10. Bodenhausen, G. & Ruben, D. J. Natural abundance nitrogen-15 NMR by enhanced heteronuclear spectroscopy. *Chemical Physics Letters* **69**, 185–189 (1980).
11. Mandal, P. K. & Majumdar, A. A comprehensive discussion of HSQC and HMQC pulse sequences. *Concepts in Magnetic Resonance Part A: An Educational Journal* **20**, 1–23 (2004).
12. Pervushin, K., Riek, R., Wider, G. & Wüthrich, K. Attenuated T₂ relaxation by mutual cancellation of dipole–dipole coupling and chemical shift anisotropy indicates an avenue to NMR structures of very large biological macromolecules in solution. *Proceedings of the National Academy of Sciences* **94**, 12366–12371 (1997).
13. LT, H., PL, L. & SE, P. european patent specification. *proteins* **3**, 375–385 (1993).
14. Wittekind, M. HNCACB, a high sensitivity 3D NMR experiment to correlate amideproton and nitrogen resonances with the α -carbon and β -carbon resonances in proteins. *J. Magn. Reson. Ser. B* **101**, 214–217 (1993).
15. Bax, A. & Ikura, M. An efficient 3D NMR technique for correlating the proton and 15 N backbone amide resonances with the α -carbon of the preceding residue in uniformly 15 N/13 C enriched proteins. *Journal of biomolecular NMR* **1**, 99–104 (1991).
16. Cavanagh, J., Fairbrother, W. J., Palmer III, A. G. & Skelton, N. J. *Protein NMR spectroscopy: principles and practice*. (Academic press, 1996).
17. Ikura, M., Kay, L. E. & Bax, A. A novel approach for sequential assignment of proton, carbon-13, and nitrogen-15 spectra of larger proteins: heteronuclear triple-resonance three-dimensional NMR spectroscopy. Application to calmodulin. *Biochemistry* **29**, 4659–4667 (1990).
18. Grzesiek, S. & Bax, A. Correlating backbone amide and side chain resonances in larger proteins by multiple relayed triple resonance NMR. *Journal of the American Chemical Society* **114**, 6291–6293 (1992).
19. Andronesi, O. C. *et al.* Determination of membrane protein structure and dynamics by magic-angle-spinning solid-state NMR spectroscopy. *Journal of the American Chemical Society* **127**, 12965–12974 (2005).
20. Renault, M., Cukkemane, A. & Baldus, M. Solid-state NMR spectroscopy on complex biomolecules. *Angewandte Chemie International Edition* **49**, 8346–8357 (2010).



Chapter 1

21. Pines, A., Gibby, M. G. & Waugh, J. S. PROTON-ENHANCED NUCLEAR INDUCTION SPECTROSCOPY. A METHOD FOR HIGH- RESOLUTION NMR OF DILUTE SPINS IN SOLIDS. *J. Chem. Phys.* **56**: No. 4, 1776-7(15 Feb 1972). (1972) doi:10.1063/1.1677439.
22. Engelborghs, Y. Dynamic aspects of microtubule assembly. in *Microtubule Proteins* 1–35 (CRC Press, 2018).
23. Katzman, S., Hurst-Kennedy, J., Barrera, A., Talley, J. & Higgins, R. *Fundamentals of Cell Biology*. (2020).
24. Binarová, P. & Tuszynski, J. Tubulin: structure, functions and roles in disease. *Cells* vol. 8 1294 (2019).
25. Fojo, A. T. *The role of microtubules in cell biology, neurobiology, and oncology*. (Springer Science & Business Media, 2009).
26. Aiken, J. *et al.* Genome-wide analysis reveals novel and discrete functions for tubulin carboxy-terminal tails. *Current Biology* **24**, 1295–1303 (2014).
27. Nogales, E., Wolf, S. & Downing, K. Structure of the $\alpha\beta$ tubulin dimer by electron crystallography (Correction). *Nature* **393**, 191 (1998).
28. Peris, L. *et al.* Motor-dependent microtubule disassembly driven by tubulin tyrosination. *Journal of Cell Biology* **185**, 1159–1166 (2009).
29. Janke, C. *et al.* Tubulin polyglutamylase enzymes are members of the TTL domain protein family. *Science* **308**, 1758–1762 (2005).
30. Edde, B. *et al.* Posttranslational glutamylation of α -tubulin. *Science* **247**, 83–85 (1990).
31. Rogowski, K. *et al.* Evolutionary divergence of enzymatic mechanisms for posttranslational polyglutamylation. *Cell* **137**, 1076–1087 (2009).
32. Janke, C. & Magiera, M. M. The tubulin code and its role in controlling microtubule properties and functions. *Nature Reviews Molecular Cell Biology* **21**, 307–326 (2020).
33. Janke, C. & Chloë Bulinski, J. Post-translational regulation of the microtubule cytoskeleton: mechanisms and functions. *Nature reviews Molecular cell biology* **12**, 773–786 (2011).
34. L'Hernault, S. W. & Rosenbaum, J. L. Chlamydomonas. α -tubulin is posttranslationally modified by acetylation on the ϵ -amino group of a lysine. *Biochemistry* **24**, 473–478 (1985).
35. Eshun-Wilson, L. *et al.* Effects of α -tubulin acetylation on microtubule structure and stability. *Proceedings of the National Academy of Sciences* **116**, 10366–10371 (2019).
36. Gadadhar, S., Hirschmugl, T. & Janke, C. The tubulin code in mammalian sperm development and function. in *Seminars in Cell & Developmental Biology* (Elsevier, 2022).
37. Bodakuntla, S., Jijumon, A., Villablanca, C., Gonzalez-Billault, C. & Janke, C. Microtubule-associated proteins: structuring the cytoskeleton. *Trends in cell biology* **29**, 804–819 (2019).
38. Fees, C. P., Aiken, J., O'Toole, E. T., Giddings Jr, T. H. & Moore, J. K. The negatively charged carboxy-terminal tail of β -tubulin promotes proper chromosome segregation. *Molecular biology of the cell* **27**, 1786–1796 (2016).
39. Serrano, L., De La Torre, J., Maccioni, R. B. & Avila, J. Involvement of the carboxyl-terminal domain of tubulin in the regulation of its assembly. *Proceedings of the National Academy of Sciences* **81**, 5989–5993 (1984).
40. Marya, P. K., Syed, Z., Fraylich, P. E. & Eagles, P. Kinesin and tau bind to distinct sites on microtubules. *Journal of Cell Science* **107**, 339–344 (1994).
41. Weingarten, M. D., Lockwood, A. H., Hwo, S.-Y. & Kirschner, M. W. A protein factor essential for microtubule assembly. *Proceedings of the National Academy of Sciences* **72**, 1858–1862 (1975).
42. Paglini, G., Peris, L., Mascotti, F., Quiroga, S. & Cáceres, A. Tau protein function in axonal formation. *Neurochemical research* **25**, 37–42 (2000).

43. Panda, D., Miller, H. P. & Wilson, L. Rapid treadmilling of brain microtubules free of microtubule-associated proteins in vitro and its suppression by tau. *Proceedings of the National Academy of Sciences* **96**, 12459–12464 (1999).
44. Shigematsu, H. *et al.* Structural insight into microtubule stabilization and kinesin inhibition by Tau family MAPs. *Journal of Cell Biology* **217**, 4155–4163 (2018).
45. Cleveland, D. W., Hwo, S.-Y. & Kirschner, M. W. Physical and chemical properties of purified tau factor and the role of tau in microtubule assembly. *Journal of molecular biology* **116**, 227–247 (1977).
46. Woody, R. W., Clark, D. C., Roberts, G. C., Martin, S. R. & Bayley, P. M. Molecular flexibility in microtubule proteins: proton nuclear magnetic resonance characterization. *Biochemistry* **22**, 2186–2192 (1983).
47. Mukrasch, M. D. *et al.* Structural polymorphism of 441-residue tau at single residue resolution. *PLoS biology* **7**, e1000034 (2009).
48. Fung, H. Y. J., McKibben, K. M., Ramirez, J., Gupta, K. & Rhoades, E. Structural characterization of tau in fuzzy tau: Tubulin complexes. *Structure* **28**, 378–384 (2020).
49. Kadavath, H. *et al.* Folding of the tau protein on microtubules. *Angewandte Chemie International Edition* **54**, 10347–10351 (2015).
50. Mukrasch, M. D. *et al.* The “jaws” of the tau-microtubule interaction. *Journal of Biological Chemistry* **282**, 12230–12239 (2007).
51. Brotzakis, Z. F. *et al.* A structural ensemble of a tau-microtubule complex reveals regulatory tau phosphorylation and acetylation mechanisms. *ACS Central Science* **7**, 1986–1995 (2021).
52. El Mammeri, N., Dregni, A. J., Duan, P., Wang, H. K. & Hong, M. Microtubule-binding core of the tau protein. *Science Advances* **8**, eabo4459 (2022).
53. Avila, J. Tau phosphorylation and aggregation in Alzheimer’s disease pathology. *FEBS letters* **580**, 2922–2927 (2006).
54. Biernat, J. *et al.* The switch of tau protein to an Alzheimer-like state includes the phosphorylation of two serine-proline motifs upstream of the microtubule binding region. *The EMBO journal* **11**, 1593–1597 (1992).
55. Wille, H., Drewes, G., Biernat, J., Mandelkow, E.-M. & Mandelkow, E. Alzheimer-like paired helical filaments and antiparallel dimers formed from microtubule-associated protein tau in vitro. *The Journal of cell biology* **118**, 573–584 (1992).
56. Bramblett, G. T. *et al.* Abnormal tau phosphorylation at Ser396 in Alzheimer’s disease recapitulates development and contributes to reduced microtubule binding. *Neuron* **10**, 1089–1099 (1993).
57. Busciglio, J., Lorenzo, A., Yeh, J. & Yankner, B. A. β -Amyloid fibrils induce tau phosphorylation and loss of microtubule binding. *Neuron* **14**, 879–888 (1995).
58. Brangwynne, C. P. Phase transitions and size scaling of membrane-less organelles. *Journal of Cell Biology* **203**, 875–881 (2013).
59. Ambadipudi, S., Biernat, J., Riedel, D., Mandelkow, E. & Zweckstetter, M. Liquid–liquid phase separation of the microtubule-binding repeats of the Alzheimer-related protein Tau. *Nature communications* **8**, 1–13 (2017).
60. Zhang, X. *et al.* RNA stores tau reversibly in complex coacervates. *PLoS biology* **15**, e2002183 (2017).
61. Hernández-Vega, A. *et al.* Local nucleation of microtubule bundles through tubulin concentration into a condensed tau phase. *Cell reports* **20**, 2304–2312 (2017).
62. Kanaan, N. M., Hamel, C., Grabinski, T. & Combs, B. Liquid-liquid phase separation induces pathogenic tau conformations in vitro. *Nature communications* **11**, 1–16 (2020).



Chapter 1

63. Chaudhary, A. R. *et al.* MAP7 regulates organelle transport by recruiting kinesin-1 to microtubules. *Journal of Biological Chemistry* **294**, 10160–10171 (2019).
64. Chowdhury, S., Ketcham, S. A., Schroer, T. A. & Lander, G. C. Structural organization of the dynein–dynactin complex bound to microtubules. *Nature structural & molecular biology* **22**, 345–347 (2015).
65. Manka, S. W. & Moores, C. A. Microtubule structure by cryo-EM: snapshots of dynamic instability. *Essays in biochemistry* **62**, 737–751 (2018).
66. Prota, A. E. *et al.* Molecular mechanism of action of microtubule-stabilizing anticancer agents. *Science* **339**, 587–590 (2013).
67. Nogales, E., Wolf, S. G. & Downing, K. H. Erratum: Structure of the $\alpha\beta$ tubulin dimer by electron crystallography. *Nature* **393**, 191–191 (1998).
68. Kraemer, J. A. Structure, Polymerization, and Dynamics of a the First Bacteriophage Tubulin: PhuZ. (University of California, San Francisco, 2014).
69. Sobel, A. *et al.* Intracellular substrates for extracellular signaling: characterization of a ubiquitous, neuron-enriched phosphoprotein (Stathmin). *Journal of Biological Chemistry* **264**, 3765–3772 (1989).
70. Gigant, B. *et al.* The 4 Å X-ray structure of a tubulin: stathmin-like domain complex. *Cell* **102**, 809–816 (2000).
71. Devred, F. *et al.* Microtubule and MAPs: thermodynamics of complex formation by AUC, ITC, fluorescence, and NMR. *Methods in cell biology* **95**, 449–480 (2010).
72. Gigant, B. *et al.* Mechanism of Tau-promoted microtubule assembly as probed by NMR spectroscopy. *Journal of the American Chemical Society* **136**, 12615–12623 (2014).
73. Sillen, A. *et al.* NMR investigation of the interaction between the neuronal protein tau and the microtubules. *Biochemistry* **46**, 3055–3064 (2007).
74. Barbier, P. *et al.* Role of tau as a microtubule-associated protein: structural and functional aspects. *Frontiers in aging neuroscience* 204 (2019).
75. King, O. D., Gitler, A. D. & Shorter, J. The tip of the iceberg: RNA-binding proteins with prion-like domains in neurodegenerative disease. *Brain research* **1462**, 61–80 (2012).
76. Patel, A. *et al.* A liquid-to-solid phase transition of the ALS protein FUS accelerated by disease mutation. *Cell* **162**, 1066–1077 (2015).
77. Tange, H. *et al.* Liquid–liquid phase separation of full-length prion protein initiates conformational conversion in vitro. *Journal of Biological Chemistry* **296**, (2021).
78. André, A. A. & Spruijt, E. Liquid–liquid phase separation in crowded environments. *International Journal of Molecular Sciences* **21**, 5908 (2020).
79. Bergeron-Sandoval, L.-P., Safaee, N. & Michnick, S. W. Mechanisms and consequences of macromolecular phase separation. *Cell* **165**, 1067–1079 (2016).
80. Wang, B. *et al.* Liquid–liquid phase separation in human health and diseases. *Signal Transduction and Targeted Therapy* **6**, 1–16 (2021).
81. Cho, W.-K. *et al.* Mediator and RNA polymerase II clusters associate in transcription-dependent condensates. *Science* **361**, 412–415 (2018).
82. Gibson, B. A. *et al.* Organization of chromatin by intrinsic and regulated phase separation. *Cell* **179**, 470–484 (2019).
83. Decker, C. J. & Parker, R. P-bodies and stress granules: possible roles in the control of translation and mRNA degradation. *Cold Spring Harbor perspectives in biology* **4**, a012286 (2012).
84. Wang, J. *et al.* A molecular grammar governing the driving forces for phase separation of prion-like RNA binding proteins. *Cell* **174**, 688–699 (2018).

85. Murthy, A. C. & Fawzi, N. L. The (un) structural biology of biomolecular liquid-liquid phase separation using NMR spectroscopy. *Journal of Biological Chemistry* **295**, 2375–2384 (2020).
86. Wong, L. E., Kim, T. H., Muhandiram, D. R., Forman-Kay, J. D. & Kay, L. E. NMR experiments for studies of dilute and condensed protein phases: application to the phase-separating protein CAPRIN1. *Journal of the American Chemical Society* **142**, 2471–2489 (2020).
87. Emmanouilidis, L. *et al.* NMR and EPR reveal a compaction of the RNA-binding protein FUS upon droplet formation. *Nature Chemical Biology* **17**, 608–614 (2021).
88. Dunckley, T. & Parker, R. The DCP2 protein is required for mRNA decapping in *Saccharomyces cerevisiae* and contains a functional MutT motif. *The EMBO journal* **18**, 5411–5422 (1999).



Chapter 2

Resonance assignments of the microtubule-binding domain of the microtubule-associated protein 7 (MAP7)

Adapted from

Adler A, Kjaer L, Beugelink W., Baldus M., van Ingen H. Resonance assignments of the microtubule-binding domain of the microtubule-associated protein 7 (MAP7). Submitted to *Biomolecular NMR Assignments* (2023), accepted

Contribution: AA performed the NMR experiments with help from Hvl and assigned the protein with input from LK and Hvl. WB and AA conducted the sec-MALLS experiments.



Abstract

The microtubule-associated protein 7 (MAP7) is a protein involved in cargo transport along microtubules (MTs) by interacting with kinesin-1 through the C-terminal kinesin-binding domain. Moreover, the protein is reported to stabilize MTs, thereby playing a key role in axonal branch development. An important element for this latter function is the 112 amino-acid long N-terminal microtubule-binding domain (MTBD) of MAP7. Here we report NMR backbone and side-chain assignments that suggest a primarily alpha-helical secondary fold of this MTBD in solution. The MTBD contains a central long α -helical segment that includes a short four-residue 'hinge' sequence with decreased helicity and increased flexibility. This chapter represents a first step towards analysing the complex interaction of MAP7 with MTs at an atomic level via NMR spectroscopy.

Introduction

Microtubules (MTs) represent a principal component of the cytoskeleton in eukaryotic cells. Besides other functions, they are essential in intracellular organisation, organelle trafficking and mitosis. The biopolymers are composed of $\alpha\beta$ -tubulin heterodimers that assemble into hollow cylinders ¹. One MTs characteristic that allows the processes guided by MTs is their highly dynamic nature ². A misbalance in these processes can lead to diseases, including cancer, Alzheimer's and Parkinson's disease ^{3,4}.

The execution of the variety of MTs tasks and the associated dynamics rely on the binding and interactions with so-called microtubule-associated proteins (MAPs) ⁵. While some MAPs have been studied to a great extent, others remain poorly characterised despite their essential functions (Goodson and Jonasson 2018).

MAP7 (also known as E-MAP-115 or Ensconsin) is a MAP that is believed to activate the transport of kinesin-1 along the MTs ⁷⁻⁹. Furthermore, parallel microtubule sliding by Kinesin-1 might be promoted by MAP7. This function is regulated by its C-terminal

kinesin binding domain¹⁰. Additionally, MAP7 is reported to stabilize and bundle MTs with its N-terminal microtubule-binding domain (MTBD) (**Fig. 2.1**)^{11,12}. This interaction seems to play an important role in regulating the MTs dynamics during axonal branch development or metaphase spindle growth^{13,14}. In addition, MAP7 plays a role in motor-driven transport along the MTs. In this role, its regulation is closely associated with that of the Alzheimer-associated protein Tau which also belongs to the class of MAPs. In contrast to the latter, Tau inhibits Kinesin-1 mobility^{15–17}. Furthermore, Tau can replace MAP7 on MTs, highlighting the complex coordination of the MTs function and their associated proteins⁷.

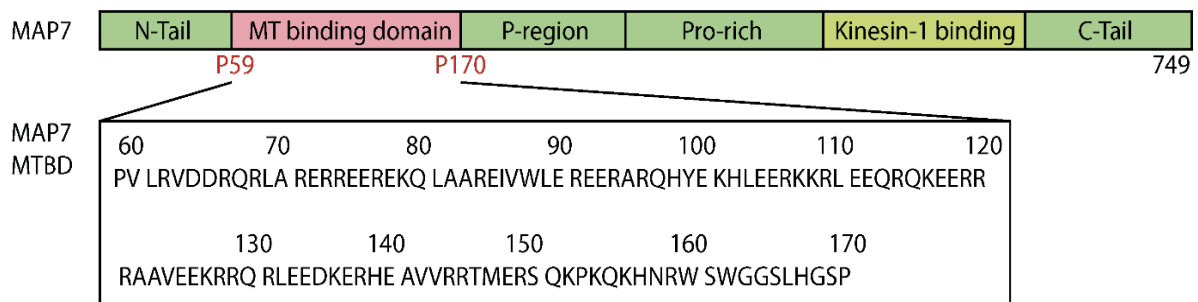


Fig. 2.1: Domain organization of MAP7. Top: Schematic representation of Full-length MAP7 including the MTBD and the kinesin-1 binding domain. **Bottom:** Amino-acid sequence of the MAP7 MTBD.

MAP7 is thought to bind along the length of MTs¹⁸. The cryogenic electron microscopy (cryo-EM) reconstruction from Ferro *et al.* 2022 revealed a 53 residue-long α -helix that binds a tubulin dimer of the MTs protofilament between the outer ridge and the site of lateral contacts (PDBid:7SGS). Due to the challenges associated with the study of MAPs binding a longer stretch than a tubulin dimer by cryo-EM, this picture might underestimate the length of the binding region. Moreover, dynamic interactions between the two binding partners remain elusive with this method. Furthermore, the appearance of the MAP7 MTBD as a single α -helix is interesting, as sequence analysis using Waggawagga¹⁹ shows high propensity for

Chapter 2

the formation of a coiled-coil but also indicates the MTBD could form a single alpha-helix (SAH) domain. Whether or not the MTBD alone is also a single α -helix in the free state is not known.

To allow for a more in-depth study of its structure and function, we have started an NMR study of MAP7 MTBD and its interaction with MTs. We adapted a purification protocol of the 112 residue MTBD construct (59-170) yielding pure protein and assigned its backbone and side chains. The resulting chemical-shift assignments reveal that the MTBD free in solution contains a central long α -helical segment that includes a short four-residue 'hinge' sequence with decreased helicity and increased flexibility.

Results

Extent of assignments and data deposition

The MAP7 MTBD (residues 59-170, with an additional N-terminal GS thrombin cleavage scar) contains 114 amino acids and has a molecular weight of 14.23 kDa. Due to its high content of arginine (22.3 %), glutamate (19.6 %), lysine (8.9 %) and glutamine (7.1 %) combined with a high alpha-helical content, the ^1H - ^{15}N TROSY spectrum is crowded (**Fig. 2.2**). The appearance of the line shapes suggests the MTBD may partly aggregate. Indeed, analysis of MAP7 MTBD with size-exclusion chromatography coupled with multi-angle light scattering (sec-MALLS) showed that the MTBD tends to oligomerize and indicated the protein is predominantly in a monomeric state at the concentration used for NMR (**Supplementary Fig. 2.1**).

Despite severe overlaps, we were able to obtain near-complete backbone assignments: $^1\text{H}_\text{N}$ (95 %: 104 out of 109 non-proline residues), ^{15}N (95 %: 104 out of 109 non-proline residues), $^{13}\text{C}\alpha$ (97 %: 109 out of 112), $^{13}\text{C}\beta$ (93 %: 104 out of 112), ^{13}CO (93 %: 104 out of 112), $^1\text{H}\alpha$ (66 %: 74 out of 112) and $^1\text{H}\beta$ (63 %: 71 out of 112). The unassigned non-proline residues were K79, E117, E118 due to the repetitive nature of the sequence and H157 and N158 because of line broadening. The chemical shift assignments (^1H , ^{15}N , ^{13}C) have been deposited in the

BioMagResBank (<http://www.bmrb.wisc.edu>) under accession number 51730. Interestingly, residues 59-61 of the extreme N-terminus and 164-169 of the extreme C-terminus gave rise to duplicate resonances, indicative of a second conformational state populated to ~30 % based on the average signal-to-noise ratios of the duplicated resonances. This might be due to proline cis-trans conformations of proline 59 and proline 170. For P59 this is supported by the C β resonance chemical shifts, with 32 ppm for the major and 34.81 ppm for the minor state, which is in line with a trans and cis configuration, respectively ²⁰. For P170 the C β chemical shift is unfortunately not assigned.

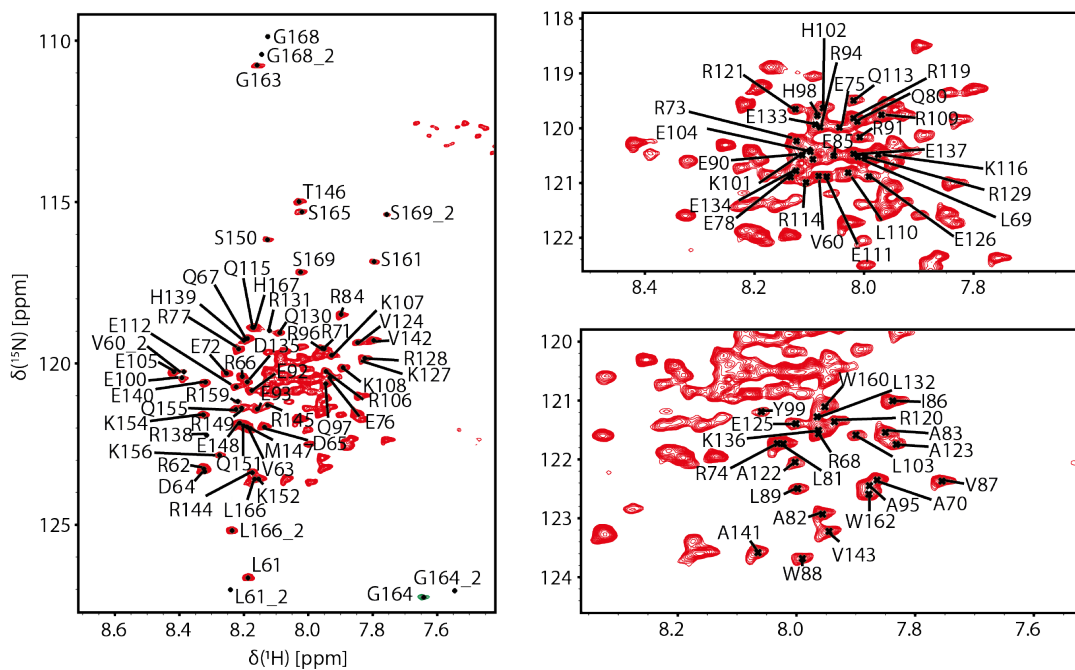


Fig. 2.2: Resonance assignment of MAP7 MTBD. Two-dimensional ¹⁵N-TROSY-HSQC of ¹³C-¹⁵N-MAP7 MTBD at 600 MHz acquired at 298 K. Reported amino acids are numbered according to the native sequence of the full-length protein. Second assignments of amino acids are denoted with a 2. Residues G164 and G164_2 are folded and displayed with green (negative) contour lines.

The secondary structure of MAP7 MTBD was predicted from the chemical shifts (¹³C α , ¹³CO, ¹H α , amide ¹HN and ¹⁵N) using the TALOS-N program ²¹. The protein forms an extended alpha-helical structure, spanning from residues 66 to 144, with disordered N- and C-termini (**Fig. 2.3A**). Residues 84 to 87 in the helical part have



Chapter 2

lower helical propensities and lower values for the random-coil-index-derived order-parameters (RCI-S²) (**Fig. 2.3B**). This indicates that MAP7 MTBD in its free state does not form a single stable helix as suggested from the AlphaFold prediction ²² (**Fig. 2.3C**), but rather includes a more flexible internal 'hinge' sequence. In addition, the C-terminal end of the helix is ill-defined with decreasing helicity and increasing flexibility observed for residues 137-149. In contrast, the helix is sharply defined at the N-terminus, starting at residue 66, where the helix is stabilized by a *hpp-xpxhx* helix-capping motif ²³ formed by residues V63 to residue A70 (VDDRQRLA). In this motif, *h/p* denotes a hydrophobic/polar residue, *x* is any residue and the - marks the helix boundary.

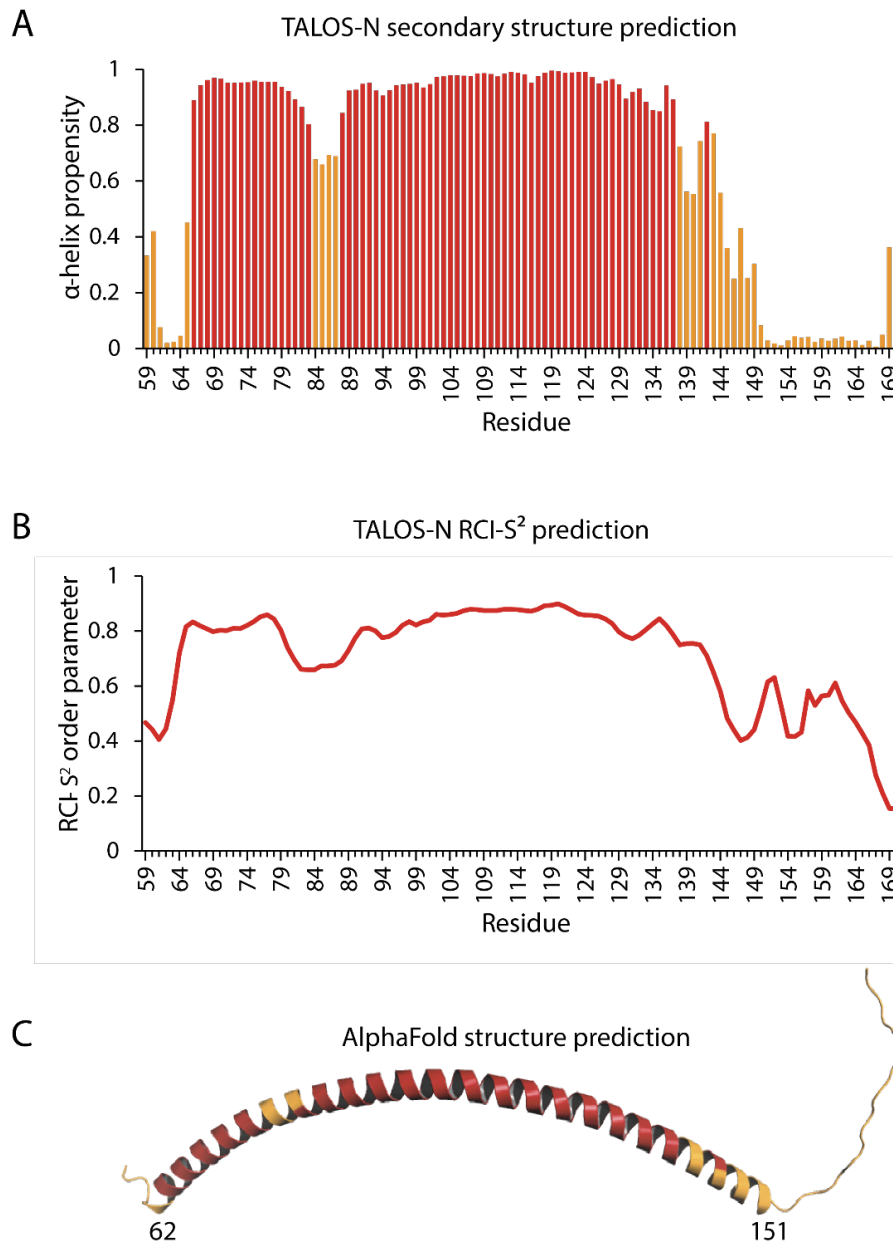


Fig. 2.3: Predicted secondary structure using TALOS-N of MAP7 MTBD (A) TALOS-N secondary structure prediction with α -helix propensities higher than 0.8 colour-coded in red and lower than 0.8 in yellow. **(B)** Random coil index order parameters (RCI-S²) predicted by TALOS-N **(C)** The AlphaFold structure prediction is showing an α -helix ranging from residue 62 up to residue 151. Colour-coded in yellow are TALOS-N α -helix propensities lower than 0.8.

Summary

This chapter reports the chemical-shift assignments and secondary structure of MAP7 MTBD in its free state in solution. MAP7 MTBD adopts a predominantly α -helical secondary structure, with a central long α -helical segment from residue 66 to 144 and including a short 'hinge' from residue 84 to 87 with decreased helicity and increased flexibility.

Interestingly, the recent cryo-EM structure of MAP7 MTBD bound to microtubules suggested that the MTBD binds via a helix spanning at least residue 83 to 134¹⁸. As we observed longer helical regions free in solution, both at the N- and C-terminus, this may indicate that the MTBD binding interface to microtubules is significantly more extended. Previously, solid-state NMR (ssNMR) has shown its potential to study MAP-MTs interactions (see, e.g. ^{24,25}) providing a strong incentive to study MAP7-MTs complexes by ssNMR. This study hence represents a first step towards studying the MAP7 MTBD interaction with MTs by ssNMR as it is later discussed in chapter 5.

Methods and experiments

The cDNA encoding the MTBD (residues 59-170) of Microtubule-associated protein 7 from *Homo sapiens* with an N-terminal His-Tag and Maltose binding protein (MBP) linked via a thrombin cleavage site (His-MBP-MAP7 MTBD), was cloned into the pLICHIS vector.

Protein expression and purification

The protein was expressed in *Escherichia coli Rosetta 2 (DE3)* cells and the bacteria were grown using M9 minimal media containing 0.5 g/L ¹⁵NH₄Cl and 2 g/L U-¹³C glucose containing 100 mg/L ampicillin and 35 mg/L chloramphenicol. The culture was induced at an OD₆₀₀ of 0.6 with 0.3 mM IPTG and incubated at 37 °C for 4 h.

The cells were spun down at $4000 \times g$, 4°C for 20 min to harvest cells. Cell pellets were resuspended with Buffer A (50 mM NaPi, pH 8; 150 mM NaCl; 1 mM beta-ME; 20 mM imidazole) with Lysozyme and stored at -80°C .

For protein purification, the cells were lysed by sonication on ice and subsequently, the cellular debris was removed by centrifugation at $40,000 \times g$, 4°C for 30 min. Then, the His-MBP-MAP7 MTBD was purified by HiTrap immobilized metal affinity chromatography (IMAC, (GE Healthcare Life Sciences)) (equilibrated with buffer A) attached to an ÄKTA Pure system. Afterwards the cell lysate was loaded onto the column and a wash with 20 column volumes (CV) with buffer A was performed before eluting the protein with buffer B (buffer A with 400 mM imidazole) supplemented with protease inhibitors (Sigma-Aldrich, cOmplete EDTA-free). The protein was concentrated in the presence of protease inhibitor using a 10 kDa molecular weight cut off Amicon filter (Sigma-Aldrich) and then diluted with cation exchange (CEX) buffer A (40 mM NaPi, pH 6.5) to a final concentration of 50 mM NaCl. Next, CEX was performed with the HiTrap HP SP chromatography column (GE Healthcare Life Sciences). The sample was loaded onto the column preequilibrated with CEX buffer A and washed with 10 CV CEX buffer A. The protein was eluted by applying a gradient to 100 % CEX buffer B (40 mM sodium phosphate buffer, 1 M NaCl, pH 6.5). The MAP7-MBP fusion protein was concentrated to a volume less than 1 mL and the His-MBP-tag was cleaved (leaving an additional two residues GS N-terminal to P59) overnight with 10 units of thrombin during dialysis with NMR buffer (40 mM phosphate buffer, 150 mM NaCl, 1 mM dithiothreitol (DTT), pH 6.5) to remove the high salt content. The His-MBP tag was removed by selective ammonium sulphate precipitation of MAP7 MTBD. In a first step 50 % $(\text{NH}_4)_2\text{SO}_4$ saturation was used to precipitate the protein. After the ammonium sulphate addition, the solution was mixed under inversion at 4°C for 30 min. Subsequently, the solution was centrifuged at $10,000 \times g$, 15 min, 4°C . The MAP7 MTBD pellet was washed with 40 % $(\text{NH}_4)_2\text{SO}_4$ saturation in NMR buffer by mixing by inversion at 4°C for 30 min followed by centrifugation as previously. The pellet was resuspended in NMR buffer and buffer exchanged to NMR buffer overnight to remove remaining ammonium sulphate. The



Chapter 2

aggregation state of the protein was assessed using sec-MALLS by injecting 5 concentrations ranging from 0.2 – 3.2 mg/mL of purified Map7 MTBD on a Superdex 75 Increase column (Cytiva) calibrated with NMR buffer. A miniDAWN TREOS detector (Wyatt) and a RID-10A differential refractive index monitor (Shimadzu) were used. Collected data was analysed using ASTRA6 software (Wyatt).

Solution-state NMR

For solution-state NMR measurements, a 150 μ M sample of U- ^{15}N , ^{13}C -labelled MAP7 MTBD in NMR buffer supplemented with 5 % D_2O was used to acquire NMR spectra at 298 K on a Bruker Avance III HD 600 spectrometer or on a Bruker Avance III HD 900 instrument equipped with triple resonance cryogenic-probes. Backbone and side-chain resonance assignments were derived from ^1H - ^{15}N TROSY, ^1H - ^{13}C constant time HSQC, HNCA, HNCACB, CBCA(CO)NH, HNCO, HN(CA)CO, HBHA(CO)NH, (H)C(CO)NH, CCH-TOCSY experiments. All spectra were processed using the Bruker TopSpin 3.6.2 software. Chemical shifts were referenced via the water resonance. Typical processing parameters were utilized, with apodization with cosine-squared window functions in all dimensions and doubling of the time domain signal by linear prediction in the indirect ^{15}N and ^{13}C dimensions. The spectra were analysed using POKY from NMRFAM-Sparky²⁶. The secondary structure (or the ϕ and ψ backbone torsion angles) predictions of the MAP7 MTBD were carried out using TALOS-N²¹ based on the chemical shifts of backbone resonances.

References

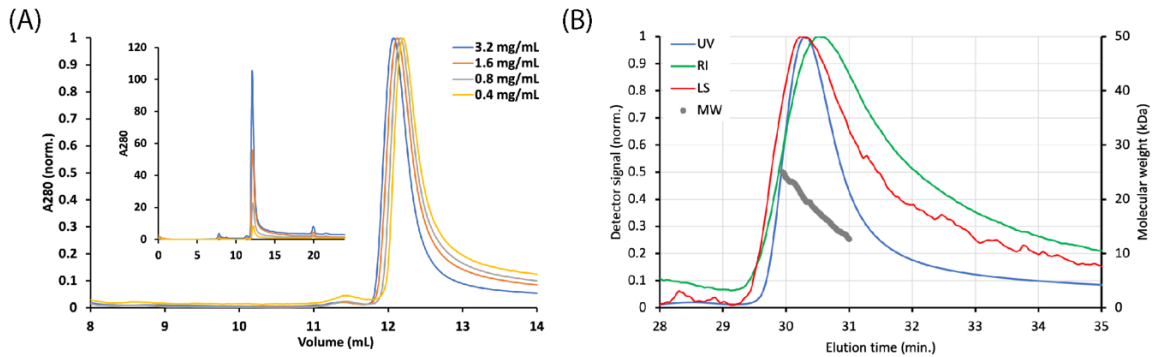
1. Mandelkow, E.-M., Schultheiß, R., Rapp, R., Müller, M. & Mandelkow, E. On the surface lattice of microtubules: helix starts, protofilament number, seam, and handedness. *The Journal of cell biology* **102**, 1067–1073 (1986).
2. Mitchison, T. & Kirschner, M. Dynamic instability of microtubule growth. *nature* **312**, 237–242 (1984).
3. Borys, F., Joachimiak, E., Krawczyk, H. & Fabczak, H. Intrinsic and extrinsic factors affecting microtubule dynamics in normal and cancer cells. *Molecules* **25**, 3705 (2020).
4. Sferra, A., Nicita, F. & Bertini, E. Microtubule dysfunction: a common feature of neurodegenerative diseases. *International journal of molecular sciences* **21**, 7354 (2020).
5. Bodakuntla, S., Jijumon, A., Villablanca, C., Gonzalez-Billault, C. & Janke, C. Microtubule-associated proteins: structuring the cytoskeleton. *Trends in cell biology* **29**, 804–819 (2019).
6. Goodson, H. V. & Jonasson, E. M. Microtubules and microtubule-associated proteins. *Cold Spring Harbor perspectives in biology* **10**, a022608 (2018).
7. Monroy, B. Y. *et al.* Competition between microtubule-associated proteins directs motor transport. *Nature communications* **9**, 1–12 (2018).
8. Métivier, M. *et al.* The Kinesin-1 binding domain of Enscosin/MAP7 promotes Kinesin-1 activation in vivo. *BioRxiv* (2018).
9. Hooikaas, P. J. *et al.* MAP7 family proteins regulate kinesin-1 recruitment and activation. *Journal of Cell Biology* **218**, 1298–1318 (2019).
10. Metzger, T. *et al.* MAP and kinesin-dependent nuclear positioning is required for skeletal muscle function. *Nature* **484**, 120–124 (2012).
11. Sun, X. *et al.* Mdp3 is a novel microtubule-binding protein that regulates microtubule assembly and stability. *Cell cycle* **10**, 3929–3937 (2011).
12. Kikuchi, K. *et al.* Map7/7D1 and Dvl form a feedback loop that facilitates microtubule remodeling and Wnt5a signaling. *EMBO reports* **19**, e45471 (2018).
13. Gallaud, E. *et al.* Enscosin/Map7 promotes microtubule growth and centrosome separation in *Drosophila* neural stem cells. *Journal of Cell Biology* **204**, 1111–1121 (2014).
14. Tymanskyj, S. R., Yang, B., Falnikar, A., Lepore, A. C. & Ma, L. MAP7 regulates axon collateral branch development in dorsal root ganglion neurons. *Journal of Neuroscience* **37**, 1648–1661 (2017).
15. Ebner, A. *et al.* Overexpression of tau protein inhibits kinesin-dependent trafficking of vesicles, mitochondria, and endoplasmic reticulum: implications for Alzheimer's disease. *The Journal of cell biology* **143**, 777–794 (1998).
16. Dixit, R., Ross, J. L., Goldman, Y. E. & Holzbaur, E. L. Differential regulation of dynein and kinesin motor proteins by tau. *Science* **319**, 1086–1089 (2008).
17. Baas, P. W. & Qiang, L. Tau: it's not what you think. *Trends in cell biology* **29**, 452–461 (2019).
18. Ferro, L. S. *et al.* Structural and functional insight into regulation of kinesin-1 by microtubule-associated protein MAP7. *Science* **375**, 326–331 (2022).
19. Simm, D., Hatje, K. & Kollmar, M. Waggawagga: comparative visualization of coiled-coil predictions and detection of stable single α -helices (SAH domains). *Bioinformatics* **31**, 767–769 (2015).
20. Schubert, M., Labudde, D., Oschkinat, H. & Schmieder, P. A software tool for the prediction of Xaa-Pro peptide bond conformations in proteins based on ^{13}C chemical shift statistics. *Journal of biomolecular NMR* **24**, (2002).



Chapter 2

21. Shen, Y. & Bax, A. Protein structural information derived from NMR chemical shift with the neural network program TALOS-N. in *Artificial neural networks* 17–32 (Springer, 2015).
22. Jumper, J. *et al.* Highly accurate protein structure prediction with AlphaFold. *Nature* **596**, 583–589 (2021).
23. Aurora, R. & Rosee, G. D. Helix capping. *Protein Science* **7**, 21–38 (1998).
24. Atherton, J. *et al.* A structural model for microtubule minus-end recognition and protection by CAMSAP proteins. *Nature structural & molecular biology* **24**, 931–943 (2017).
25. Pines, A. *et al.* Direct observation of dynamic protein interactions involving human microtubules using solid-state NMR spectroscopy. *Nature communications* **11**, 1–10 (2020).
26. Lee, W., Rahimi, M., Lee, Y. & Chiu, A. POKY: a software suite for multidimensional NMR and 3D structure calculation of biomolecules. *Bioinformatics* **37**, 3041–3042 (2021).

Supplementary Information



Supplementary Fig. 2.1: Sec-MALLS of MAP7 MTBD (A) Normalized UV signal measured at 280 nm for a serial dilution of analytical size-exclusion chromatography (SEC) runs (unscaled traces in the inset). MAP7 MTBD elutes in a tailing peak, typical for low-affinity interactions with fast kinetics, at a concentration-dependent elution volume. Both are indicative of concentration-dependent oligomerization. Note that the distinct non-globular nature of the MAP7 MTBD likely causes the rather high elution volume. Also note that a single helix vs. coiled-coil will have much less impact on elution volume than in case of dimerization of globular proteins. **(B)** Best-effort MALLS estimation of the MAP7 MTBD molecular weight at 120 μ M (1.6 mg/mL). The misalignment of the UV, light scattering (LS) and refraction index (RI) peaks indicates a heterogeneity in the elution profile. The estimated molecular weights are in the range of 12-25 kDa with median value 18 kDa. This median value would correspond to 75 % monomer and 25 % dimer.



Chapter 3

Solid-State NMR Spectroscopy for Studying Microtubules and Microtubule-Associated Proteins

Adapted from

Luo, Y., Xiang, S., Paioni, A. L., Adler, A., Hooikaas, P. J., Jijumon, A. S., ... & Baldus, M. (2021). Solid-State NMR Spectroscopy for Studying Microtubules and Microtubule-Associated Proteins. In *Structural Proteomics: High-Throughput Methods* (pp. 193-201). New York, NY: Springer US



Abstract

In this chapter, we describe the preparatory and spectroscopic procedures for conducting solid-state NMR experiments on microtubules (MTs) obtained from human cells and their complexes with microtubule-associated proteins (MAPs). Next to labelling and functional assembly of MTs and MT-MAP complexes, we discuss solid-state NMR approaches, including fast MAS and hyperpolarization methods that can be used to examine these systems. Such studies can provide novel insight into the dynamic properties of MTs and MT-MAP complexes.

Introduction

For more than four decades, solid-state Nuclear Magnetic Resonance (ssNMR) spectroscopy has been used to study complex biomolecular systems and recent advancements in ssNMR instrumentation and methodology have greatly expanded the utility and scope of such studies ^{1,2}. Next to spectroscopic aspects, preparative procedures, in particular the generation of suitably (isotope-)labelled biomolecules have significantly enlarged the scope of research. Next to the well-established use of bacterial expression systems, significant progress has recently been made to produce functional and properly folded human protein targets for NMR studies, for example, by using yeast, insect, or mammalian cells ³. Our group has previously shown that mammalian cell lines can indeed be used to conduct ssNMR studies on membrane proteins ⁴. More recently, we introduced ssNMR approaches to study soluble proteins inside human cells that were pre-labelled using bacterial expression systems ⁵. In the latter case, we made use of electroporation procedures that provide an avenue for the delivery of selectively labelled specific proteins in an otherwise unlabelled cell background ⁶.

This chapter describes, how to adapt these procedures to study microtubules (MTs) and associated proteins using isotope-labelled microtubules obtained from human cells. MTs are cytoskeletal polymers composed of tubulin subunits, which are

essential for many biological processes, including cell division, migration, polarization, and intracellular trafficking. The dynamics and organization of MTs are regulated by nucleotide binding and many microtubule-associated proteins (MAPs). Previously, solid- and solution-state NMR have been used to study the interactions between MTs and isotope-labelled MAPs or small drugs ⁷⁻¹³. In spite of the progress in producing isotope-labelled soluble tubulin for solution-state NMR studies, extending such experiments to using labelled MTs has failed so far. Firstly, production of recombinant, functional α/β -tubulin dimers from bacteria, which are commonly used to obtain labelled proteins, has not been possible, most likely due to the lack of chaperones and cofactors for tubulin folding and dimerization. In addition, previous protocols for tubulin purification from mammalian cells did not provide sufficient yields to obtain isotope-labelled MTs for NMR studies. Here, we describe how to prepare and label MTs and MAPs for ssNMR studies. In the latter case, we utilize the CKK domain that is important for the minus-end recognition of the Calmodulin-regulated spectrin-associated protein (CAMSAP) ^{9,13}. Subsequently, we discuss solid-state NMR methods, including ultra-fast magic angle spinning (MAS) and hyperpolarization methods (such as Dynamic Nuclear Polarization (DNP)) that can be used to study these systems. Such studies can provide novel insight into the dynamic interactions of MTs tails ¹⁴. As we have shown recently for the case of mRNA processing bodies ¹⁵, such experiments could also reveal dynamic interactions leading to the compartmentalization of the MTs lattice by condensation of Tau or other MAPs.



Materials

Cell Culture

1. HeLa S3 cell line (ATCC® CCL-2.2™).
2. Dulbecco's Modified Eagle Medium (DMEM, without amino acids, with 1 g/L glucose), [¹³C, ¹⁵N] labelled algal amino acid mixture, 200 mM stable L-glutamine, glucose, dialyzed fetal bovine serum (FBS), penicillin-streptomycin (P/S). Add 1 g/L algal amino acid mixture to DMEM and adjust the final concentration of glucose to 3.5 g/L. When the compounds are completely dissolved, filter-sterile the medium by passing through the membrane filter with 0.2µm pore size. Include 10 % dialyzed FBS and 1 % P/S to the medium. Store at 4 °C.
3. 15 cm mammalian cell culture dishes, 1 L mammalian cell culture using Corning Erlenmeyer flasks and a cell culture incubator that includes a shaker.

Preparation of Isotope-Labelled MTs

1. Phosphate-buffered saline (PBS).
2. BRB80 buffer: 80 mM PIPES pH 6.8, 1 mM EGTA, 1 mM MgCl₂. Store at 4 °C.
3. Lysis buffer: 80 mM PIPES pH 6.8, 1 mM EGTA, 1 mM MgCl₂, 1 mM β-mercaptoethanol, 1 mM PMSF, protease inhibitors. Store at 4 °C.
4. High-molarity PIPES buffer: 1 M PIPES pH 6.8, 10 mM MgCl₂, 20 mM EGTA. Store at 4 °C.

5. 100 mM guanosine triphosphate (GTP) solution, 10 mM Paclitaxel dissolved in DMSO, glycerol.
6. Ultracentrifuges such as an optimal I-90k ultracentrifuge (Beckman Coulter) (rotor type TLA-55) and an Optima™ LE-80K ultracentrifuge (Beckman Coulter) (rotor type 70.1 Ti) as well as a French-press homogenizer.

Purification of Isotope-Labelled CKK Domain from Bacteria

1. Washing buffer for His-tag purification: 50 mM phosphate buffer, 200 mM NaCl, 1 mM β -mercaptoethanol, 1 mM PMSF, 10 mM imidazole, protease inhibitors, pH 8.0. Store at 4 °C.
2. Elution buffer for His-tag purification: 50 mM phosphate buffer, 200 mM NaCl, 1 mM β -mercaptoethanol, 1 mM PMSF, 400 mM imidazole, protease inhibitors, pH 8.0. Store at 4 °C.
3. Buffer for size exclusion chromatography (SEC) for CKK: 40 mM phosphate buffer, 500 mM NaCl, 1 mM dithiothreitol (DTT), pH 7.0. Store at 4 °C.
4. Buffer for storage of CKK: 40 mM phosphate buffer, 150 mM NaCl, 1 mM dithiothreitol (DTT), pH 7.0. Store at 4 °C.



Methods

Suspension Cell Culture for Isotope Labelling

1. Culture HeLa S3 in two 15 cm cell culture dishes in labelled DMEM, and then transfer the cells into 12 dishes with the same medium to grow until a confluence of ~80–90 %. (5–6 days).
2. Harvest the cells by trypsinization.
3. Count the number of cells with a cell counter.
4. Transfer the cells into 2.1 L labelled medium to a cell density of ~150,000 cells/mL. The cells are grown at 37°C, 5 % CO₂ and 120 rpm in 1L Corning Erlenmeyer flasks. Each flask contains 300 mL medium. Let the cells grow until the cell density reaches $\sim 1.2\text{--}1.5 \times 10^6$ cells/mL (4–5 days).
5. Harvest the cells by centrifugation at 500 × g for 20 min at 4 °C. Collect the cell pellet and resuspend in PBS, centrifuge the cells again at 500 × g for 15 min at 4 °C, and use the cell pellet for MTs preparation.

Sample Preparation of Isotope-Labelled MTs (See also ref ¹⁶)

1. Resuspend the harvested cells with 1 mL of lysis buffer per 1 g of cells. Lyse cells on ice by passing through a French-press homogenizer three times at 1000 psi. Spin down the cell lysate at 120,000 × g at 4 °C for 30 min and collect the supernatant containing the tubulin. Centrifuge the supernatant again at 5000 × g at 4 °C for 15 min to remove the remaining cell debris before the next step.
2. Add half volume of glycerol and 1 mM GTP to the supernatant and mix well. Incubating the mixture at 30 °C for 30 min for MTs polymerization.

Subsequently, spin down the crude MTs pellet at $150,000 \times g$ (Type 70.1 Ti, Beckman Coulter) at $30\text{ }^{\circ}\text{C}$ for 30 min. Discard the supernatant and keep the pellet on ice.

3. Resuspend the pellet in BRB80 supplemented with protease inhibitors and keep on ice for 30 min to allow for MTs depolymerization. For a more efficient depolymerization, resuspend the solution frequently (once every 5 min). Subsequently, centrifuge the solution at $150,000 \times g$ (Type 70.1 Ti, Beckman Coulter) at $4\text{ }^{\circ}\text{C}$ for 30 min, and collect the supernatant containing the soluble tubulin (see **Note 1**).
4. Add an equal volume of high-molarity PIPES buffer, together with an equal volume of glycerol and 1 mM GTP to the supernatant and mix well. Polymerize the tubulin at $30\text{ }^{\circ}\text{C}$ for 30 min with the high-molarity PIPES buffer to inhibit residual MAPs binding to MTs. Subsequently, add $20\mu\text{M}$ Paclitaxel to the reaction and incubate for 20 min to generate Taxol-stabilized MTs. Spin down the Taxol-MTs at $150,000 \times g$ (TLA-55, Beckman Coulter) at $30\text{ }^{\circ}\text{C}$ for 30 min. Wash the pellet with BRB80 containing $20\mu\text{M}$ Paclitaxel and protease inhibitors and repeat the centrifugation to collect the MTs (**Fig. 3.1**) (see **Notes 2-4**).



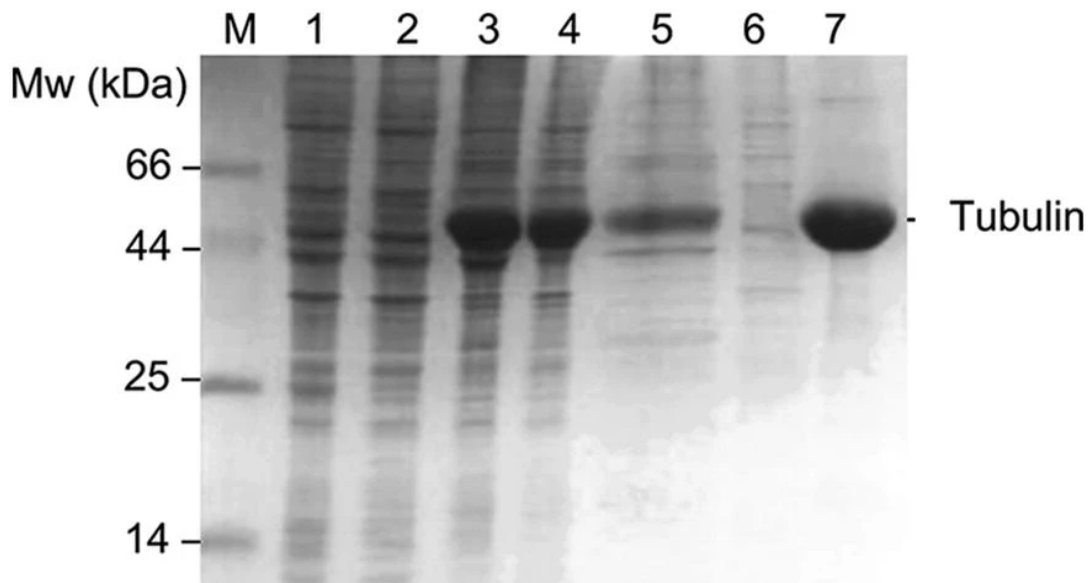


Fig. 3.1: Tubulin purification. SDS-PAGE analysis of tubulin purification from HeLa S3 cells. Lane M corresponds to the protein marker. From left to right the lanes show: the total cell lysate (lane 1); the supernatant of the first polymerization (lane 2); the pellet of the first polymerization (lane 3); the supernatant of the depolymerization (lane 4) as well as the associated pellet (lane 5); the supernatant of the second polymerization (lane 6) and the pellet of the second polymerization indicating the purified MTs (lane 7).

Purification of Isotope-Labelled CKK from Bacteria

1. Express the protein of interest from *E. coli* in isotope-labelled M9 medium. Harvest the bacteria and resuspend in washing buffer for His-tag purification. Lyse the bacteria by sonication and collect the cell lysate by centrifugation at $40,000 \times g$ for 30 min at 4 °C.
2. Filter the lysate by passing through a membrane filter with 0.45 μ m pore size. Load the lysate to a Ni²⁺ column and elute the bound proteins with the elution buffer.
3. Collect the eluate from the His-tag purification. Load the solution onto a Superdex 75 26/60 column equilibrated with the buffer for SEC.

4. Collect the eluted CKK from SEC and buffer-exchange to the storage buffer with ultra-filtration with a membrane filter with 3 kDa pore size. Concentrate the protein and store at 4 °C.

ssNMR and DNP Experiments on MTs and MT-MAP Complexes

1. Resuspend the MTs pellet in warm BRB80 buffer with 20 μ M Paclitaxel. Add the MAPs of interest in the solution and incubate the reaction for 30 min at 30 °C. Centrifuge the solution at 150,000 \times g (TLA-55, Beckman Coulter) at 30 °C for 30 min. Wash the pellet with warm BRB80 without disturbing the pellet.
2. Transfer the pellet into the rotor filling tool and fill the rotor by centrifugation at 115,500 \times g (SW32 Ti, Beckman Coulter) at 30 °C for 30 min.
3. Use 1.3 mm rotor and spin samples to 44 kHz or higher and maintain set temperature around 270 K. For ^{31}P experiments, larger MAS rotor dimensions and higher sample temperature (e.g., 290 K) are preferred.
4. For ^1H - ^{15}N , ^1H - ^{13}C , or ^1H - ^{31}P polarization transfer experiments, use cross-polarization schemes involving ramps such as a 100–50 % ramp on the ^1H -channel, with 1.2 ms CP contact times. For ^1H (proton) decoupling, employ SPINAL decoupling¹⁷ during evolution and detection times at around 90 kHz decoupling fields. Reference ^{13}C , ^{15}N , and ^{31}P spectra using adamantane (methylene, CH_2 peak), ^{15}N -labelled histidine (CO peak), and phosphate buffer, pH 7, by setting the respective peaks to 31.48 ppm and 0 ppm, respectively. The ^{15}N frequency was referenced indirectly via the ^{13}C signal.
5. For 2D ssNMR experiments on MT-MAP complexes, use dipolar correlation experiments such as PDSO (mixing time typically 10–200 ms), NCA (transfer time typically 3 ms), NCACX, (CC transfer times between 5 and 200 ms), DQ-



Chapter 3

SQ (with DQ excitation and reconversion times of 2.5 ms, ^{13}C - ^{13}C radio frequency-driven recoupling (RFDR) ¹⁸, NH, and CANH (using NH transfer times of 600 μs).

6. For ssNMR experiments that probe mobile MTs and/or MAP segments, use ^{15}N -HSQC, ^{13}C HSQC, and 3D ^{15}N -edited ^1H - ^1H spin diffusion experiments. Use a ^1H - ^1H mixing time of 200 ms for ^{15}N -edited ^1H - ^1H spin diffusion experiments.
7. In order to improve the signal-to-noise ratio, perform Dynamic Nuclear Polarization (DNP) experiments (Fig. 2), in which polarization is transferred from free electrons to the nuclei of interest, therefore enhancing the ssNMR sensitivity.
8. For DNP experiments on labelled MTs or MT-MAP complexes, modify procedure described under Subheading “ssNMR and DNP Experiments on MTs and MTs-MAP Complexes”, **step 1** as follows. Wash the MTs or the MTs-MAP sample with BRB80 in D_2O containing 30 % glycerol- d_8 , 20 μM Taxol and centrifuge at 150,000 \times g (TLA-55, Beckman Coulter) at 30 $^\circ\text{C}$ for 30 min.
9. Subsequently, resuspend with the DNP radical solution, obtained by dissolving the DNP agent AMUPol ¹⁹ in 60 % glycerol- d_8 , 30 % D_2O , and 10 % BRB80 with a radical concentration of 15 mM.
10. Transfer the sample in a Bruker 3.2 mm sapphire rotor, snap-freeze, and store in liquid nitrogen until use.
11. In preparation of DNP experiments, cool DNP MAS probe down to 100 K. Measure T_1 to determine optimal recycle delay. If needed, optimize DNP enhancements by adjusting field values (requires sweepable NMR magnet). The enhancement is obtained from comparison of the signal amplitude with and without microwaves. DNP Signal enhancement factors should typically

range between 19 (**Fig. 3.2A**) and 70 on the 800 MHz/527 GHz and 400 MHz/263 GHz DNP instruments, respectively.

Notes

1. In the depolymerization step for MTs preparation, the added BRB80 buffer should be kept at small volume (300–400 μ L buffer is used if starting with 8–10 mL harvested cell pellet). This helps obtaining a more efficient depolymerization resulting in more tubulin yield for the next steps. See also ref. ¹⁶.
2. Wear gloves when dissolving Paclitaxel to avoid exposing DMSO to skin and the Paclitaxel solution can be stored at -20 °C for 1 year. Prepare the GTP solution on the day of the preparation and keep the solution on ice. Avoid thawing and freezing of GTP. See also ref. ¹⁶.
3. We find that it is best to prepare the buffers fresh each time. (See ref. ¹⁴)
4. When because of time limitations it is not possible to purify tubulin on the same day of harvesting cells, the purification can be stopped after the first polymerization. Store the polymerized MTs pellet at -80 °C and continue the purification on the second day. See also ref. ¹⁶.



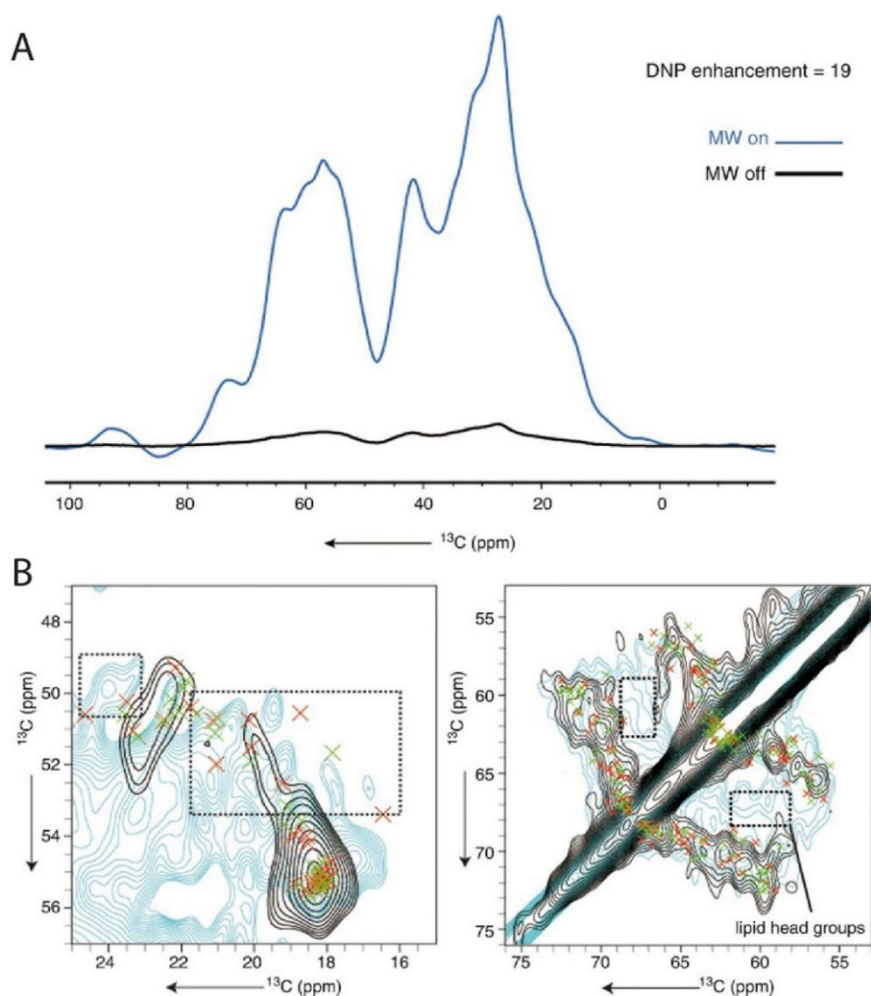


Fig. 3.2: DNP vs. standard ssNMR experiments. (A) DNP enhancement factor obtained on 800 MHz/527 GHz system. 1D ^1H - ^{13}C CP experiments of Taxol-stabilized MTs were measured on an 800 MHz spectrometer with DNP system. The black spectrum was recorded without microwave irradiation (therefore no DNP effect) and the blue spectrum was recorded with microwave irradiation (therefore enhanced by the DNP effect). An enhancement factor of 19 was obtained under the DNP conditions. (B) DNP-ssNMR experiments with [^{13}C , ^{15}N]-labelled, Taxol-MTs. Left Panel: Zoom-in on alanine $\text{C}\alpha$ - $\text{C}\beta$ regions on the ^{13}C - ^{13}C PDSD recorded with DNP at 100 K and MAS of 10.5 kHz (cyan) and RFDR at ambient temperature with MAS of 44 kHz (black). Chemical shift predictions²⁰ for alanine in random coil structures are highlighted in dash-line boxes. Right Panel: Zoom-in on serine and threonine $\text{C}\alpha$ - $\text{C}\beta$ regions on the same spectra. Extra signals that do not match prediction (stemming from co-purified lipids) were detected in the DNP experiment (dash-line boxes).

References

1. Renault, M., Cukkemane, A. & Baldus, M. Solid-state NMR spectroscopy on complex biomolecules. *Angewandte Chemie International Edition* **49**, 8346–8357 (2010).
2. Quinn, C. M. & Polenova, T. Structural biology of supramolecular assemblies by magic-angle spinning NMR spectroscopy. *Quarterly reviews of biophysics* **50**, e1 (2017).
3. Boisbouvier, J. & Kay, L. E. Advanced isotopic labelling for the NMR investigation of challenging proteins and nucleic acids. *Journal of Biomolecular NMR* vol. 71 115–117 (2018).
4. Kaplan, M. *et al.* EGFR dynamics change during activation in native membranes as revealed by NMR. *Cell* **167**, 1241–1251 (2016).
5. Narasimhan, S. *et al.* DNP-supported solid-state NMR spectroscopy of proteins inside mammalian cells. *Angewandte Chemie* **131**, 13103–13107 (2019).
6. Theillet, F.-X. *et al.* Structural disorder of monomeric α -synuclein persists in mammalian cells. *Nature* **530**, 45–50 (2016).
7. Kumar, A. *et al.* Interaction of Epothilone B (Patupilone) with Microtubules as Detected by Two-Dimensional Solid-State NMR Spectroscopy. *Angewandte Chemie* **122**, 7666–7669 (2010).
8. Yan, S. *et al.* Atomic-resolution structure of the CAP-Gly domain of dynactin on polymeric microtubules determined by magic angle spinning NMR spectroscopy. *Proceedings of the National Academy of Sciences* **112**, 14611–14616 (2015).
9. Atherton, J. *et al.* A structural model for microtubule minus-end recognition and protection by CAMSAP proteins. *Nature structural & molecular biology* **24**, 931–943 (2017).
10. Kubo, S. *et al.* A gel-encapsulated bioreactor system for NMR studies of protein–protein interactions in living mammalian cells. *Angewandte Chemie* **125**, 1246–1249 (2013).
11. Kesten, C. *et al.* The companion of cellulose synthase 1 confers salt tolerance through a Tau-like mechanism in plants. *Nature communications* **10**, 857 (2019).
12. Kadavath, H. *et al.* The binding mode of a tau peptide with tubulin. *Angewandte Chemie International Edition* **57**, 3246–3250 (2018).
13. Atherton, J. *et al.* Structural determinants of microtubule minus end preference in CAMSAP CCK domains. *Nature communications* **10**, 1–16 (2019).
14. Luo, Y. *et al.* Direct observation of dynamic protein interactions involving human microtubules using solid-state NMR spectroscopy. *Nature communications* **11**, 1–10 (2020).
15. Damman, R. *et al.* Atomic-level insight into mRNA processing bodies by combining solid and solution-state NMR spectroscopy. *Nature communications* **10**, 1–11 (2019).
16. Souphron, J. *et al.* Purification of tubulin with controlled post-translational modifications by polymerization–depolymerization cycles. *Nature protocols* **14**, 1634–1660 (2019).
17. Fung, B., Khitritin, A. & Ermolaev, K. An improved broadband decoupling sequence for liquid crystals and solids. *Journal of magnetic resonance* **142**, 97–101 (2000).
18. Bennett, A. E. *et al.* Homonuclear radio frequency-driven recoupling in rotating solids. *The Journal of chemical physics* **108**, 9463–9479 (1998).
19. Sauvée, C. *et al.* Highly efficient, water-soluble polarizing agents for dynamic nuclear polarization at high frequency. *Angewandte Chemie International Edition* **52**, 10858–10861 (2013).
20. Gradmann, S. *et al.* Rapid prediction of multi-dimensional NMR data sets. *Journal of biomolecular NMR* **54**, 377–387 (2012).



Chapter 4

¹H-detected characterization of carbon-carbon networks in highly flexible protonated biomolecules using MAS NMR

Adapted from

Salima Bahri*, Adil Safeer, Agnes Adler, Hanneke Smedes, Hugo van Ingen, and Marc Baldus* ¹H-detected characterization of carbon-carbon networks in highly flexible protonated biomolecules using MAS NMR, submitted

Contribution: SB, Hvl and MB contributed to the study conception and design. Material preparation was performed by AA, AS and HS. SB, AS, and Hvl collected and analysed data.



Abstract

In the last three decades, the scope of solid-state NMR has expanded to exploring complex biomolecules, from large protein assemblies to intact cells at atomic-level resolution. This diversity in macromolecules frequently features highly flexible components whose insoluble environment precludes the use of solution NMR to study their structure and interactions. While High-resolution Magic-Angle Spinning (HR-MAS) probes offer the capacity for gradient-based ^1H -detected spectroscopy in solids, such probes are not commonly used for routine MAS NMR experiments. As a result, most exploration of the flexible regime entails either ^{13}C -detected experiments, the use of partially perdeuterated systems, or ultra-fast MAS. Here we explore proton-detected pulse schemes probing through-bond ^{13}C - ^{13}C networks to study mobile protein sidechains as well as polysaccharides in broadband manner. In this chapter we demonstrate the use of such schemes to study a mixture of microtubule-associated protein (MAP) Tau and human microtubules (MTs), and the cell wall of the fungus *Schizophyllum commune* using 2D and 3D spectroscopy, to show its viability for obtaining unambiguous correlations using standard fast-spinning MAS probes at high and ultra-high magnetic fields.

Introduction

Magic Angle Spinning (MAS) NMR is a powerful technique to study the structure, dynamics, and intermolecular interactions of insoluble biomolecules and materials. Over the last three decades, the nature of biomolecules that can be studied with MAS NMR have become more complex, from short peptides ¹⁻⁶ to whole cells ⁷⁻⁹. Concomitant technological advances have brought fast- to ultra-fast spinning probes ¹⁰⁻¹² for ^1H -detection using progressively smaller rotors, which reduce linewidths in the case of homogeneous broadening ^{13,14} while maintaining practical sensitivity due to the relatively large ^1H gyromagnetic ratio ¹⁵. Such advances have led to the development of MAS ^1H -detection techniques of fully protonated samples, circumventing the expense and loss of information of sample deuteration ¹⁶⁻¹⁹. As a

¹H-detected characterization of C-C networks in highly flexible protonated biomolecules using MAS NMR

result, a suite of ¹H-detected experiments for *de novo* chemical shift assignments^{10,20,21} are increasingly commonplace and include frequent use of dipolar or scalar ¹³C-¹³C mixing schemes such as RFDR^{22–25}, TOBSY^{26,27}, WALTZ²¹, and DIPSI^{24,28}. Typical uses for these mixing techniques have occurred within the rigid part of biomolecular assemblies, as selected by cross-polarization at the start of the pulse sequence²⁹.

However, for insoluble systems comprising flexible components, INEPT transfers select for nuclei in the fast-motion regime where dipolar self-averaging occurs. The INEPT-TOBSY experiment is frequently used to map ¹³C-¹³C connectivities in conjunction with dipolar-based counterparts, typically in a ¹³C-detected fashion^{27,30–32}. Heteronuclear ¹H-¹³C-detected correlations can provide additional assignments for the flexible regime^{31,33–35}. In the case of limited sample quantities, it is instead desirable to amplify the signal using ¹H-detection, which requires an INEPT transfer back to the ¹H channel following ¹³C evolution, mixing, and water suppression³⁶. Variants of a scalar 2D hCH J-HSQC experiment have been used to characterize complex systems including fungal cell walls³⁷, human microtubules^{38,39}, viral capsids⁴⁰, protein condensates³¹ and membrane-bound proteins⁴¹. In addition, INEPT based homonuclear 1-bond transfers have been used to obtain sequential backbone correlations in highly mobile amyloid-fibrils^{42,43}.

In the following, we explore the use of ¹H detected experiments that involve an additional broadband through-bond CC transfer step to increase spectral dispersion in applications on complex biomolecular systems containing dynamic molecular (sub)species and are difficult to prepare in deuterated form. Such an INEPT-based 3D hCCH through-bond sequence with longitudinal mixing has previously been used at moderate spinning (20 kHz) on deuterated samples recrystallized in 90 % D₂O, to obtain residual protonated methyl group assignments while avoiding ¹H₂O suppression (Agarwal et al. 2008). In addition, a 2D hC(c)H TOCSY experiment with DIPSI-2 mixing was used to obtain highly resolved spectra on a fully protonated



peptidoglycan with an ultra-fast spinning probe ⁴⁴. However, in our hands, such usage of longitudinal homonuclear mixing is prone to producing antiphase artifacts generated by resonances with especially long coherence lifetimes. We found that these artifacts are resolved either by using long phase cycles that render extension to a 3D experiment impractical, or by instead using transverse mixing with a prior trim pulse ⁴⁵ to purge unwanted coherences, similarly implemented as in solution-state NMR. We apply these schemes to study the flexible region of two complex insoluble systems using hCCH TOCSY, with DIPSI3 ²⁸ and WALTZ ⁴⁶ homonuclear carbon mixing in gradient-free MAS probes. We demonstrate that such schemes provide broadband ¹³C-¹³C correlations at both high and ultra-high field NMR conditions.

Results

In the following, we explore the flexible regions of two complex insoluble systems using hCCH TOCSY, with broadband DIPSI3 ²⁸ and WALTZ ⁴⁶ homonuclear carbon mixing in gradient-free probes using the pulse schemes given in **Fig. 4.1**. We tested the pulse scheme in **Fig. 4.1** on a sample of [¹³C, ¹⁵N] labelled Tau in complex with unlabelled microtubules (MTs). Tau is an intrinsically disordered protein that maintains microtubule stability ^{47,48}, and whose function is modulated by a series of posttranslational modifications including phosphorylation, nitration, and glycosylation ⁴⁹. In the current context we used the K32 variant (~20.5 kDa of the full length), corresponding to the microtubule binding domain Q244-K369 (R1, R2, R3, R4), the N-terminal proline-rich region S198-Q244 (P2), and the C-terminal R' region K369- K369-Y394 ⁴⁷. For labelled Tau bound to MTs, application of the 2D hC(c)H experiments shown in **Fig. 4.1** using DIPSI-3 mixing with 2 ms of preparatory C_x spin lock in addition to 25 ms of DIPSI-3 mixing, revealed multiple-bond CH correlations, to assign the aliphatic backbone and non-aromatic sidechains (**Fig. 4.2, blue**). For reference, a 2D spectrum with 0 ms of mixing is shown in red.

¹H-detected characterization of C-C networks in highly flexible protonated biomolecules using MAS NMR

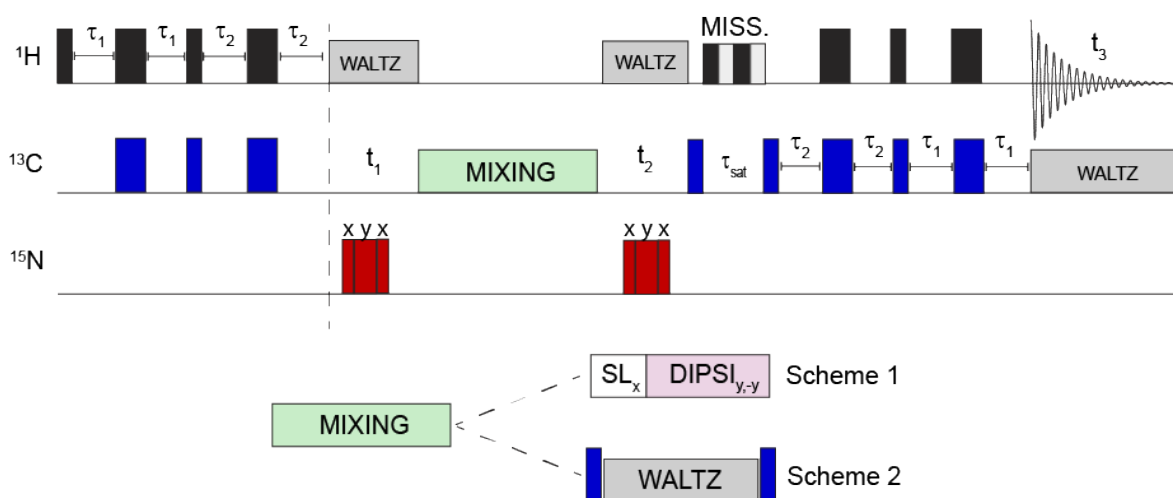


Fig. 4.1: hCCH 3D used in this work. First, an INEPT block transfers magnetization through-bond from ¹H to ¹³C prior to an evolution period to encode the ¹³C chemical shift. After the t_1 period, an x-phase spin-lock of 2ms is applied prior to DIPSI-3 mixing. Afterwards, the chemical shift is again encoded during the t_2 period. The carbon magnetization is then stored longitudinally during the water suppression period, prior to INEPT transfer back to protons for detection. Narrow and wide rectangles indicate 90°/180° pulses, respectively. The 2D hC(c)H experiments were collected by not evolving the t_2 period



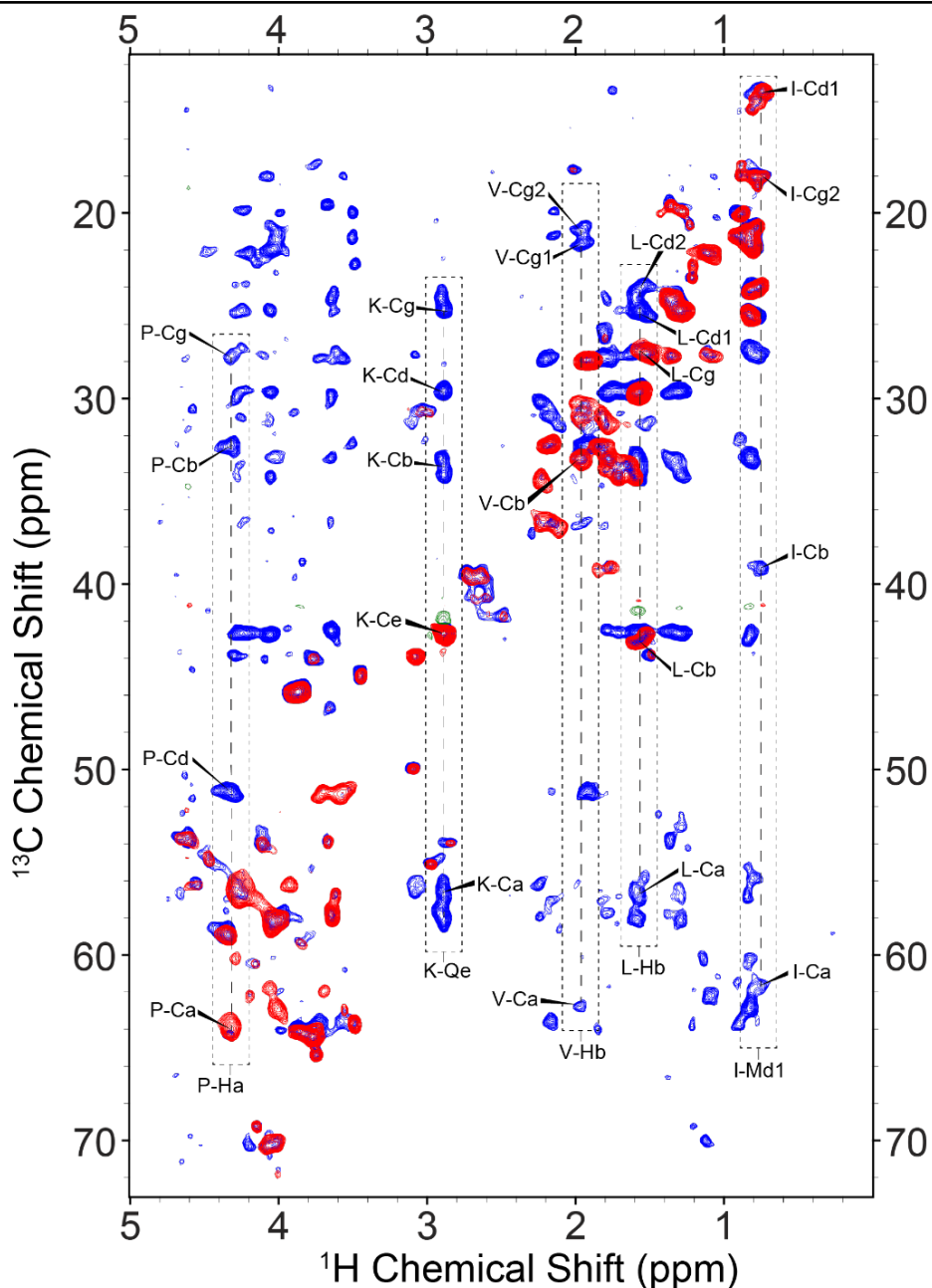


Fig. 4.2: 2D-hC(c)H spectral overlay of 0ms (red/green) and 25ms (blue/orange) of DIPSI mixing. In the dashed boxes we show examples of cross-peaks corresponding to complete intraresidual (along the side chain) scalar transfers within various residues, with unambiguous correlations as determined in the 3D shown in **Fig. 4.3**. In each vertical strip, the peaks in red are the resonance from which the first $^1\text{H} \rightarrow ^{13}\text{C}$ transfer originates before transferring to the blue crosspeaks.

¹H-detected characterization of C-C networks in highly flexible protonated biomolecules using MAS NMR

In line with previous work ⁵⁰ we expect that the observed correlations result from flexible Tau residues not involved in strong binding to MTs. While typical chemical shift assignments allow for immediate recognition of some of these resonances (e.g. Ile), chemical shift degeneracy results in a heavy degree of spectral overlap, which was alleviated by adding a second dimension to the experiment after the DIPSI-3 mixing period. **Fig. 4.3** shows the resulting strips corresponding to Ile, Leu, Lys, Pro, and Val sidechains. We also identified additional Ile and Lys residues in the 3D spectrum (not shown), indicating its usefulness in distinguishing like residues whose chemical shift dispersion results in significant overlap in lower dimensional experiments. Finally, we observe several distinct Ala, Thr and Gly residues (not shown). Currently, our survey of identifiable residues is in agreement with those observed previously ⁵⁰, though we find that our 3D hCCH correlations lead to more complete chemical shift assignments from backbone and sidechain resonances. Amino-acid selective assignments and proton linewidths for the residues highlighted in **Fig. 4.3** are provided in **Supplementary table 4.2**. While the average linewidth is less than 0.1 ppm, the observed variations did not correlate with backbone versus sidechain topology or degree of protonation.



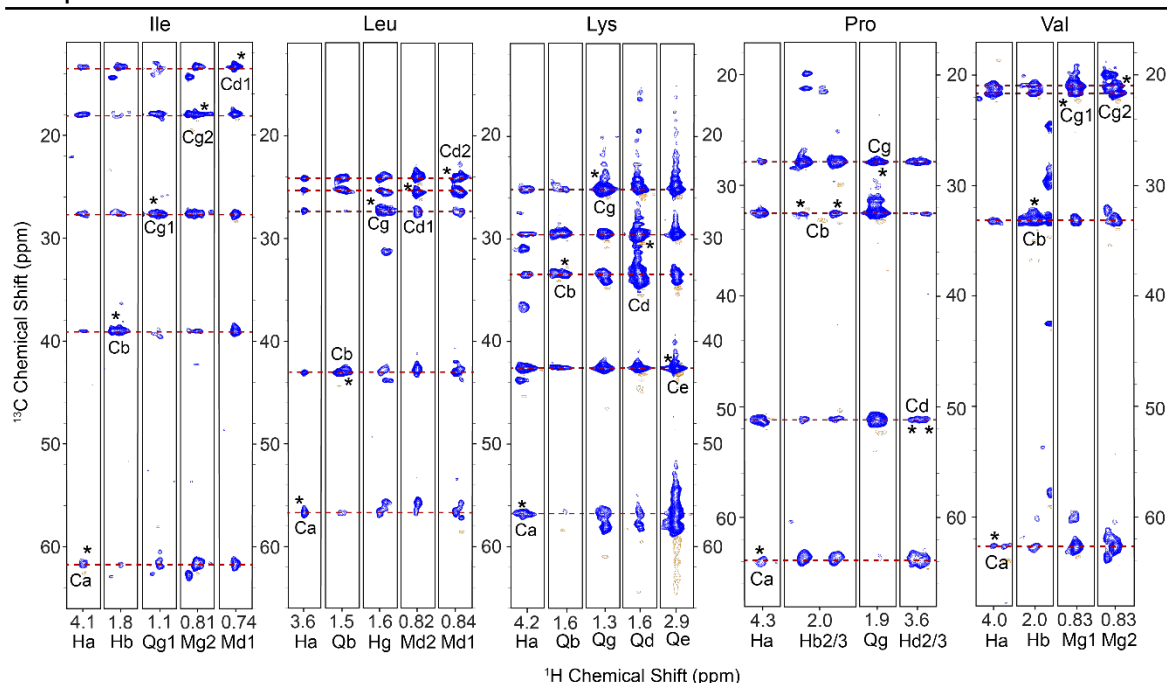


Fig. 4.3: Strips from a 3D hCCH TOCSY experiment using 25ms of DIPSI mixing, in which we show out-and-back correlations from the backbone and sidechain of four example residues: Isoleucine, Leucine, Lysine, Proline and Valine. Asterisks indicate peaks along the diagonal of the CC plane. For Proline, we observe doubled peaks for protons originating from Cb/Cd diagonal peaks.

Next, we tested the suitability of INEPT-based ¹³C-¹³C scalar transfers to explore the dynamic region of the cell wall of *S. commune*. Previous studies of ¹³C/¹⁵N-labelled *S. commune* reveal that it is composed of a complex mixture of proteins and various kinds of polysaccharides^{37,51}. Consequentially, the carbon spectrum features a larger protonated ¹³C chemical shift dispersion (~100ppm) while the non-aromatic ¹H shift range remains small (0-6ppm). As a result, low-power irradiation for homonuclear CC transfer leads to shorter-range transfer, especially at ultra-high field.

For this system, we used a variant of the sequence as shown in **Supplementary Fig. 4.1**, in which $\tau_1 = \tau_2 = 1/(4J_{HC})$, favouring the CH groups from polysaccharides and aliphatic (non-glycine) amino acids to alleviate spectral congestion. **Fig. 4.4** shows overlays of 3 spectra with 0ms (red), 4.8ms (cyan), and 11.2ms (blue) of

¹H-detected characterization of C-C networks in highly flexible protonated biomolecules using MAS NMR

isotropic WALTZ-16 mixing, which has a larger bandwidth than DIPSI-3 and may thus be advantageous at ultra-high field (Shaka et al. 1988). In spite of these relatively short mixing times, low-power irradiation (15kHz) resulted in efficient transfers among nuclei within the polysaccharide region (~65-105ppm). We highlight unambiguous assignments corresponding to the reducing ends of α - (**Ra**, left) and β -glucan (**Rb**, right), which are both formed from a tetrahydropyranose ring in chair conformation, in which C3 links the ring to the C1 successive sugar subunit via a hemiacetal linkage. We observe nearly all correlations from the pyranose ring with 11.2 ms of mixing, with the exception of C3 and C6; the former is observed only weakly in INEPT-based experiments due to its reduced mobility, while the latter has been filtered out by our choice in τ_2 INEPT delays. Notably, we also observe weak correlations between the amino acid backbone and sidechain resonances at 11.2ms of mixing (**Fig. 4.4, right**). As shown for K32-Tau, stronger correlations in this region may require longer mixing for complete transfer. Higher transfer efficiency might also be attained with the use of DIPSI instead of WALTZ mixing, which has higher transfer efficiency though at the cost of a narrower bandwidth ²⁸.



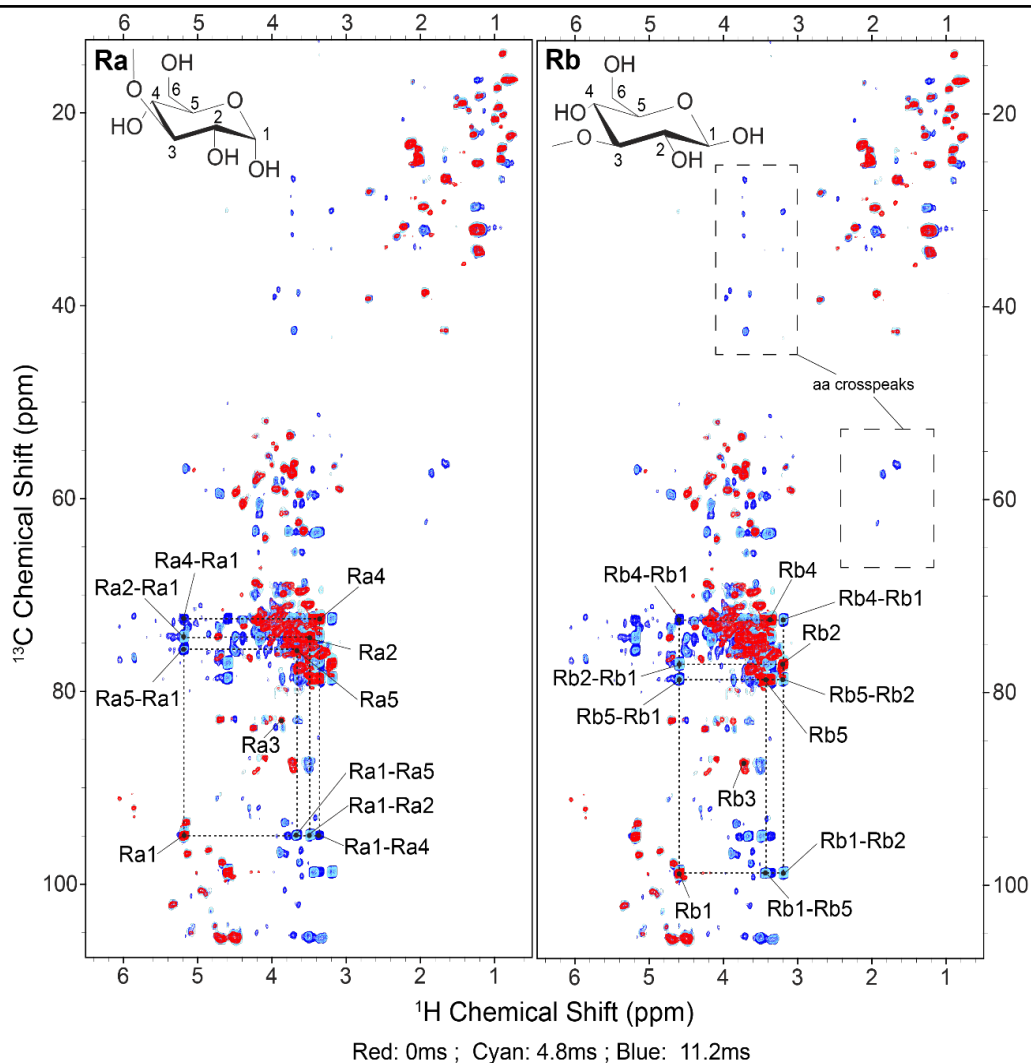


Fig. 4.4: Comparing hC(c)H spectra of varying TOCSY lengths, using WALTZ-16. We specifically show peaks belonging to the reducing ends of α -glucan (**Ra**, left) and β -glucan (**Rb**, right) as they are relatively well-isolated and show prominent transfer. In red we show the spectrum with no mixing, so that all peaks correspond to directly bonded C-H pairs. The cyan (4.8ms) and blue (11.2ms) spectra instead show multiple bond correlations corresponding to various combinations of C-H pairs within the pyranose ring (structure shown). We also observe correlations among the amino acid region (dashed boxes).

Notably, we found little overlap between peaks that appear in the INEPT-based spectrum in **Fig. 4.4** and a CP-based hCH correlation experiment of the same sample of *S. commune*³⁷. We thus expect that all observable correlations arise from the flexible domain of the fungal cell wall where chemical shift anisotropies and

¹H-detected characterization of C-C networks in highly flexible protonated biomolecules using MAS NMR

dipolar couplings are averaged out. Interestingly, when comparing the ¹H linewidths between the Tau 3D spectra (**Supplementary Table 4.1**) and fungal 2Ds ³⁷, we observe slightly broader average ¹H linewidths for the Tau data (~0.093ppm), which was collected at 44 KHz MAS vs. 60kHz MAS for *S. commune* (~0.067ppm), This improvement may be attributed to the nature of the sample or differences in effective temperature, and the larger magnetic field in the case of *S. commune*.

Discussion

In this chapter we have introduced two and three-dimensional ¹³C-¹³C-¹H correlation experiments that allowed us to characterize dynamic carbons networks of complex biomolecular systems without the need of deuteration, HR-MAS probes ^{41,52-54} or ultra-fast MAS in ¹H-detected TOCSY experiments ^{55,56}. Our data show that we can indirectly determine through-bond ¹³C-¹³C connectivities with refocused INEPT-based pulse sequences in a selective manner as determined by the choice of *J*-coupling and delays. We obtained 2D hC(c)H spectra of exceptionally high resolution on fully protonated mixture of ¹³C/¹⁵N-labelled K32-Tau and unlabelled human microtubules as well as fungal cell wall preparations of *Schizophyllum commune* ⁵¹. We extended the sequence to a 3D hCCH experiment to alleviate chemical shift degeneracy for obtaining unambiguous correlations. This experiment could be further tuned to additional selectivity, by adjusting the length of the τ_2 delay. Combination with the sequential HNCcCA and HNCa experiments ^{42,43,57,58} would lead to full sequential assignments of dynamic protein stretches.

This method can also be used in conjunction with CP-based ¹H-detected schemes – which require fast-to-ultrafast MAS techniques for fully protonated samples – and also enable one to study biopolymers within native conditions. Adapting solution NMR methodology in this way will allow Magic Angle Spinning NMR to explore a wider scope of biomolecules with a large flexible domain, such as membrane proteins with whose main functions lies in the extra membrane space e.g. integrins



⁵⁹, growth hormone receptors ⁶⁰, and membrane-anchored lipoproteins ⁶¹. In addition, such analysis is not restricted to biomolecules, but could also be used to identify soluble organic intermediates and byproducts in industrial catalysts ^{62,63}. We thus predict widespread usage of such sequences using standard MAS probes to thoroughly characterize organic components across various applications.

Material and Methods

Expression of Tau K32:

The gene encoding Tau K32 inserted in a pNG2 plasmid was kindly gifted to us by the Mandelkow group of the German Center for Neurodegenerative Diseases, Bonn, Germany. The vector was transfected in *E. coli BL21 (DE3)* competent cells and expression was induced in M9 minimal media with 0.3 mM isopropyl--D-thiogalactopyranoside (IPTG) when the OD₆₀₀ reached 0.6 for 16 h at 20 °C.

Purification of Tau K32:

[¹³C,¹⁵N] labelled Tau K32 was purified according to the protocol described by Barghorn et al. ⁶⁴ Small adaptations to the protocol are described below. Firstly, 1 mM NaN₃ was added to the buffers, to minimize the risk of growth in them. Moreover, cells were lysed either with a French pressure cell as described previously or by sonication. The cation exchange chromatography that was utilized was a HiTrap SP column of 5 mL and for gel filtration chromatography a HiLoad 26/60 Superdex 75 prep grade column. The protein concentration was measured by a BCA assay with a Thermo Scientific Pierce BCA Protein Assay Kit.

MTs polymerization and preparation of solid-state NMR samples:

Lyophilized tubulin (Cytoskeleton, Inc.) was solubilised in Brb80 buffer (80 mM PIPES, 2 mM MgCl₂, 1 mM EGTA, pH 6.8, 1 mM NaN₃, 1 mM DTT, pH 6.8), to a final concentration of 2 mg/mL. The polymerization was induced by adding 1 mM

¹H-detected characterization of C-C networks in highly flexible protonated biomolecules using MAS NMR

Guanosine-5'-triphosphate (GTP) and incubation for 15 minutes at 30 °C. Then, 20 μM paclitaxel (taxol, SIGMA) was used to stabilize the MTs and incubation took place for another 15 minutes at 30 °C. The MTs were spun down at 180.000 xg (Beckman TLA-55 rotor) for 30 minutes at 30 °C and the pellet was resuspended in warm Brb80 buffer with 20 μM paclitaxel. Subsequently, a 1 to 1 ratio of ¹³C¹⁵N Tau K32 was added. The interaction partners were incubated for 30 minutes at 37 °C. In the following isotopically labelled Tau K32 in complex with MTs was separated from the unbound, non-polymerized fraction by centrifugation at 180.000 xg (Beckman TLA-55 rotor) for 30 minutes at 30 °C. Afterwards, the pellet was washed with 40 mM phosphate buffer, pH 7, with protease inhibitor (as described earlier) and 1 mM NaN₃, without disturbing the pellet. A 1.3 mm rotor was packed with the pellet.

MAS NMR Experiments:

Table 4.1 Basic experimental details for each sample used in this manuscript. Further details are provided in the materials and methods section, and **Table S4.1**

Sample	Tau+MT	S. commune
$\gamma_H B_0/2\pi$	700 MHz	1200 MHz
$\omega_r/2\pi$	44 kHz	60 kHz
Sequence Scheme	Scheme 1	Scheme 2
τ_1	1.72 ms ($1/4J_{HC}$)	1.72 ms ($1/4J_{HC}$)
τ_2	1.15 ms ($1/6J_{HC}$)	1.72 ms ($1/4J_{HC}$)
¹³ C- ¹³ C Mixing, $\gamma_C B_1/2\pi$	SL _x +DIPSI, 17kHz	WALTZ-16, 15kHz

MAS NMR experiments for the Tau-microtubule mixture used a 3-channel HXY 1.3mm probe at $\omega_{oH}/2\pi = 700\text{MHz}$ with a Bruker Avance 3 console. The MAS rate was set to 44kHz, with a set temperature of 280K, which results in a sample temperature of ~303K based on calibration using KBr ⁶⁵. The pulse program



Chapter 4

corresponding to this sample is provided schematically in **Supplementary Fig. 4.1**, with the full sequence in the supporting information. Pulse amplitudes for INEPT transfers and ^{15}N J -refocusing were the following: $\omega_{1\text{H}}/2\pi = 127\text{kHz}$, $\omega_{13\text{C}}/2\pi = 83\text{kHz}$, and $\omega_{15\text{N}}/2\pi = 75\text{kHz}$. MISSISSIPPI was used for water suppression³⁶. 2D experiments were collected by not evolving the t_2 dimension of the pulse scheme shown in **Fig. 4.1**. For 0 ms mixing, neither the SL_x nor the $\text{DIPSI}_{y,y}$ blocks were executed, while in the case of mixing we used 2ms of SL_x at the same amplitude as the DIPSI strength^{45,66}. The 2D experiments were processed in Topspin: the data was zero-filled, and a QSine window function was applied with a sinebell shift of 2.5. For the 3D, non-uniform sampling was used with a Poisson Gap distribution schedule with 25 % sampling density⁶⁷, out to ~9ms of acquisition time in both indirect ^{13}C dimensions. The data was then reconstructed using the SMILE NUS reconstruction algorithm⁶⁸ in NMRBox⁶⁹ using NMRPipe⁷⁰ for preparatory and post-processing. Each dimension was zero-filled, and sine bell-squared window processing was used for both indirect dimensions, with an offset of 0.5, endpoint of 0.95, and exponent 1.0. For SMILE processing, the noise factor for signal cutoff was set to 5, with an 80 % threshold for signal detection. In both the 2D and 3D experiments, the ^1H dimension was referenced using water at 4.7ppm, while the ^{13}C dimension was referenced indirectly with a correction factor determined from the gyromagnetic ratio. Chemical shift and linewidth analysis was performed in NMRFAM Sparky software⁷¹.

S. Commune: The $^{13}\text{C}/^{15}\text{N}$ -labelled sample was prepared as discussed in previous publications^{37,51}. MAS NMR experiments used a 3-channel HXY 1.3 mm probe at $\gamma B_{0\text{H}}/2\pi = 1.2\text{ GHz}$ with a Bruker NEO console. The MAS spin rate was set to 60kHz, and the sample was cooled to 260K leading to a sample temperature of ~20°C. The pulse sequence outlined in **Supplementary Fig. 4.1B** was used. The strength of the hard pulses on each channel were set as follows: $\omega_{1\text{H}}/2\pi = 100\text{kHz}$, $\omega_{13\text{C}}/2\pi = 67\text{kHz}$, and $\omega_{15\text{N}}/2\pi = 50\text{kHz}$. The ^1H dimension was referenced using water resonating at 4.7ppm, while the ^{13}C dimension was referenced to previously published work⁵¹. B_0

¹H-detected characterization of C-C networks in highly flexible protonated biomolecules using MAS NMR

field drift artifacts in the *S. commune* spectra were corrected using previously published scripts ⁷². Further information regarding data acquisition for both samples can be found in **Supplementary table 4.1**.



References

1. Fu, R. & Cross, T. A. Solid-state nuclear magnetic resonance investigation of protein and polypeptide structure. *Annual review of biophysics and biomolecular structure* **28**, 235–268 (1999).
2. Griffin, R. Dipolar recoupling in MAS spectra of biological solids. *Nature structural biology* **5**, 508–512 (1998).
3. Jaroniec, C. P., Filip, C. & Griffin, R. G. 3D TEDOR NMR experiments for the simultaneous measurement of multiple carbon- nitrogen distances in uniformly ¹³C, ¹⁵N-labeled solids. *Journal of the American Chemical Society* **124**, 10728–10742 (2002).
4. Luca, S., Heise, H. & Baldus, M. High-Resolution Solid-State NMR Applied to Polypeptides and Membrane Proteins. *Acc. Chem. Res.* **36**, 858–865 (2003).
5. Rienstra, C. M., Hohwy, M., Hong, M. & Griffin, R. G. 2D and 3D ¹⁵N–¹³C–¹³C NMR Chemical Shift Correlation Spectroscopy of Solids: Assignment of MAS Spectra of Peptides. *J. Am. Chem. Soc.* **122**, 10979–10990 (2000).
6. Tycko, R. BIOMOLECULAR SOLID STATE NMR: Advances in Structural Methodology and Applications to Peptide and Protein Fibrils. *Annual Review of Physical Chemistry* **52**, 575–606 (2001).
7. Ghassemi, N. *et al.* Solid-state NMR investigations of extracellular matrixes and cell walls of algae, bacteria, fungi, and plants. *Chemical reviews* **122**, 10036–10086 (2021).
8. Narasimhan, S. *et al.* DNP-supported solid-state NMR spectroscopy of proteins inside mammalian cells. *Angewandte Chemie* **131**, 13103–13107 (2019).
9. Renault, M. *et al.* Solid-State NMR Spectroscopy on Cellular Preparations Enhanced by Dynamic Nuclear Polarization. *Angewandte Chemie International Edition* **51**, 2998–3001 (2012).
10. Barbet-Massin, E. *et al.* Rapid proton-detected NMR assignment for proteins with fast magic angle spinning. *Journal of the American Chemical Society* **136**, 12489–12497 (2014).
11. Penzel, S. *et al.* Spinning faster: protein NMR at MAS frequencies up to 126 kHz. *Journal of Biomolecular NMR* **73**, 19–29 (2019).
12. Samoson, A. (2021). 0.2 MHz MAS. Experimental Nuclear Magnetic Resonance Conference, Virtual Conference.
13. Maricq, M. M. & Waugh, J. S. NMR in rotating solids. *The Journal of Chemical Physics* **70**, 3300–3316 (1979).
14. Schledorn, M. *et al.* Protein NMR Spectroscopy at 150 kHz Magic-Angle Spinning Continues To Improve Resolution and Mass Sensitivity. *ChemBioChem* **21**, 2540–2548 (2020).
15. Agarwal, V. *et al.* De novo 3D structure determination from sub-milligram protein samples by solid-state 100 kHz MAS NMR spectroscopy. *Angewandte Chemie International Edition* **53**, 12253–12256 (2014).
16. Guo, C. *et al.* Fast magic angle spinning NMR with heteronucleus detection for resonance assignments and structural characterization of fully protonated proteins. *Journal of biomolecular NMR* **60**, 219–229 (2014).
17. Paulson, E. K. *et al.* High-Sensitivity Observation of Dipolar Exchange and NOEs between Exchangeable Protons in Proteins by 3D Solid-State NMR Spectroscopy. *J. Am. Chem. Soc.* **125**, 14222–14223 (2003).
18. Zhou, D. H. *et al.* Proton-Detected Solid-State NMR Spectroscopy of Fully Protonated Proteins at 40 kHz Magic-Angle Spinning. *J. Am. Chem. Soc.* **129**, 11791–11801 (2007).
19. Zhou, D. H. *et al.* Solid-state NMR analysis of membrane proteins and protein aggregates by proton detected spectroscopy. *Journal of Biomolecular NMR* **54**, 291–305 (2012).

¹H-detected characterization of C-C networks in highly flexible protonated biomolecules using MAS NMR

20. Fricke, P. *et al.* Backbone assignment of perdeuterated proteins by solid-state NMR using proton detection and ultrafast magic-angle spinning. *Nature Protocols* **12**, 764–782 (2017).
21. Stanek, J. *et al.* NMR Spectroscopic Assignment of Backbone and Side-Chain Protons in Fully Protonated Proteins: Microcrystals, Sedimented Assemblies, and Amyloid Fibrils. *Angewandte Chemie International Edition* **55**, 15504–15509 (2016).
22. Asami, S. & Reif, B. Proton-detected solid-state NMR spectroscopy at aliphatic sites: application to crystalline systems. *Accounts of chemical research* **46**, 2089–2097 (2013).
23. Bennett, A., Griffin, R., Ok, J. & Vega, S. Chemical shift correlation spectroscopy in rotating solids: Radio frequency-driven dipolar recoupling and longitudinal exchange. *The Journal of chemical physics* **96**, 8624–8627 (1992).
24. Paluch, P. *et al.* NMR Assignment of Methyl Groups in Immobilized Proteins Using Multiple-Bond ¹³C Homonuclear Transfers, Proton Detection, and Very Fast MAS. *Frontiers in Molecular Biosciences* **9**, (2022).
25. Sarkar, S. *et al.* Atomic-Resolution Structure of SARS-CoV-2 Nucleocapsid Protein N-Terminal Domain. *J. Am. Chem. Soc.* **144**, 10543–10555 (2022).
26. Baldus, M., Iulucci, R. & Meier, B. Probing through-bond connectivities and through-space distances in solids by magic-angle-spinning nuclear magnetic resonance. *Journal of the American Chemical Society* **119**, 1121–1124 (1997).
27. Baldus, M. & Meier, B. H. Total correlation spectroscopy in the solid state. The use of scalar couplings to determine the through-bond connectivity. (1996).
28. Shaka, A., Lee, C. & Pines, A. Iterative schemes for bilinear operators; application to spin decoupling. *Journal of Magnetic Resonance (1969)* **77**, 274–293 (1988).
29. Barbet-Massin, E. *et al.* Out-and-back ¹³C–¹³C scalar transfers in protein resonance assignment by proton-detected solid-state NMR under ultra-fast MAS. *Journal of biomolecular NMR* **56**, 379–386 (2013).
30. Andronesi, O. C. *et al.* Determination of membrane protein structure and dynamics by magic-angle-spinning solid-state NMR spectroscopy. *Journal of the American Chemical Society* **127**, 12965–12974 (2005).
31. Damman, R. *et al.* Atomic-level insight into mRNA processing bodies by combining solid and solution-state NMR spectroscopy. *Nature communications* **10**, 1–11 (2019).
32. Heise, H. *et al.* Molecular-level secondary structure, polymorphism, and dynamics of full-length α -synuclein fibrils studied by solid-state NMR. *Proceedings of the National Academy of Sciences* **102**, 15871–15876 (2005).
33. Alam, T. & Holland, G. ¹H–¹³C INEPT MAS NMR correlation experiments with ¹H–¹H mediated magnetization exchange to probe organization in lipid biomembranes. *Journal of Magnetic Resonance* **180**, 210–221 (2006).
34. Elena, B., Lesage, A., Steuernagel, S., Böckmann, A. & Emsley, L. Proton to carbon-13 INEPT in solid-state NMR spectroscopy. *Journal of the American Chemical Society* **127**, 17296–17302 (2005).
35. Siemer, A. B. Advances in studying protein disorder with solid-state NMR. *Solid State Nuclear Magnetic Resonance* **106**, 101643 (2020).
36. Zhou, D. H. & Rienstra, C. M. High-performance solvent suppression for proton detected solid-state NMR. *Journal of magnetic resonance* **192**, 167–172 (2008).
37. Safeer, A. *et al.* Probing Cell-Surface Interactions in Fungal Cell Walls by High-Resolution ¹H-Detected Solid-State NMR Spectroscopy. *Chemistry – A European Journal* **29**, e202202616 (2023).

Chapter 4

38. Pines, A. *et al.* Direct observation of dynamic protein interactions involving human microtubules using solid-state NMR spectroscopy. *Nature communications* **11**, 1–10 (2020).
39. Savastano, A., Jaipuria, G., Andreas, L., Mandelkow, E. & Zweckstetter, M. Solid-state NMR investigation of the involvement of the P2 region in tau amyloid fibrils. *Scientific Reports* **10**, 21210 (2020).
40. Callon, M. *et al.* Fast Magic-Angle-Spinning NMR Reveals the Evasive Hepatitis B Virus Capsid C-Terminal Domain. *Angewandte Chemie* **134**, e202201083 (2022).
41. Howarth, G. S. & McDermott, A. E. High-Resolution Magic Angle Spinning NMR of KcsA in Liposomes: The Highly Mobile C-Terminus. *Biomolecules* **12**, 1122 (2022).
42. Falk, A. S. & Siemer, A. B. Dynamic domains of amyloid fibrils can be site-specifically assigned with proton detected 3D NMR spectroscopy. *Journal of biomolecular NMR* **66**, 159–162 (2016).
43. Zhang, S. *et al.* Conformational Dynamics of an α -Synuclein Fibril upon Receptor Binding Revealed by Insensitive Nuclei Enhanced by Polarization Transfer-Based Solid-State Nuclear Magnetic Resonance and Cryo-Electron Microscopy. *J. Am. Chem. Soc.* **145**, 4473–4484 (2023).
44. Bougault, C., Ayala, I., Vollmer, W., Simorre, J.-P. & Schanda, P. Studying intact bacterial peptidoglycan by proton-detected NMR spectroscopy at 100 kHz MAS frequency. *Journal of structural biology* **206**, 66–72 (2019).
45. Bax, A., Clore, G. M. & Gronenborn, A. M. ^1H – ^1H correlation via isotropic mixing of ^{13}C magnetization, a new three-dimensional approach for assigning ^1H and ^{13}C spectra of ^{13}C -enriched proteins. *Journal of Magnetic Resonance (1969)* **88**, 425–431 (1990).
46. Shaka, A. J., Keeler, J., Frenkiel, T. & Freeman, R. An improved sequence for broadband decoupling: WALTZ-16. *Journal of Magnetic Resonance (1969)* **52**, 335–338 (1983).
47. Brotzakis, Z. F. *et al.* A structural ensemble of a tau-microtubule complex reveals regulatory tau phosphorylation and acetylation mechanisms. *ACS Central Science* **7**, 1986–1995 (2021).
48. Kadavath, H. *et al.* Folding of the tau protein on microtubules. *Angewandte Chemie International Edition* **54**, 10347–10351 (2015).
49. Martin, L., Latypova, X. & Terro, F. Post-translational modifications of tau protein: Implications for Alzheimer’s disease. *Neurochemistry International* **58**, 458–471 (2011).
50. El Mammeri, N., Dregni, A. J., Duan, P., Wang, H. K. & Hong, M. Microtubule-binding core of the tau protein. *Science Advances* **8**, eabo4459 (2022).
51. Ehren, H. L. *et al.* Characterization of the cell wall of a mushroom forming fungus at atomic resolution using solid-state NMR spectroscopy. *The Cell Surface* **6**, 100046 (2020).
52. Blicharski, J. & Sobol, W. A new type of magnetic field gradient coil for NMR measurements. *Journal of Magnetic Resonance (1969)* **46**, 1–8 (1982).
53. Zupancic, I. & Pirs, J. Coils producing a magnetic field gradient for diffusion measurements with NMR. *Journal of Physics E: Scientific Instruments* **9**, 79 (1976).
54. Li, W., Lee, R. E. B., Lee, R. E. & Li, J. Methods for Acquisition and Assignment of Multidimensional High-Resolution Magic Angle Spinning NMR of Whole Cell Bacteria. *Anal. Chem.* **77**, 5785–5792 (2005).
55. Ikura, M., Kay, L. E. & Bax, A. A novel approach for sequential assignment of proton, carbon-13, and nitrogen-15 spectra of larger proteins: heteronuclear triple-resonance three-dimensional NMR spectroscopy. Application to calmodulin. *Biochemistry* **29**, 4659–4667 (1990).
56. Kay, L. E., Ikura, M., Tschudin, R. & Bax, A. Three-dimensional triple-resonance NMR Spectroscopy of isotopically enriched proteins. *Journal of Magnetic Resonance* **213**, 423–441 (2011).
57. Linser, R., Fink, U. & Reif, B. Proton-detected scalar coupling based assignment strategies in MAS solid-state NMR spectroscopy applied to perdeuterated proteins. *Journal of Magnetic Resonance* **193**, 89–93 (2008).

¹H-detected characterization of C-C networks in highly flexible protonated biomolecules using MAS NMR

58. Linsler, R., Fink, U. & Reif, B. Assignment of Dynamic Regions in Biological Solids Enabled by Spin-State Selective NMR Experiments. *J. Am. Chem. Soc.* **132**, 8891–8893 (2010).
59. Bergonzini, C., Kroese, K., Zweemer, A. J. & Danen, E. H. Targeting integrins for cancer therapy—disappointments and opportunities. *Frontiers in Cell and Developmental Biology* **10**, (2022).
60. Kaplan, M. *et al.* EGFR dynamics change during activation in native membranes as revealed by NMR. *Cell* **167**, 1241–1251 (2016).
61. Xiang, S., Pinto, C. & Baldus, M. Divide and Conquer: A Tailored Solid-state NMR Approach to Study Large Membrane Protein Complexes. *Angewandte Chemie International Edition* **61**, e202203319 (2022).
62. Chowdhury, A. D. *et al.* Electrophilic aromatic substitution over zeolites generates Wheland-type reaction intermediates. *Nature Catalysis* **1**, 23–31 (2018).
63. Chowdhury, A. D. *et al.* Bridging the gap between the direct and hydrocarbon pool mechanisms of the methanol-to-hydrocarbons process. *Angewandte Chemie International Edition* **57**, 8095–8099 (2018).
64. Barghorn, S., Biernat, J. & Mandelkow, E. Purification of recombinant tau protein and preparation of Alzheimer-paired helical filaments in vitro. in *Amyloid proteins* 35–51 (Springer, 2005).
65. Thurber, K. R. & Tycko, R. Measurement of sample temperatures under magic-angle spinning from the chemical shift and spin-lattice relaxation rate of ⁷⁹Br in KBr powder. *Journal of Magnetic Resonance* **196**, 84–87 (2009).
66. Clore, G. M., Bax, A., Driscoll, P. C., Wingfield, P. T. & Gronenborn, A. M. Assignment of the side-chain proton and carbon-13 resonances of interleukin-1. beta. using double- and triple-resonance heteronuclear three-dimensional NMR spectroscopy. *Biochemistry* **29**, 8172–8184 (1990).
67. Maciejewski, M. W., Mobli, M., Schuyler, A. D., Stern, A. S. & Hoch, J. C. Data Sampling in Multidimensional NMR: Fundamentals and Strategies. in *Novel Sampling Approaches in Higher Dimensional NMR* (eds. Billeter, M. & Orekhov, V.) 49–77 (Springer Berlin Heidelberg, 2012). doi:10.1007/128_2011_185.
68. Ying, J., Delaglio, F., Torchia, D. A. & Bax, A. Sparse multidimensional iterative lineshape-enhanced (SMILE) reconstruction of both non-uniformly sampled and conventional NMR data. *Journal of Biomolecular NMR* **68**, 101–118 (2017).
69. Maciejewski, M. W. *et al.* NMRbox: A Resource for Biomolecular NMR Computation. *Biophysical Journal* **112**, 1529–1534 (2017).
70. Delaglio, F. *et al.* NMRPipe: a multidimensional spectral processing system based on UNIX pipes. *Journal of biomolecular NMR* **6**, 277–293 (1995).
71. Lee, W., Tonelli, M. & Markley, J. L. NMRFAM-SPARKY: enhanced software for biomolecular NMR spectroscopy. *Bioinformatics* **31**, 1325–1327 (2015).
72. Najbauer, E. E. & Andreas, L. B. Correcting for magnetic field drift in magic-angle spinning NMR datasets. *Journal of Magnetic Resonance* **305**, 1–4 (2019).



¹H-detected characterization of C-C networks in highly flexible protonated biomolecules using MAS NMR

Supplementary table 4.1 Acquisition/processing parameters for the Tau+MTs mixture and *S. commune*.

Sample	Tau+MT 2D	Tau+MT 3D	S. commune
$\gamma_H B_0 / 2\pi$	700 MHz	700 MHz	1200 MHz
$\omega_f / 2\pi$	44 kHz	44 kHz	60 kHz
Carrier (¹ H / ¹³ C)	3.5/38 ppm	3.5/39 ppm	3.0/51 ppm
Evolution Time, ¹³ C	12.7 ms	8.9 ms *	5 ms
Spectral Window, ¹³ C	**67, 65 ppm/11,792 Hz	67 ppm/11,792 Hz *	130 ppm/39,000 Hz
Evolution Time, ¹ H	31.7 ms	31.7 ms	30 ms
Spectral Window, ¹ H	18 ppm/12,600 Hz	18 ppm/12,600 Hz	25 ppm/30,000 Hz
¹³ C- ¹³ C Mixing, $\gamma_C B_1 / 2\pi$	SL _x +DIPSI, 17kHz	SL _x +DIPSI, 17kHz	WALTZ-16, 15kHz
Decoupling (¹ H, ¹³ C)	WALTZ-16, 13kHz	WALTZ-16, 13kHz	WALTZ-16, 10kHz
Water Suppression	120ms, 26 kHz	120ms, 26 kHz	160ms, 22 kHz
Number of Scans	16	16	64
τ_1	1.72 ms (1/4J _{HC})	1.72 ms (1/4J _{HC})	1.72 ms (1/4J _{HC})
τ_2	1.15 ms (1/6J _{HC})	1.15 ms (1/6J _{HC})	1.72 ms (1/4J _{HC})
Quadrature Mode	States-TPPI	States-TPPI*	States-TPPI
Complex Points	800 x 300	800 x 210 x 210	1754 x 400
Zero Filling	1024 x 512	- ***	2048 x 1024

* parameters for both ¹³C indirect dimensions

** 67ppm SW in the ¹³C dimension was used for 0ms of mixing, whereas a 65ppm SW was used for the 2D obtained with mixing

*** ZF was applied according to automated smile3D.com parameters



Chapter 4

Supplementary table 4.2 ^1H chemical shifts and linewidths of Tau resonances (**Fig. 4.3** as determined in Sparky. Unresolved peaks are highlighted in yellow. Linewidths were measured in the directly bonded CH plane, in the 3D slice corresponding to the diagonal CC peak.

Isoleucine	Chemical Shift (ppm)	Linewidth (Hz)
Ha	4.07	56.2
Hb	1.76	73.6
Qg1	1.07	73.1
Mg2	0.81	73.4
Md1	0.74	52.0
Leucine	Chemical Shift (ppm)	Linewidth (Hz)
Ha	3.59	40.1
Qb	1.55	75.9
Hg	1.59	56.0
Md1	0.82	53.8
Md2	0.84	48.0
Lysine	Chemical Shift (ppm)	Linewidth (Hz)
Ha	4.23	83.9
Qb	1.65	74.6
Qg	1.33	54.2
Qd	1.58	60.2
Qe	2.89	53.4
Proline	Chemical Shift (ppm)	Linewidth (Hz)
Ha	4.3	75.6
Hb2	2.18	58.9
Hb3	1.82	63.1
Qg	1.89	74.8
Hd2	3.68	79.9
Hd3	3.56	100.0
Valine	Chemical Shift (ppm)	Linewidth (Hz)
Ha	4.01	57.9
Hb	1.97	77.2
Mg1	0.83	57.1
Mg2	0.83	57.3

¹H-detected characterization of C-C networks in highly flexible protonated biomolecules using MAS NMR

Pulse Sequence, Bruker Format

```
;$COMMENT= hCCH 3D, arbitrary contact and decoupling schemes
;$CLASS=Solids
;$DIM=3D
;$TYPE=INEPT
;$OWNER=Bruker

;p1 : H90 pulse length
;p2 : C90 pulse length
;p3 : N90 pulse length
;p20 : MISSISSIPPI pulse length
;p9 : f2 channel - 90 degree low power pulse (DIPSI)

;p11 : H90 pulse power
;p12 : C90 pulse power
;p13 : N90 pulse power
;p113 : H WALTZ decoupling
;p129 : C WALTZ decoupling
;p114 : C DIPSI3 power

;cnst2 : H-C J-coupling
;cnst24 : frequency hop for water suppression
;cnst3 : relection for echo, 6 to select all 13C

;i1 : to set length of DIPSI mixing
;i2 : MISSISSIPPI loops

define delay JCH1
define delay JCH2
define delay JCH2t
define delay mix

"d0 = 0"
"i0 = 0"
"d10 = 0"
"i10 = 0"

"in0 = inf1"
"in10 = inf2"

"p5 = 2000u"
"d16 = 0.636*p1"
"mix=(p9*54.33*4)*i1"
"JCH1 = 1/(4*cnst2)"
"JCH2 = 1/(cnst3*cnst2)"
"JCH2t = JCH2 - 0.636*p2"

1 ze
2 d1 do:f2 do:f1
  (p1 pl1 ph1):f1
  JCH1
  (center (p1*2 pl1 ph0):f1 (p2*2 pl2 ph0):f2)
  JCH1
  (center (p1 pl1 ph2):f1 (p2 pl2 ph3):f2)
  JCH2t
  (center (p1*2 pl1 ph0):f1 (p2*2 pl2 ph0):f2)
  JCH2 pl13:f1 pl3:f3

  if "i0 == 1" {
    "d0 = in0 - 0.3u"
  }
  if "i0 > 0" {
    (center (d0 cpds1):f1 (p3 ph20 p3*2 ph21 p3 ph20):f3)
    0.3u do:f1
  }
}
```

Chapter 4

#ifdef tocsy ; note for no mixing, remove tocsy flag

(p5 pl5 ph0):f2
0.3u pl14:f2
9 (p9*2.722 ph21):f2
(p9*4.389 ph23):f2
(p9*2.778 ph21):f2
(p9*3.056 ph23):f2
(p9*0.333 ph21):f2
(p9*2.556 ph23):f2
(p9*4.000 ph21):f2
(p9*2.722 ph23):f2
(p9*4.111 ph21):f2
(p9*3.778 ph23):f2
(p9*3.889 ph21):f2
(p9*2.889 ph23):f2
(p9*3.000 ph21):f2
(p9*0.333 ph23):f2
(p9*2.500 ph21):f2
(p9*4.050 ph23):f2
(p9*2.830 ph21):f2
(p9*4.389 ph23):f2
(p9*2.722 ph23):f2
(p9*4.389 ph21):f2
(p9*2.778 ph23):f2
(p9*3.056 ph21):f2
(p9*0.333 ph23):f2
(p9*2.556 ph21):f2
(p9*4.000 ph23):f2
(p9*2.722 ph21):f2
(p9*4.111 ph23):f2
(p9*3.778 ph21):f2
(p9*3.889 ph23):f2
(p9*2.889 ph21):f2
(p9*3.000 ph23):f2
(p9*0.333 ph21):f2
(p9*2.500 ph23):f2
(p9*4.050 ph21):f2
(p9*2.830 ph23):f2
(p9*4.389 ph21):f2
(p9*2.722 ph23):f2
(p9*4.389 ph21):f2
(p9*2.778 ph23):f2
(p9*3.056 ph21):f2
(p9*0.333 ph23):f2
(p9*2.556 ph21):f2
(p9*4.000 ph23):f2
(p9*2.722 ph21):f2
(p9*4.111 ph23):f2
(p9*3.778 ph21):f2
(p9*3.889 ph23):f2
(p9*2.889 ph21):f2
(p9*3.000 ph23):f2
(p9*0.333 ph21):f2
(p9*2.500 ph23):f2
(p9*4.050 ph21):f2
(p9*2.830 ph23):f2
(p9*4.389 ph21):f2
(p9*2.722 ph21):f2
(p9*4.389 ph23):f2
(p9*2.778 ph21):f2
(p9*3.056 ph23):f2
(p9*0.333 ph21):f2
(p9*2.556 ph23):f2
(p9*4.000 ph21):f2
(p9*2.722 ph23):f2
(p9*4.111 ph21):f2
(p9*3.778 ph23):f2
(p9*3.889 ph21):f2

¹H-detected characterization of C-C networks in highly flexible protonated biomolecules using MAS NMR

```

(p9*2.889 ph23):f2
(p9*3.000 ph21):f2
(p9*0.333 ph23):f2
(p9*2.500 ph21):f2
(p9*4.050 ph23):f2
(p9*2.830 ph21):f2
(p9*4.389 ph23):f2
lo to 9 times l1
      ;end DIPS13
0.3u
#endif

if "l10 == 1" {
"d10 = in10 - 0.3u"
}
if "l10 > 0" {
(center (d10 cpds1):f1 (p3 ph20 p3*2 ph21 p3 ph20):f3)
0.3u do:f1
}

(p2 pl2 ph6):f2 (0.3u fq=cnst24):f1
;=====water saturation=====
4 (p20 pl20 ph20):f1
  (p20 pl20 ph21):f1
  (p20 pl20 ph22):f1
  (p20 pl20 ph23):f1
  (p20 pl20 ph23):f1
  (p20 pl20 ph22):f1
  (p20 pl20 ph21):f1
  (p20 pl20 ph20):f1
lo to 4 times l2
;=====end water saturation=====

      (p2 pl2 ph7):f2 (0.3u fq=0):f1
JCH2
(center (p1*2 pl1 ph0):f1 (p2*2 pl2 ph0):f2)
JCH2
(center (p1 pl1 ph8):f1 (p2 pl2 ph9):f2)
JCH1
(center (p1*2 pl1 ph10):f1 (p2*2 pl2 ph0):f2)
JCH1 pl29:f2

d16
go=2 ph31 cpds2:f2 finally do:f2 do:f1
1m do:f2 do:f1
10m mc #0 to 2
  F1PH(calph(ph3, +90), caldel(d0, +in0) & calclc(l0,1))
  F2PH(calph(ph6, -90), caldel(d10, +in10) & calclc(l10,1))

HaltAcqu, 1m
exit

ph0 = 0
ph1 = 0
ph2 = 3
ph3 = 0 2
ph6 = 1
ph7 = 3 3 1 1
ph8 = 0 0 0 0 2 2 2 2
ph9 = 2
ph10 = 0 2
ph11 = 2 0
ph20 = 0
ph21 = 1
ph22 = 2
ph23 = 3
ph31 = 0 2 2 0 2 0 0 2

```



Chapter 5

A structural and dynamic visualization of the interaction between the microtubule-associated protein 7 (MAP7) and microtubules

Adapted from

A structural and dynamic visualization of the interaction between the microtubule-associated protein 7 (MAP7) and microtubules. Agnes H. Adler **,



Mamata Bangera^{# **}, Salima Bahri, Hugo van Ingen, Carolyn A. Moores[#], Marc Baldus^{*}, *in preparation*

Contribution: AA carried out protein purification, MT assemblies, the ssNMR measurements with the help of SB. M. Ban conducted the EM experiments.

Abstract

Microtubules (MTs) are key components of the eukaryotic cytoskeleton and are essential for intracellular organization, organelle trafficking and mitosis. MT tasks depend on binding and interactions with MT-associated proteins (MAPs). MT-associated protein 7 (MAP7) has the unusual ability to both MT binding and activate kinesin-1-mediated cargo transport along MTs. Additionally, the protein is reported to stabilize MTs with its 112 amino-acid long MT-binding domain (MTBD). Here we investigate the structural basis of the interaction of MAP7 MTBD with the MT lattice. Using a combination of solid and solution-state nuclear magnetic resonance with electron microscopy, fluorescence anisotropy and isothermal titration calorimetry, we shed light on the binding mode of MAP7 to MTs at an atomic level. Our results show that both strong as well as weak dynamic protein-protein interactions between MAP7 and the structured and unstructured regions of the MTs lattice contribute to the formation of the MAP7-MT complex. Furthermore, we established MAP7's helix boundaries in the MT bound form and pinpoint specific protein regions of the MAP7-MT interaction including the MT carboxy-terminal tails.

Introduction

Mitosis, cell migration, and polarization are dependent on microtubules (MTs). An imbalance in their structure or function is associated with human disorders such as ciliopathies, cancer and neurodegeneration ¹. These biopolymers are hollow cylinders of α/β -tubulin heterodimers interacting in a "head-to-tail" and side by side fashion ^{2,3}. MT are highly dynamic structures that undergo continuous assembly and

A structural and dynamic visualization of the interaction between the microtubule-associated protein 7 (MAP7) and microtubules

disassembly both in vitro and in vivo in a process termed “dynamic instability”⁴. This process is driven by hydrolysis of guanosine 5'-triphosphate (GTP) in the MTs lattice⁵. MT-associated proteins (MAPs) are proteins that interact with MTs, can regulate their dynamics, and mediate MT functions in particular physiological contexts through sophisticated regulation⁶. The roles and mechanisms of MAPs such as MAP1, MAP2, MAP4, Tau, MAP6, DCX, MAP7 and MAP9 have recently been identified and characterized, particularly in the context of MT-rich neurons^{6,7}. The less well understood MAP7, also known as E-MAP-115 or Ensconsin, is found to bind and stabilize MTs in axons^{8,9}, possibly playing a role in the development of axonal branches. It has been implicated in the growth of metaphase spindles in neural stem cells^{10,11} and its upregulation has been observed in different forms of cancer¹²⁻¹⁴. Additionally, MAP7 is a required cofactor for kinesin-1-driven transport along MTs¹⁵. Mutations in the gene encoding MAP7 and/or kinesin-1 affect nuclear positioning in myotubes of *Drosophila* embryos as well as mammalian cells leading to muscle defects¹⁶.

Shedding light on the MAP7–MT interaction is of interest to understand its physiological function and the wider regulation of molecular processes involving the cytoskeleton. The interaction of MAP7 with MTs is mediated by its 112 residues long MT binding domain (MTBD) (residue 59-170) (**Fig. 5.1A**). According to solution-state resonance NMR assignments, the MAP7 MTBD exhibits a long α -helix with a short hinge region comprising residues 84-87¹⁷. A recent cryo-electron microscopy (cryo-EM) study of the MAP7-MT complex revealed a 53 residue-long α -helix (residues 87-139)¹⁸ bound to the MT (PDBid:7SGS) between the outer protofilament ridge and the site of lateral contact. However, a comprehensive view of the structural organization of the entire MAP7 MTBD on MTs as well as insight into the atomic interactions between MAP7 and the MT C-terminal tails (CTTs) of α - and β -tubulin, as suggested by previous solid-state NMR experiments¹⁹ is not yet available. These CTTs are subject to a variety of post-translational modifications (PTMs)²⁰ affecting the binding of many MAPs to MTs^{18,21,22}, but little is known about the mechanism(s)



by which they contribute to MT binding partner interactions. Although cryo-EM has made great progress in unravelling the structure of MTs and of MAP-MT complexes giving insights into their atomic structure and organisation^{6,23}, information about the dynamic segments of MAPs that often contain large intrinsically disordered regions (IDRs) as well as the CTTs are largely missing. NMR has the advantage of not being limited by protein dynamics, making it a suitable tool to study flexible MAP-MT interactions. In addition, the use of magic angle spinning solid-state NMR allows for the investigation of large biomolecules^{24,25}. For example, solid-state NMR has been used to study small ligands^{26,27} as well as MAP and motor proteins binding to MT^{19,28–32} and we previously used ssNMR to examine the modulation of CTTs by MAP7.

In this study, we establish a more precise picture of the binding of MAP7 MTBD to MTs by utilizing a combination of nuclear magnetic resonance spectroscopy (NMR) and electron microscopy (EM), supported by fluorescence anisotropy and isothermal titration calorimetry experiments. Our results suggest an interaction with micromolar affinity between an extended α -helix and two tubulin dimers, extending the previously determined MAP7-MT binding interface by around 25 residues and leaving only the N- and C- termini of the MTBD dynamic, explaining MAP7-promoted MT stabilization. We found that binding of MAP7 MTBD stabilizes the MT lattice via longitudinal interactions along the protofilaments. In addition, we employed solution-state NMR titration experiments using peptides comprising the tubulin CTTs to study the dynamic interactions between MAP7 MTBD and these flexible regions at residue-specific level. We identified two important regions in MAP7 MTBD that interact with the CTTs and might be critical for recruitment of MAP7 on the MT lattice. Taken together, our experiments reveal how both strong as well as weak dynamic protein-protein interactions organize formation of the MAP7-MT complex.

Results

MAP7 MTBD binds with micromolar dissociation constant to MTs

The binding of MAP7's 112 residue long MTBD (**Fig. 5.1A**) to MT was analysed using solution-state NMR titrations of MTs to labelled MAP7 MTBD and isothermal titration calorimetry (ITC). Strong signal decreases in the NH-TROSY of the MAP could be observed without traceable chemical shift changes. This hints to a fairly dynamic binding with significant interconversion of free and MT-bound MAP7 MTBD (**Supplementary Fig. 5.1A and 5.1B**). For the ITC experiments, MAP7 MTBD was titrated to the MT and a K_D of $0.94 \mu\text{M} \pm 0.73 \mu\text{M}$ could be observed with a stoichiometry of 0.51 ± 0.085 (MAP7 MTBD to tubulin) (**Fig. 5.1B**). These values are similar to previous results which observed a K_D of $1.39 \pm 0.5 \mu\text{M}$ with TIRF-M of MAP7 Δ C (aa 1–353) in (30 mM HEPES pH 7.4, 150 mM K-acetate, 2 mM Mg-acetate, 1 mM EGTA, and 10 % glycerol) ³³. At low ionic strengths (30 mM HEPES, 5 mM MgSO₄, 1 mM EGTA, pH 7.0) an ~10x higher affinity has been reported (K_D 111 ± 12 nM) ¹⁸ indicating a significant contribution of electrostatic interactions in MTBD-MT binding.



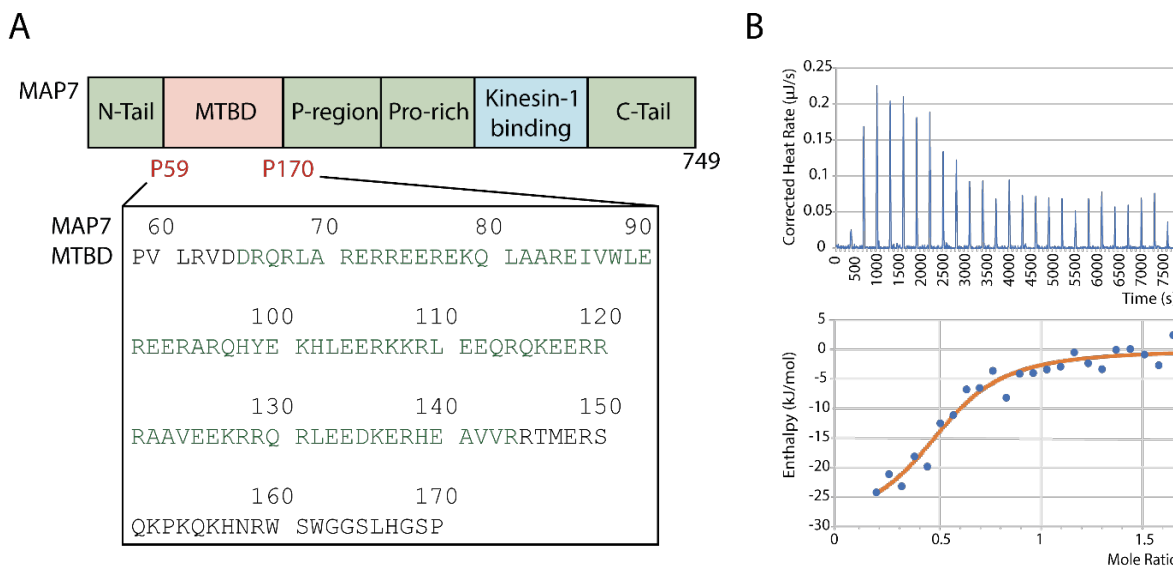


Fig. 5.1: Binding of MAP7 MTBD to MT **(A)** Top: Schematic representation of full-length MAP7 including the MTBD and the kinesin-1 binding domain. Bottom: Amino-acid sequence of the MAP7 MTBD, residues that are predicted to be α -helical are coloured in green ¹⁷. **(B)** Representative isothermal titration calorimetry (ITC) data of MAP7 MTBD to Taxol-stabilized MT.

MAP7 MTBD binds along the MT protofilament and stabilizes the MT lattice

We first used EM to directly visualize the effect of MAP7 MTBD interaction with MTs during polymerisation. 5 μM tubulin (below its critical concentration) +GTP were incubated with different concentrations of MAP7 MTBD and the resulting MTs were imaged using negative stain EM, demonstrating that MAP7 MTBD supports MT polymerization. We observed an increase in number of MTs at increasing molar ratios of 0.25:1 and 0.5:1 of MAP7 MTBD:tubulin, whereas no MTs were observed when MAP7 was not included (**Supplementary Fig. 5.2**). In samples containing tubulin and MAP7 MTBD in equal amounts, bundling of MTs was observed, while at higher concentration ratios of 2:1 for MAP7 MTBD and tubulin, thick-walled short MTs were observed, in which an additional layer of protein, potentially composed of tubulin was observed (**Supplementary Fig. 5.2**).

A structural and dynamic visualization of the interaction between the microtubule-associated protein 7 (MAP7) and microtubules

To further understand the MAP7 MTBD–MTs interaction, and based on the distribution and number of MTs formed, we used the ratio of 1:1 (MAP7 MTBD:tubulin) to polymerise MTs for cryo-EM experiments. Using our established reconstruction pipeline^{35,36} and treating the α/β -tubulin dimer as the asymmetric unit of the reconstruction, we obtained a symmetrised 3D reconstruction of MAP7 MTBD bound MT with an overall resolution of 3.7 Å which showed extra density corresponding to MAP7 MTBD along the protofilament (**Supplementary Fig. 5.3A**). However, the density corresponding to MAP7 MTBD, was only visible at low map thresholds. To further improve the occupancy of MAP7 MTBD on the MT lattice, additional MAP7 MTBD was added to the stabilized MTs adsorbed on the grid before vitrification. The resulting symmetrised 3D reconstruction of MAP7 MTBD bound MT thus obtained had an overall resolution of 3.5 Å and revealed improved density corresponding to MAP7 MTBD at the protofilament crest, ~ 25 Å away from its centre (**Fig. 5.2A, Supplementary Fig. 5.3B**). To facilitate interpretation, we also used AlphaFold 2 multimer³⁷ to predict the structure of MAP7 MTBD bound to a tubulin dimer (**Fig. 5.2B, ribbon model**). The predicted model illustrated that the helical part of the MAP7 MTBD extends beyond a single tubulin dimer, and its precise mode of interaction is therefore obscured through averaging in our reconstruction. Information about the extended MTBD-MT interaction could not be deconvoluted despite efforts to apply modern cryo-EM processing strategies. This, together with the a priori probability of MAP7 MTBD interacting out of phase with tubulin dimers in neighbouring protofilaments around the MTs resulted in lower resolution of the MAP7 MTBD density (~4 Å) compared to the rest of the structure, and an inability to visualize the MTBD boundaries. We nevertheless, fitted the model with the highest confidence score ($pTm+ipTM=0.88$) into the electron density map to gain insight into this interaction (**Fig. 5.2B**). MAP7 MTBD forms a long helix that spans 13.5 nm and its position in the predicted model aligned well with the corresponding density in the map (**Fig. 5.3B**) confirming its binding position and helical conformation. The binding site and register of the MAP7 MTBD helix on the MTs also matches that obtained



from 3D reconstruction of MAP7 MTBD bound to Taxol stabilized-MTs¹⁹, demonstrating that MAP7 interacts with MTs in the same way independently of how they are stabilized (**Supplementary Fig. 5.3C**). Based on this fit, the MAP7 MTBD helix extends across ~2 tubulin dimers. Further, extension of density for both alpha and beta tubulin's H12 helix could be observed in the map and additional CTT residues 438-440 for α -tubulin and residues 429-430 for β -tubulin were modelled into the density. The ordering of these usually disordered residues could be explained by an interaction between the tubulin CTTs and MAP7; however, the direct interaction is not visible in our reconstruction and is presumably less ordered (**Fig. 5.2C**).

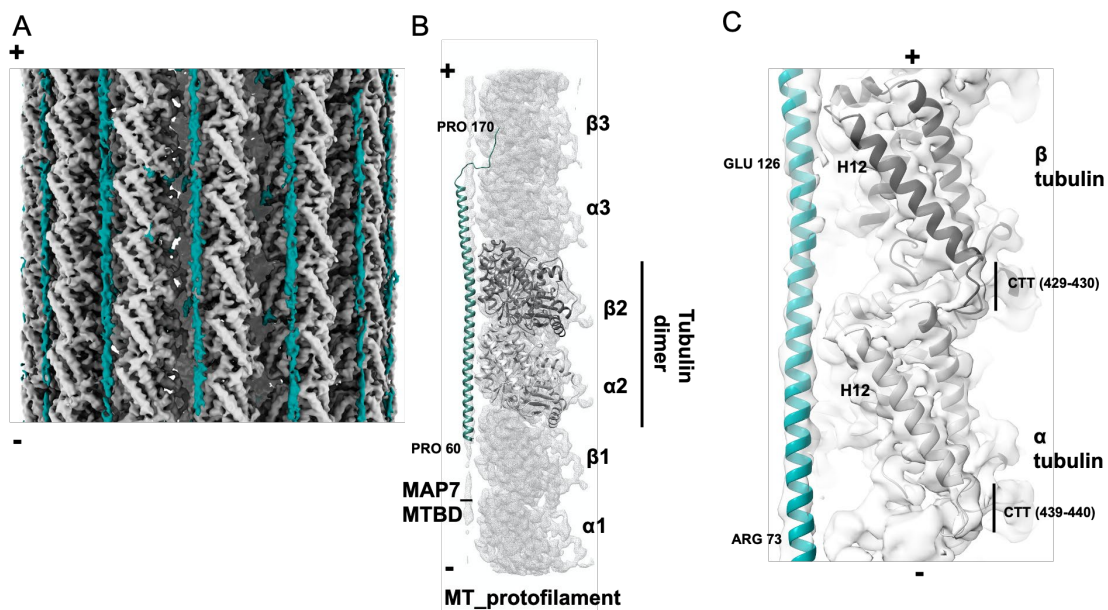


Fig. 5.2: Cryo-electron microscopy reveals the binding site of MAP7 and its interactions along MT protofilaments (A) Cryo-EM density map (symmetrised reconstruction) of MAP7 MTBD bound MT. Density for the MT and MAP7 MTBD is shown in grey and teal respectively. (B) Segment of symmetrised cryo-EM reconstruction corresponding to a protofilament shown in surface representation with atomic model of MAP7 MTBD (teal) bound tubulin dimer (alpha tubulin: light grey; beta tubulin: dark grey) obtained from AlphaFold2 fitted in. Tubulins flanking the central tubulin heterodimer have been indicated. (C) Map density corresponding to H12 helix in both α - and β -tubulin shown in surface representation with fitted atomic models depicted in cartoon representation. Tubulin CTTs and residues along MAP7 MTBD are indicated for register.

MAP7 MTBD shows an extended α -helix and dynamic terminal regions upon MT binding

To further probe the relative distribution of the bound region of the MAP7 MTBD (**Fig. 5.3A**) on the MT, we conducted dipolar and J coupling (scalar)-based magic-angle spinning (MAS) solid-state NMR experiments, which provide complementary information about complex biomolecules that comprise both rigid as well as dynamic protein domains^{20,38}. For our studies, we prepared samples in which [¹³C-¹⁵N] labelled MAP7 MTBD was mixed with Taxol-stabilized MTs at a 1 to 2 ratio of MAP7 MTBD to tubulin.

The two-dimensional ¹³C-¹H correlation experiments give a fingerprint of the rigid (**Fig. 5.3B, blue**) and flexible (**Fig. 5.3B, red**) components of the MAP7 MTBD bound to MTs. For reference, the solution-state assignments of MAP7 MTBD (**Supplement table 5.1**,¹⁷) are included as black crosses. A comparison of these data sets strongly suggests that the dipolar- and scalar-based ssNMR experiments probe different domains of MAP7. For further analysis, we made use of our previous solution NMR assignments which cover 97 % of CA and 93 % of CB resonances as well as 73 % of the HA and 69 % of the HB assignments (**Fig. 5.3A, Supplement table 5.1**). Because of overlap, missing assignments in side-chains and chemical shift perturbations, a direct transfer of the solution-state chemical shift assignments to the ssNMR spectra was hindered. Instead, we used in these cases average BMRB chemical-shift values (**Supplement table 5.1**).

Panels **(I)-(VI)** show that Pro, Val, Ala, Asp, Met and Asn residue types are largely dynamic, whereas Gln, Trp and Lys are mostly found to be rigid. Residues K154, H167 were additionally identified to be dynamic. Most other residue types revealed ssNMR correlations in both rigid and dynamic protein regimes (**Supplementary methods chapter 5**). In summary, analysis of our 2D ssNMR data sets suggests that flexible residues are more likely to be located at the N- or C-terminus of the



protein, while rigid residues are mainly found in the α -helical region of MAP7 (**Fig. 3C**).

Interestingly, additional correlations appeared in our dipolar ssNMR spectra in the proton region between 4.7 and 6 ppm (**Fig. 5.3B, purple dashed box**), which cannot be explained by our solution NMR data or a protein species that comprise α -helical or random-coil conformations. Instead, these signals exhibit β -strand character (vide infra). Notably, aggregation of MAPs with MT stabilizing function has been observed for MAP1b, MAP2, TPPP and Tau. Additional aggregation and bundling of MT, as seen in EM was previously observed for MAP4³⁸⁻⁴¹.

A structural and dynamic visualization of the interaction between the microtubule-associated protein 7 (MAP7) and microtubules

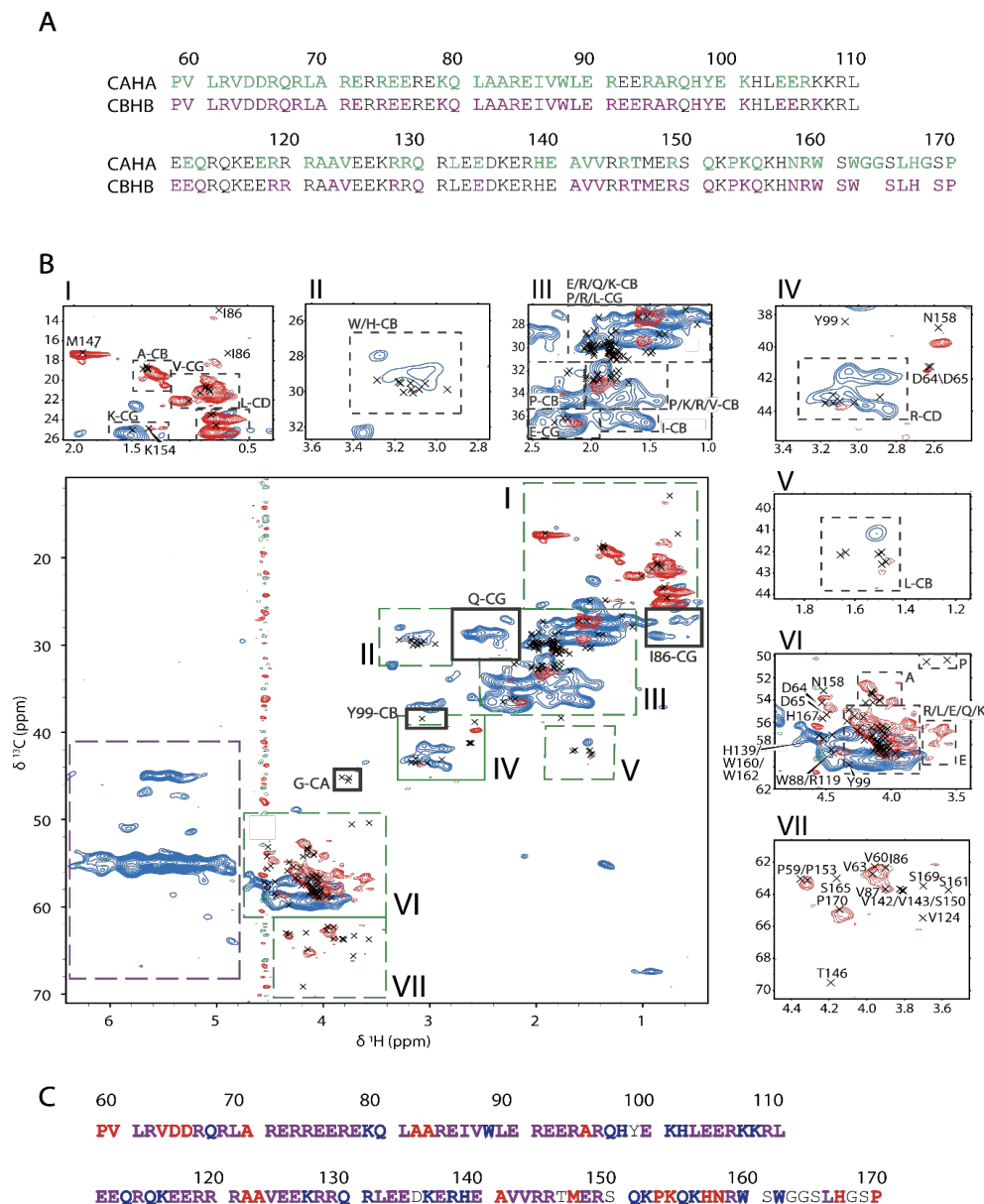


Fig. 5.3: 2D ssNMR of [^{13}C - ^{15}N] MAP7 bound to Taxol-stabilized MT. **(A)** Solution-state assignments of MAP7 MTBD of CAHA (green) and CBHB (purple) resonances **(B)** Overlay of scalar (flexible) CH (red) and dipolar (rigid) CH (blue) with solution-state assignments of MAP7 MTBD (black crosses). Signal attributed to β -sheet chemical shifts is shown in the purple dashed box. Green roman numbers and boxes are used to indicate regions that are enlarged. **(C)** Summary of the observations from the 2D NMR spectra. Red are residues overlaying with the scalar CH, blue those overlaying with the dipolar and purple those overlaying with both.



To validate these findings and to obtain further residue-specific information we conducted three-dimensional CCH solid-state NMR spectra (**Fig. 5.4, Supplementary Fig. 5.4A**) using both dipolar as well as scalar-based transfer steps.

The 3D scalar spectrum (probing dynamic MAP7 residues in the complex) shows good agreement with the solution-state assignments. Here, we were able to assign several residues of MAP7 MTBD in the MT-bound state (**Fig. 5.4A and 5.4C**). For Pro 59- Asp64, Leu 69, Glu 148, Pro 153, Gln 155, Asn 158, Arg 159 and Pro 170 resonances for both backbone and sidechains could be identified (**Fig. 5.4A and 5.5A**), while for Ala 70, Ala 82, Ile 86, Thr 146, Met 147, Lys 154 and Leu 166 only certain side-chain resonances were found (**Supplementary methods chapter 5.5**). Intriguingly, all of these residues are located at the C- and N-terminus of MAP7 MTBD (**Fig. 5.5A**), in line with weak or no binding to MT for MAP7 residues Pro 59- Ala 70 and Glu 148-Pro 170. In addition, several resonances corresponding to residue types could be partly identified in the scalar CCH 3D. Namely, one Glu, Ser, Gln, Leu and two additional Arg (**Fig. 5.4A**). Furthermore we compared the overall abundance of each resonance type to the number of resonances of that type present in the aforementioned terminal domains. Taking the information gained from the experimental signal intensity together with the observed residue we find our scalar based experiments to be in reasonable agreement with the MAP7 regions Pro 59- Ala 70 and Glu 148-Pro 170 (**Fig. 5.5B, Supplementary Fig. 5.4B, Supplementary Methods chapter 5**).

For the dipolar spectra (**Fig. 5.4B & D, Supplementary Fig. 5.4C**), we were able to assign Ala, Glu, Lys, Leu, Met, Gln, Arg, Ser and Val residue types with distinct chemical-shift signatures (**Supplement table 5.2**). These MAP7 MTBD residues are more abundant in the central α -helical region as seen in the prediction model fit into EM density and extend to approximately residue 150 (**Fig. 5.5A and 5.5C**). Indeed, these residue types exhibit α -helical shifts, underlining the α -helical secondary fold of the bound part of the MAP7 MTBD (**Fig. 5.5D**). It is interesting that Gln CBHB is an exception to the rule, as the chemical shift is more typical of random coil shifts

A structural and dynamic visualization of the interaction between the microtubule-associated protein 7 (MAP7) and microtubules

than the average Gln CBHB chemical shift in solution. However, we identified only one Gln CBHB in the 3D CCH (**Supplement table 5.2**), which could be located in a region at the beginning or end of the helical part of MAP7 MTBD and was hence separated enough from the overlapping Gln resonances to identify it (e.g.: Gln 80 or Gln 151).



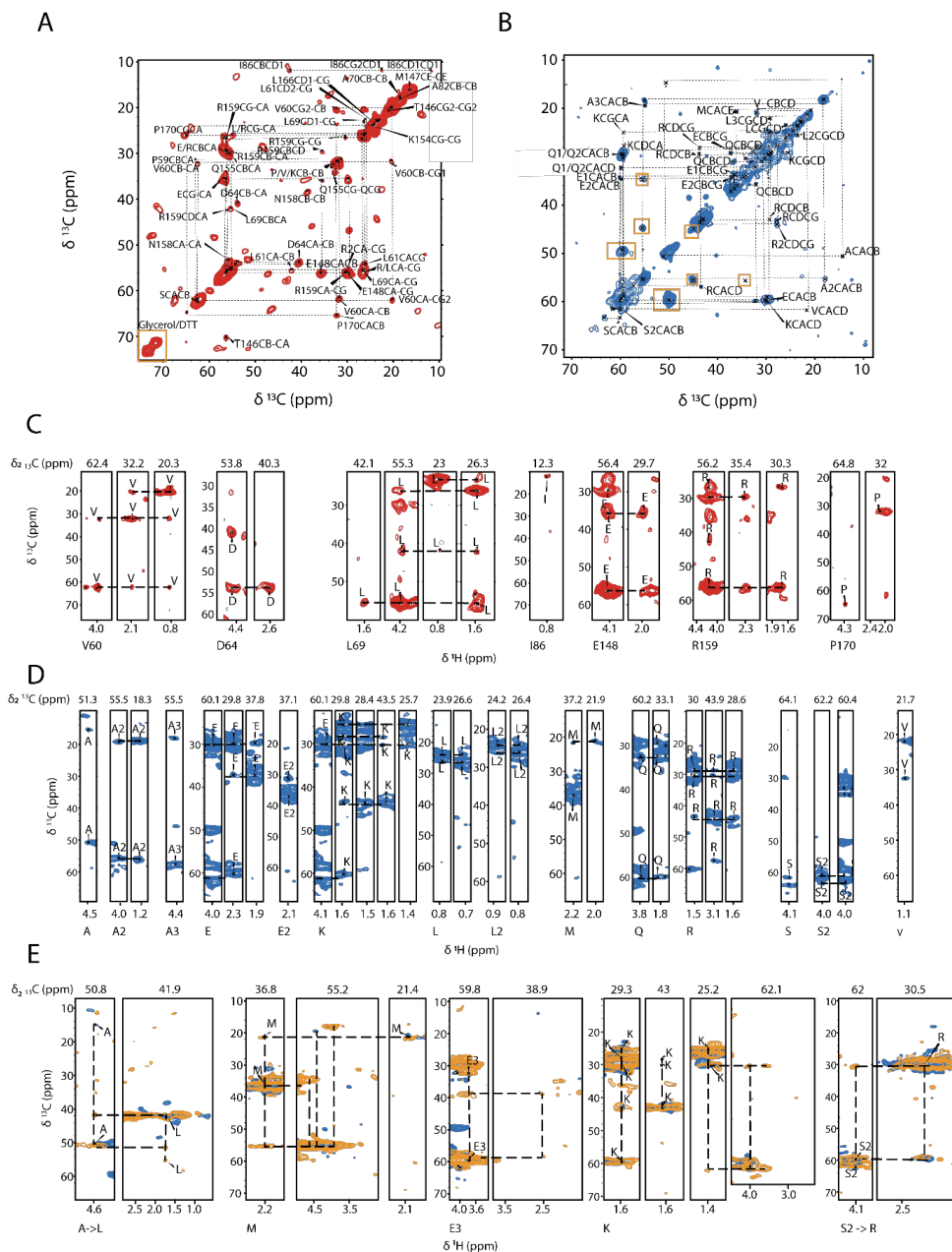


Fig. 5.4: 3D ssNMR of $[^{13}\text{C}-^{15}\text{N}]$ -MAP7 bound to Taxol-stabilized MT. **(A)** CC-plane of 3D 16 ms DIPSII with assigned resonances. In the yellow box is signal produced by buffer components. **(B)** CC-plane of 3D 1.7 ms RFDR with assigned resonances. Yellow boxes indicate chemical shifts coming from the β -sheet signal. **(C)** Assigned strips of the scalar 3D CCH. **(D)** Assigned strips of the dipolar 3D CCH. **(E)** Assigned strips in the dipolar spectrum with 3.4 ms RFDR mixing time (yellow) with sequential connectivity compared to 1.7 ms RFDR (blue).

We note that the aforementioned correlations are the ones that were unambiguously assignable. However, there are several spectral regions in which overlap precludes the assignments of individual resonances but still allows for a residue type analysis. Similar to the scalar case, we calculated the relative abundance of these resonance-type regions dividing the integral of the resonance region in the CH projection of the 3D CCH spectrum by the average of the integral of peaks corresponding to one assignment only (**Fig. 5.5C**). The residue abundance is in good agreement with the number of these residues in the region Ala 70-Glu 148 (**Fig. 5.5C, right and Supplementary Fig. 5.4B**), the domain that we previously found not be present in the scalar spectrum (**Fig. 5.5A**). This notion is confirmed by the presence of all expected Ala, Arg, Val, His, Gln and Trp side-chain resonances. Nonetheless, fewer Lys resonances were observed and none for Asp. The discrepancies may be due the fact that some of the residues exhibit a certain degree of motion which reduces dipolar transfer and cross peak intensities in our dipolar ssNMR spectra.

In addition to the ssNMR data presented above, we also obtained sequential assignments from dipolar 3D CCH experiments recorded with a longer RFDR mixing time (3.4 ms) (**Fig. 5.4E**). By comparing this 3D data set to results of the dipolar 3D experiment with shorter mixing time we could connect two residue pairs. Firstly, a sequential Ala-Leu contact would only be consistent with pairs 69-70 and 81-82. Because we identified Leu 69 in the scalar 3D, we tentatively assigned this correlation to Leu 81-Ala 82. Moreover, we observed sequential transfer from Ser to Arg which must stem from residues Arg 149 to Ser 150. Therefore, it seems likely that the rigid region extends up to approximately residue Ser 150, with possibly weaker binding starting from Thr 146 (**Fig. 5.4E and 5.5C**). The assigned resonances can be found in the supplementary table (**Supplement table 5.2**).

Similar to the analysis of the α -helical region, we also attempted a residue-specific analysis of the putative β -strand region. By verifying connections in the CAHA region of the dipolar spectrum corresponding to the aforementioned β -sheet resonances,



Chapter 5

we could attentively assign residues that best agree with Ala 83, Arg 84, Glu 85 and Ile 86, Val 87 (**Supplementary Fig. 5.4B and Supplementary methods chapter 5.5**). These residues would be in line with the aggregation propensity for MAP7 evaluated by AGGRESCAN, which claims residues 84-89 to be aggregation-prone⁴³. Interestingly this region corresponds to the hinge, that was observed in the free MAP7 MTBD α -helix (residue 84-87) (³, Chapter 2). The rest of the aggregate could not be observed in the NMR spectra. This might be due to great heterogeneity or intermediate exchange dynamics.

A structural and dynamic visualization of the interaction between the microtubule-associated protein 7 (MAP7) and microtubules

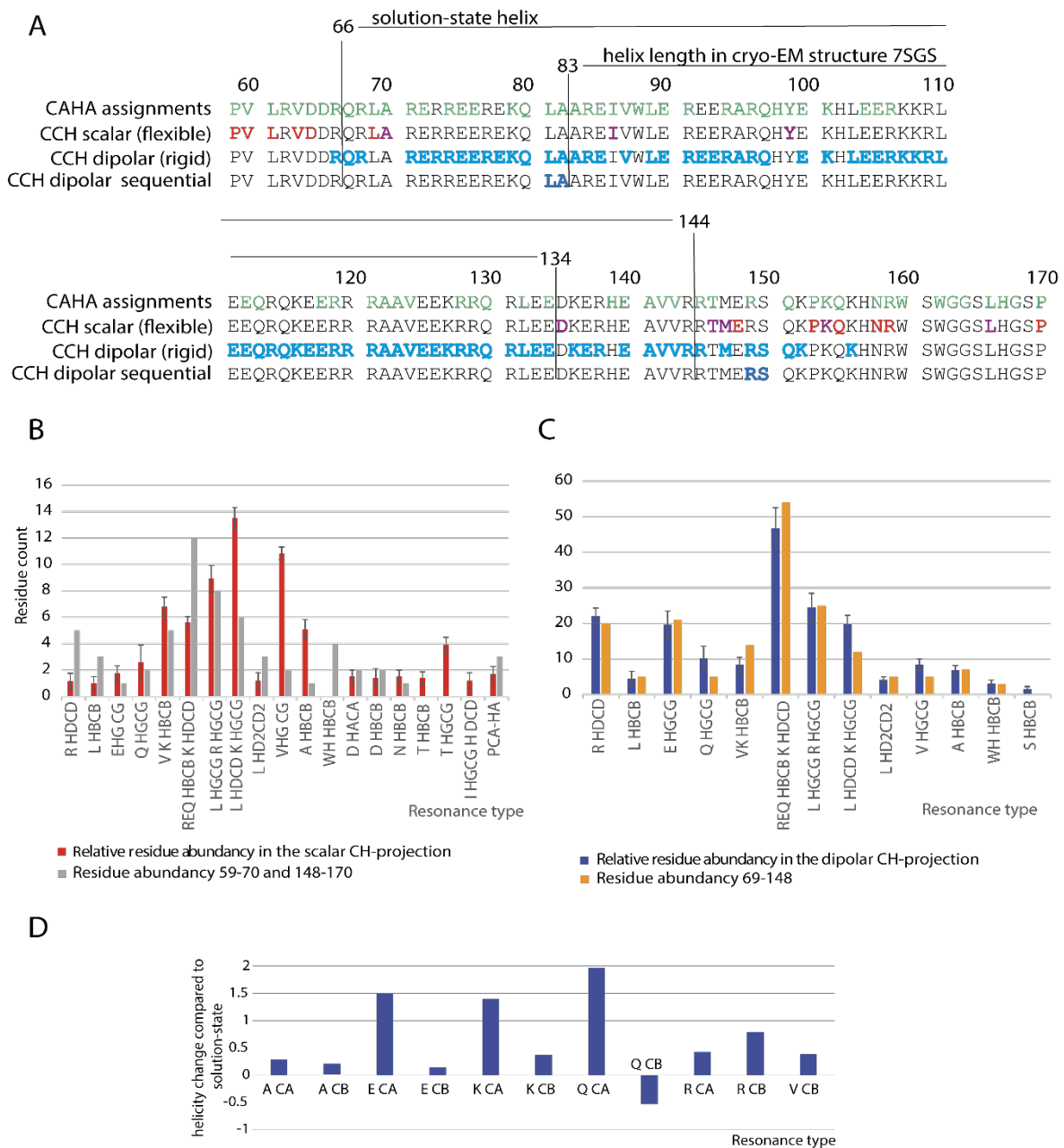


Fig. 5.5: Analysis of 3D CCH ssNMR experiments (**A**) Distribution of assigned residues indicated on the MAP7 MTBD sequence. Top: CAHA assignments in solution (green), 2nd row: assigned residues in the CCH scalar 3D (red for several resonances, pink for only side-chain assignments), 3rd row: residue types found in dipolar CCH (blue), bottom row: residue pairs identified in sequential dipolar CCH. The length of the helix found in solution and in cryo-EM are indicated by black squares. The intensities for identified residue detected in



scalar CCH (**B**) and the dipolar CCH (**C**) regions were integrated. The integrated intensities were divided by the signal average of cross-peaks attributed to one resonance only. (**D**) Comparison of helicity of solution-state assignment average for residue A70-E148 to average chemical shift helicity of the assigned same residue type in the dipolar CCH.

Taken together, from our spectral analysis of dipolar- and scalar-based spectra, a picture emerges where certain residues are either flexible or rigid as it is depicted in **Fig. 5.5A**. We conclude that dynamics is prevalent in the N-terminus, before residue 70 and after residue 148.

Two protein regions play a role in the MT carboxy-terminal tail interaction with MAP7 MTBD

Previous work hinted at the importance of the tubulin CTTs in binding of MAP7 to MT as indicated by a reduction in the scalar signal of the CTTs ³¹. To examine the binding of MAP7 MTBD to the tubulin CTTs, we designed peptides comprising residues Ser 439-Tyr 451 and Asp 427-Ala 444 of HeLa S3 α - and β -tubulin, respectively (**Fig. 5.6A**). By titrating these to isotopically labelled MAP7 MTBD in solution (**Fig. 5.6B**), we were able to observe chemical-shift changes (**Fig. 5.6C**). Interestingly, we identified two main regions (82-AAREIVW-88) and (141-AVVRRT-146) that are affected by the presence of the CTTs peptides, while the latter region seems to be less modulated by the β -tubulin tail (**Fig. 5.6C**). Notably, we also detected other residues with smaller sensitivity to the presence of the CTT peptides, i.e., Asp 65, Glu 75, Arg 106, Ala 122 and Ser 150. We determined the binding affinity for the α -CTT with fluorescence anisotropy by attaching NHS-fluorescein to the peptide (**Fig. 5.6D**). The experiments resulted in a dissociation constant (K_D) of 91.29 μ M \pm 17.5. This binding affinity seems therefore to be 90 times weaker than the small micromolecular interaction observed for binding of MAP7 to entire MTs (**Fig. 5.1B**). The electrostatic character of the CTT–MAP7 interaction was validated by NMR measurements of MAP7 MTBD with 10-fold α -CTT at different salt concentrations.

A structural and dynamic visualization of the interaction between the microtubule-associated protein 7 (MAP7) and microtubules

A reduction of chemical shifts due to salt increase could be observed, leading to a disappearance of any relevant chemical shift perturbations at 500 mM salt (**Fig. 5.6E**). The dynamic binding behaviour was also verified as a previous study has shown a 4-times reduction in the binding of the MAP7 MTBD to MTs upon removal of the CTTs via subtilisin cleavage by total internal reflection fluorescence experiments ¹⁸.

Our findings, in conjunction with the highly negative charge of the CTTs, suggest that the charged residues of the interacting stretches play a crucial role in an electrostatic binding event between MAP7 and MTs. Furthermore, the electrostatic character of the interaction is underlined by the observation, that the FGE and EGE repeats of the CTTs are the binding residues on the MT side and therefore negatively charged residues might interact with the charged MAP7 residues ¹⁹.



Chapter 5

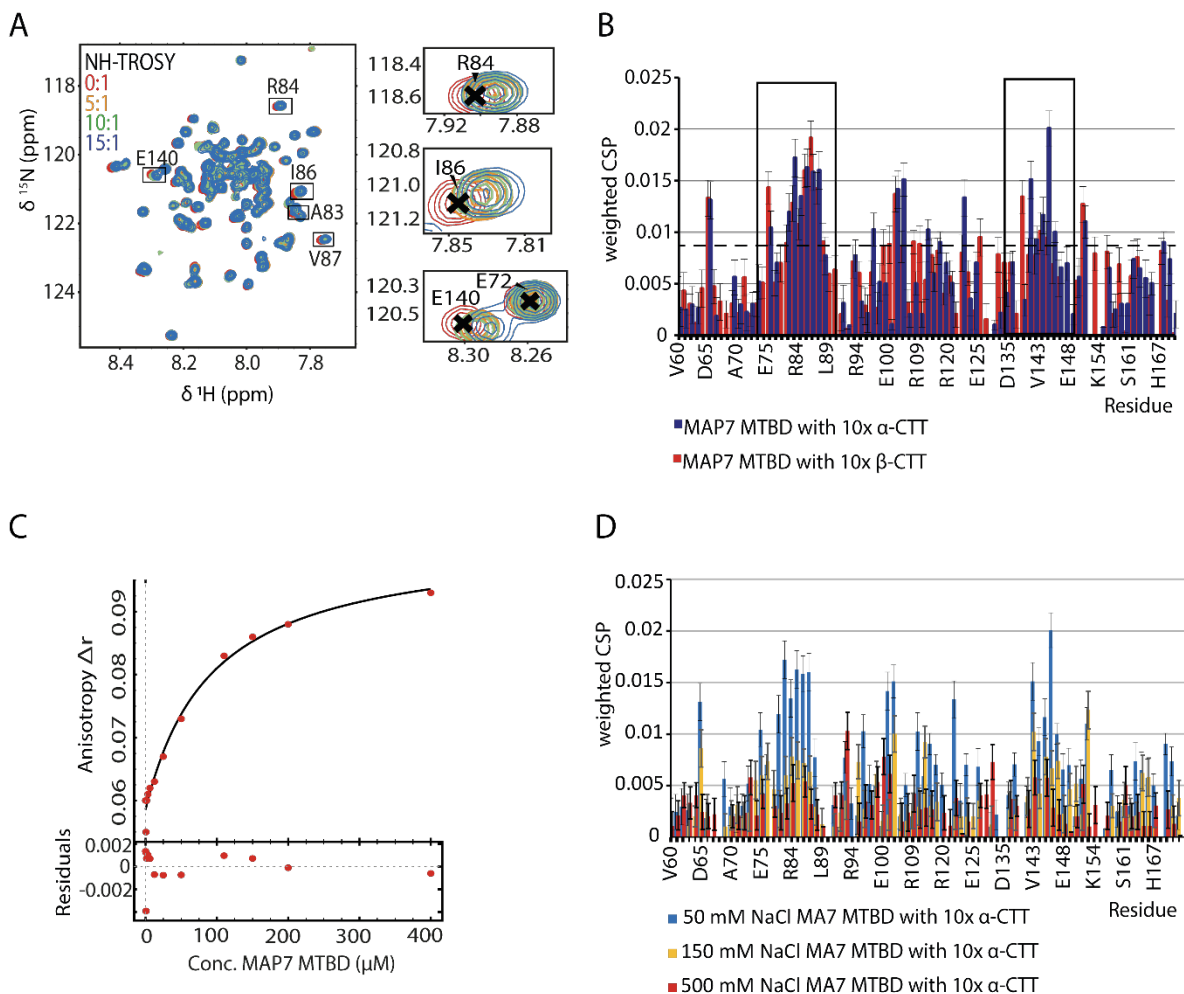


Fig. 5.6: Titration of peptides comprising the MT carboxy-terminal peptides to $[^{13}\text{C}-^{15}\text{N}]$ -MAP7 MTBD **(A)** Sequences of the two tubulin C-terminal tails (CTT) that are most common in HeLa S3 cells. **(B)** NH-TROSYs of the titration of increasing concentrations of α -CTT to MAP7 MTBD in solution-state NMR **(C)** CSP upon α - and β -CTT binding. Stretches with significant CSPs are marked with a box. The black dotted line indicates the mean plus one standard deviation. **(D)** Fluorescence anisotropy with fluorescein labelled α -CTT gives a K_D of $91.29 \mu\text{M} \pm 17.5$ for the interaction with the MAP7 MTBD. **(E)** CSP in labelled MAP7 MTBD upon addition of 10x α -CTT at different salt concentrations.

Discussion

MAP7 mediates recruitment of kinesin-1 to the MT lattice and plays a crucial role in the organization and transport of cellular cargo via MT-based motors, in organelle movement and spindle segregation^{43–45}. Here, we have studied the interaction between MAP7 MTBD and MTs by NMR and EM, allowing visualization of this interaction in the bound state. Despite the high repetitiveness of R, E, K residue types, we were able to acquire 2D and 3D solid-state NMR (ssNMR) spectra of labelled MAP7 MT-binding domain (MTBD) in complex with Taxol-stabilized MTs with remarkable spectral resolution. As confirmed by a combination of cryo-EM 3D reconstructions and AlphaFold2 prediction, MAP7 MTBD adopts an extended helical conformation when bound to MTs and its binding site on MTs when polymerized in presence of MAP7 MTBD is similar to that obtained when bound directly to Taxol-stabilized MTs. The recorded ssNMR experiments allowed us to identify the rigid and flexible parts of the protein, establish the helix boundaries, and pinpoint specific interacting regions of the MAP7-MT interaction.

Because residues R65-R67 and R149-S150 are rigid, our data show that the MT binding interface of MAP7 extends beyond a single α/β -tubulin heterodimer (**Fig. 5.7 I. and IV.**). The register is supported by the observation of more flexible residues in the clefts between the tubulin subunits (**Fig. 5.7 V. and VI.**) as well as by AlphaFold 2 multimer predictions, and are also consistent with a previous cryo-EM model¹⁸. The resulting bridging of two tubulin dimers is predicted to support MT stabilization, as was shown when MTs were polymerized in sub-stoichiometric concentration ratios of 1:0.5 (tubulin:MAP7 MTBD) in vitro (**Supplementary Fig. 5.2**), and is consistent with its observed stabilizing activity at axonal branches⁴⁶. This interaction of MAP7 with MTs is associated not only with MT remodelling but also kinesin-1-mediated transport in cells¹¹. As a result, studying this interaction may aid in



understanding these cellular processes, which are linked to cancer-associated metastatic growth and neurodegenerative diseases ^{12,33,47,48}.

In addition to our earlier ssNMR results that revealed the binding site of MAP7 to the MT tails ⁹, solution-state NMR here provided insights into the dynamic interaction between tubulin's carboxy-terminal tails (CTTs) and the MAP7 MTBD (**Fig. 5.7 II. and III.**). We identified two regions with residue stretches that displayed significant chemical shift changes. The first region (residues 82 - 88) was found to interact with both the α - and β -CTTs, while the second region (residues 141-146) had a preference for interacting with the α -CTT. This interaction is further supported by the partial ordering of the tubulin CTTs that were observed in the cryo-EM reconstructions. Together with previous studies that revealed the binding site of MAP7 to the MT tails ¹⁹, we were able to form a better understanding of the interaction between CTTs and MAP7. Our previous data suggest that the CTT EGE and FGE motifs interact with the identified regions. Fast exchange between the tail peptides and the protein may help to recruit MAPs from the cytoplasm to the MTs. Once binding has occurred, the relatively weak interaction between CTTs and MAP7 contributes to stabilizing the MAP7-MT protofilament complex. This notion is in line with observed weaker binding affinities of MAP7 to subtilisin-treated MTs ¹⁸. In **Fig. 5.7 II. and III.** the two involved regions are depicted. Based on our ssNMR data, it is not clear whether the Arg involved in CTT binding are rigidified by the tail interaction or by the protofilament binding. In addition, we cannot exclude the possibility that the CTTs may interact with the distal MAP7 bound to the neighbouring protofilament. Further studies with shorter MAP7 constructs might help to evaluate the importance of the N- and C-terminal interacting parts for MT stabilization. Such studies may involve cell-culture assays to monitor proliferation, biophysical experiments on binding affinities and MT stability, length and bundling or NMR experiments on altered binding behaviours. On the other hand, our approach could also be extended to study longer MAP constructs that are known to contain larger IDP regions ⁴⁹, including MAP7 constructs containing the kinesin-1 binding domain. Finally,

A structural and dynamic visualization of the interaction between the microtubule-associated protein 7 (MAP7) and microtubules

investigating post-translational modifications (PTMs)⁵⁰ of MT tails may provide insights into the importance of the “tubulin code” for binding affinities and binding rates leading to a more comprehensive understanding of these modifications and their implication in health and disease.

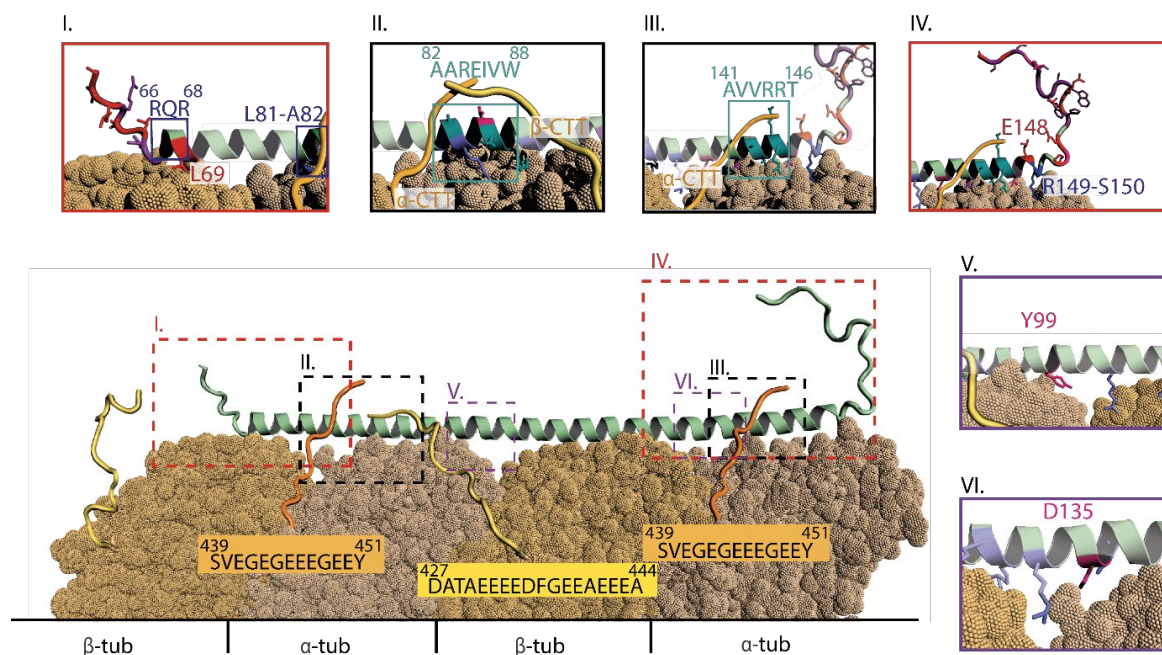


Fig. 5.7: Model of MAP7 MTBD binding to MT based on the cryo-EM and NMR data. MAP7 MTBD binds MT from around residue R66 to residue E148. On the N-terminal side backbone resonances with fast dynamics are only found prior to R66, with the exception of L69 and on the C-terminal side after E148 (red coloured, box I. and IV.). On the C-terminal side (panel IV.) a region with flexible and rigid residues is observed from T146 until S150. For T146 and M147 only side chain resonances are observed (pink). Box II. And III. show where the MAP7 MTBD is interacting with the tubulin CTT. The residue stretches undergoing significant chemical shift perturbations are indicated by a square (box II.: A82-W88; box III.: A141-T146). I86 has flexible side-chains (pink). In both cases, the CTTs are long enough to reach the identified MAP7 regions and also the ones of the MAP7 on the neighbouring protofilament. Panel V. and VI. show residues with intermediate side-chain dynamics (pink) located between tubulins.

Materials and Methods

MAP7 MTBD expression and purification

The cDNA encoding the MTBD (residues 59-170) of MAP7 from *Homo sapiens* with an N-terminal His-Tag and Maltose binding protein (MBP) linked via a thrombin cleavage site (His-MBP-MAP7 MTBD), cloned into the pLICHIS vector was expressed in *Escherichia coli Rosetta 2 (DE3)* cells and purified with immobilized metal affinity chromatography, cation exchange chromatography, thrombin cleavage and ammonium sulphate precipitation according Chapter 2 ¹⁷.

Negative stain sample preparation and EM

Porcine brain tubulin (Cytoskeleton, Cat No. T240) (5 μ M) was incubated with MAP7 MTBD in BRB80 buffer (80mM PIPES, 2 mM MgCl₂, 1 mM EGTA, pH 6.8) at indicated molar concentration ratios in a water bath maintained at 37°C for an hour. 3 μ L of each sample was applied to glow discharged continuous carbon film coated, 400 mesh copper grids (Pacific Grid Tech) and blotted using a Whatman filter paper, Grade No. 1 after 30 seconds. Staining solution (2 % uranyl acetate in water) was then added to the grid, blotted off after 30 seconds and the grids were air dried. Images were recorded using Digital Micrograph™ software (Gatan) on a Tecnai T12 microscope (FEI) operating at 120 keV with a US4000 4K \times 4K CCD camera (Gatan) at 3200x (overview) and 42000x (high) magnifications corresponding to pixel sizes of 13.5 nm and 2.5 Å respectively.

Cryo-EM sample preparation

5 μ M porcine brain tubulin (Cytoskeleton, Cat No. T240) and 5 μ M MAP7_MTBD were mixed with 2 mM GTP (final concentration) in BRB80 buffer (80mM PIPES pH 6.5, 1 mM MgCl₂ and 1 mM EGTA) and incubated on ice for 5 minutes. The mixture was then incubated in a water bath maintained at 37 °C for an hour. C-Flat 2/2 Holey Carbon grids (Protochips) were glow discharged in air for 1 minute at 0.3 mPa using a PELCO easiGlow (Ted Pella, Inc.). 3 μ l of the above sample was applied to a glow

A structural and dynamic visualization of the interaction between the microtubule-associated protein 7 (MAP7) and microtubules

discharged grid and incubated on the grid for 30 seconds at room temperature following which, excess sample was wicked off and 3.5 μL of 10 μM or 25 μM MAP7 MTBD was immediately added to the grid. The grid was then mounted in a humidified Vitrobot Mark IV (ThermoFisher) chamber pre-set to a temperature of 25 $^{\circ}\text{C}$ and humidity of 100 %. After incubation for 60 seconds, excess liquid was blotted out and the grid was plunge frozen in liquid ethane.

Cryo-EM data collection

Data were collected using a Titan Krios D3771 operating at an accelerating voltage of 300keV attached to a K3 detector (Gatan) and GIF Quantum LS Imaging Filter (Gatan). The sample was imaged using the automated EPU software at a nominal magnification of 81,000x resulting in a pixel size of 1.067 \AA and with defocus range of -0.6 to -2.4 μm . Movie frames were recorded in counting mode with a total dose of 49.37 electrons/ \AA^2 for 3.4 seconds fractionated over 50 frames. An energy filter with a slit width of 20eV was used during data collection.

Cryo-EM image processing

Initial processing involved manual inspection of data for presence of contaminating ice and filament quality and poor-quality movies were discarded. All subsequent image processing steps were carried out using RELION v3.1^{51,52} and the customized Microtubule RELION-based Pipeline (MiRP)^{34,35}. Beam induced motion of particles in the movies were corrected using inbuilt function of MotionCor2⁵³ in RELION. CTF estimation was performed on dose-weighted and motion corrected summed images using CTFFIND 4.1⁵⁴ within RELION's GUI. Particle picking was performed manually using RELION's helical picker⁵⁵ and particles were extracted using a box size of 568 pixels and overlapping inter-box distance of 82 \AA . The next steps of protofilament number segregation and Euler angle alignments were carried out using 2x binned particles and references with the help of MiRP v2 scripts integrated into RELION v3.1. MT segments with different protofilament numbers



Chapter 5

were segregated by supervised 3D classification using references for 11 to 16 protofilament containing MTs. 14 protofilament MTs formed the major fraction of the population and were selected for further processing. Rotational angle and X/Y coordinate fitting and shift assignments were carried out using 3D classification against a 15 Å low pass filtered reference (EMD 7973) with enhanced pixels for S9-S10 and H1-S2 loop regions in tubulin ⁵⁶. Seam checking was carried out by supervised 3D classification using 28 rotated and shifted references. At this stage, aligned unbinned particles from 2 datasets (corresponding to 10 μM and 25 μM MAP7 externally applied) were combined. Finally, a symmetrized 3D reconstruction was obtained with a 3D auto-refine step using unbinned aligned particles and a 10 Å lowpass filtered reference. Per particle CTF refinement and Bayesian polishing were carried out in RELION and the final displayed reconstruction was sharpened using local resolution in RELION.

Model generation

Protein sequences for porcine brain tubulin: porcine brain alpha-1A tubulin (UniPROT ID: P02550), beta-2B tubulin (UniPROT ID: P02554) and the symmetrized electron density map with a mask around the tubulin dimer in the centre of the protofilament opposite the seam were provided as inputs to locally installed ModelAngelo ⁵⁷. The obtained model was further checked and refined manually by model building in Coot ⁵⁸ followed by real-space refinement in Phenix ^{59,60}. The resolution of the electron density corresponding to MAP7 MTBD was insufficient to accurately build a model de novo. All images were made in ChimeraX ^{61,62}.

Data collection statistics and model refinement statistics

Microscope	Titan Krios D3771
Voltage	300keV
Detector and mode	K3 detector and super-resolution counting mode
Pixel size (Å)	1.067
Defocus range (μm)	-0.6 to -2.4

A structural and dynamic visualization of the interaction between the microtubule-associated protein 7 (MAP7) and microtubules

Software used	EPU
Total electron dose (electrons/ Å ²)	49.37
Dose rate (electrons/pixel/s)	16.53
Exposure time (s)	3.4
Frames per movie	50
Number of micrographs	2190
Symmetry	Pseudo-helical
Initial number of particles	83471
Final number of particles	15857
Resolution (Å)	3.5
Map sharpening factor (Å ²)	-50
Initial model used	7973

AlphaFold2 multimer prediction

Protein sequences for porcine brain alpha-1A tubulin (UniPROT ID: P02550), beta-2B tubulin (UniPROT ID: P02554) and MAP7 MTBD (Residues 60-170 from UniPROT ID: Q14244) were used as inputs for locally installed AlphaFold2 multimer³⁶. Out of the 25 models obtained, the best model assessed by pTM+ipTM score was used for fitting and analyses. The model obtained was docked into the EM density using the 'Fit in Map' option of Chimera^{63,64}.

Preparation of solid-state NMR samples

For the preparation of solid-state NMR samples lyophilized tubulin (cytoskeleton) was solubilised in Brb80 buffer (80 mM PIPES, 2 mM MgCl₂, 1 mM EGTA, pH 6.8, 1 mM NaN₃, 1 mM DTT, pH 6.8 supplemented with protease inhibitor (Sigma-Aldrich, cOmplete EDTA-free)), to a final concentration of 2 mg/mL. Then 1 mM Guanosine-5'-triphosphate (GTP) was added and incubation took place for 15 minutes at 30 °C. In the following, 20 µM paclitaxel (Taxol, SIGMA) was used to stabilize the MT and incubation took place for another 15 minutes at 30 °C. The MT were spun down at 180.000 xg (Beckman TLA-55 rotor) for 30 minutes at 30 °C and the pellet was



resuspended in warm Brb80 buffer with 20 μM paclitaxel. Subsequently 0.55 mg/mL [^{13}C - ^{15}N]-MAP7 MTBD was added. The interaction partners were incubated for 30 minutes at 30 °C. In the following [^{13}C - ^{15}N]-MAP7 MTBD in complex with MT was separated from the unbound, non-polymerised fraction by centrifugation at 180.000 xg (Beckman TLA-55 rotor) for 30 minutes at 30 °C. Afterwards, the pellet was washed with Brb80 buffer containing protease inhibitor, without disturbing the pellet. A 1.3 mm rotor was packed with the pellet.

Solid-state NMR

Solid-state NMR experiments on [^{13}C - ^{15}N]-MAP7 MTBD with Taxol-stabilized MT were measured on a 700 MHz Bruker Avance III spectrometer with a 1.3 mm MAS rotor, at 55 kHz with a set temperature of 260 K, resulting in an effective sample temperature of approximately 299 K. All experiments were carried out with a $^1\text{H}/\text{X}/\text{Y}$ triple-resonance MAS probe. Scalar-based 2D hCH and 3D hCCH correlation experiments were executed with 0 ms and 16 ms DIPSI ⁶⁵ mixing time (Bahri et al., Chapter 4). Dipolar-based sequences were used with cross-polarization (CP) steps with an amplitude ramp of 80-100 % on ^1H and 13 kHz PISSARO decoupling ⁶⁶ during detection periods. CP transfer times were set to 700 μs and 150 μs . The dipolar 2D hCH and 3D hCCH experiments were recorded with 0 ms, 1.7 ms and 3.4 ms RFDR ⁶⁷ mixing times. MISSISSIPPI was used for water suppression ⁶⁸. All spectra were processed with the Bruker TopSpin 3.6.2 software. The data was zero-filled and an EM window function with a LB of 120 for the dipolar spectra and one of 30 for the scalar ones was applied. Linear prediction in the indirect ^{13}C dimensions was utilized with acquisition times (ms) of direct-/indirect-dimension of 24/32/32 for the 3D dipolar, 30/7 for the 2D dipolar, 32/12 for the 2D scalar and 32/18/18 for the 3D scalar. Chemical shifts were referenced via the water resonance. The spectra were analysed using POKY from NMRFAM-Sparky ⁶⁹.

Solution-state NMR

Solution-state NMR measurements for titration with MT were performed in NMR buffer (40 mM NaPi pH 6.5, 150 mM NaCl, 1 mM DTT) with 1 mM NaN₃ and 1 mM DTT, in 10 % D₂O. Two-dimensional (2D) ¹H-¹⁵N TROSY experiments of starting concentration 30 μM [¹³C-¹⁵N]-labelled MAP7 MTBD, were recorded at 295 K on a 600 MHz Bruker Avance III spectrometer.

For the experiments with carboxy-terminal tails, peptides with the sequences SVEGEGEEEGEEY (α-CTT) and DATAEEEEEDFGEEAEEEEA (β-CTT) were purchased from Sigma-Aldrich and used without further purification. For the experiments the peptides were solubilised in NMR buffer and their pH adapted. For the NMR measurements increasing stoichiometric ratios of peptides to MAP7 MTBD were added to 80 μM [¹³C-¹⁵N]-MAP7 MTBD in NMR buffer. The 2D ¹H-¹⁵N TROSY were recorded at 298 K on a 900 MHz Bruker Avance III spectrometer.

Fluorescence Anisotropy

0.1 mg α-CTT was dissolved in 100 μL NMR buffer (40 mM NaPi pH 6.5, 150 mM NaCl, 1 mM DTT) and the pH adjusted to 8.3 by adding 30 μL of 0.5 M Na₂HPO₄. The concentration of the α-CTT was measured with a BCA assay (the same as previously mentioned). 40 mM NaPi, 150 mM NaCl, pH 8.3 was added to obtain a 500 μM α-CTT concentration. From here, the experiment was performed in the dark due to the light-sensitivity of NHS-fluorescein. 4 times molar ratio NHS-fluorescein to α-CTT was incubated for 2 hours at room temperature, inverted, whilst protected from light. The NHS-fluorescein-labelled α-CTTs was dialysed against NMR buffer (40 mM NaPi pH 6.5, 150 mM NaCl, 1 mM DTT) overnight at 4 °C in a 1 kDa cut-off dialysis tube, with a buffer exchange after 2 hours, to remove unbound NHS- fluorescein. By measuring the absorbance at 494 nm, combined with the extinction coefficient of 68/M*cm and the concentration of α-CTT from the BCA the concentration of labelled α-CTT was calculated. A dilution series of MAP7 MTBD resulting in a concentration range from 200 to 0 μM in a 384-well plate was prepared and NHS-fluorescein-



labelled α -CTT to concentration of 1 μ M was added to each well. We measured the fluorescence anisotropy at 494 nm with a plate reader and analysed the results with the DynaFit software (BioKin Ltd.)²².

Isothermal titration calorimetry assay

Lyophilized tubulin (cytoskeleton) was solubilized in Brb80 buffer (80 mM PIPES, 2 mM MgCl₂, 1 mM EGTA, pH 6.5, 1 mM NaN₃, 1 mM DTT, pH 6.5 supplemented with protease inhibitor (Sigma-Aldrich, cOmplete EDTA-free)), to a final concentration of 2 mg/mL. Then 1 mM Guanosine-5'-triphosphate (GTP) was added and incubation took place for 15 minutes at 30 °C. In the following, 20 μ M paclitaxel (Taxol, SIGMA) was used to stabilize the MT and incubation took place for another 15 minutes at 30 °C. The MT were spun down at 180.000 xg (Beckman TLA-55 rotor) for 30 minutes at 30 °C and the pellet was resuspended in warm Brb80 buffer with 20 μ M paclitaxel. The Brb80 buffer was then exchanged to warm NMR buffer with 1 mM β -mercaptoethanol (β -ME) instead of DTT and 1 mM GTP with a PD-10 desalting column.

Isothermal titration calorimetry was performed with the NanoITC (Waters LLC, New Castle, DE, United States) to determine the interaction between Taxol-stabilized MT and MAP7 MTBD in NMR buffer with 1 mM β -ME instead of DTT and supplemented with 1 mM GTP. Samples were degassed before. 150 μ M MAP7 MTBD was titrated in 2 μ L steps to 164 μ L of 15 μ M Taxol-stabilized MT. The protein was titrated at a rate of 2 μ L/300 s with a stirring rate of 300 rpm. Experiments were performed at 37°C. Control experiments were performed with buffer titration. The dissociation constant (K_D) value was calculated using the Nano Analyse Software (Waters LLC).

References

1. Gadadhar, S., Bodakuntla, S., Natarajan, K. & Janke, C. The tubulin code at a glance. *Journal of cell science* **130**, 1347–1353 (2017).
2. Mandelkow, E.-M., Schultheiß, R., Rapp, R., Müller, M. & Mandelkow, E. On the surface lattice of microtubules: helix starts, protofilament number, seam, and handedness. *The Journal of cell biology* **102**, 1067–1073 (1986).
3. Akhmanova, A. & Steinmetz, M. O. Control of microtubule organization and dynamics: two ends in the limelight. *Nature reviews Molecular cell biology* **16**, 711–726 (2015).
4. Desai, A. & Mitchison, T. J. Microtubule polymerization dynamics. *Annual review of cell and developmental biology* **13**, 83–117 (1997).
5. Alushin, G. M. *et al.* High-resolution microtubule structures reveal the structural transitions in $\alpha\beta$ -tubulin upon GTP hydrolysis. *Cell* **157**, 1117–1129 (2014).
6. Bodakuntla, S., Jijumon, A., Villablanca, C., Gonzalez-Billault, C. & Janke, C. Microtubule-associated proteins: structuring the cytoskeleton. *Trends in cell biology* **29**, 804–819 (2019).
7. Goodson, H. V. & Jonasson, E. M. Microtubules and microtubule-associated proteins. *Cold Spring Harbor perspectives in biology* **10**, a022608 (2018).
8. Kikuchi, K. *et al.* Map7/7D1 and Dvl form a feedback loop that facilitates microtubule remodeling and Wnt5a signaling. *EMBO reports* **19**, e45471 (2018).
9. Sun, X. *et al.* Mdp3 is a novel microtubule-binding protein that regulates microtubule assembly and stability. *Cell cycle* **10**, 3929–3937 (2011).
10. Gallaud, E. *et al.* Ensconsin/Map7 promotes microtubule growth and centrosome separation in Drosophila neural stem cells. *Journal of Cell Biology* **204**, 1111–1121 (2014).
11. Tymanskyj, S. R., Yang, B., Falnikar, A., Lepore, A. C. & Ma, L. MAP7 regulates axon collateral branch development in dorsal root ganglion neurons. *Journal of Neuroscience* **37**, 1648–1661 (2017).
12. Zhang, L., Liu, X., Song, L., Zhai, H. & Chang, C. MAP7 promotes migration and invasion and progression of human cervical cancer through modulating the autophagy. *Cancer cell international* **20**, 1–8 (2020).
13. Fu, L. *et al.* High expression of MAP7 predicts adverse prognosis in young patients with cytogenetically normal acute myeloid leukemia. *Scientific reports* **6**, 1–9 (2016).
14. Wang, X., Cao, X., Wu, Y. & Chen, T. MAP7 promotes proliferation and migration of breast cancer cells and reduces the sensitivity of breast cancer cells to paclitaxel. *Journal of Chemotherapy* 1–9 (2022).
15. Hooikaas, P. J. *et al.* MAP7 family proteins regulate kinesin-1 recruitment and activation. *Journal of Cell Biology* **218**, 1298–1318 (2019).
16. Metzger, T. *et al.* MAP and kinesin-dependent nuclear positioning is required for skeletal muscle function. *Nature* **484**, 120–124 (2012).
17. Adler, A. *et al.* Resonance Assignments of the microtubule-binding domain of the microtubule-associated protein 7 (MAP7), *Biomol NMR Assign* (2023), in press. (2023).
18. Ferro, L. S. *et al.* Structural and functional insight into regulation of kinesin-1 by microtubule-associated protein MAP7. *Science* **375**, 326–331 (2022).
19. Luo, Y. *et al.* Direct observation of dynamic protein interactions involving human microtubules using solid-state NMR spectroscopy. *Nature Communications* **11**, 18 (2020).



Chapter 5

20. Wloga, D., Joachimiak, E., Louka, P. & Gaertig, J. Posttranslational modifications of tubulin and cilia. *Cold Spring Harbor perspectives in biology* **9**, a028159 (2017).
21. Sataric, M. V., Sekulic, D. L., Zdravkovic, S. & Ralevic, N. M. A biophysical model of how α -tubulin carboxy-terminal tails tune kinesin-1 processivity along microtubule. *Journal of Theoretical Biology* **420**, 152–157 (2017).
22. Skiniotis, G. *et al.* Modulation of kinesin binding by the C-termini of tubulin. *The EMBO Journal* **23**, 989–999 (2004).
23. Nogales, E., Wolf, S. & Downing, K. Structure of the ab tubulin dimer by electron crystallography (Correction). *Nature* **393**, 191 (1998).
24. Renault, M., Cukkemane, A. & Baldus, M. Solid-state NMR spectroscopy on complex biomolecules. *Angewandte Chemie International Edition* **49**, 8346–8357 (2010).
25. Quinn, C. M. & Polenova, T. Structural biology of supramolecular assemblies by magic-angle spinning NMR spectroscopy. *Quarterly reviews of biophysics* **50**, e1 (2017).
26. Kumar, A. *et al.* Interaction of Epothilone B (Patupilone) with Microtubules as Detected by Two-Dimensional Solid-State NMR Spectroscopy. *Angewandte Chemie* **122**, 7666–7669 (2010).
27. Li, Y. *et al.* Conformation of microtubule-bound paclitaxel determined by fluorescence spectroscopy and REDOR NMR. *Biochemistry* **39**, 281–291 (2000).
28. Yan, S. *et al.* Atomic-resolution structure of the CAP-Gly domain of dynactin on polymeric microtubules determined by magic angle spinning NMR spectroscopy. *Proceedings of the National Academy of Sciences* **112**, 14611–14616 (2015).
29. Atherton, J. *et al.* A structural model for microtubule minus-end recognition and protection by CAMSAP proteins. *Nature structural & molecular biology* **24**, 931–943 (2017).
30. El Mammeri, N., Dregni, A. J., Duan, P., Wang, H. K. & Hong, M. Microtubule-binding core of the tau protein. *Science Advances* **8**, eabo4459 (2022).
31. Luo, Y. *et al.* Solid-State NMR Spectroscopy for Studying Microtubules and Microtubule-Associated Proteins. in *Structural Proteomics* 193–201 (Springer, 2021).
32. Zhang, C. *et al.* Magic-angle-spinning NMR structure of the kinesin-1 motor domain assembled with microtubules reveals the elusive neck linker orientation. *Nature Communications* **13**, 6795 (2022).
33. Monroy, B. Y. *et al.* Competition between microtubule-associated proteins directs motor transport. *Nature communications* **9**, 1–12 (2018).
34. Cook, A. D., Manka, S. W., Wang, S., Moores, C. A. & Atherton, J. A microtubule RELION-based pipeline for cryo-EM image processing. *Journal of Structural Biology* **209**, 107402 (2020).
35. Cook, A. D. *et al.* Cryo-EM structure of a microtubule-bound parasite kinesin motor and implications for its mechanism and inhibition. *Journal of Biological Chemistry* **297**, 101063 (2021).
36. Evans, R. *et al.* *Protein complex prediction with AlphaFold-Multimer.* <http://biorxiv.org/lookup/doi/10.1101/2021.10.04.463034> (2021) doi:10.1101/2021.10.04.463034.
37. Damman, R. *et al.* Atomic-level insight into mRNA processing bodies by combining solid and solution-state NMR spectroscopy. *Nature communications* **10**, 1–11 (2019).
38. Tokuraku, K., Katsuki, M., Nakagawa, H. & Kotani, S. A new model for microtubule-associated protein (MAP)-induced microtubule assembly: The Pro-rich region of MAP4 promotes nucleation of microtubule assembly in vitro. *European journal of biochemistry* **259**, 158–166 (1999).
39. Wang, Z. *et al.* DJ-1 can inhibit microtubule associated protein 1 B formed aggregates. *Molecular neurodegeneration* **6**, 1–10 (2011).

A structural and dynamic visualization of the interaction between the microtubule-associated protein 7 (MAP7) and microtubules

40. Oláh, J. *et al.* Microtubule-associated proteins with regulatory functions by day and pathological potency at night. *Cells* **9**, 357 (2020).
41. Xie, C. *et al.* Identification of key amino acids responsible for the distinct aggregation properties of microtubule-associated protein 2 and tau. *Journal of Neurochemistry* **135**, 19–26 (2015).
42. Conchillo-Solé, O. *et al.* AGGRESCAN: a server for the prediction and evaluation of "hot spots" of aggregation in polypeptides. *BMC bioinformatics* **8**, 1–17 (2007).
43. Tymanskyj, S. R., Yang, B. H., Verhey, K. J. & Ma, L. MAP7 regulates axon morphogenesis by recruiting kinesin-1 to microtubules and modulating organelle transport. *Elife* **7**, e36374 (2018).
44. Chaudhary, A. R. *et al.* MAP7 regulates organelle transport by recruiting kinesin-1 to microtubules. *Journal of Biological Chemistry* **294**, 10160–10171 (2019).
45. Mchedlishvili, N., Matthews, H. K., Corrigan, A. & Baum, B. Two-step interphase microtubule disassembly aids spindle morphogenesis. *BMC biology* **16**, 1–16 (2018).
46. Tymanskyj, S. R. & Ma, L. MAP7 prevents axonal branch retraction by creating a stable microtubule boundary to rescue polymerization. *Journal of Neuroscience* **39**, 7118–7131 (2019).
47. Blum, C. *et al.* The expression ratio of Map7/B2M is prognostic for survival in patients with stage II colon cancer. *International journal of oncology* **33**, 579–584 (2008).
48. Borys, F., Joachimiak, E., Krawczyk, H. & Fabczak, H. Intrinsic and extrinsic factors affecting microtubule dynamics in normal and cancer cells. *Molecules* **25**, 3705 (2020).
49. Guharoy, M., Szabo, B., Martos, S. C., Kosol, S. & Tompa, P. Intrinsic structural disorder in cytoskeletal proteins. *Cytoskeleton* **70**, 550–571 (2013).
50. Janke, C. & Magiera, M. M. The tubulin code and its role in controlling microtubule properties and functions. *Nature Reviews Molecular Cell Biology* **21**, 307–326 (2020).
51. Scheres, S. H. W. A Bayesian View on Cryo-EM Structure Determination. *Journal of Molecular Biology* **415**, 406–418 (2012).
52. Scheres, S. H. W. RELION: Implementation of a Bayesian approach to cryo-EM structure determination. *Journal of Structural Biology* **180**, 519–530 (2012).
53. Zheng, S. Q. *et al.* MotionCor2: anisotropic correction of beam-induced motion for improved cryo-electron microscopy. *Nat Methods* **14**, 331–332 (2017).
54. Rohou, A. & Grigorieff, N. CTFFIND4: Fast and accurate defocus estimation from electron micrographs. *Journal of Structural Biology* **192**, 216–221 (2015).
55. He, S. & Scheres, S. H. W. Helical reconstruction in RELION. *Journal of Structural Biology* **198**, 163–176 (2017).
56. Adib, R. *et al.* Mitotic phosphorylation by NEK6 and NEK7 reduces the microtubule affinity of EML4 to promote chromosome congression. *Sci. Signal.* **12**, eaaw2939 (2019).
57. Jamali, K., Kimanius, D. & Scheres, S. H. W. A Graph Neural Network Approach to Automated Model Building in Cryo-EM Maps. Preprint at <http://arxiv.org/abs/2210.00006> (2023).
58. Emsley, P., Lohkamp, B., Scott, W. G. & Cowtan, K. Features and development of *Coot*. *Acta Crystallogr D Biol Crystallogr* **66**, 486–501 (2010).
59. Adams, P. D. *et al.* PHENIX: a comprehensive Python-based system for macromolecular structure solution. *Acta Crystallogr D Biol Crystallogr* **66**, 213–221 (2010).
60. Afonine, P. V. *et al.* Real-space refinement in PHENIX for cryo-EM and crystallography. *Acta Crystallogr D Struct Biol* **74**, 531–544 (2018).
61. Goddard, T. D. *et al.* UCSF ChimeraX: Meeting modern challenges in visualization and analysis: UCSF ChimeraX Visualization System. *Protein Science* **27**, 14–25 (2018).

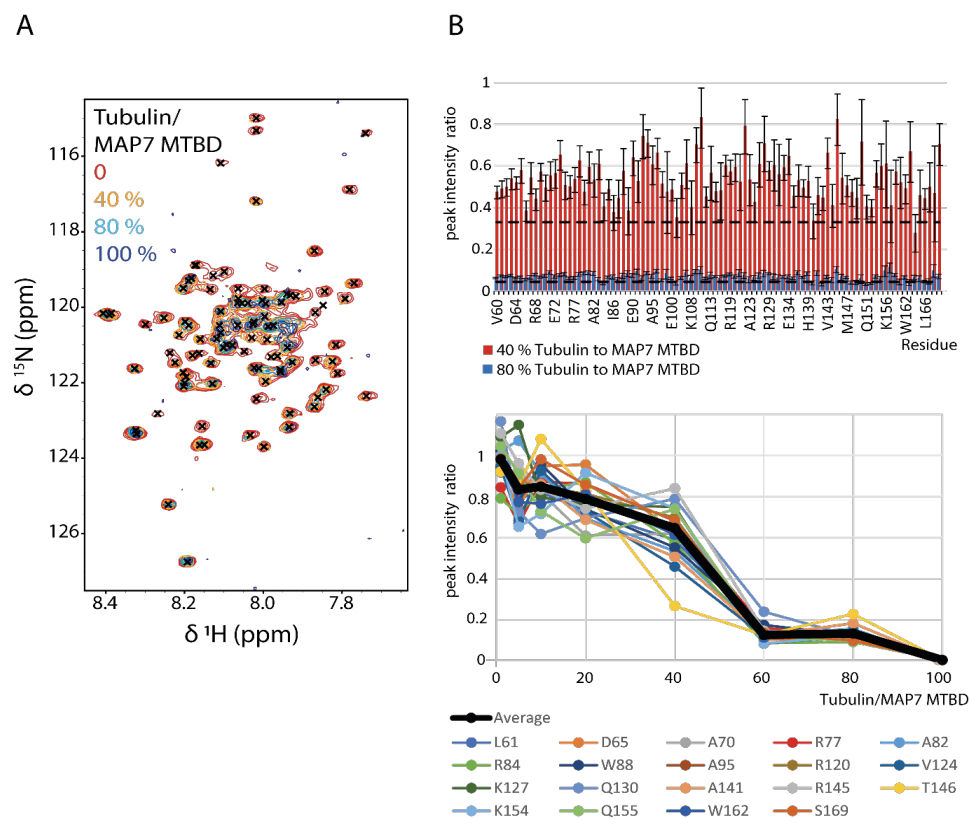


Chapter 5

62. Pettersen, E. F. *et al.* UCSF CHIMERAX : Structure visualization for researchers, educators, and developers. *Protein Science* **30**, 70–82 (2021).
63. Pettersen, E. F. *et al.* UCSF Chimera?A visualization system for exploratory research and analysis. *J. Comput. Chem.* **25**, 1605–1612 (2004).
64. Goddard, T. D., Huang, C. C. & Ferrin, T. E. Visualizing density maps with UCSF Chimera. *Journal of Structural Biology* **157**, 281–287 (2007).
65. Shaka, A., Lee, C. & Pines, A. Iterative schemes for bilinear operators; application to spin decoupling. *Journal of Magnetic Resonance (1969)* **77**, 274–293 (1988).
66. Weingarth, M., Bodenhausen, G. & Tekely, P. Low-power decoupling at high spinning frequencies in high static fields. *Journal of Magnetic Resonance* **199**, 238–241 (2009).
67. Bennett, A., Griffin, R., Ok, J. & Vega, S. Chemical shift correlation spectroscopy in rotating solids: Radio frequency-driven dipolar recoupling and longitudinal exchange. *The Journal of chemical physics* **96**, 8624–8627 (1992).
68. Zhou, D. H. & Rienstra, C. M. High-performance solvent suppression for proton detected solid-state NMR. *Journal of magnetic resonance* **192**, 167–172 (2008).
69. Lee, W., Rahimi, M., Lee, Y. & Chiu, A. POKY: a software suite for multidimensional NMR and 3D structure calculation of biomolecules. *Bioinformatics* **37**, 3041–3042 (2021).

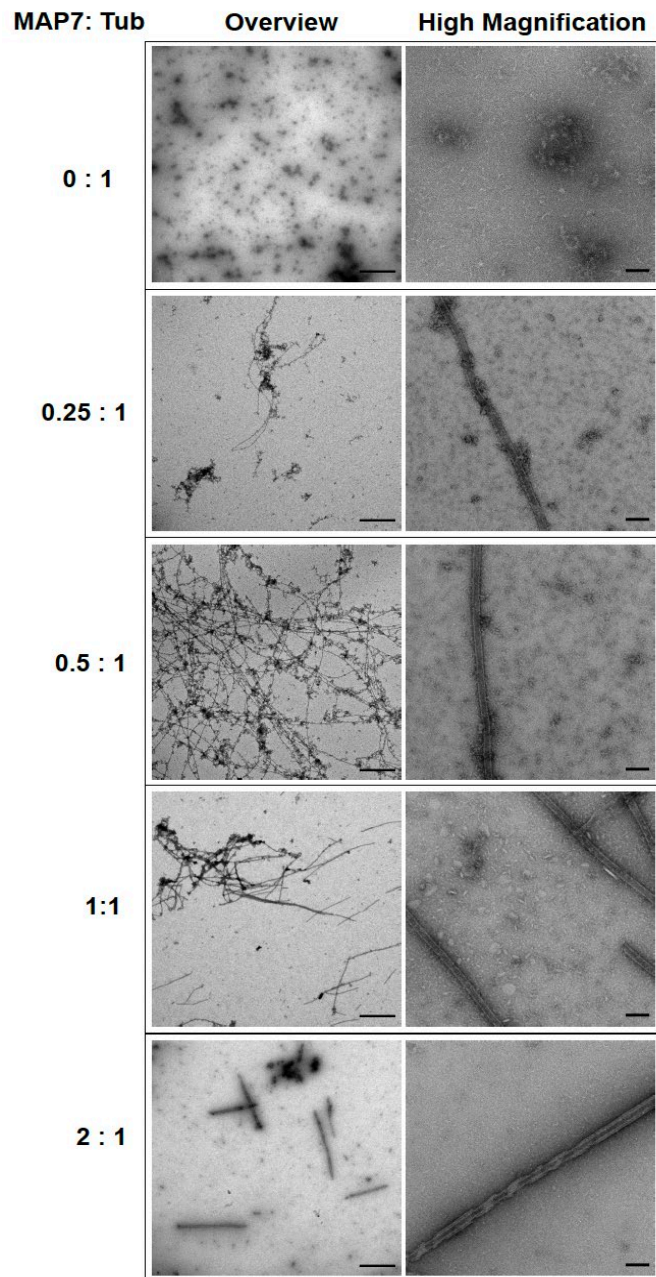
A structural and dynamic visualization of the interaction between the microtubule-associated protein 7 (MAP7) and microtubules

Supplementary information



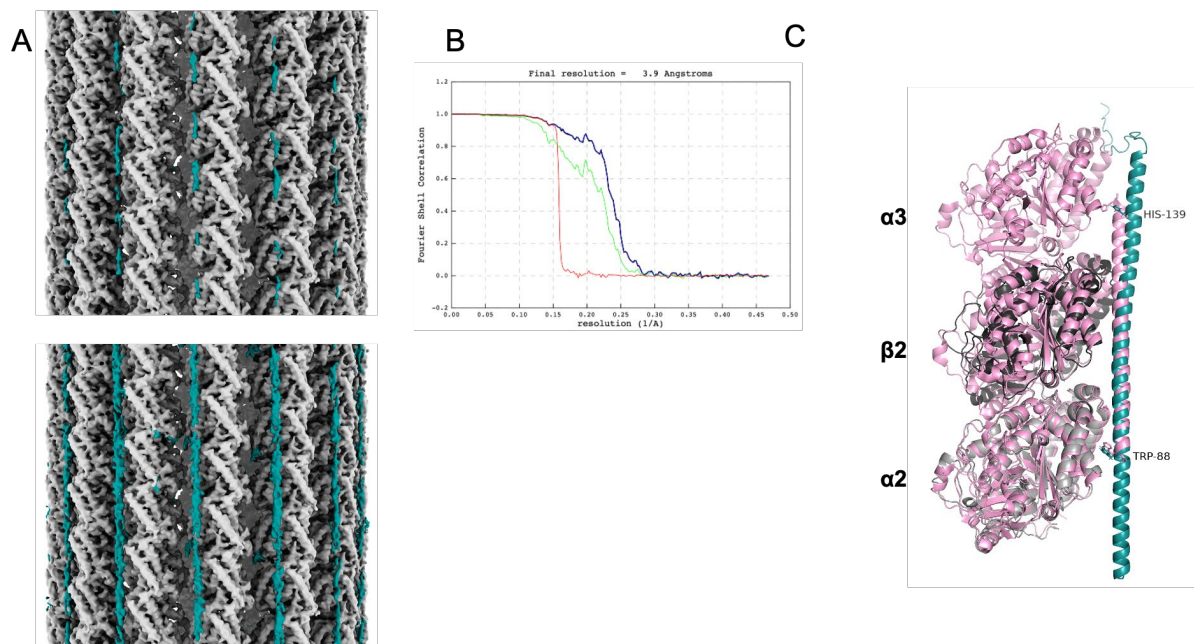
Supplementary Fig. 5.1: Titration of Taxol-stabilized MT to $[^{13}\text{C}-^{15}\text{N}]$ - MAP7 MTBD in solution (A) Overlay of ^1H - ^{15}N TROSY spectra of varying MT concentrations added to MAP7 MTBD. (B) Intensity ratio over whole MAP7 (top) upon adding 40 % or 80 % polymerized tubulin dimers to MAP7 MTBD. The black dotted lines are the 10 % trimmed average. Considering that the ITC data indicate that one MTBD binds two tubulin dimers, one would expect saturation of MTBD upon addition of 2 molar equivalents of tubulin dimers, i.e. at 200 %. Addition of 40 % or 80 % tubulin dimers would thus leave a large fraction of MTBD unbound (80 % and 40 % of MTBD, respectively). Assuming that only the free MTBD is NMR-observable, the expected signal intensity would be 80% and 40% in case there is no exchange between free and bound forms. As the observed relative MTBD intensity is much lower (53 %, respectively, 7 %) this indicates that there is considerable exchange between free and bound MTBD. Exploratory simulations indicate the lifetime of the complex is on the order of 10 ms at most. Intensity ratio decrease over titration of selected residues (bottom). The sharp drop in peak intensity around 50 % tubulin dimers added is suggestive of a degree of cooperativity in binding.





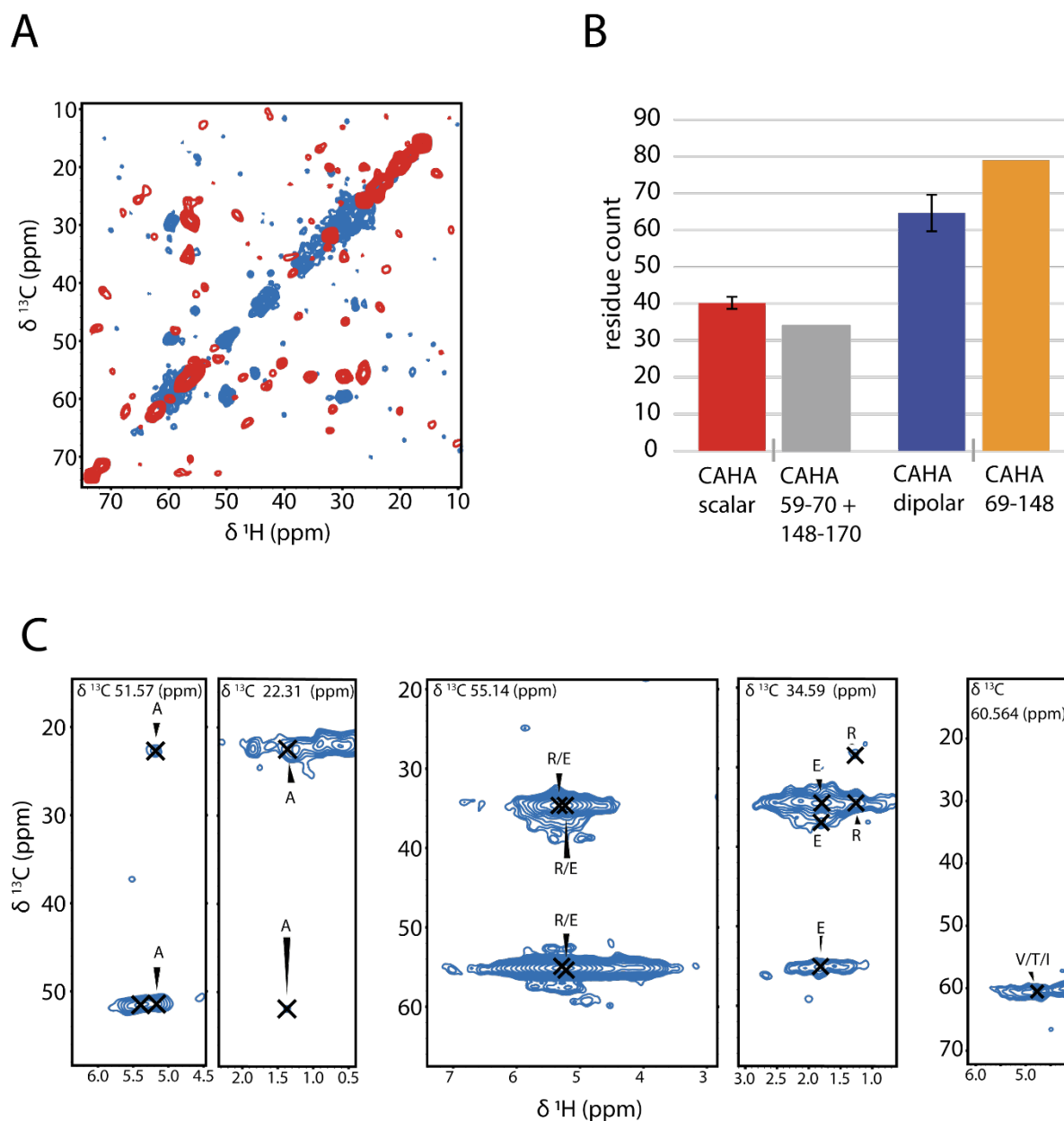
Supplementary Fig. 5.2: Negative stain EM shows that MAP7 MTBD stabilizes dynamic MTs. Left and right panels show micrographs at low (overview) and high magnifications respectively for MAP7 MTBD and tubulin incubated at molar concentration ratios of 0:1 (no MAP7 MTBD), 0.25:1 , 0.5:1 , 1:1 and 2:1. Concentration of tubulin used is 5 μ M. Scale bars represent 2 μ m and 100 nm for the left and right panels respectively.

A structural and dynamic visualization of the interaction between the microtubule-associated protein 7 (MAP7) and microtubules



Supplementary Fig. 5.3: CryoEM of MAP7 MTBD bound to MTs (A) Cryo-EM density map (Symmetrised reconstructions) of MAP7_MTBd bound MT (1:1 for MTBD and tubulin) when no MAP7 MTBD is added externally at high (top panel) and low (bottom panel) respectively. Density for the MT and MAP7_MTBd is shown in grey and teal respectively. **(B)** Fourier shell correlation plot of the half maps for symmetrised reconstruction (Fig. 5.2A) of the MAP7 MTBD-MT complex. The resolution was estimated based on 0.143 criterion of half maps. **(C)** Cartoon representation of model predicted by AlphaFold2 multimer (green, same as Fig. 5.2B) superposed upon MAP7 MTBD:MT model (pink) previously determined by cryoEM (PDB ID: 7SGS). Bulky residues corresponding to the ends of the 53-residue segment are shown as stick representation in both models and labelled.





Supplementary Fig. 5.4: 3D CCH experiments (A) CC- planes of $[^{13}\text{C}-^{15}\text{N}]$ -MAP7 MTBD bound to MT. Scalar and dipolar experiments are given in red and blue, respectively. **(B)** CAHA abundancy in MAP7 MTBD regions compared to peak integration of CAHA regions in the scalar and dipolar CH projections of the 3D CCH spectra **(C)** Assigned strips of correlations in the dipolar 3D CCH that exhibit β -strand like chemical shifts.

A structural and dynamic visualization of the interaction between the microtubule-associated protein 7 (MAP7) and microtubules

Supplementary Table 5.1: assigned chemical shifts from CH solution-state

Assignment	¹³ C Shift	¹ H Shift
P59CA-HA	63.03	4.35
P59CB-HB2	32.00	2.19
P59CB-HB3	32.00	1.77
V60CA-HA	62.29	3.96
V60CB-HB	32.76	1.93
V60CG1-HG1	21.14	0.83
L61CA-HA	54.88	4.32
L61CB-HB3	42.59	1.49
L61CD1-HD1	23.51	0.82
R62CA-HA	55.89	4.34
R62CB-HB2	31.01	1.79
R62CB-HB3	31.01	1.69
R62CD-HD	43.03	3.13
V63CA-HA	62.72	3.97
V63CB-HB	32.82	1.98
V63CG1-HG1	20.64	0.86
D64CA-HA	54.23	4.53
D64CB-HB2	41.24	2.63
D64CB-HB3	41.24	2.61
D65CA-HA	55.32	4.49
D65CB-HB2	41.23	2.62
R66CA-HA	58.36	4.01
R66CB-HB2	30.08	1.83
R66CD-HD	43.51	3.13
R66CG-HG	27.21	1.53
Q67CA-HA	57.56	4.13
Q67CB-HB2	28.71	2.04
R68CA-HA	58.26	4.03
R68CB-HB2	32.71	1.98
R68CB-HB3	32.71	1.78
L69CA-HA	56.56	4.09
L69CB-HB2	42.04	1.64
L69CB-HB3	42.04	1.49
L69CD1-HD1	23.36	0.80
A70CA-HA	54.04	4.09
A70CB-HB	18.58	1.37
R71CA-HA	58.10	4.06
R71CB-HB2	30.25	1.85
R71CB-HB3	30.25	1.84
R71CD-HD	43.49	3.02
E72CA-HA	58.23	4.07
E72CB-HB2	29.86	2.00
R74CA-HA	58.20	4.11
R74CB-HB2	30.32	1.76
R74CB-HB3	30.32	1.54
R74CD-HD	43.35	3.10
E75CA-HA	58.37	4.08
E75CB-HB2	30.32	2.02
E75CB-HB3	30.32	1.83
E76CA-HA	58.40	4.10
E76CB-HB2	30.41	1.86
E76CB-HB3	30.41	1.82
K79CA-HA	58.15	4.11
K79CB-HB2	32.67	2.05
K79CB-HB3	32.67	1.83
K79CG-HG	25.05	1.50
E100CA-HA	58.28	4.07
K101CA-HA	58.37	4.09
K101CB-HB2	31.00	1.84
K101CB-HB3	31.00	1.78
E104CA-HA	58.81	4.08
E104CB-HB2	29.57	1.86
E104CB-HB3	29.57	1.83
E105CA-HA	58.32	4.08
E105CB-HB2	29.77	2.05
E105CB-HB3	29.77	2.01
R106CA-HA	58.99	3.92
K107CB-HB2	32.51	1.84
E111CB-HB2	29.47	1.99
E111CB-HB3	29.47	1.85
E112CA-HA	59.03	4.04
E112CB-HB3	29.46	1.84
Q113CA-HA	58.56	4.14
Q113CB-HB2	28.49	1.98
Q113CB-HB3	28.49	1.79
E118CA-HA	58.79	4.04
R119CA-HA	58.79	4.44
R119CB-HB2	30.22	1.85
R120CB-HB2	30.24	1.85
R120CB-HB3	30.24	1.78
R121CA-HA	58.81	3.97
A122CA-HA	54.20	4.13
A123CA-HA	54.29	4.18
A123CB-HB	18.35	1.38
V124CA-HA	65.48	3.71
V124CB-HB	32.19	1.83
V124CG2-HG2	22.13	1.01
E125CG1-HG1	36.13	2.24
R128CA-HA	58.28	4.08
R128CB-HB2	29.65	1.97
R128CB-HB3	29.65	1.80
R129CA-HA	57.38	4.08
Q130CA-HA	57.60	4.21
Q130CB-HB2	28.78	1.42
Q130CB-HB3	28.78	1.37
L132CA-HA	56.73	4.07
L132CD1-HD1	24.58	0.78
E134CA-HA	57.91	4.10
E134CB-HB2	30.05	2.06
E134CB-HB3	30.05	2.01
H139CA-HA	57.16	4.45
H139CB-HB2	30.05	3.16
H139CB-HB3	30.05	3.11
E140CA-HA	57.45	4.05
A141CA-HA	53.47	4.14
A141CB-HB	18.89	1.36
V142CA-HA	63.71	3.82
V142CB-HB	32.45	2.04
V142CG1-HG1	20.79	0.87
V142CG2-HG2	21.28	0.91
V143CA-HA	63.67	3.81
V143CB-HB	32.34	1.94



Chapter 5

Q80CA-HA	57.16	4.14
Q80CB-HB2	28.79	2.05
Q80CB-HB3	28.79	1.83
L81CA-HA	56.40	4.11
L81CB-HB2	42.15	1.66
L81CB-HB3	42.15	1.50
L81CG-HG	27.25	1.60
A82CA-HA	53.28	4.15
A82CB-HB	18.82	1.37
A83CA-HA	53.35	4.15
A83CB-HB	18.83	1.36
R84CA-HA	57.05	4.05
R84CB-HB2	30.63	1.98
E85CA-HA	57.38	4.15
E85CB-HB2	30.11	1.97
E85CG-HG	36.50	2.31
I86CA-HA	62.34	3.90
I86CB-HB	38.36	1.77
I86CD1-HD1	12.78	0.76
I86CG1-HG1	27.92	1.10
I86CG2-HG2	17.25	0.67
V87CA-HA	63.65	3.90
V87CB-HB	32.32	1.95
V87CG1-HG1	20.88	0.83
W88CA-HA	58.45	4.46
W88CB-HB2	29.42	3.29
W88CB-HB3	29.42	3.18
L89CA-HA	56.38	4.07
L89CB-HB3	42.48	1.48
E90CA-HA	58.04	4.03
E90CB-HB2	29.78	1.99
E90CB-HB3	29.78	1.85
R91CA-HA	58.15	4.02
R91CB-HB2	30.41	1.98
R91CB-HB3	30.41	1.80
E92CB-HB2	29.70	1.95
E93CB-HB3	29.68	1.83
R94CA-HA	56.73	4.26
R94CB-HB2	30.25	1.78
R94CB-HB3	30.25	1.48
A95CA-HA	54.01	4.09
A95CB-HB	18.85	1.40
R96CA-HA	58.18	4.02
R96CB-HB2	30.24	2.00
R96CB-HB3	30.24	1.85
Q97CA-HA	58.23	4.09
H98CA-HA	57.70	4.11
H98CB-HB2	29.89	3.12
Y99CA-HA	59.84	4.32
Y99CB-HB2	38.44	3.07

R145CA-HA	56.99	4.24
R145CB-HB2	30.70	1.80
R145CB-HB3	30.70	1.76
R145CD-HD	43.46	3.18
T146CB-HB	69.57	4.18
M147CB-HB2	32.83	1.99
M147CE-HE	16.90	2.00
E148CG1-HG1	36.20	2.20
R149CA-HA	56.48	4.24
R149CB-HB2	30.69	1.82
R149CB-HB3	30.69	1.73
S150CB-HB3	63.82	3.81
Q151CA-HA	55.46	4.28
Q151CB-HB2	29.66	2.03
Q151CB-HB3	29.66	1.89
P153CA-HA	63.14	4.32
P153CB-HB2	32.18	2.21
P153CB-HB3	32.18	1.79
P153CD-HD	50.41	3.57
P153CG-HG	27.32	1.94
K154CA-HA	56.49	4.15
K154CB-HB	32.98	1.68
K154CG-HG	24.87	1.35
Q155CA-HA	55.53	4.21
Q155CB-HB2	29.78	1.91
Q155CB-HB3	29.78	1.84
N158CA-HA	53.15	4.52
N158CB-HB3	38.81	2.58
R159CA-HA	56.61	4.03
R159CB-HB2	30.43	1.85
R159CB-HB3	30.43	1.49
R159CD-HD	43.13	2.89
R159CG-HG	26.65	1.20
W160CA-HA	57.20	4.56
W160CB-HB3	29.53	3.06
S161CB-HB2	63.75	3.57
W162CA-HA	57.51	4.52
W162CB-HB2	29.55	3.17
W162CB-HB3	29.55	3.13
G163CA-HA	45.58	3.77
G164CA-HA	45.24	3.76
S165CB-HB2	62.98	4.16
H167CA-HA	55.65	4.53
H167CB-HB2	29.89	3.08
H167CB-HB3	30.16	2.94
G168CA-HA	45.17	3.83
S169CB-HB3	63.47	3.71
P170CA-HA	64.90	4.15
P170CD-HD	50.56	3.73
P170CD-HD	50.56	3.73

A structural and dynamic visualization of the interaction between the microtubule-associated protein 7 (MAP7) and microtubules

Supplementary Table 5.2: assigned chemical shifts in CCH spectra

Dipolar CCH		
Residue	Atom	Shift
A	CA	50.25
A	HA	4.57
A2	CA	54.80
A2	CB	18.23
A2	HA	4.05
A2	HB	1.33
A3	CA	54.91
A3	CB	19.37
A3	HA	4.43
E	CA	59.72
E	CB	29.59
E	CG	36.53
E	HB2	2.28
E	HA	3.98
E	HG2	1.93
E2	CB	31.06
E2	CG	36.70
E2	HG2	2.10
K	CA	59.66
K	CB	31.69
K	CD	29.44
K	CE	43.06
K	CG	25.21
K	HD2	1.57
K	HA	3.78
K	HG2	1.86
K	HB2	1.57
K	HE2	1.70
L	CD2	22.42
L	CG1	28.56
L	CD1	25.92
L	HD1	0.93
L	HD2	0.73
L	HG	0.80
L2	CD	25.49
L2	HD1	0.79
L2	HD2	0.82
M	CB	36.53
M	CE	20.61
M	HB2	2.20
M	HE	1.92
Q	CA	59.84
Q	CB	29.21
Q	CG	32.22
Q	HB2	1.88
Q	HA	4.07
Q	HG2	1.69
Q2	CB	29.30
Q2	HG2	1.68
E3	CB	30.32
E3	CG	34.26

Scalar CCH		
Residue	Atom	Shift
D64	CA	53.98
D64	CB	40.42
D64	HA	4.47
D64	HB	2.61
E	CA	56.30
E	CG	35.70
E	CB	29.62
E	HA	4.10
E	HB2	2.16
E	HG3	1.96
E148	CA	56.42
E148	CB	29.56
E148	CG	35.69
E148	HA	4.12
E148	HG3	1.95
E/R	CA	55.75
E/R	CB	30.23
E/R	HA	4.23
I86	CD1	11.81
I86	CD2	22.50
I86	CG2	12.15
I86	HD1	0.75
I86	HG2	0.81
K154	CD	28.39
K154	CG	24.15
K154	HD3	1.58
K154	HG3	1.34
L1	CD2	23.17
L1	HD2	0.83
L166	CB	41.01
L166	CD1	23.85
L166	HD1	0.82
L2	CD2	23.24
L2	HD2	0.79
L61	CA	54.35
L61	CB	42.13
L61	CD2	22.84
L61	CG	26.06
L61	HB	1.61
L61	HG	1.51
L69	CA	55.34
L69	CB	42.17
L69	CD1	26.36
L69	CD2	23.04
L69	CG	26.42
L69	HA	4.17
L69	HD1	1.57
L69	HD2	0.77
L69	HG	1.56
M147	CA	60.15
M147	CE	16.42



Chapter 5

E3	HG2	1.25
E3	HA	3.78
R	CA	57.01
R	CB	29.62
R	CD	42.98
R	CG	27.91
R	HD2	3.11
R	HB2	1.50
R	HG2	1.58
R2	CG	28.20
R2	CA	59.45
R2	HD2	3.11
R2	HB2	1.65
R3	HG2	1.58
S	CA	59.93
S	CB	61.97
S	HB2	4.18
S2	CA	59.84
S2	CB	62.21
S2	HB2	4.01
V	CB	31.94
V	CG	21.47
V	HG1	1.16

M147	HE	1.92
N158	CA	53.54
N158	CB	38.50
N158	HA	4.57
N158	HB	2.59
P170	CA	64.86
P170	CB	31.96
P170	HA	4.18
P170	HB2	2.13
P59	CA	62.28
P59	CB	31.60
P59	HA	4.33
P/V/K	CB	32.67
P/V/K	HB3	1.74
Q1	CA	55.22
Q1	HA	3.90
Q155	CA	55.27
Q155	CB	30.38
Q155	CG	33.32
Q155	HA	3.89
Q155	HG3	2.20
R159	CA	56.11
R159	CB	30.37
R159	CD	42.69
R159	CG	26.87
R159	HA	4.16
R159	HB2	2.22
R159	HG2	1.71
R2	CA	56.20
R2	CB	30.41
R2	CG	26.49
R2	HG2	1.78
R/L	CA	55.93
R/L	CD	42.12
R/L	CG	26.50
R/L	HG3	1.59
S	CB	62.28
S	HB3	3.51
T146	CA	62.47
T146	CB	70.36
T146	CG2	20.96
T146	HA	4.12
T146	HB	4.09
T146	HG2	1.10
V60	CA	62.07
V60	CB	31.73
V60	CG1	20.41
V60	CG2	20.26
V60	HA	3.95
V60	HB	1.97
V60	HG1	0.85

Supplementary Methods

Spectral analysis of 2D and 3D ssNMR data sets

The analysis of scalar and dipolar 2D ^{13}C - ^1H correlation experiments in **Fig. 5.3B** was performed on the basis of previous solution NMR assignments and average BMRB chemical-shift values. For example, in panel **(I)**, we find good agreement between peak positions for the Ala, Val and Leu side-chain resonances seen in the complex using J-based ssNMR (red) and solution-state results (crosses). In the same vein, correlations corresponding to Met 147 CE-HE, Lys 154 CG-HG and two peaks corresponding to Ile 86 QG1-HG1 and Ile 86 CD1-QD1 (where Q stands for one peak for multiple protons) are visible. On the other hand, most Lysine CG-QG side-chain correlations seem to appear in a spectral region only detected in the dipolar spectrum. Likewise, His and Trp CH-HB resonances seem to only appear in panel **(II)** in the dipolar-based ssNMR data. Region **(III)** shows side-chain resonances of Glu, Arg, Gln, Lys, Val, Leu, and Pro. In this region, both dipolar and scalar signals can be seen. Interestingly, Ile 86 CB-HB correlations seen in solution appears rigid (Blue, indicate in panel **III**), while as mentioned above for panel (I), Ile CD-QD and CG-QG might be flexible as there is only one Ile residue in the sequence. Region **(IV)** contains Arg CD-QD, Asp CB-HB, Tyr 99 CB-HB and Asn 158 CB-HB resonances. With some exceptions, MAP7 MTBD seems to have rigid Arg CD-QDs, suggesting stabilization of arginine sidechains after complex formation. On the other hand, the solution-state NMR CB-HB resonances associated with Asp 64, Asp 65 and Asn 158 are in good agreement with the scalar signals in the complex. The Leu CB-HB region that is depicted in panel **(V)** gives scalar, as well as dipolar signals. Panel **(VI)** shows the crowded CA-HA region. There are no resonances found for Pro CD-QD. Flexible CA-HAs include Ala CA-HA, several Glu CA-HAs and CA-HA of Asp 64, Asp 65, Asn 158 and His 167. For the crowded Arg, Glu, Leu, Gln, and Lys region both dipolar and scalar signals appear. Lastly, panel **(VII)** depicts well-dispersed Pro, Ser, Val, Ile CA-HA resonances that only appear in the mobile ssNMR



experiments and correlate well with the solution assignments of free MAP7. Particularly, Pro 59, Val 60, Ile 86, Val 87, Pro 153, and Pro 170 overlap. In addition, it is intriguing to note that the Gln CG-HG region is mainly visible in the dipolar spectrum. Interestingly we did not detect observe signals in the Gly region, although 3 Gly are at the end of the MAP7 MTBD sequence. Those residues might exhibit dynamics at intermediate time scales that escape detection in our ssNMR experiments ¹.

3D ssNMR data analysis

For the analysis of the 3D scalar spectrum (probing dynamic MAP7 residues in the complex) we observed good agreement with the solution-state assignments. Therefore, we were able to assign several residues of MAP7 MTBD in the MT-bound state (**Fig. 5.4A and 5.4C**). For Pro 59, Val 60, Leu 61, Val 63, Asp64, Leu 69, Glu 148, Pro 153, Gln 155, Asn 158, Arg 159 and Pro 170 resonances for both backbone and sidechains could be identified (**Fig. 5.4A and 5.5A**), while for Ala 70 and Ala 82 only CB was found. In addition, we could tentatively assign Ile 86 CG and CD, Thr 146 CA-CB, CG, Met 147 CA-CE, CE; for Lys 154 CD-CG and Leu 166 CD-CG. Intriguingly, all of these residues are located at the C- and N-terminus of MAP7 MTBD (**Fig. 5.5A**), in line with weak or no binding to MT for MAP7 residue Pro 59-Ala 70 and Glu 148-Pro 170. In addition, several resonances corresponding to residue types could be partly identified in the scalar CCH 3D. Namely, one Glu, Ser, Gln, Leu and two additional Arg (**Fig. 5.4A**). Comparing these residues with the MAP7 MTBD sequence, they may also reflect residues at the extreme N- or C-terminus. Furthermore we compared the overall abundance of non-overlapping resonance types to the number of resonances of that type present in the aforementioned terminal domains, suggesting that the experimental signal intensity observed in our scalar based experiments is in reasonable agreement with the relative occurrence of amino-acids in the protein segments Pro 59-Ala 70 and Glu 148-Pro 170 (**Fig. 5.5B, Fig. S5.4B**). Note that our spectral analysis estimates a larger fraction of flexible Leu side chains than present in the N- and C- terminal region, which would be compatible with sidechain motion even in the helical binding

140

region. For example, Leu 103 is located between tubulins and might therefore exhibit flexibility.

Analysis of putative MAP7 MTBD A83-V87 beta-strand

By verifying connections in the CAHA region of the dipolar spectrum corresponding to the aforementioned β -strand resonances, we could identify Ala, Glu, Arg and a CAHA correlation corresponding to Val, Ile or Thr (**Supplementary Fig. S5.4B**). The presence of an Ala is supported by the peak integral of the residue in the CCH spectra which exceeds the expected number of Ala in the MAP sequence. (**Fig. 5.5B and 5.5C**). The same is the case for Val. Therefore, the CAHA correlation attributable to Val, Ile or Thr mentioned above might be a Val (**Supplementary Fig. S5.4B, right**). Additionally, the resonance could be attributed to Ile 86 because there are two resonances observed for Ile 86 CB-HB and CG-HG in the dipolar 2D spectra, even though the MAP7 MTBD sequence contains only one Ile (**Fig. 5.4B**). Hence, this correlation remains unidentified. The residues that we identified for the β -strand resonances agree with residues Ala 83, Arg 84, Glu 85 and Ile 86, Val 87. These residues would be in line with the aggregation propensity for MAP7 evaluated by AGGRESCAN, which claims residues 84-89 to be aggregation-prone². Interestingly this region corresponds to the hinge, that was observed in the free MAP7 MTBD α -helix (residue 84-87) (³, Chapter 2). The rest of the aggregate could not be observed in the NMR spectra. This might be due to great heterogeneity or intermediate exchange dynamics.

Supplementary references

1. Schanda, P. & Ernst, M. Studying dynamics by magic-angle spinning solid-state NMR spectroscopy: Principles and applications to biomolecules. *Progress in nuclear magnetic resonance spectroscopy* **96**, 1–46 (2016).
2. Conchillo-Solé, O. *et al.* AGGRESCAN: a server for the prediction and evaluation of "hot spots" of aggregation in polypeptides. *BMC bioinformatics* **8**, 1–17 (2007).
3. Adler, A. Resonance Assignments of the microtubule-binding domain of the microtubule-associated protein 7 (MAP7), *Biomol NMR Assign* (2023), in press. (2023).



Chapter 6

Analysis of the dynamic interaction of Tau and microtubules

Adapted from:

Analysis of the dynamic interaction of Tau and microtubules. Agnes Adler, Hanneke Smedes, Salima Bahri, Hugo v. Ingen, Marc Baldus*, *in preparation*

Contribution: AA carried out protein purification with contribution of HS, MTs assemblies, the solid-state NMR measurements with the help of SB



Abstract

Tau is a microtubule-binding protein that is essential for the proper assembly and stabilization of microtubules (MTs). MTs are responsible for many cellular functions, including cell motility, cell division, and intracellular transport. Tau has been shown to be involved in a number of neurodegenerative diseases, including Alzheimer's disease, frontotemporal dementia, and Parkinson's disease. Disturbing the interaction of Tau with MTs may be related to the development of Alzheimer's disease. However, the exact role of the Tau-MTs interaction in the disease process is not yet fully understood. A key challenge in studying this interaction is the disordered nature of the Tau protein. Here we aim to shed light on this dynamic interaction at atomic resolution by combining solution- and solid-state nuclear magnetic resonance spectroscopy (NMR). We obtained a model with increased rigidity towards the later repeat regions of Tau and pinpoint the interaction side of the carboxy-terminal tails of tubulin to Tau.

Introduction

Microtubules (MTs) are hollow structures formed by the protein tubulin. They are a key component of the cytoskeleton. α - and β -tubulin heterodimers assemble in an α/β -alternating manner to form a polar protofilament with α -tubulin exposed on the so-called minus end and β -tubulin on the plus end. MTs are essential in almost all cellular processes, such as cell division, motility, shape, and transport ¹. MT structure, dynamics, and mechanics are modulated by tubulin isoforms and post-translational modifications (PTMs) together with a large repertoire of regulatory proteins. A central location for PTMs are the tubulin's carboxy-terminal tails (CTTs) ². These highly negatively charged, unstructured regions comprise residues S439 to Y451 in the α -tubulin tail (α -CTT) and residues D427 to A444 for the β -tubulin tail (β -CTT) in the most common HeLa S3 isotype (**Fig. 6.1A**). The CTTs are exposed at

the MTs surface and therefore in proximity to the binding sites of most MT-associated proteins (MAPs) and MT motor proteins such as kinesin-1^{3,4}. MAP proteins regulate MTs and allow MTs fine-tuning through complex interactions⁵ and several MAPs stabilize the function of MTs⁶.

Although data has been published discussing the importance of the highly negatively charged CTTs for interaction of kinesin 1 with MTs^{3,4}, much less is known about the specific binding sites and modes for MAPs. These proteins usually have a positive net charge in their microtubule-binding domain (MTBD), enabling electrostatic interactions with the more negatively charged MTs surface.

The protein Tau interacts strongly with the exposed MT surface. Disruption of Tau binding to MTs is associated with a number of neurodegenerative diseases, including Alzheimer's disease, frontotemporal dementia, and Parkinson's disease⁷. Therefore, the investigation of this interaction is of high interest and numerous studies have been performed. Tau belongs to the class of intrinsically disordered proteins (IDP) and is found to maintain a disordered character upon binding to MTs⁸. The human central nervous system expresses six Tau isoforms produced by alternative splicing. The C-terminal part of Tau is composed of three or four imperfect 18-amino acid repeat regions R1-R4^{9,10}. These MT-binding repeats are flanked N-terminally by the proline-rich P2 region and C-terminally by the pseudo repeat R' region (**Fig. 6.1B**).

A number of studies showed that Tau interacts with and stabilizes MTs at the interface between the tubulin heterodimers¹¹⁻¹⁴. With its near-atomic view of the complex, cryo-EM also revealed that the MT-binding repeats adopt an extended structure along the protofilament¹². Recent NMR experiments suggest the same for the R' repeat domain¹⁵. Meta-analysis cryo-EM found MT-bound Tau to contain highly dynamic regions and suggested both weak and strong binding residues in the repeat regions¹⁶, raising the idea of an asymmetric zipping mechanism. In this process, Tau is thought to be released from the MTs from the P2 region. Previous



Chapter 6

solution-state NMR and ITC experiments on an α -CTT peptide gave first insights into the interaction between CTTs and Tau¹⁷. Despite these advances, additional information is needed to understand the stabilization of MTs by Tau due to the dynamics of the studied system.

A

HeLa S3 CTT main form

α -tubulin CTT 439 SVEGEGEEEGEEY 451

β -tubulin CTT 427 DATAEEEEEDFGEEAEAAA 444

B

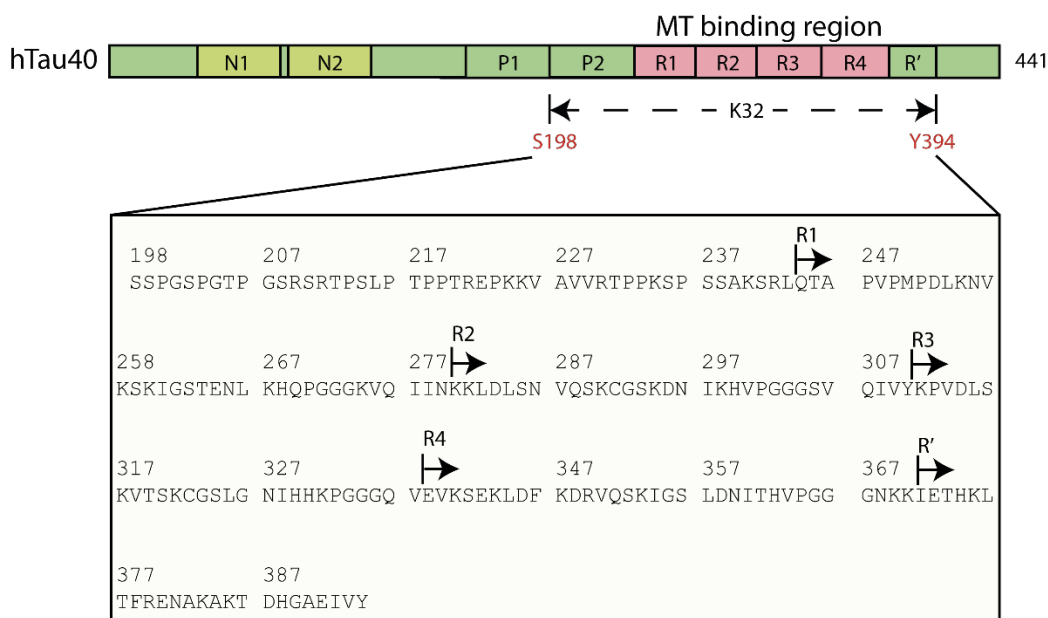


Fig. 6.1: Domain organization and sequences (A) Sequences of the two tubulin C-terminal tails (CTT) that are most common in HeLa S3 cells. **(B)** Domain organization of the longest Tau isoform hTau40. The microtubule binding region (MTBR) comprises the four repeat regions (R1-R4). The amino acid sequence of K32 is depicted below it shows the P2 N-terminal to the MTBR, the MTBR and R' in the C-terminal domain.

Here, we investigate the interaction of a Tau construct comprising the P2, R1-R4 and R' region (Tau K32, Ser¹⁹⁸-Tyr³⁹⁴) with MT, with a special focus on Tau binding to the tubulin CTTs. Using a combination of ¹H-detected solid-state NMR, solution-

state NMR titrations and fluorescence anisotropy, we gained residue-specific insights into the binding interface between Tau and MT.

Results

NMR Analysis suggests Tau binding to MTs via R1-R' domains, but not with the P2 region

Despite previous efforts¹⁵ obtaining complete de-novo ssNMR assignments of tau bound to MTs remains challenging. For this reason, we used solution-state NMR assignments obtained on Tau K32 as a spectroscopic reference. In detail we assigned 60 % of the Ca, Cb, Ha and Hb chemical shifts with 3D CbCaCoNH and HbHaCoNH and 2D NH-HSQC and CH-HSQC experiments on the basis of the NH-assignment by Mukrasch et al.¹⁸ (**Fig. 6.2A, Supplementary Fig. S6.1, Supplementary table 6.1**).

To investigate the binding region of Tau K32 to MTs we measured dipolar and scalar (J-coupling)-based magic-angle spinning (MAS) solid-state NMR spectra as it was previously used for the study of large biomolecules^{19–21}. For this purpose, we prepared a sample in which [¹³C-¹⁵N] Tau K32 was mixed with Taxol-stabilized MTs at a molar ratio of 1 to 1 of Tau K32 to tubulin (**Fig. 6.2B, see Materials and Methods Chapter 6**).



Chapter 6

A

198	207	217	227	237	247
CAHA	SSPGSPGTP	GSRSRTPPSLP	TPPTREPKKV	AVVRTPPKSP	SSAKSRLQTA
CBHB	SSP SP TP	SRSRTPPSLP	TPPTREPKKV	AVVRTPPKSP	SSAKSRLQTA
257	267	277	287	297	307
CAHA	KSKIGSTENL	KHQPGGGKVQ	IINKKLDLSN	VQSKCGSKDN	IKHVPGGGSV
CBHB	KSKI STENL	KHQP KVQ	IINKKLDLSN	VQSKC SKDN	IKHVP SV
317	327	337	347	357	367
CAHA	KVTSKCGSLG	NIHHKPGGGQ	VEVKSEKLDLF	KDRVQSKIGS	LDNITHVPGG
CBHB	KVTSKC SLG	NIHHKP Q	VEVKSEKLDLF	KDRVQSKI S	LDNITHVP
377	387				
CAHA	TFRENAKAKT	DHGAEIVY			
CBHB	TFRENAKAKT	DH AEIVY			

B

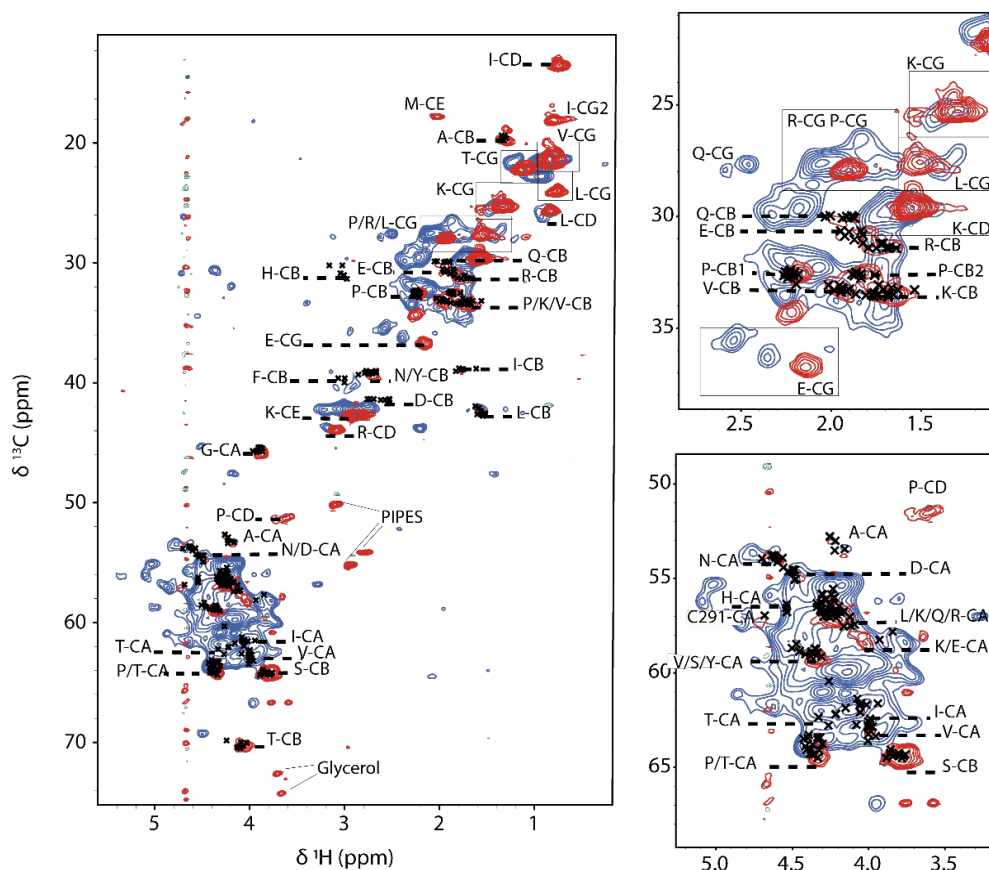


Fig. 6.2: 2D dipolar and scalar ssNMR of [^{13}C - ^{15}N] Tau K32 bound to Taxol-stabilized MTs (A) Solution-state assignments of Tau K32 of CAHA (green) and CBHB (purple) resonances. (B) Overlay of scalar (flexible) CH (red) and dipolar (rigid) CH (blue) based ssNMR experiments with the solution-state CA-HA/ CB-HB assignments from Tau K32 (black crosses).

Many correlations observed in the scalar CH spectrum (**Fig. 6.2B**, red) were in good agreement with the solution-state assignments (**Fig. 6.2B**, black crosses) and the CH-HSQC spectrum of Tau K32 in solution (**Supplementary Fig. 6.2**) in line with tau regions that do not bind to MTs and still exhibit fast tumbling similar to an isotropic solution in the complex (**Supplementary methods chapter 6**). The dipolar CH spectrum (**Fig. 6.2B**, blue) gives rise to broader signals with little or no signal observed for Met, Ala, Pro and Thr (**Supplementary methods chapter 6**).

Analysis of 3D solid-state NMR spectra

As Tau is an intrinsically disordered protein, spectral dispersion in the 2D spectrum is limited and therefore makes an in-depth analysis challenging. To further increase spectral resolution and to obtain residue-specific correlations, we hence turned to 3D ssNMR, recording scalar- and dipolar-CCH experiments. Based on the recorded spectra (**Fig. 6.3**), specific residues were identified on a flexible- or rigid-motion timescale.



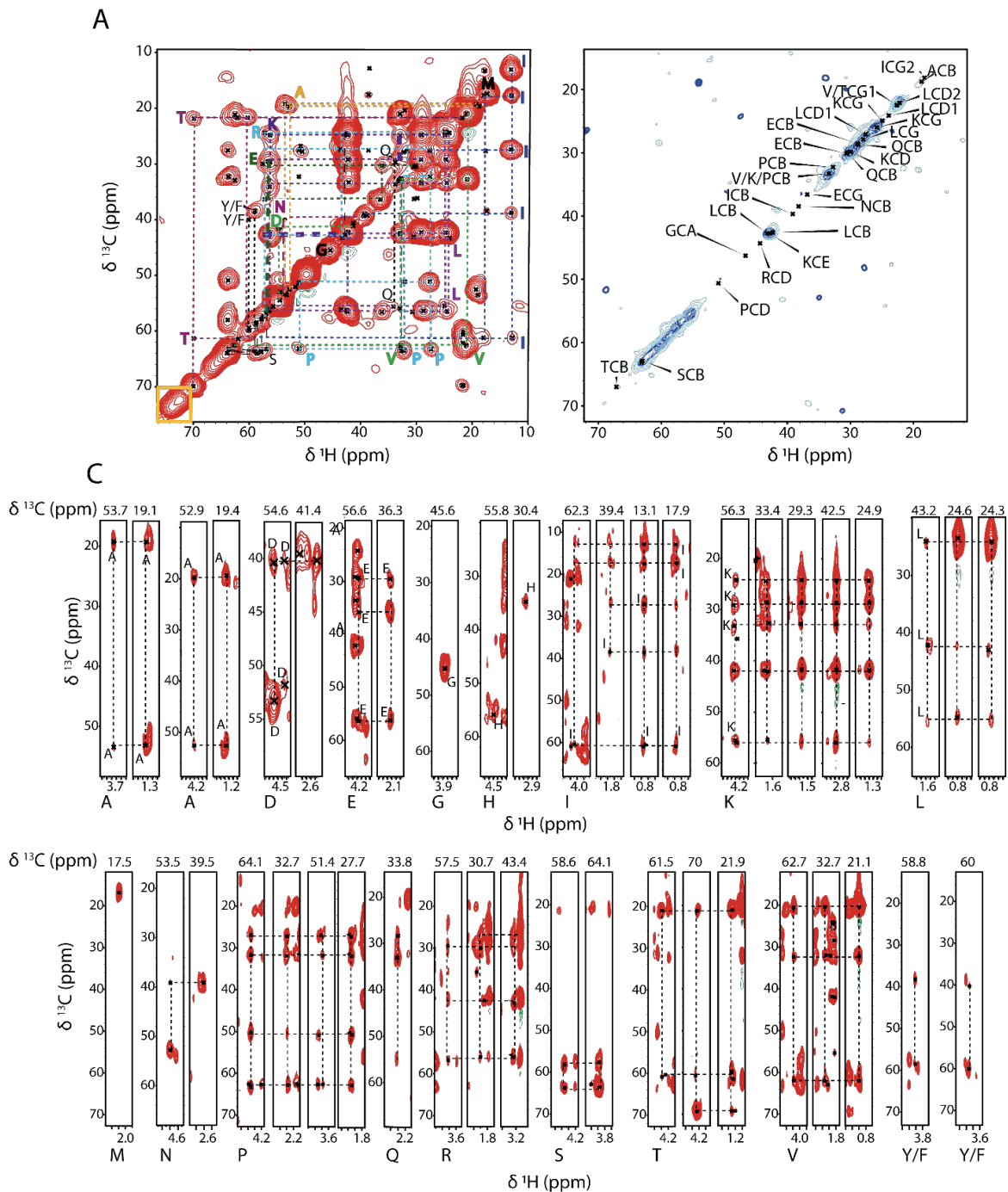


Fig. 6.3: ssNMR of [^{13}C - ^{15}N] Tau K32 bound to Taxol-stabilized MTs (A) CC-plane of 3D 22 ms DIPSI with assigned resonances. (B) CC-plane of 3D 1.7 ms RFDR with assigned resonances (dark blue) overlaid with CC-plane with 3.4 ms RFDR (light blue). (C) Assigned strips of the scalar 3D CCH.

We first analysed the 3D scalar-CCH spectrum (**Fig. 6.3A and 6.3C**) and identified CAHA and CBHB correlations for all amino-acid types except for Gln and Cys (**Supplement table 6.2**) which can only be found in the repeat regions of Tau K32. Residue-specific assignments within a given residue type were hindered by spectral overlap. Nonetheless, we were able to attentively assign several CAHA and CBHB correlations which mainly resides in the P2 region (**Supplementary methods chapter 6**).

To further analyse the spectra, we estimated the abundance of a residue type by integrating the corresponding correlations/spectral regions (**Fig. 6.3**) and normalized the resulting intensity by the overall number of residues of a particular amino-acid type in the Tau K32 sequence (**Fig. 6.4A**). The residue type abundance observed in the scalar spectrum is in good agreement with the residue frequency of the P2 region with additional dynamic residues found in R1 (**Supplementary methods chapter 6**).

Next, we turned to the dipolar-CCH spectrum (**Fig. 6.3B and Supplementary Fig. 6.3**). Residues observed in this spectrum can be assumed to be involved in the binding of Tau K32 to MTs because they rigidify upon interaction. Intriguingly, even though C-H magnetization is transferred, no C-C cross peaks appeared. This observation would be consistent with remaining Tau dynamically disorder even in the bound state. Increasing the transfer (mixing) time from 1.7 ms to 3.4 ms didn't result in the appearance of cross peaks (**Fig. 6.3B**).

Nonetheless, we were able to assign resonances to Ala, Asp, Glu/Gln, Gly, His, Ile, Lys, Leu, Asn, Pro, Gln, Arg, Ser and Thr residues based on their characteristic C-C-H connectivity (**Fig. 6.3B and Supplement table 6.3**). Their chemical shifts are distinct from solution-state assignments prohibiting sequence-specific assignments. El Mammeri et al. ¹⁵ recently published dipolar-based ssNMR data on Tau K32-MTs complexes obtained at a sample temperature of 278 K which is about 20 degrees below our experimental settings (see Material and Methods). Additionally, their



construct extends ours by 5 residues. These experiments detected similar residues to our current study and reported partial resonance assignments for the R' (I354-P397) stretch. Despite small differences, our data is in line with El Mammeri et al. (**Supplementary methods chapter 6 and Supplementary table 6.3**) which would be compatible with the notion that these residues are located in the R4 and R' region. That we didn't observe cross peaks in our dipolar CCH spectrum, while they observed them, might be rooted in several differences in sample conditions. Firstly, a higher measurement temperature might lead to greater flexibility, and secondly, we measured with a 150 μ s cross polarization transfer time (compared to 800 μ s), which could result in the detection of completely rigid entities and connectivity.

In the case of the scalar CH, we identified the same resonances as El Mammeri et al. (**Supplementary Fig. 6.4**). However, with the help of the 3D CCH, we were able to clarify their findings by showing that the flexible residues are located in P2 and R1. Furthermore, we were able to add Asp and Tyr/Phe to the kinds of flexible residues. For further analysis, we turned to quantitatively analysing the dipolar 2D CH spectrum (**Fig. 6.4C**). The residue kind abundance gives rise to a pattern of rigid residues in R'-R4 (**Supplementary methods chapter 6 and Fig. 6.4E**).

Comparing the proportion of CAHA and CBHB being flexible and rigid we found an approximately 1 to 2 ratio (50:110) between dynamic and rigid CAHA correlations. For the CBHB also around 50 flexible residues could be found, while for the dipolar the number decreases to 35. This shows that Tau K32 remains largely dynamic, even in the fully bound form. It is interesting to note that the amount of CAHA scalar resonances adds up to only slightly more than the number of residues in the P2 region, which confirms a partially dynamic R1 and R2 region and the flexible C terminus. The 110 rigid residues are in accordance with this theory of intermediate dynamics in about a quarter of the protein.

Analysis of the dynamic interaction of Tau and microtubules

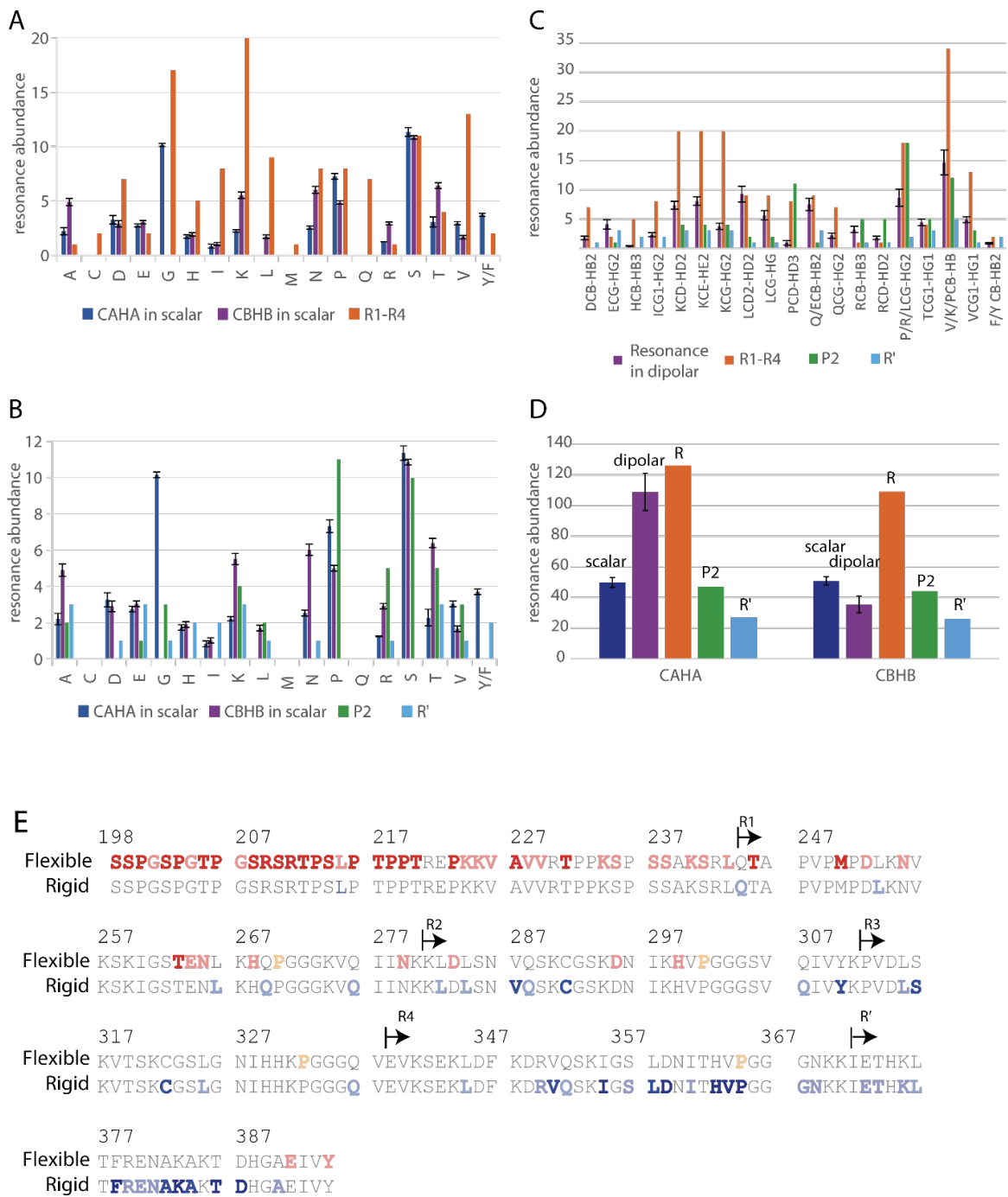


Fig.6.4 . Analysis of 3D CCH ssNMR experiments. All error bars were derived from the signal-to-noise ratios. **(A)** Comparison of residue type number in R1-R4 of Tau K32 to the number of found residues in the scalar CCH spectrum. **(B)** Residue abundancy in the scalar CCH spectrum compared to the amount of a residue type in P2 and R'. **(C)** Plot of dipolar CH signal abundance compared to residue type number in different Tau K32 regions. The

peak integration was performed on the dipolar 2D CH. **(D)** Comparison of dipolar and scalar CAHA and CBHB signal intensity. **(E)** Distribution of flexible (red) and rigid (blue) residues in the Tau K32 sequence. Higher confidence assignments are coloured with strong blue and red, while more ambiguous ones are in light red and blue. In yellow are residues suggested to have intermediate dynamics.

Tubulin's carboxy-terminal tails interact with their EGE motif to Tau K32

To probe mobile MTs protein segments including the carboxy-terminal tubulin tails (CTTs), we carried out scalar-based ssNMR experiments on [^{13}C - ^{15}N]-Taxol stabilized MTs in the presence and absence of Tau K32 (**Fig. 6.5A**).

As shown previously by Luo et al. 2D ^{15}N -HSQC spectra contain several signals with limited spectral dispersion and can largely be assigned to the CTTs²². With the help of these assignments, we could observe a signal reduction for certain residues of the CTTs (**Fig. 6.5B**). Strong signal attenuation is found in G, as well as E of the EGE motif of the α -CTT. Additionally, Y451 and other flexible E residues seem to become more rigid upon Tau K32 binding. In contrast, little change is observed in the signal intensity of G in the FGE motif, and A residues. The later residues are only found in the β -CTT (Fig. 4B bottom). Note that the scalar spectrum also contains signals from R-side chains, which are rigidified upon MTs binding in line with earlier observations. These observations strongly suggest that the α -CTT is involved in the interaction, while the β -CTT is largely unaffected. Additional scalar CH-spectra of MTs [^{13}C - ^{15}N]-Taxol stabilized MTs with and without Tau K32 are given in **Supplementary Fig. 6.5**.

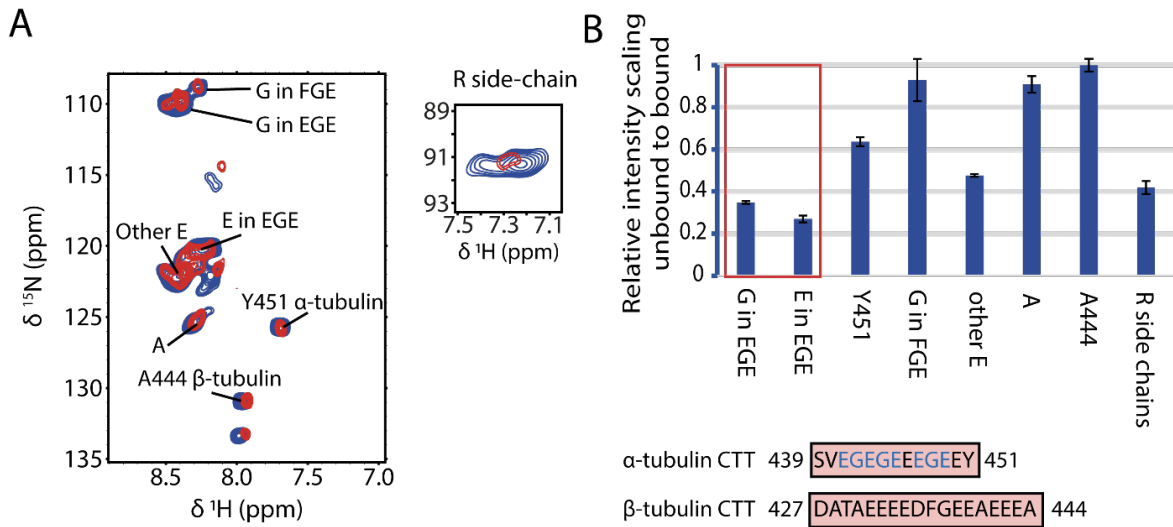


Fig. 6.5: Interaction of $[^{13}\text{C}-^{15}\text{N}]$ Taxol-stabilized MTs C-terminal tails with Tau K32 (A) Comparison of 2D ^1H ^{15}N -HSQC spectra obtained from $[^{13}\text{C}-^{15}\text{N}]$ -Taxol-stabilized MTs (blue) and unlabelled Tau K32 in complex with $[^{13}\text{C}-^{15}\text{N}]$ -Taxol-stabilized MTs (red). **(B)** Top: Signal intensity ratios of resolved peaks in ^1H ^{15}N -HSQC between Tau K32 bound Taxol-stabilized MTs and free ones. Bottom: Sequence of the CTTs with the EGE motifs highlighted.

Tau K32 interacts with the tubulin carboxy-terminal tails through its sequence prior to the PGGG motif of each repeat region

To study the interaction of Tau K32 with the carboxy-terminal region of microtubules, we prepared peptides comprising residues S439-Y451 and D427-A444 from HeLa S3 α - and β -tubulin. By gradually adding these peptides to $[^{13}\text{C}-^{15}\text{N}]$ -Tau K32 in solution, we were able to observe specific chemical-shift changes (**Fig. 6.6**). Interestingly, we discovered that four regions at the end of each repeat, that are located just before the PGGG motif, are sensitive to the addition of CTT peptides. The shifting residues in these regions share a common sequence of K/H/T-H-Q/V/K. The chemical shift perturbation observed upon adding α -CTT was about twice as large as that observed with β -CTT (**Fig. 6.6B**). In addition to these changes, smaller perturbations were also seen in the P2-motif and the R'-region. Notably, solution-state NMR titrations with intact MTs produced a similar shift pattern (**Fig. 6.6C**) and



a similar pattern was previously observed by Mukrasch et al.¹⁸. The addition of MT, in contrast to the CTTs leads to signal attenuations in the R-regions (**¹⁸ and Supplementary Fig. 6.6**). Removing the tails through subtilisin cleavage resulted in a loss of the chemical shifts in the aforementioned regions (**Fig. 6.6C and Supplementary Fig. 6.7**). The electrostatic character of the interaction between the highly negatively charged α -CTT and the (positively)-charged interacting residues of Tau K32 was confirmed by repeating the experiment at higher salt concentrations (**Supplementary Fig. 6.6**) where chemical shift perturbations disappeared, confirming our previous findings. With the help of fluorescence anisotropy we obtained a dissociation constant of $140 \mu\text{M} \pm 34 \mu\text{M}$ of tau to tails (**Supplementary Fig. 6.6**).

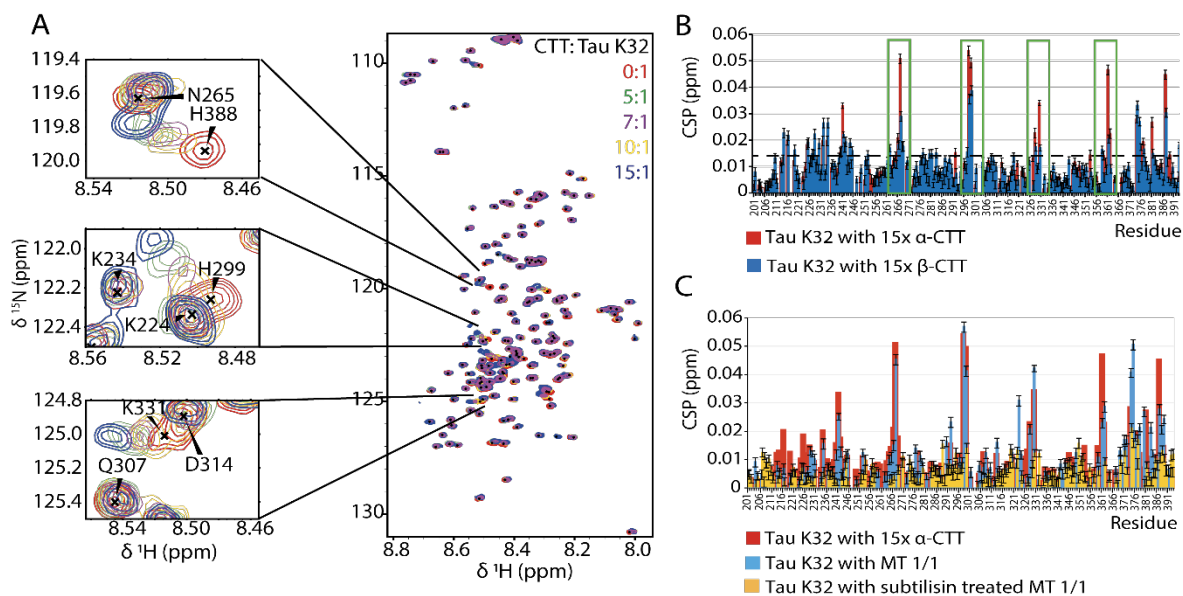


Fig. 6.6: Interaction of [¹³C-¹⁵N]-Tau K32 with Tubulin C-terminal tails (A) Titration of increasing concentrations of the α -CTT to Tau K32 in solution-state NMR (40 mM NaPi, 50 mM NaCl, pH 6.5). **(B)** Chemical shift perturbations observed upon α - and β -CTT peptide binding in Tau K32. Regions that are similar in the four repeat regions and exhibit a noticeable perturbation are highlighted by a green box. **(C)** CSP of Tau K32 upon MTs addition (blue) and α -CTT addition (red) compared to the addition of subtilisin treated MTs (yellow).

Discussion

Here we investigated the binding register and the tubulin carboxy-terminal tail interaction of Tau K32 and MT. Our study indicates that Tau preserves a flexible character even upon binding, forming a fuzzy MT-Tau complex without defined binding boundaries. This is in line with previous experiments and modelling approaches^{23,24}.

The interaction of the MT binding region of Tau (Tau K32) with MTs seems to be mediated by its R and R' regions, while the N-terminal P2 region is flexible and does not contribute to binding (**Fig. 6.7**). Our data suggest that the first two of the R regions seem to be flexible. In agreement with El Mammeri et al.¹⁵, we observe rigidity in R4 and R' in the complex. Also, Kadavath et al. observed the binding of R' to the MTs²⁵. In our analysis, however, the R3 region also seems to be overall rigid, while the data for the last 5 residues of R' are not conclusive. A possible explanation could be the higher temperature at which we conducted the experiments and the 5 residues shorter construct on the C-terminus, which truncates R'. Our data is also in line with previous studies showing the binding of the different repeat regions to Tau, proposing decreasing heterogeneity from R1 to R4²⁴. This would speak against the notion that all repeat regions are of equal importance for the Tau-MT binding¹². Nonetheless, various previous experiments emphasize that all tau regions contribute similarly to the binding affinity^{26–29}, which suggests a cooperative interaction.

Moreover data on mutations, for example, P301L, K369I and E372G hint at a more complex binding mechanism^{30–33}. This complex interaction mode might be important for the regulation of the Tau binding to MTs. The highly evolutionary-conserved R' region³⁴ was seen to increase the stoichiometry of the Tau-tubulin complex, suggesting its importance in differentiating itself from other R regions³⁵. These observations would be in line with our observed R'-MT interaction.



Additionally, the binding of more than the R' and R4 region might explain the binding of Tau to multiple tubulin dimers, as it has been shown that constructs with repeat regions and R' enhance cross-linking^{8,36,37}. The complexity of the interaction is supported by several studies observing the binding of Tau to MTs in a biphasic manner. These findings suggest that Tau first binds to one/two tubulin dimers, to later extend to several additional heterodimers^{23,24,38}. Such a process would be supported by the tubulin carboxy-terminal tails (CTTs) interactions with all four repeat regions as seen in our experiments (**Fig. 6.7B**).

Previous studies showed a 3x decrease of binding affinity upon CTT removal^{39,40} and solution-state NMR experiments identified CTT Glu 441 was influenced by Tau binding³³. This residue is located at the beginning of the α -CTT's EGE sequence. With our observation of the importance of the K/H/T-H-Q/V/K sequence, we build on the finding that the His plays a significant part in Tau-MTs binding⁴¹. Consistent with our observation of an electrostatic interaction, Charafeddine et. al found that increased intracellular pH decreases Tau binding in cancer cells⁴².

Taken together our results (**Fig. 6.7**) are in a good agreement with previous ssNMR studies¹⁵. The presence of Taxol might slightly alter the binding behaviour of Tau K32^{43,44}. In addition, several studies suggest that different phases of Tau might coexist on the MT surface, possibly leading to island formation but also diffusion along the protofilament⁴⁵⁻⁴⁷. Nevertheless, our results may aid therapeutic efforts to treat Alzheimer's disease by compensating for loss of Tau binding⁴⁸ and to study the effect of CTT PTMs that are associated with ADs⁴⁹.

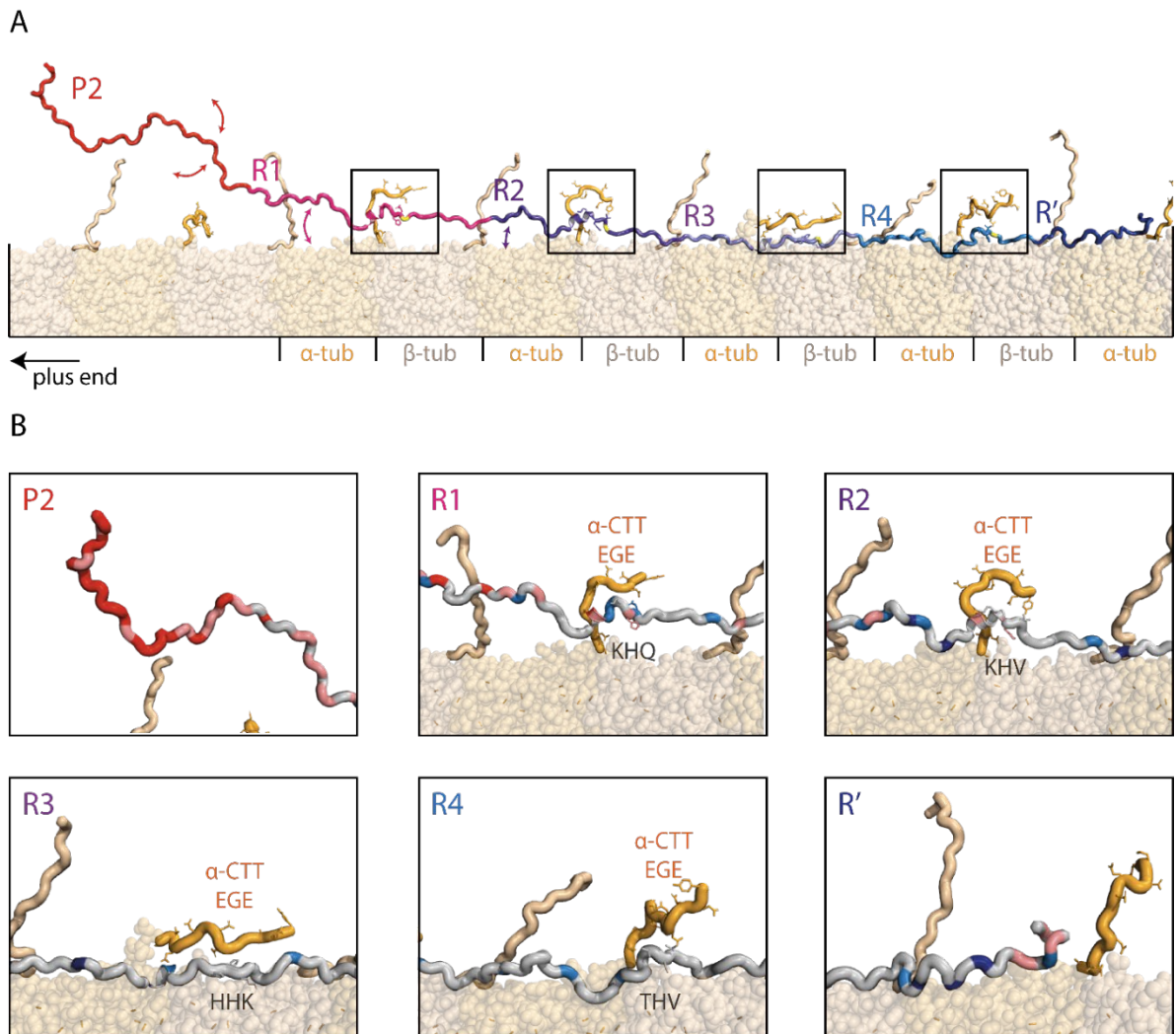


Fig. 6.7: Model of Tau K32 binding to MTs (modified on basis of the Brotzakis et al. modelling²⁴). **(A)** Tau K32 P2 (red) region stays dynamic, while the R1 (pink) and R2 (purple) region exhibit some flexibility and R3 (violet), R4 (light blue) and most of R' (dark blue) are tightly binding. The boxes highlight regions of CTT and Tau K32 interaction. The P of the PGGG motif is coloured in yellow. **(B)** The schematic representations of the Tau K32 regions. In red are residues found to be flexible, in rose residues that are probably flexible, in light blue those that are probably rigid and in blue rigid ones. The CTTs-Tau K32 binding site is highlighted by depicting the side-chains and the interacting residues.



Material and Methods

α - and β -CTTs, α - and β -tubulin and isotopically labelled microtubules Lyophilized CTTs with the sequence SVEGEGEEEGEEY and DATAEEEEEDFGEEAEEEE were purchased from Sigma-Aldrich in powder form. >99 % pure, lyophilized tubulin powder from porcine brain was purchased from cytoskeleton. [^{13}C - ^{15}N] -labelled microtubule were purified from HeLa S3 cells, according to the protocol as published by Luo et al. (2021) ²⁰.

Expression of Tau K32

The gene encoding Tau K32 inserted in a pNG2 plasmid was kindly gifted to us by the Mandelkow group of the German Center for Neurodegenerative Diseases, Bonn, Germany. The vector was transfected in *E. coli BL21 (DE3)* competent cells and expression was induced in M9 minimal media with 0.3 mM isopropyl-D-thiogalactopyranoside (IPTG) when the OD₆₀₀ reached 0.6 for 16 h at 20 °C.

Purification of Tau K32

[^{13}C - ^{15}N] labelled Tau K32 was purified according to the protocol described by Barghorn et al. (Barghorn et al. 2005) Small adaptations to the protocol are described below. Firstly, 1 mM NaN₃ was added to the buffers, to minimize the risk of bacterial growth in them. Moreover, cells were lysed either with a French pressure cell as described previously or by sonication. The cation exchange chromatography that was utilized was a HiTrap SP column of 5 mL and for gel filtration chromatography a HiLoad 26/60 Superdex 75 prep grade column. The protein concentration was measured by a BCA assay with a Thermo Scientific Pierce BCA Protein Assay Kit.

MTs purification

The purification of isotopically labelled MTs was performed as previously described by Yanzhang et al. ²⁰.

Fluorescence Anisotropy

0.1 mg α -CTT was dissolved in 100 μ L NMR buffer (40 mM NaPi pH 6.5, 150 mM NaCl, 1 mM DTT) and the pH adjusted to 8.3 by adding 30 μ L of 0.5 M Na_2HPO_4 . The concentration of the α -CTT was measured with a BCA assay (the same as previously mentioned). 40 mM NaPi, 150 mM NaCl, pH 8.3 was added to obtain a 500 μ M α -CTT concentration. From here, the experiment was performed in the dark due to the light-sensitivity of NHS-fluorescein. 4 times molar ratio NHS-fluorescein to α -CTT was incubated for 2 hours at room temperature, inverted, whilst protected from light. The NHS-fluorescein-labelled α -CTTs was dialyzed against NMR buffer (40 mM NaPi pH 6.5, 150 mM NaCl, 1 mM DTT) overnight at 4 °C in a 1 kDa cut-off dialysis tube, with a buffer exchange after 2 hours, to remove unbound NHS- fluorescein. By measuring the absorbance at 494 nm, combined with the extinction coefficient of 68/M*cm and the concentration of α -CTT from the BCA the concentration of labelled α -CTT was calculated. A dilution series of Tau K32 resulting in a concentration range from 200 to 0 μ M in a 384-well plate was prepared and NHS- fluorescein-labelled α -CTT to concentration of 1 μ M was added to each well. We measured the fluorescence anisotropy at 494 nm with a plate reader and analysed the results with Dynafit ⁵⁰.

Subtilisin treatment

Subtilisin was kindly provided by the Akhmanova group at Utrecht University. 20 mg/mL tubulin was polymerized for 30 min at 37 °C in PBS (37 mM NaCl, 3 mM KCl, 10 mM Na_2HPO_4 , 2 mM KH_2PO_4 , pH 7.4) the presence of 1 mM GTP and 10 μ M paclitaxel (taxol, SIGMA). Subsequently, subtilisin was added in a 1 to 5 ratio to the MTs and the cleavage was performed for 2 h at 30 °C. The reaction was inhibited by adding 1 mM phenylmethylsulfonyl fluoride (PMSF). For harvesting the tail-less MTs



the sample was spun at 200.000 xg, 30 min, 30 °C. The pellet was resuspended to 20 mg/mL tubulin with PBS (37 mM NaCl, 3 mM KCl, 10 mM Na₂HPO₄, 2 mM KH₂PO₄, pH 7.4) supplemented with 1 mM GTP and 10 μM paclitaxel (taxol, SIGMA).

MTs polymerization and preparation of solid-state NMR samples

Lyophilized tubulin (Cytoskeleton, Inc.) was solubilized in Brb80 buffer (80 mM PIPES, 2 mM MgCl₂, 1 mM EGTA, pH 6.8, 1 mM NaN₃, 1 mM DTT, pH 6.8), to a final concentration of 2 mg/mL. The polymerization was induced by adding 1 mM Guanosine-5'-triphosphate (GTP) and incubation for 15 minutes at 30 °C. Then, 20 μM paclitaxel (taxol, SIGMA) was used to stabilize the MTs and incubation took place for another 15 minutes at 30 °C. The MTs were spun down at 180.000 xg (Beckman TLA-55 rotor) for 30 minutes at 30 °C and the pellet was resuspended in warm Brb80 buffer with 20 M paclitaxel. Subsequently, a 1 to 1 ratio of [¹³C-¹⁵N] Tau K32 was added. The interaction partners were incubated for 30 minutes at 37 °C. In the following isotopically labelled Tau K32 in complex with MTs was separated from the unbound, non-polymerized fraction by centrifugation at 180.000 xg (Beckman TLA-55 rotor) for 30 minutes at 30 °C. Afterwards, the pellet was washed with 40 mM phosphate buffer, pH 7, with protease inhibitor (as described earlier) and 1 mM NaN₃, without disturbing the pellet. A 1.3 mm rotor was packed with the pellet.

Solution-state NMR measurements and analysis

Solution-state NMR measurements for titration with α-CTTs or MTs (subtilisin treated or not) were performed in PBS (37 mM NaCl, 3 mM KCl, 10 mM Na₂HPO₄, 2 mM KH₂PO₄, pH 7.4) or NMR buffer buffer (40 mM NaPi pH 6.5, 150 mM NaCl, 1 mM DTT) with 1 mM NaN₃ and 1 mM DTT, in 10 % D₂O. Two-dimensional (2D) ¹H-¹⁵N-TROSY experiments of starting concentration 33 μM ¹⁵N-labelled Tau K32 were recorded at 278 K on a 600 MHz Bruker Avance III spectrometer.

For solution-state NMR assignments, a 90 μM sample of U-¹⁵N, ¹³C-labelled Tau K32 in NMR PBS buffer supplemented with 5 % D₂O was used to acquire NMR spectra at 278 K on a Bruker Avance III HD 600 spectrometer equipped with triple resonance

cryogenic-probes. CAHA and CBHB resonance assignments were derived from ^1H - ^{15}N TROSY, ^1H - ^{13}C echo-antiecho constant time HSQC, CBCA(CO)NH, HBHA(CO)NH and (H)C(CO)NH experiments.

All spectra were processed using the Bruker TopSpin 3.6.2 software. Chemical shifts were referenced via the water resonance. Typical processing parameters were utilized, with apodization with cosine-squared window functions in all dimensions and doubling of the time domain signal by linear prediction in the indirect ^{15}N and ^{13}C dimensions. The spectra were analysed using POKY from NMRFAM-Sparky ⁵¹.

Solid-state NMR measurements and analysis

Bruker Avance III 700 MHz spectrometer equipped with a 1.3 mm rotor was used to measure NMR measurements on [^{13}C - ^{15}N]-Tau with Taxol-stabilized MTs at 55 kHz MAS with a set temperature of 260 K, resulting in a real temperature of approximately 299 K. The experiments were carried out using a $^1\text{H}/\text{X}/\text{Y}$ triple-resonance MAS probe. Using 2D hCH and 3D hCCH correlations with 0 ms and 22 ms DIPSI mixing times, scalar-based correlation experiments were conducted (Bahri et al., submitted) ⁵². Dipolar-based signals were detected with cross-polarization (CP) steps with an amplitude ramp of 80-100 % on ^1H and 13 kHz PISSARO decoupling during detection periods ⁵³. A RFDR mixing time of 0 ms, 1.7 ms, and 3.4 ms was used for the dipolar 2D hCH and 3D hCCH experiments. Mississippi was used for water suppression ⁵⁴. Bruker's TopSpin 3.6.2 software was used to process all data. Data were zero-filled and EM window functions were applied with LBs of 150 for dipolar spectra and a Qsin window function for scalar spectra. The sine bell shift was 2. Linear prediction in the indirect ^{13}C dimensions was utilized with a coefficient of 32 for dipolar spectra. Chemical shifts were referenced via the water resonance. The spectra were analysed using POKY from NMRFAM-Sparky ⁵⁵.



References

1. Nogales, E. Structural insights into microtubule function. *Annual review of biochemistry* **69**, 277–302 (2000).
2. Wloga, D., Joachimiak, E., Louka, P. & Gaertig, J. Posttranslational modifications of tubulin and cilia. *Cold Spring Harbor perspectives in biology* **9**, a028159 (2017).
3. Sataric, M. V., Sekulic, D. L., Zdravkovic, S. & Ralevic, N. M. A biophysical model of how α -tubulin carboxy-terminal tails tune kinesin-1 processivity along microtubule. *Journal of Theoretical Biology* **420**, 152–157 (2017).
4. Skiniotis, G. *et al.* Modulation of kinesin binding by the C-termini of tubulin. *The EMBO Journal* **23**, 989–999 (2004).
5. Bodakuntla, S., Jijumon, A., Villablanca, C., Gonzalez-Billault, C. & Janke, C. Microtubule-associated proteins: structuring the cytoskeleton. *Trends in cell biology* **29**, 804–819 (2019).
6. Hirokawa, N. Microtubule organization and dynamics dependent on microtubule-associated proteins. *Current opinion in cell biology* **6**, 74–81 (1994).
7. Muralidar, S., Ambi, S. V., Sekaran, S., Thirumalai, D. & Palaniappan, B. Role of tau protein in Alzheimer's disease: The prime pathological player. *International journal of biological macromolecules* **163**, 1599–1617 (2020).
8. Kadavath, H. *et al.* Tau stabilizes microtubules by binding at the interface between tubulin heterodimers. *Proc Natl Acad Sci U S A* **112**, 7501–7506 (2015).
9. Goode, B. L. *et al.* Functional interactions between the proline-rich and repeat regions of tau enhance microtubule binding and assembly. *Molecular biology of the cell* **8**, 353–365 (1997).
10. Kolarova, M., García-Sierra, F., Bartos, A., Ricny, J. & Ripova, D. Structure and pathology of tau protein in Alzheimer disease. *International journal of Alzheimer's disease* **2012**, (2012).
11. Kadavath, H. *et al.* Tau stabilizes microtubules by binding at the interface between tubulin heterodimers. *Proceedings of the National Academy of Sciences* **112**, 7501–7506 (2015).
12. Kellogg, E. H. *et al.* Near-atomic model of microtubule-tau interactions. *Science* **360**, 1242–1246 (2018).
13. Tapia-Rojas, C. *et al.* It's all about tau. *Progress in neurobiology* **175**, 54–76 (2019).
14. Venkatramani, A. & Panda, D. Regulation of neuronal microtubule dynamics by tau: Implications for tauopathies. *International journal of biological macromolecules* **133**, 473–483 (2019).
15. El Mammeri, N., Dregni, A. J., Duan, P., Wang, H. K. & Hong, M. Microtubule-binding core of the tau protein. *Science Advances* **8**, eabo4459 (2022).
16. Brotzakis, Z. F. *et al.* A Structural Ensemble of a Tau-Microtubule Complex Reveals Regulatory Tau Phosphorylation and Acetylation Mechanisms. *ACS Cent. Sci.* **7**, 1986–1995 (2021).
17. Lefèvre, J. *et al.* The C terminus of tubulin, a versatile partner for cationic molecules: binding of Tau, polyamines, and calcium. *Journal of Biological Chemistry* **286**, 3065–3078 (2011).
18. Mukrasch, M. D. *et al.* Structural polymorphism of 441-residue tau at single residue resolution. *PLoS biology* **7**, e1000034 (2009).
19. Xiang, S. *et al.* Site-Specific Studies of Nucleosome Interactions by Solid-State NMR Spectroscopy. *Angewandte Chemie International Edition* **57**, 4571–4575 (2018).
20. Luo, Y. *et al.* Solid-State NMR Spectroscopy for Studying Microtubules and Microtubule-Associated Proteins. in *Structural Proteomics* 193–201 (Springer, 2021).
21. Damman, R. *et al.* Atomic-level insight into mRNA processing bodies by combining solid and solution-state NMR spectroscopy. *Nature communications* **10**, 1–11 (2019).

Analysis of the dynamic interaction of Tau and microtubules

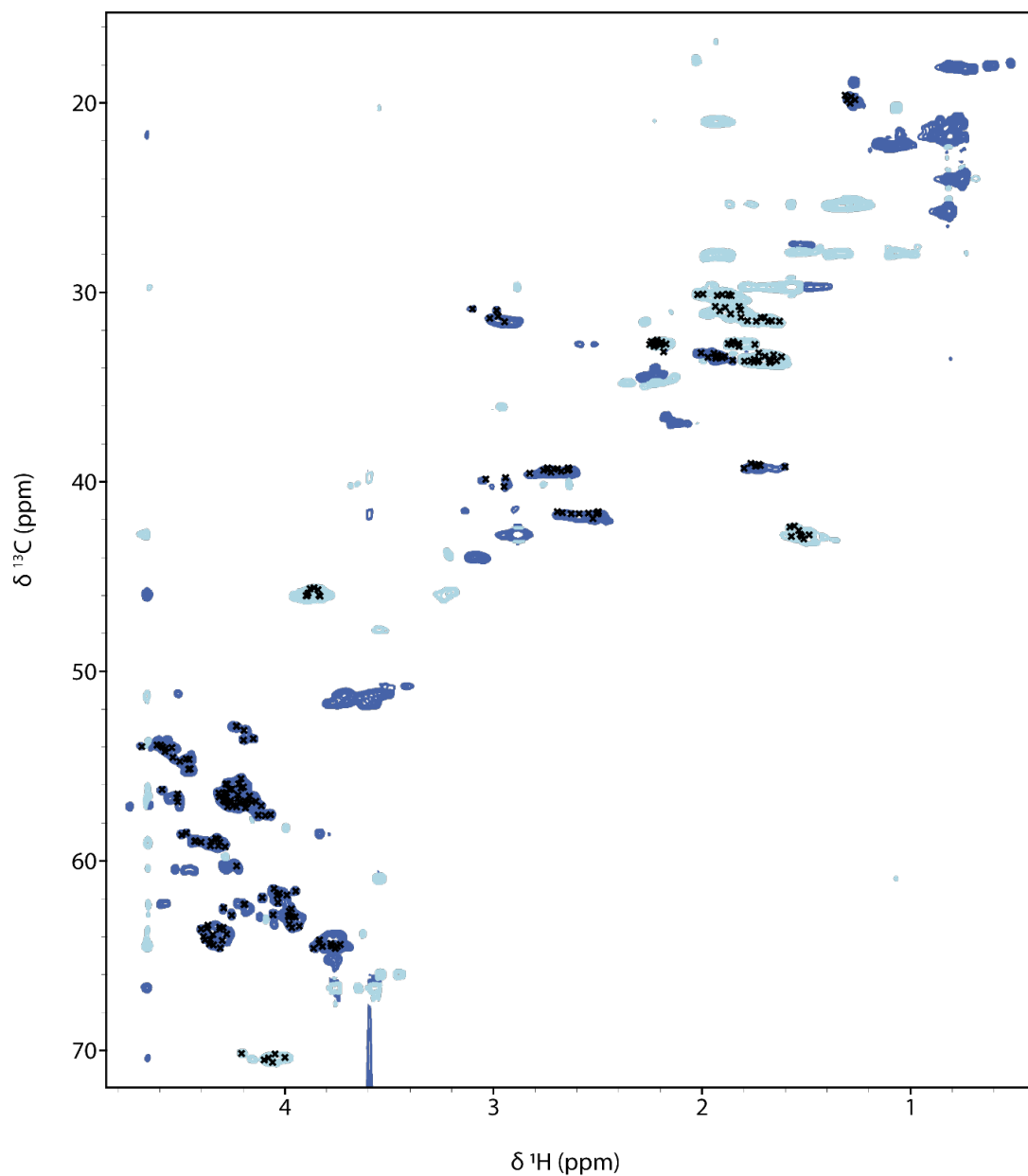
22. Pines, A. *et al.* Direct observation of dynamic protein interactions involving human microtubules using solid-state NMR spectroscopy. *Nature communications* **11**, 1–10 (2020).
23. Fung, H. Y. J., McKibben, K. M., Ramirez, J., Gupta, K. & Rhoades, E. Structural characterization of tau in fuzzy tau: Tubulin complexes. *Structure* **28**, 378–384 (2020).
24. Brotzakis, Z. F. *et al.* A structural ensemble of a tau-microtubule complex reveals regulatory tau phosphorylation and acetylation mechanisms. *ACS Central Science* **7**, 1986–1995 (2021).
25. Kadavath, H. *et al.* The binding mode of a tau peptide with tubulin. *Angewandte Chemie International Edition* **57**, 3246–3250 (2018).
26. Gustke, N., Trinczek, B., Biernat, J., Mandelkow, E.-M. & Mandelkow, E. Domains of tau protein and interactions with microtubules. *Biochemistry* **33**, 9511–9522 (1994).
27. Kadavath, H. *et al.* Folding of the tau protein on microtubules. *Angewandte Chemie International Edition* **54**, 10347–10351 (2015).
28. Martinho, M. *et al.* Two Tau binding sites on tubulin revealed by thiol-disulfide exchanges. *Scientific Reports* **8**, 13846 (2018).
29. Goode, B. L. & Feinstein, S. C. Identification of a novel microtubule binding and assembly domain in the developmentally regulated inter-repeat region of tau. *The Journal of cell biology* **124**, 769–782 (1994).
30. Dayanandan, R. *et al.* Mutations in tau reduce its microtubule binding properties in intact cells and affect its phosphorylation. *FEBS letters* **446**, 228–232 (1999).
31. Strang, K. H., Golde, T. E. & Giasson, B. I. MAPT mutations, tauopathy, and mechanisms of neurodegeneration. *Laboratory investigation* **99**, 912–928 (2019).
32. Neumann, M. *et al.* Pick's disease associated with the novel Tau gene mutation K369I. *Annals of Neurology: Official Journal of the American Neurological Association and the Child Neurology Society* **50**, 503–513 (2001).
33. Tacik, P. *et al.* FTDP-17 with Pick body-like inclusions associated with a novel tau mutation, p. E372G. *Brain Pathology* **27**, 612–626 (2017).
34. Niewidok, B. *et al.* Presence of a carboxy-terminal pseudorepeat and disease-like pseudohyperphosphorylation critically influence tau's interaction with microtubules in axon-like processes. *Molecular biology of the cell* **27**, 3537–3549 (2016).
35. Li, X.-H. & Rhoades, E. Heterogeneous tau-tubulin complexes accelerate microtubule polymerization. *Biophysical journal* **112**, 2567–2574 (2017).
36. Li, X.-H., Culver, J. A. & Rhoades, E. Tau binds to multiple tubulin dimers with helical structure. *Journal of the American Chemical Society* **137**, 9218–9221 (2015).
37. Gigant, B. *et al.* Mechanism of Tau-promoted microtubule assembly as probed by NMR spectroscopy. *Journal of the American Chemical Society* **136**, 12615–12623 (2014).
38. Tsvetkov, P. O., Makarov, A. A., Malesinski, S., Peyrot, V. & Devred, F. New insights into tau-microtubules interaction revealed by isothermal titration calorimetry. *Biochimie* **94**, 916–919 (2012).
39. Di Maio, I. L., Barbier, P., Allegro, D., Brault, C. & Peyrot, V. Quantitative analysis of tau-microtubule interaction using FRET. *International Journal of Molecular Sciences* **15**, 14697–14714 (2014).
40. Lefèvre, J. *et al.* The carboxy terminal of tubulin: a versatile cationic-partner: Binding of Tau, polyamines, and calcium. *J Biol Chem* **286**, 3065–3078 (2010).
41. Mukrasch, M. D. *et al.* The “jaws” of the tau-microtubule interaction. *Journal of Biological Chemistry* **282**, 12230–12239 (2007).



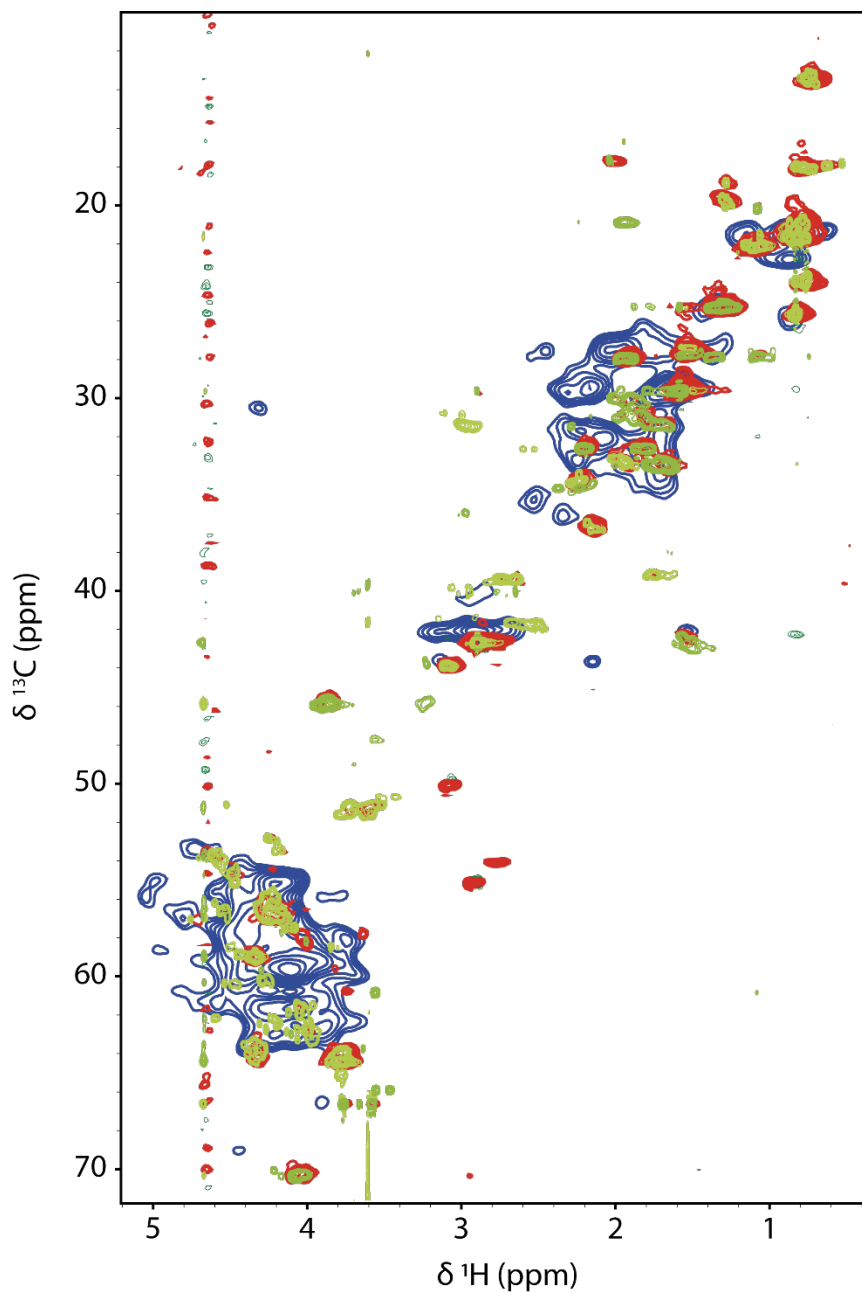
Chapter 6

42. Charafeddine, R. A. *et al.* Tau repeat regions contain conserved histidine residues that modulate microtubule-binding in response to changes in pH. *Journal of Biological Chemistry* **294**, 8779–8790 (2019).
43. Ross, J. L., Santangelo, C. D., Makrides, V. & Fygenson, D. K. Tau induces cooperative Taxol binding to microtubules. *Proceedings of the National Academy of Sciences* **101**, 12910–12915 (2004).
44. Kar, S., Fan, J., Smith, M. J., Goedert, M. & Amos, L. A. Repeat motifs of tau bind to the insides of microtubules in the absence of taxol. *The EMBO journal* **22**, 70–77 (2003).
45. McVicker, D. P., Hoepflich, G. J., Thompson, A. R. & Berger, C. L. Tau interconverts between diffusive and stable populations on the microtubule surface in an isoform and lattice specific manner. *Cytoskeleton* **71**, 184–194 (2014).
46. Siahhaan, V. *et al.* Kinetically distinct phases of tau on microtubules regulate kinesin motors and severing enzymes. *Nature cell biology* **21**, 1086–1092 (2019).
47. Gyparaki, M. T. *et al.* Tau forms oligomeric complexes on microtubules that are distinct from tau aggregates. *Proceedings of the National Academy of Sciences* **118**, e2021461118 (2021).
48. Das, G. & Ghosh, S. Why microtubules should be considered as one of the supplementary targets for designing neurotherapeutics. *ACS Chemical Neuroscience* **10**, 1118–1120 (2019).
49. Zhang, F. *et al.* Posttranslational modifications of α -tubulin in alzheimer disease. *Translational neurodegeneration* **4**, 1–9 (2015).
50. Kuzmič, P. Program DYNAFIT for the analysis of enzyme kinetic data: application to HIV proteinase. *Analytical biochemistry* **237**, 260–273 (1996).
51. Lee, W., Tonelli, M. & Markley, J. L. NMRFAM-SPARKY: enhanced software for biomolecular NMR spectroscopy. *Bioinformatics* **31**, 1325–1327 (2015).
52. Shaka, A., Lee, C. & Pines, A. Iterative schemes for bilinear operators; application to spin decoupling. *Journal of Magnetic Resonance (1969)* **77**, 274–293 (1988).
53. Weingarth, M., Bodenhausen, G. & Tekely, P. Low-power decoupling at high spinning frequencies in high static fields. *Journal of Magnetic Resonance* **199**, 238–241 (2009).
54. Zhou, D. H. & Rienstra, C. M. High-performance solvent suppression for proton detected solid-state NMR. *Journal of magnetic resonance* **192**, 167–172 (2008).
55. Lee, W., Rahimi, M., Lee, Y. & Chiu, A. POKY: a software suite for multidimensional NMR and 3D structure calculation of biomolecules. *Bioinformatics* **37**, 3041–3042 (2021).

Supplementary information

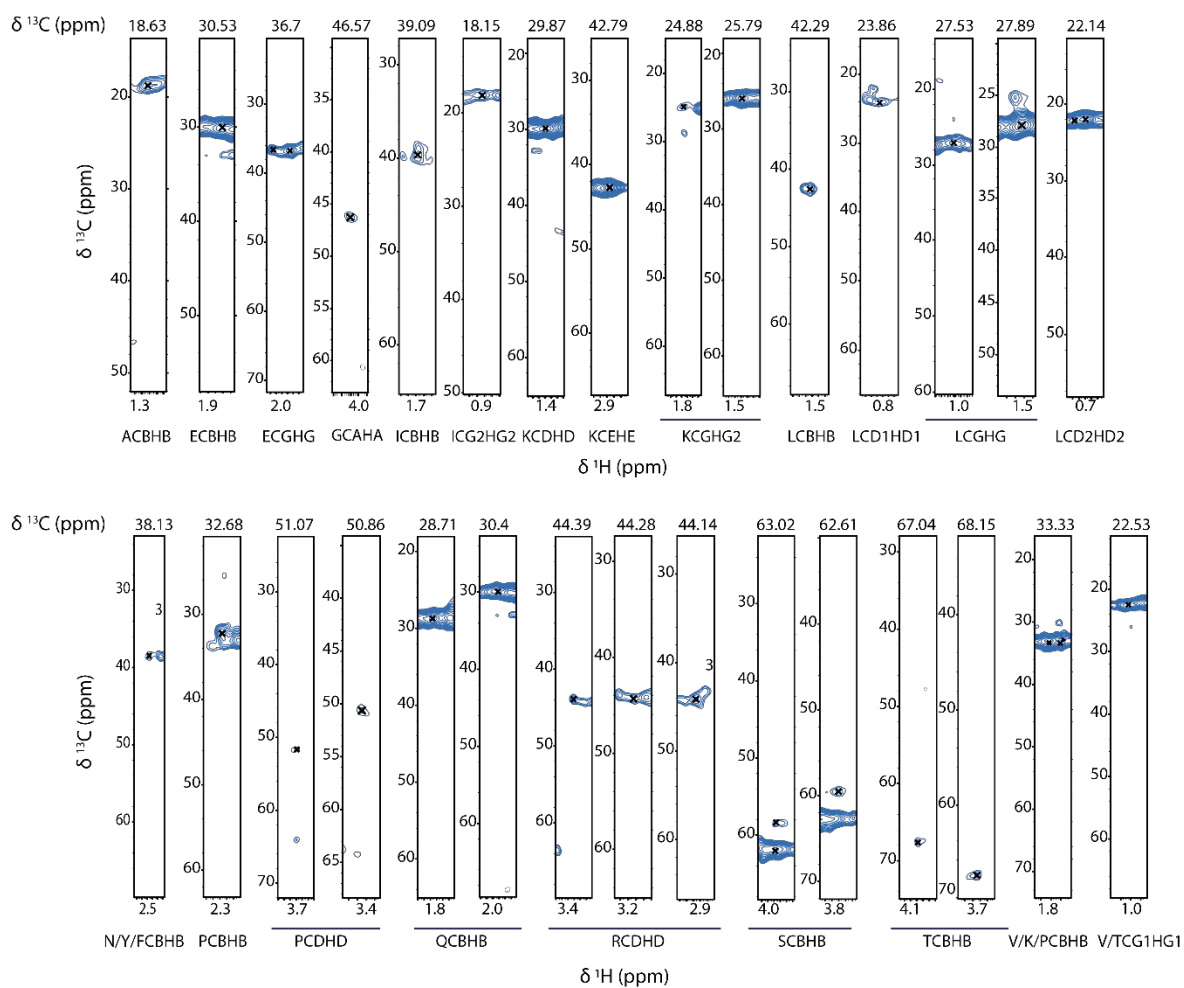


Supplementary Fig. 6.1: Solution-state CH assignments of ^{13}C - ^{15}N -Tau K32 depicted with black crosses on an CH-HSQC spectrum. The assigned chemical shifts are in supplementary table 1.

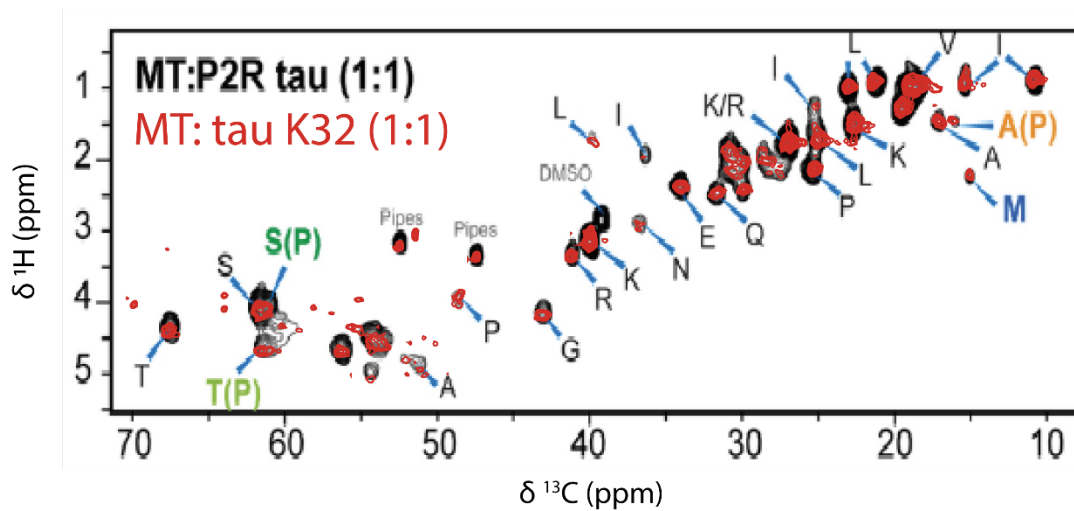


Supplementary Fig. 6.2: Solution-state CH of $[^{13}\text{C}-^{15}\text{N}]$ -Tau K32 compared to solid-state CH spectra of $[^{13}\text{C}-^{15}\text{N}]$ -Tau K32 in interaction with MTs. Depicted in green is the CH-HSQC spectrum, in red the scalar (flexible) solid-state NMR CH spectrum and in blue the dipolar (rigid) solid-state NMR CH spectrum.

Analysis of the dynamic interaction of Tau and microtubules



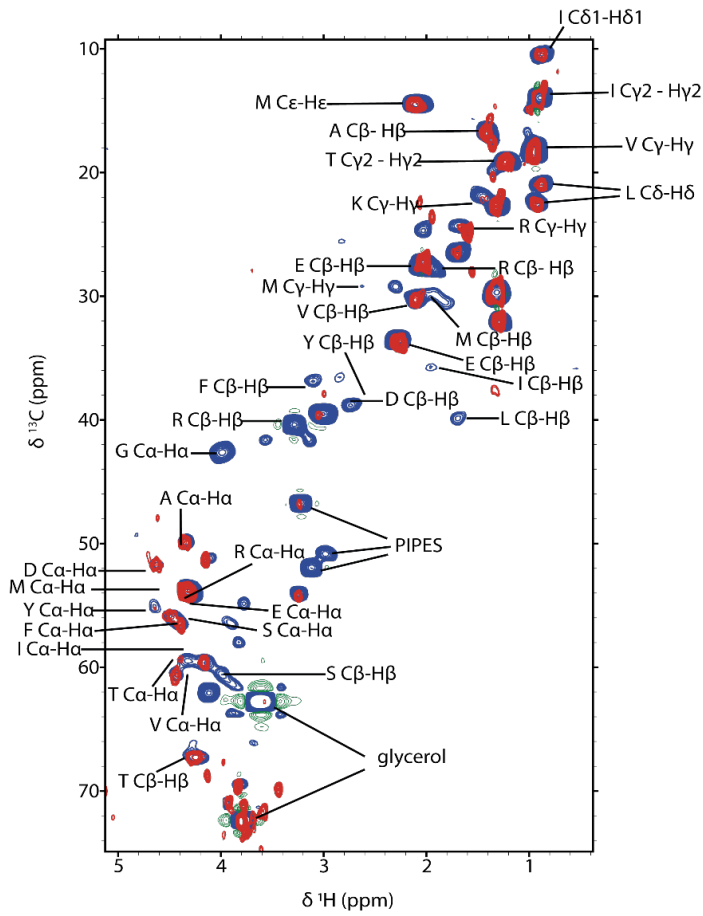
Supplementary Fig. 6.3: Assigned strips of the dipolar 3D CCH of Tau K32 in complex with MTs.



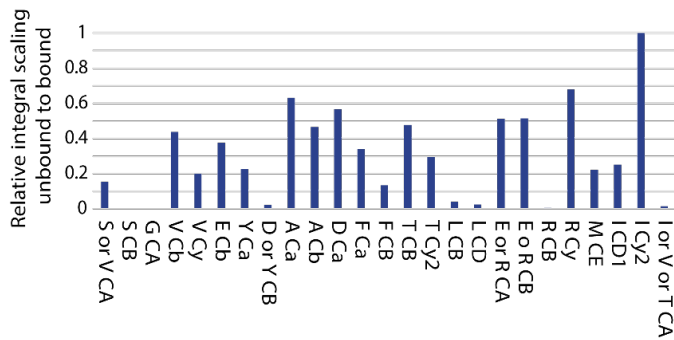
Supplementary Fig. 6.4: Comparison of the 2D scalar CH to the one of El Mammeri et al., 2022¹. In black is the scalar CH spectrum from El Mammeri et al. and in red is the one we recorded.

Analysis of the dynamic interaction of Tau and microtubules

A

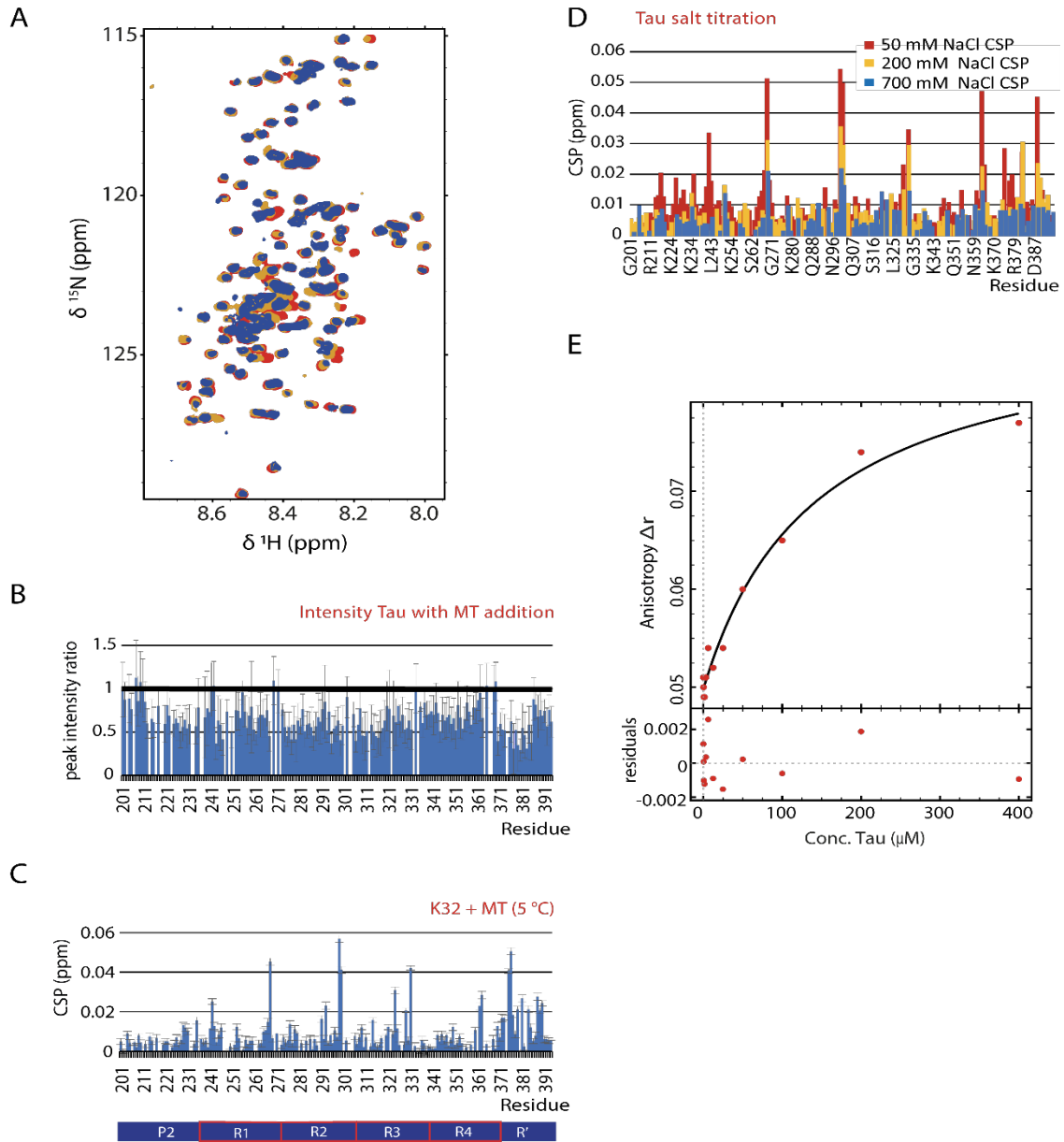


B



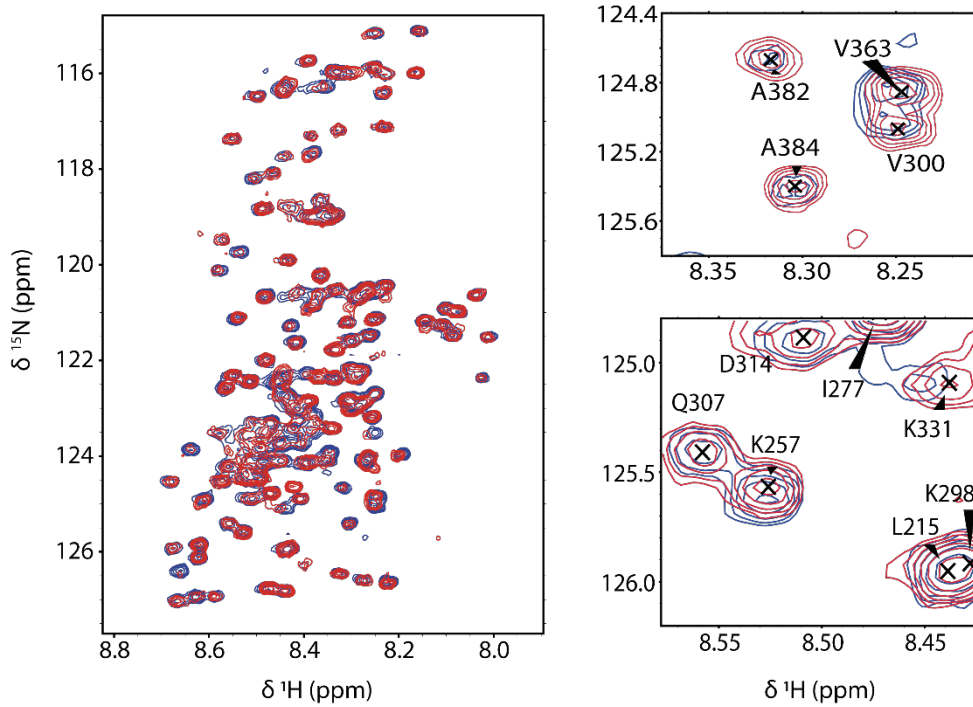
Supplementary Fig. 6.5: CH ssNMR of 13C-15N-Taxol-stabilized MT (A) CH ssNMR of 13C-15N-Taxol-stabilized MT in free (blue) or to Tau K32 bound form (red). **(B)** Signal attenuation upon Tau K32 interaction.



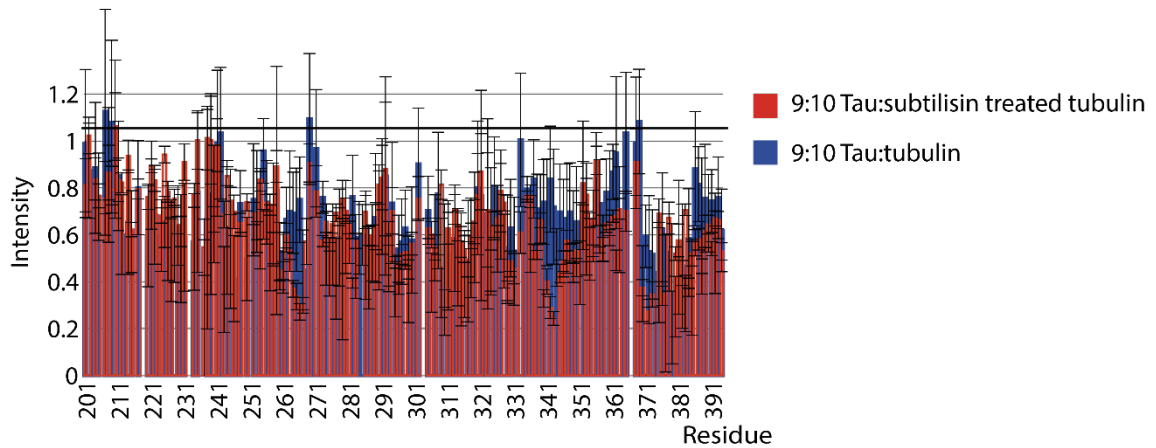


Supplementary Fig. 6.6: Titration of MT to ^{13}C - ^{15}N -Tau K32. (A) NH-TROSY spectra of the titration of MT to ^{13}C - ^{15}N -Tau K32. **(B)** Intensity reduction of Tau K32 signal after adding a 9 to 10 ratio of tubulin to Tau K32. **(C)** CSP upon MT interaction at a ratio of 9 to 10 tubulin to Tau K32. **(D)** Decrease in CSP due to higher salt concentrations. **(E)** A binding affinity of $140 \mu\text{M} \pm 34 \mu\text{M}$ was found for the addition of α -CTT to Tau K32 with fluorescence anisotropy.

A



B



Supplementary Fig. 6.7: Tau K32 with subtilisin treated MT. (A) Tau K32 without MT (blue) compared to a 9 to 10 ratio of Tau K32 to subtilisin treated polymerised tubulin (red). **(B)** Intensity ratio of Tau K32 with MT in a 9:10 ratio to tubulin with subtilisin treated MT (red) and untreated ones (blue).

Chapter 6

Supplemental table 6.1: CH assignments Tau K32 solution-state NMR

Assignment	¹³ C	¹ H			
P200-CA-HA	64.44	4.34	V287-CA-HA	63.72	3.98
P200-CB-HB	32.61	2.22	V287-CB-HB	33.14	2.18
G201-CA-HA	45.60	3.86	S289-CA-HA	59.20	4.32
P203-CA-HA	64.39	4.36	S289-CB-HB	64.50	3.78
P203-CB-HB	32.51	2.22	C291-CA-HA	56.31	4.70
G204-CA-HA	45.63	3.88	I297-CA-HA	61.84	4.04
P206-CA-HA	64.60	4.31	I297-CB-HB	39.15	1.74
P206-CB-HB	32.61	1.85	P301-CA-HA	64.18	4.38
P206-CB-HB	32.61	2.25	P301-CB-HB	32.71	2.22
G207-CA-HA	45.87	3.89	P301-CB-HB	32.71	1.87
R209-CA-HA	56.81	4.30	S305-CA-HA	58.95	4.43
R209-CB-HB	31.32	1.70	S305-CB-HB	64.63	3.76
R209-CB-HB	31.32	1.81	I308-CA-HA	61.80	3.99
R211-CA-HA	56.63	4.32	Y310-CA-HA	58.59	4.45
R211-CB-HB	31.52	1.78	Y310-CB-HB	39.56	2.83
R211-CB-HB	31.52	1.67	V313-CA-HA	62.86	4.06
P213-CA-HA	63.91	4.35	V313-CB-HB	33.43	1.97
P213-CB-HB	32.87	2.23	D314-CA-HA	54.25	4.58
P213-CB-HB	32.87	1.82	D314-CB-HB	41.60	2.73
S214-CA-HA	58.83	4.33	L315-CA-HA	56.58	4.17
S214-CB-HB	64.42	3.74	L315-CB-HB	42.18	1.59
P216-CA-HA	63.56	4.37	S316-CA-HA	60.39	4.24
P216-CB-HB	32.62	2.19	S316-CB-HB	64.18	3.83
P219-CA-HA	63.60	4.40	K317-CA-HA	56.70	4.29
P219-CB-HB	32.70	1.83	K317-CB-HB	33.65	1.80
P219-CB-HB	32.70	2.23	K317-CB-HB	33.65	1.67
T220-CB-HB	70.50	3.98	L325-CA-HA	56.23	4.27
R221-CA-HA	56.43	4.28	L325-CB-HB	42.80	1.49
R221-CB-HB	31.54	1.74	G326-CA-HA	45.92	4.12
R221-CB-HB	31.54	1.63	H330-CA-HA	56.99	4.42
P223-CA-HA	63.62	4.31	H330-CB-HB	31.56	2.95
P223-CB-HB	32.77	2.20	P332-CA-HA	64.16	4.36
K224-CA-HA	56.87	4.14	G334-CA-HA	46.02	3.90
K224-CB-HB	33.63	1.67	G335-CA-HA	45.69	3.84
K225-CA-HA	56.74	4.23	Q336-CA-HA	56.40	4.28
K225-CB-HB	33.70	1.67	Q336-CB-HB	30.14	1.87
V226-CA-HA	62.68	3.98	V337-CA-HA	62.99	3.98
V226-CB-HB	33.50	1.93	V337-CB-HB	33.39	1.93
A227-CA-HA	52.89	4.23	E338-CA-HA	56.89	4.22
A227-CB-HB	19.85	1.27	E338-CB-HB	31.15	1.86
V228-CA-HA	62.96	3.95	V339-CA-HA	62.95	3.97
V228-CB-HB	33.46	1.90	V339-CB-HB	33.31	1.93
V229-CA-HA	62.90	3.98	K340-CA-HA	56.82	4.26
V229-CB-HB	33.35	1.92	K340-CB-HB	33.69	1.68
R230-CA-HA	56.44	4.32	S341-CA-HA	58.86	4.32
R230-CB-HB	31.53	1.68	S341-CB-HB	64.51	3.75
P233-CA-HA	63.52	4.31	E342-CA-HA	57.16	4.23
P233-CB-HB	32.73	2.20	E342-CB-HB	30.94	1.82
K234-CA-HA	56.85	4.19	L344-CA-HA	55.68	4.21
K234-CB-HB	33.72	1.67	L344-CB-HB	43.02	1.51
P236-CA-HA	64.01	4.39	D345-CA-HA	54.66	4.46
P236-CB-HB	32.77	1.86	D345-CB-HB	41.95	2.52
P236-CB-HB	32.77	2.25	F346-CA-HA	59.12	4.39
S237-CA-HA	59.21	4.36	F346-CB-HB	39.86	2.97
S237-CB-HB	64.36	3.84	F346-CB-HB	39.86	3.04
S238-CA-HA	58.99	4.35	K347-CA-HA	57.62	4.09
S238-CB-HB	64.53	3.82	K347-CB-HB	33.31	1.66
A239-CA-HA	53.64	4.20	D348-CA-HA	55.15	4.46
A239-CB-HB	19.60	1.31	D348-CB-HB	41.70	2.51
K240-CA-HA	57.21	4.19	R349-CA-HA	56.94	4.20
K240-CB-HB	33.53	1.75	R349-CB-HB	31.34	1.72

Analysis of the dynamic interaction of Tau and microtubules

K240-CB-HB	33.53	1.68
S241-CA-HA	59.25	4.29
S241-CB-HB	64.38	3.78
L243-CA-HA	55.96	4.22
L243-CB-HB	42.88	1.52
Q244-CA-HA	56.41	4.29
Q244-CB-HB	30.13	1.90
Q244-CB-HB	30.13	2.02
T245-CA-HA	62.28	4.19
T245-CB-HB	70.60	4.08
P249-CA-HA	63.54	4.30
P249-CB-HB	32.75	1.75
P251-CA-HA	63.87	4.28
P251-CB-HB	32.73	2.17
D252-CA-HA	54.63	4.47
D252-CB-HB	41.60	2.50
D252-CB-HB	41.60	2.66
L253-CA-HA	56.16	4.21
L253-CB-HB	42.57	1.54
K254-CA-HA	57.53	4.05
K254-CB-HB	33.20	1.73
N255-CA-HA	53.89	4.61
N255-CB-HB	39.36	2.64
N255-CB-HB	39.36	2.74
V256-CA-HA	63.36	3.98
V256-CB-HB	33.20	2.01
K259-CA-HA	56.93	4.26
K259-CB-HB	33.62	1.77
I260-CA-HA	62.20	4.03
I260-CB-HB	39.04	1.77
S262-CA-HA	58.98	4.43
S262-CB-HB	64.62	3.86
E264-CA-HA	57.66	4.14
E264-CB-HB	30.76	1.94
E264-CB-HB	30.76	1.82
N265-CA-HA	54.08	4.57
N265-CB-HB	39.26	2.64
N265-CB-HB	39.26	2.74
L266-CA-HA	56.12	4.20
L266-CB-HB	42.78	1.53
K267-CA-HA	57.14	4.27
K267-CB-HB	33.41	1.53
K267-CB-HB	33.41	1.62
H268-CA-HA	56.68	4.52
H268-CB-HB	31.26	2.98
G272-CA-HA	46.00	3.90
G273-CA-HA	45.69	3.84
Q276-CA-HA	56.21	4.26
Q276-CB-HB	30.19	1.93
Q276-CB-HB	30.19	1.86
I277-CA-HA	61.76	4.03
I277-CB-HB	39.08	1.73
I278-CA-HA	61.48	4.05
I278-CB-HB	39.15	1.74
N279-CB-HB	39.50	2.72
K280-CA-HA	57.15	4.10
K280-CB-HB	33.66	1.73
K281-CB-HB	33.38	1.70
K281-CB-HB	33.38	1.89
D283-CA-HA	54.54	4.54
D283-CB-HB	41.61	2.71
D283-CB-HB	41.61	2.50
L284-CA-HA	55.94	4.29
L284-CB-HB	42.33	1.56

V350-CA-HA	63.46	3.93
V350-CB-HB	33.21	1.94
Q351-CA-HA	56.52	4.23
Q351-CB-HB	30.09	2.00
Q351-CB-HB	30.09	1.88
S356-CA-HA	59.04	4.31
S356-CB-HB	64.48	3.77
D358-CA-HA	55.18	4.46
D358-CB-HB	41.69	2.50
D358-CB-HB	41.69	2.59
N359-CA-HA	54.00	4.59
N359-CB-HB	39.33	2.69
I360-CA-HA	61.95	4.11
I360-CB-HB	39.21	1.79
T361-CA-HA	62.83	4.26
T361-CB-HB	70.22	4.06
P364-CA-HA	64.21	4.30
P364-CB-HB	32.66	1.85
P364-CB-HB	32.66	2.23
N368-CA-HA	53.89	4.60
N368-CB-HB	39.45	2.68
K369-CA-HA	57.01	4.19
I371-CA-HA	61.71	4.03
I371-CB-HB	39.12	1.72
E372-CA-HA	56.89	4.29
E372-CB-HB	30.99	1.92
T373-CA-HA	63.40	4.37
T373-CB-HB	70.09	4.22
H374-CA-HA	56.90	4.51
H374-CB-HB	31.11	3.01
K375-CA-HA	56.85	4.18
K375-CB-HB	33.62	1.64
L376-CA-HA	55.97	4.28
L376-CB-HB	42.88	1.57
T377-CA-HA	62.25	4.31
T377-CB-HB	70.68	4.10
F378-CA-HA	58.80	4.48
F378-CB-HB	40.20	2.97
E380-CA-HA	57.56	4.07
E380-CB-HB	30.82	1.89
N381-CA-HA	54.03	4.54
N381-CB-HB	39.36	2.71
A382-CA-HA	53.56	4.14
A382-CB-HB	19.68	1.29
K383-CA-HA	56.92	4.16
K383-CB-HB	33.58	1.73
A384-CA-HA	53.13	4.20
A384-CB-HB	19.86	1.31
K385-CA-HA	57.10	4.25
K385-CB-HB	33.69	1.75
T386-CA-HA	62.32	4.20
T386-CB-HB	70.74	4.07
D387-CA-HA	54.75	4.51
D387-CB-HB	41.67	2.55
H388-CA-HA	56.88	4.51
H388-CB-HB	30.47	3.00
H388-CB-HB	30.47	3.13
G389-CA-HA	46.00	3.84
A390-CA-HA	52.92	4.23
A390-CB-HB	20.03	1.29
I392-CA-HA	61.73	3.92
I392-CB-HB	39.07	1.58
V393-CA-HA	62.54	3.97
V393-CB-HB	33.59	1.85



Chapter 6

N286-CA-HA	53.92	4.68
N286-CB-HB	39.41	2.65
N286-CB-HB	39.41	2.76

Supplement table 6.2: assignment of the CCH scalar

Assignment	¹³ C	¹³ C	¹ H
ACA-CA-HA	53.64	53.70	3.68
ACA-CA-HA	52.67	53.17	4.22
ACA-CB-HB	53.65	19.38	1.37
ACA-CB-HB	52.69	19.71	1.29
ACB-CA-HA	19.40	53.96	3.68
ACB-CA-HA	19.85	53.19	4.22
ACB-CB-HB	19.45	19.69	1.28
ACB-CB-HB	19.76	19.53	1.35
DCA-CA-HA	54.60	54.93	4.46
DCA-CA-HA	54.10	54.87	4.34
DCB-CA-HA	41.67	55.17	4.47
DCB-CA-HA	41.50	54.94	4.35
DCB-CB-HB3	41.23	41.77	2.50
DCB-CB-HB3	40.73	41.37	2.70
ECA-CA-HA	56.78	56.86	4.19
ECA-CB-HB3	56.68	31.12	1.82
ECA-CG-HG3	56.69	36.58	2.16
ECB-CA-HA	29.72	57.03	4.19
ECB-CB-HB3	30.55	30.46	1.94
ECB-CG-HG3	30.31	36.55	2.16
ECG-CA-HA	36.51	57.59	4.16
ECG-CA-HA	36.45	56.86	4.18
ECG-CB-HB3	36.28	30.25	1.82
ECG-CB-HB3	36.44	30.83	1.94
ECG-CG-HG3	36.52	36.88	2.16
GCA-CA-HA3	45.66	45.83	3.87
H?CA-CA-HA	55.70	56.08	4.52
HCB-CB-HB3	30.53	30.72	2.97
ICA-CA-HA	61.05	62.07	4.10
ICA-CD1-HD1	61.30	13.16	0.75
ICA-CG2-HG2	61.36	18.33	0.79
ICB-CB-HB	39.18	39.71	1.75
ICB-CD1-HD1	38.91	13.39	0.74
ICB-CG2-HG2	38.57	17.80	0.78
ICD1-CA-HA	12.98	62.21	4.08
ICD1-CB-HB	12.56	38.82	1.77
ICD1-CD1-HD1	13.20	13.40	0.73
ICD1-CG2-HG2	13.42	18.12	0.79
ICG1-CB-HB	27.67	38.99	1.73
ICG1-CD1-HD1	27.54	13.39	0.73
ICG1-CG2-HG2	27.83	17.81	0.77
ICG2-CB-HB	17.69	38.99	1.76
ICG2-CD1-HD1	17.90	13.34	0.73
ICG2-CG2-HG2	17.84	18.27	0.76
K2CD-KCA-HA	29.86	56.63	4.27
KCA-CA-HA	56.33	56.64	4.22
KCA-CB-HB3	56.11	33.37	1.66
KCA-CD-HD3	56.53	29.15	1.58
KCA-CE-HE2	56.64	42.72	2.89
KCA-CG-HG3	56.62	24.89	1.32
KCB-CA-HA	34.25	56.69	4.26
KCB-CB-HB3	32.79	33.02	1.78
KCB-CB-HB3	33.35	33.58	1.63

Analysis of the dynamic interaction of Tau and microtubules

KCB-CD-HD3	33.54	29.49	1.58
KCB-CE-HE2	33.44	42.55	2.89
KCB-CG-HG	42.42	29.51	1.57
KCB-CG-HG3	33.52	24.96	1.33
KCD-CB-HB3	29.19	33.38	1.67
KCD-CD-HD3	29.35	29.54	1.57
KCD-CE-HE2	29.34	42.65	2.88
KCD-CG-HG3	29.32	25.15	1.31
KCE-CA-HA	42.70	56.63	4.26
KCE-CB-HB3	42.74	33.33	1.65
KCE-CB-HB3	42.57	33.33	1.73
KCE-CE-HE2	42.42	42.66	2.88
KCE-CG-HG3	42.45	25.18	1.32
KCG-CA-HA	24.97	56.62	4.21
KCG-CB-HB3	25.10	33.30	1.70
KCG-CD-HD3	24.94	29.50	1.57
KCG-CE-HE2	24.94	42.71	2.88
KCG-CG-HG3	24.99	25.25	1.33
LCA-CB-HB3	56.34	42.92	1.58
LCA-CD1-HD1	55.60	25.37	0.83
LCB-CB-HB3	42.88	43.21	1.57
LCB-CD1-HD1	43.47	24.45	0.83
LCD2-CB-HB2	24.79	43.38	1.62
LCD2-CB-HB3	24.64	42.81	1.54
LCD2-CD1-HD1	24.33	25.24	0.81
LCD2-CD2-HD2	24.56	24.49	0.77
MCE-CE-HE	17.53	17.72	2.01
NCA-CA-HA	53.48	53.92	4.61
NCB-CA-HA	39.86	54.01	4.61
NCB-CB-HB3	39.38	39.27	2.73
NCB-CB-HB3	39.52	39.83	2.64
PCA-CA-HA	63.33	64.26	4.40
PCA-CA-HA	64.05	64.26	4.34
PCA-CB-HB2	63.66	32.60	2.18
PCA-CD-HD2	63.33	51.41	3.73
PCA-CD-HD3	63.27	51.46	3.59
PCA-CG-HG3	63.36	27.78	1.91
PCB-CA-HA	32.40	64.13	4.33
PCB-CB-HB	32.72	32.81	2.22
PCB-CD-HD3	32.41	51.46	3.59
PCB-CG-HG3	32.41	27.94	1.92
PCD-CA-HA	51.03	64.17	4.33
PCD-CB-HB2	51.26	32.48	2.20
PCD-CD-HD2	52.21	52.06	3.76
PCD-CD-HD2	51.48	51.48	3.71
PCD-CG-HG3	51.24	27.98	1.92
PCG-CA-HA	27.66	64.20	4.33
PCG-CB-HB2	28.03	32.69	2.21
PCG-CD-HD2	27.92	50.88	3.72
PCG-CD-HD3	26.91	51.14	3.56
PCG-CD-HD3	27.64	51.45	3.64
PCG-CG-HG2	27.75	28.00	1.93
QCA-CG-HG3	55.73	34.51	2.25
QCB-CG-HG3	29.06	34.20	2.21
QCG-CG-HG3	33.81	34.20	2.24
RCA-CA-HA	57.52	57.87	3.65
RCA-CD-HD3	56.30	43.89	3.10
RCB-CA-HA	30.11	57.96	3.66
RCB-CB-HB2	30.67	30.84	1.82
RCD-CA-HA	42.81	57.54	3.65
RCD-CB-HB3	43.23	30.84	1.71
RCD-CD-HD3	43.36	43.67	3.07
RCG-CA-HA	24.57	57.57	3.65
RCG-CB-HB2	27.78	32.06	1.81



Chapter 6

RCG-CD-HD3	27.55	44.03	3.10
S2CA-CA-HA	56.92	57.37	4.73
S3CB-CA-HA	63.72	59.36	4.42
SCA-CA-HA	58.57	59.08	4.34
SCA-CA-HA	57.98	58.20	4.01
SCA-CB-HB2	58.14	64.25	3.78
SCB-CA-HA	63.39	57.29	4.72
SCB-CA-HA	64.10	58.99	4.34
SCB-CA-HA	63.88	58.21	4.02
SCB-CB-HB3	64.10	64.39	3.78
TCB-CA-HA	21.84	60.66	4.50
TCA-CA-HA	59.53	60.44	4.51
TCA-CA-HA	61.56	62.35	4.20
VCA-CA-HA	63.37	64.01	4.02
TCA-CB-HB	61.46	70.35	4.12
TCA-CG2-HG2	62.27	22.09	1.08
TCA-CG2-HG2	60.43	22.02	1.13
TCA-CG2-HG2	60.76	22.05	1.13
TCB-CB-HB	70.01	70.41	4.08
TCB-CG2-HG2	69.91	22.16	1.13
TCB-CG2-HG2	69.88	21.98	1.02
TCG2-CA-HA	21.83	62.50	4.21
TCG2-CB-HB	22.00	70.27	4.06
TCG2-CG2-HG2	21.87	22.17	1.11
VCA-CA-HA	62.68	63.09	3.99
VCA-CB-HB	62.79	33.22	1.95
VCA-CB-HB	63.68	33.04	1.86
VCA-CG2-HG2	62.70	21.47	0.82
VCB-CA-HA	33.06	62.99	4.00
VCB-CB-HB	32.71	33.19	1.90
VCB-CG2-HG2	32.89	21.28	0.82
VCG2-CA-HA	21.29	62.90	4.00
VCG2-CB-HB	21.15	33.32	1.95
VCG2-CB-HB	20.52	32.49	2.16
VCG2-CG2-HG2	21.10	21.39	0.81
Y/FCA-CA-HA	59.99	60.37	3.74
Y/FCB-CA-HA	40.15	60.48	3.73
Y/NCA-CA-HA	58.84	59.24	3.84
Y/NCB-CA-HA	38.57	59.38	3.84

Analysis of the dynamic interaction of Tau and microtubules

Supplement table 6.3: CCH dipolar assignments and comparison to Mammeri et al. 2022¹. We subtracted 2.2 ppm from the ¹³C chemical shifts, to compare the assignments. In green are assignments that are comparable, while in black are the once where no corresponding correlation was found in the paper of Mammeri et al.

Assignment	¹³ C	¹³ C	¹ H	S/N	minus 2.2 ppm for comparison		Comparison to Mammeri et al.
ACB-CB-HB	18.76	18.70	1.22	8	16.56	16.50	Could be Ala 382
ACB-CB-HB	18.25	18.44	1.60	7	16.05	16.24	No Ala fits
ACB-CB-HB	21.71	21.71	1.12	7	19.51	19.51	Ala 2
E/QCA-CB-HB2	60.44	28.82	2.28	6	58.24	26.62	No Glu/Gln fits
E/QCB-CB-HB2	28.54	28.83	2.25	9	26.34	26.63	
E/QCB-CB-HB3	30.11	30.60	1.78	13	27.91	28.40	
E/QCG-CG-HG3	36.75	36.80	1.96	9	34.55	34.60	
E/QCG-CG-HG3	36.60	36.86	2.25	8	34.40	34.66	
GCA-CA-HA2	46.27	46.64	4.10	6	44.07	44.44	G367
ICB-CB-HB	39.66	39.15	1.68	7	37.46	36.95	Could be Ile 2 or I354
ICG2-CG1-HG12	18.93	28.00	1.34	6	16.73	25.80	Could be Ile1
ICG2-CG2-HG2	18.13	18.22	0.93	7	15.93	16.02	Could be Ile
KCD-CD-HD3	29.85	29.94	1.49	18	27.65	27.74	could be K383
KCE-CE-HE2	42.74	42.86	2.86	17	40.54	40.66	could be K383
KCB-CB-HB	36.03	36.40	1.78	8	33.83	34.20	Could be K383
KCG-CG-HG2	24.90	24.95	1.87	6	22.70	22.75	No Lys fits
KCG-CG-HG3	25.97	25.86	1.39	14	23.77	23.66	could be K383
LCB-CB-HB2	42.60	42.36	1.63	7	40.40	40.16	could be L357
LCB-CB-HB3	42.73	43.19	1.47	6	40.53	40.99	could be L357
LCD1-CD1-HD1	24.12	23.93	0.86	6	21.92	21.73	could be L357
LCG1-CG1-HG1	27.06	27.60	1.11	9	24.86	25.40	could be Leu 1
LCG1-CG2-HG2	25.18	28.10	1.60	7	22.98	25.90	could be Leu 1
LCD2-CD2-HD2	21.98	22.21	0.69	15	19.78	20.01	No Leu fits but Leu 1 has no CD
LCD2-CD2-HD2	22.11	22.19	0.87	14	19.91	19.99	No Leu fits but Leu 1 has no CD
LCG-CG-HG	27.88	27.96	1.53	14	25.68	25.76	No Leu fits
NCB-CB-HB3	38.47	38.20	2.56	6	36.27	36.00	Asn/Asp
NCB-CB-HB4	39.91	39.04	2.53	6	37.71	36.84	Asn/Asp
PCB-CB-HB2	32.24	32.74	2.37	8	30.04	30.54	P364
PCD-CD-HD2	51.66	51.14	3.79	5	49.46	48.94	P364
PCD-CD-HD3	50.62	50.93	3.45	6	48.42	48.73	P364
QCB-CB-HB3	29.94	30.47	1.91	11	27.74	28.27	Gln/Glu 1
QCB-CB-HB3	28.71	28.78	1.87	13	26.51	26.58	No Q fits
RCD-CD-HD2	43.92	44.46	3.31	7	41.72	42.26	No R
RCD-CD-HD2	44.32	44.35	3.13	6	42.12	42.15	No R
RCD-CD-HD3	44.14	44.21	2.97	7	41.94	42.01	No R
SCA-CB-HB2	59.52	63.09	3.97	6	57.32	60.89	No S fits
SCA-CB-HB3	59.53	62.68	3.80	6	57.33	60.48	No S fits
SCB-CB-HB2	62.89	62.98	3.98	12	60.69	60.78	No S fits
SCB-CB-HB2	63.18	63.15	3.98	12	60.98	60.95	S356
TCB-CB-HB	67.62	67.11	3.98	6	65.42	64.91	Could be Thr 1
TCB-CB-HB	67.64	68.22	3.74	6	65.44	66.02	T386
V/K/PCB-CB-HB	33.30	33.40	1.84	14	31.10	31.20	V 2/3/5 V363 and P364
V/K/PCB-CB-HB	33.38	33.34	1.61	12	31.18	31.14	V 2/3/5 V363 and P364
V/TCG1-CG1-HG1	22.48	22.60	1.04	13	20.28	20.40	Val 5/ Thr 5
DCB-CB-HB3	40.56	41.17	2.71	6	38.36	38.97	D358/D387/F/Y
HCB-CB-HB3	30.38	30.45	2.95	6	28.18	28.25	H362

Supplementary Methods

Spectral analysis of 2D and 3D ssNMR data sets

2D solid-state NMR spectra

The analysis of scalar and dipolar 2D ^{13}C - ^1H correlation experiments in **Fig. 5.3B** was performed on the basis of previous solution NMR assignments and average BMRB chemical-shift values. Scalar signals observed in Ile, Met, Ala, Pro, and Thr side-chains furthermore suggest that they are largely flexible. The same is true for the Gly CAHA resonances. There is only one Met in the sequence at position 250 (**Fig. 6.2A**). Moreover, Pro can only be found in the proline-rich region N-terminal of the sequence and in the PGGG motifs of each repeat region. Ala is present only before residue 247 and after residue 381. Therefore, it has to be in the P2 region and at the end of R'. Gly residues are within the PGGG motifs of each repeat and at the start of the N-terminal repeat. Also in each repeat, there is an I/C G S sequence. In contrast, Gln CBHBs are largely rigid. The first Gln in the sequence is at the start of R1 and the last one is at the end of R4.

Scalar-based 3D solid-state NMR spectra

For the analysis of the 3D scalar spectrum (probing dynamic Tau K32 residues in the complex) we noticed spectral overlap, which largely hindered residue specific assignments. Nonetheless, we found CAHA and CBHB correlations for Arg 209 and Arg 211. We could also assign one of the Ala CAHA and CBHB pairs to Ala 227 or Ala 390. The solution-state assignments of Ser 316, Val 287, and Val 350 do not overlap with our experimental J-based ssNMR data, indicating these residues are bound to MTs.

According to the estimated abundance of residue types (**Fig. 6.4**), Ala, Tyr and Phe are largely flexible. Tyr resonances only occur at the C-terminus of the sequence at positions 310 and at position 395. The Y310 chemical shift is distinguishable in

solution-state NMR but disappeared in our J-based ssNMR data in the complex. Phe can be found in R4 as residue 346 and in R' as 378.

According to the aforementioned analysis, half of the 8 Asp residues show flexibility in CAHA and CBHB. There are 7 Asp in the R regions (1 in R1, 2 in R2, 1 in R3 and 2 in R4) and one in R'. For Gly 10 of the resonances can be found in the scalar CCH spectrum of which only 3 could be assigned to the P2 region. Of the 7 His, there are two flexible. This is of particular interest, as His is not found in the P2 region. For Asn a similar trend is apparent with approximately three flexible Asn residues. The observation of these residues implicates backbone dynamics in the R regions. Considering that around half of the Asp, Asn and two of the His are flexible, it is likely that the first two of the R regions are weaker binding, as well as the end of the R' because the residue distribution is in reasonable accordance with these findings. The disappearance of all but one Ile that could account for an Ile in R1 or the C-terminus suggests that there is still some interaction.

For Ser there are around 11 residues in the scalar spectrum. There might be 10 in the P2 region. In addition, several Ser shifts overlap with the solution-state assignments of this region. This is also confirmed by the abundance of Pro residues. This combination and amount of Pro and Ser are only found in the P2 region. Moreover, the amount of flexible Leu, Val and Lys is in line with the amount of these residues in the P2 region. Intriguingly there are fewer Arg and one to two more Glu found in comparison to how many are in the P2 region. One of the Glu might be in R1 and the second one at the C-terminus. There is only one Arg CAHA assigned, but 3 CBHB. It is likely, that these Arg resonances can be assigned to the P2 region, as there is overall flexibility observed. A 3D CCH assignment for these CAHAs might be not assigned due to spectral overlap and therefore difficulties to distinguish the resonances. This is confirmed by the higher abundance of CBHB.



Dipolar-based 3D solid-state NMR spectra

A comparison of our dipolar-based 3D signal sets and the reported data from El Mammeri et al., 2022 ¹ revealed that assignments of residues 354, 356-358, 362-364, 367, 382, 383 and 386, 387 might be transferable (**Supplement table 6.3**). While no equivalents for G355, G365-G367 and H388, as well as G389, were identified. Also, in comparison to El Mammeri et al., we were able to assign resonances in line with their Ala 2, Ile 1, Leu 1, two of the four Asn, Gln/Glu 1, Thr 1 and Val/Thr 5. Fewer Val resonances in our study may be due to the shorter construct. Additionally, we found resonances of type 1x Lys, 1x Leu, 2x Gln/Glu, 1x Gln, 2x Arg and 1x Ser. These extra residues are particularly consistent with the notion that the rigid resonances are located in R4 and R', as they are in accordance with by El Mammeri et al. none assigned residues in R4 and R'.

For further analysis, we turned to quantitatively analysing the dipolar 2D CH spectrum (**Fig. 6.4C**). Especially Leu side chains seem to be largely rigid. This is also in line with the proportionally few Leu resonances detected in the scalar 3D experiment. The number of Leu CDs matches the amount in the R1-R4 + R' region. There are no Met side chains and Ala and Thr could only be identified in the 3D dipolar CCH. With the help of peak integration, we assigned CBHB resonances to at least 2-3 Ala and 4 Thr residues. The 2-3 Ala have to belong to the R' region, as there are otherwise only Ala in P2, which we already found to be flexible. The four Thr are most likely in the R regions. There are 6 Thr, one in R1, one in R3, one in R4 and three in R'. Also worth noticing is that Gln residues could be found in the dipolar spectrum, but not in the scalar one, accounting for around half of the Gln resonances. One to two of the Phe/Tyr resonances seem rigid. The Tau K32 has 2 Phe in positions 346 and 378, which correspond to R4 and R'. Phe CBHB only shows a very weak signal in the dipolar spectrum. This signal may account for Phe 378, as there is a good overlap with the solution-state assignment. One Pro is found to be rigid. Therefore, the Pro of the PGGG motifs might exhibit intermediate dynamics.

Supplementary References

- 1 El Mammeri, N., Dregni, A. J., Duan, P., Wang, H. K. & Hong, M. Microtubule-binding core of the tau protein. *Science Advances* **8**, eabo4459 (2022).



Chapter 7

Utilizing solid-state NMR to investigate mRNA processing bodies

Contribution: Agnes Adler packed the ssNMR rotors and recorded and analysed the NMR spectra. Christina Krempl from the University of Regensburg produced the proteins and conducted the PBs maturation. Remco Sprangers from the University of Regensburg and Marc Baldus from Utrecht University supervised the project.



Abstract

Phase separation is a physical process where two miscible phases separate into two or more distinct phases. In recent years, it has been discovered that phase separation is a common mechanism for organizing biomolecules within cells. For example, phase separation is thought to play a role in the formation of mRNA processing bodies (PBs). PBs are large complexes of RNA and protein that are found in the cell and are involved in the degradation of mRNA. A central hub of these foci, and important for the liquid-liquid phase separation (LLPS) process in yeast is the enhancer of decapping 3 (Edc3). Edc3 interacts with the decapping protein 2 (Dcp2), which catalyses the decapping of mRNA. In this study, we aim at elucidating the role of Edc3 and Dcp2 in mRNA turnover using solid-state NMR. This allows us to probe the states of proteins in the condensed phase, which might reflect protein dynamics in PBs.

Introduction

Liquid-liquid phase separates (LLPS) are membrane-less organelles of high protein density and slower diffusion, which allow for enhanced catalysis of certain biochemical reactions ^{1,2}. Examples are nuclear condensates mediating transcription ³, chromatin condensates ⁴ or the control of RNA degradation in so-called processing bodies ⁵.

Weak interactions enable the function of the involved proteins in LLPS, by allowing the necessary dynamic ⁶. Proteins that initiate phase separation often contain intrinsically disordered regions for transient, multivalent interactions. In this state, a constant exchange with the environment is observed. Interactions between the involved proteins might strengthen over time leading to a more mature state and eventually to a solid phase. The review of Wang et al. ⁶ describes in greater detail how the physiological function of these LLPS can be understood. In spite of these advancements, our understanding of how these condensates are organized on a detailed level is still limited ^{2,7}.

An array of techniques has been used to investigate the structure and mechanism of LLPS. Nonetheless, the study of the processes leading to condensation on an atomic level has proven challenging due to the dynamic nature and heterogeneity in the interactions between the involved molecules⁸. Cryo-electron microscopy and X-ray crystallography are vital tools to shed light on the proteins involved in condensation, but give little insight into the physiological relevant form⁹. Solution-state NMR can partly overcome this issue and was therefore extensively employed to gain information on the components of LLPS^{10–12}. Finally, solid-state NMR (ssNMR) allows for studying the gel-like phase separation by probing both the ensemble's rigid and flexible parts¹³. Therefore, ssNMR can provide the essential link to understanding the importance of the intrinsically disordered regions and the oligomerization process which have been proven essential for LLPS.

Several studies report on the function of the different proteins involved in mRNA processing bodies (PBs)^{14,15}. Decapping proteins 1 and 2 (Dcp1 and Dcp2) were identified as the mRNA decapping complex and the enhancer of decapping 1 (Edc1) as an activator of the aforementioned Dcp2^{16–18}. Moreover, the enhancer of decapping 3 has been coined to be a central hub and necessary for LLPS in yeast^{19–21}.

Previously we have shown that combining solution- and ssNMR provides an avenue to study the maturation mechanism of PBs revealing the dynamic conformation of Edc3 which is a central hub in the phase-separated state²². Edc3 is a 50 kDa protein with an N-terminal LSM domain, that interacts with Dcp2²³, a C-terminal YjeF_N dimerization domain²⁴ and a linker that is an intrinsically disordered region (IDR) (**Fig. 7.1A**). Phase separation was observed by direct interaction of the IDR and the YjeF_N domain²⁴. The IDR has been shown to interact with an RNA helicase and RNA²⁵. On the other hand, little is known about the conformational state of proteins catalysing enzymatic reactions in the LLPS state. Dcp2 is responsible for removing the 5' N⁷-methylguanosine (m⁷G) cap structure from mRNAs, which triggers their degradation¹⁷. This is critical for the mRNA decay pathway from the 5' end. Dcp2 of



S.pombe comprises three domains. The N-terminal regulatory domain (ND; AA 1-95) interacts with Dcp1, the catalytic NUDIX domain (CD; AA 96-243) and a C-terminal intrinsically disordered region (IDR; AA 244-743) (**Fig. 7.1B**). The ND and CD are connected by a flexible linker allowing conformational changes of the enzyme depending on the presence or absence of interaction partners^{23,26–28}. As a result, Dcp2 adopts three conformations. Firstly, a “closed” state where the ND and CD are in close proximity, secondly an “open” conformation in which the domains are more separated and thirdly an active state¹¹. The Dcp2 construct we are studying here comprises residues 1-270, presenting the minimal fragment that can bind Dcp1 and Edc3. Binding of the Edc3 LSm domain to Dcp2 increases the substrate binding affinity by a factor 2 for a 40-nt RNA and enhances the enzymatic activity of Dcp2²⁹. In complex with Dcp1 the catalytic activity of Dcp2 is enhanced^{30,31}. Moreover, Dcp2 is found to interact with Edc1, which is shown to promote a conformational change in the Dcp1:2 (Dcp1 in complex with Dcp2) complex²⁹ (**Fig. 7.1C**). Additionally, the interaction of Dcp1:2 with Edc1:3 (Edc1 in complex with Edc3) and m⁷G shows the active conformation (**Fig. 7.1C and D**)^{32,33}.

In the past, it has been demonstrated that PB-like assemblies can be reconstituted *in vitro* from purified components^{22,34}. These experiments showed that an insoluble gel-like state is formed over time as Edc3-containing foci mature. Moreover, it has been demonstrated that Edc3 and RNA interact in solution. In addition, the properties of Edc3 in its mature state were investigated²², showing the LSm domain to remain flexible while the YjeF_N domain has a rigid core. Additionally, it became evident that the IDR and YjeF_N domains interact to form the LLPS.

Here we intend to extend our understanding of the system by studying Edc3 interactions with other PB components in the matured phase using MAS solid-state NMR. In detail, we investigated how Edc3 interacts with Dcp1 and Dcp2, as well as with RNA. Moreover, we zoom in at the state of the enzymatic component Dcp2 by global ¹⁵N and ¹³C-specific methionine labelling of the protein. Our study reveals the dynamic behaviour of various matured PB systems, with molecular weights up to 188

Utilizing solid-state NMR to investigate mRNA processing bodies

126 kDa. We identify interacting regions of Edc3 in the presence of Dcp1:2 and RNA. In addition, we probe the conformational state of Dcp2 in complexes with Dcp1, m⁷G, Edc1 and Edc3 and combinations thereof.

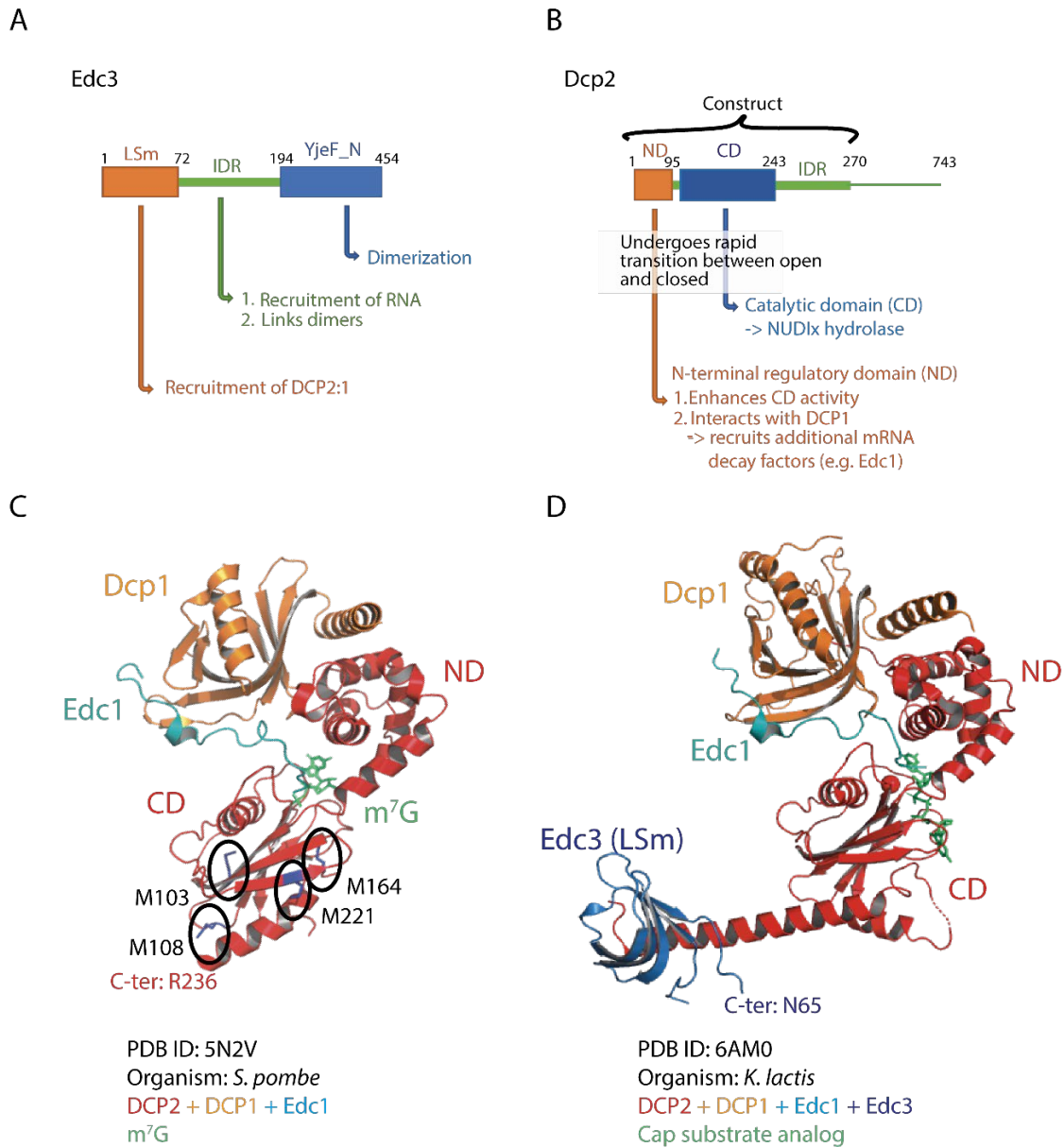


Fig. 7.1: Structure and organization of PB proteins (A) Overview of the Edc3 domain organization of *S.pombe*. Residue numbers are indicated on top and recorded functions underneath. **(B)** Domain organization of Dcp2. **(C)** Structure and observed conformation of Dcp2 in *S.pombe* in interaction with m⁷G, Dcp1 and Edc1 ²⁹. In the circles are methionine residues of Dcp2. **(D)** Observed structure and interactions of Dcp2 in *K.lactis* ³³.

Results

The YjeF_N fold remains preserved in the mature state of Edc3

To probe the fold of Edc3 in the PBs we compared ^1H -detected dipolar NH ssNMR spectra of full-length (FL) ^{13}C - ^{15}N solid-phase Edc3 to matured preparations containing different interaction partners (**Fig. 7.2 left**). These spectra resemble the spectrum of the solid-phase YjeF_N domain of Edc3 alone (**Fig. 7.2A blue**) indicating that its fold is largely conserved in the studied mature state conditions. The agreement of the YjeF_N fold with the domain in solution was previously studied by Damman et al. ²². Nonetheless, there are some differences in the spectra. Especially some additional peaks (**Fig. 7.2A left, boxes**) seem to be observable between the Edc3 (**Fig. 7.2A red**) and the YjeF_N domain (**Fig. 7.2A blue**). This difference can be readily explained by additional residues of the longer construct that contribute to the dipolar spectrum. Signal overlap and the flexibility of the LSm and IDR domains may explain why we observe relatively few additional signals. The observed chemical shift differences are possibly due to the presence of the LSm and IDR-domain in Edc3, which leads to slightly changed environments of the YjeF_N domain. To study changes in protein dynamics upon maturation, we recorded ^1H -detected scalar NH ssNMR spectra on ^{13}C - ^{15}N Edc3 and the solid-phase YjeF_N domain (**Fig. 7.2A middle**). Several additional signals were observed in the FL Edc3 protein (**Fig. 7.2A red**), which can be attributed mainly to the flexible IDR domain and partially to the LSm domain. Counterintuitively, there are also three signals that disappear in the longer sequence (**Fig. 7.2A boxes**). Two of them are Trp side-chain resonances. These resonances might belong to the YjeF_N domain, which exhibit mobility in the isolated domain but become more rigid or exhibit chemical-shift changes in the presence of the N-terminal addition of the IDR and/or LSm domain in the full-length construct. Previously an interaction of the IDR with the YjeF_N domain was observed, where W393 was one of the interacting residues ²².

Utilizing solid-state NMR to investigate mRNA processing bodies

Edc3 (^{15}N , ^{13}C)

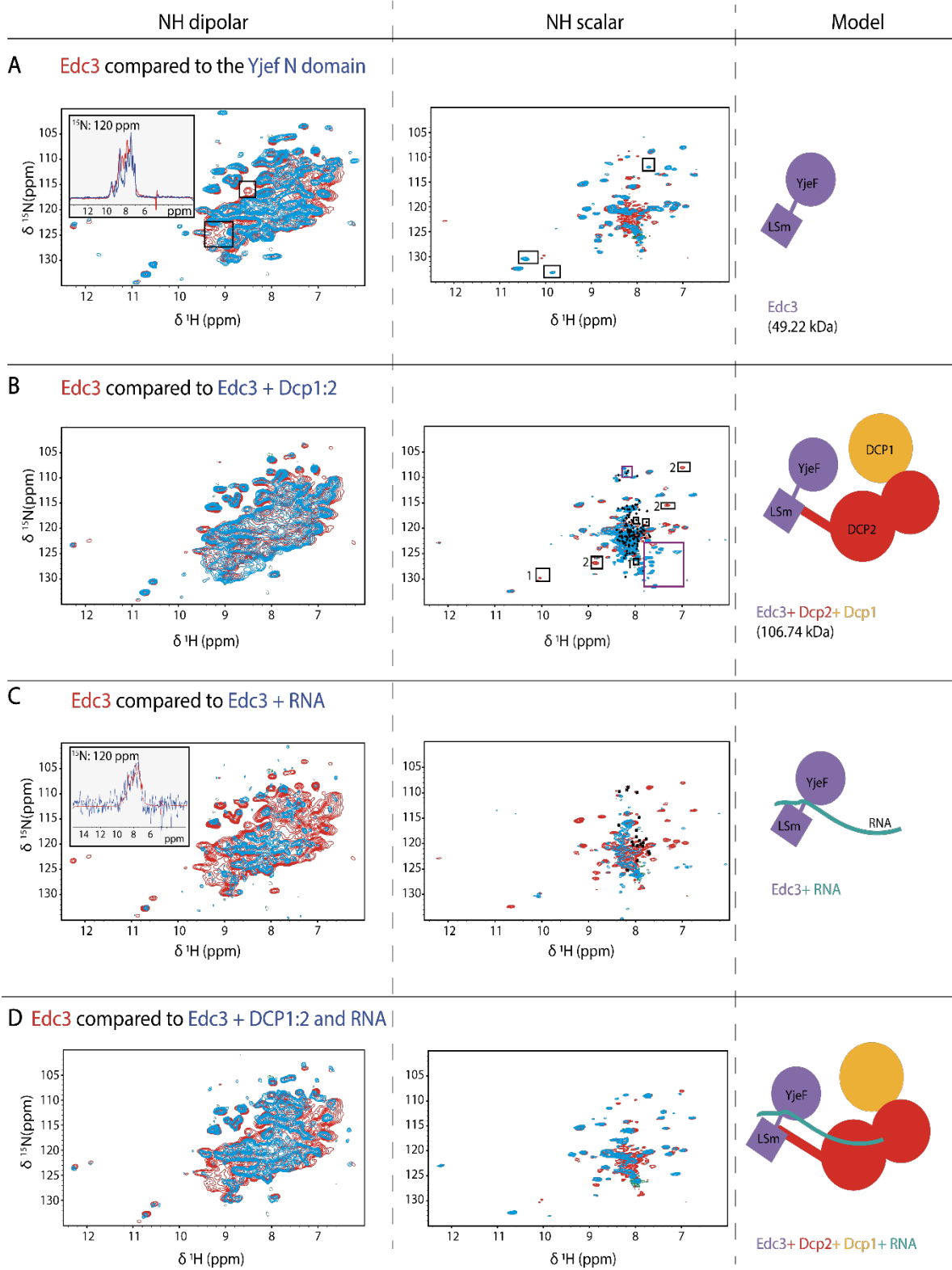


Fig. 7.2: Comparison of full-length [^{13}C , ^{15}N] Edc3 (red spectra) to [^{13}C , ^{15}N] Edc3 in contact with different interaction partners (blue spectra). Dipolar (rigid) NH spectra are displayed on the left side and scalar-based (flexible) NH spectra are shown in the middle panel. On the right panel, models displaying the different states of Edc3 are depicted. **(A)** Comparison of the solid-phase ^{13}C - ^{15}N YjeF N domain with ^{13}C - ^{15}N Edc3 FL. The boxes indicate peaks appearing or disappearing in the longer construct. **(B)** Overlay of ^{13}C - ^{15}N Edc3 in complex with Dcp1:2 and ^{13}C - ^{15}N Edc3. The middle panel shows in addition the solution-state assignments of the IDR domain (black crosses) overlaid with the scalar-NH spectra. Black boxes indicate resonances only present in the absence of Dcp1:2, while purple squares stand for new correlations appearing upon the interaction. The number one on a box indicates a residue from the LSm domain, while two stands for residues stemming from the YjeF_N domain. **(C)** Spectral changes upon addition of RNA to ^{13}C - ^{15}N Edc3. **(D)** Complex of ^{13}C - ^{15}N Edc3 with Dcp1:2 and RNA.

Dcp1:2 rigidifies Edc3

Next, we assessed the changes induced in Edc3 upon Dcp1:2 binding (**Fig. 7.2B**). The experimental dipolar NH ssNMR spectra are in reasonable agreement (**Fig. 7.2B left**) without a significant increase in line width when moving from Edc3 (50 kDa) to the Edc3:Dcp2:Dcp1 complex (106 kDa, monomeric complex). In contrast, we observe spectral changes in the scalar-NH spectrum overlay (**Fig. 7.2B middle**) after the addition of Dcp1:2 to Edc3, indicating the interaction of Dcp1:2 with Edc3. The corresponding residues most likely are located in the folded LSm domain (**marked by squares and the number 1**), as these peaks neither overlap with signals of the IDR (**Fig. 7.2B middle, black crosses**) nor the YjeF_N (**Fig. 7.2A middle, Fig. 7.2B middle, indicated by squares and the number 2**) domains. IDR assignments that are not observed in mature LLPS may belong to residues interacting with YjeF_N and therefore are rigid²². Surprisingly, new peaks appear in the scalar NH spectrum (**purple boxes**), which are neither observed in the FL protein nor in the IDR or YjeF_N. We were not able to assign these peaks to a specific region, but the spectral region suggests that they must result from degraded protein.

The IDR domain becomes rigid in the presence of RNA

The addition of RNA to Edc3 seems to cause significant signal broadening in the dipolar NH spectrum of [¹³C-¹⁵N] Edc3 (**Fig. 7.2C left**). Such a decrease in observed peak intensity in the Edc3 with RNA sample may suggest increased dynamics or conformational changes in the YjeF_N domain. In addition, we cannot exclude the disappearance or chemical-shift changes of other Edc3 signals in the rigid spectrum due to the high signal-to-noise ratio in the recorded spectrum. Drawing general conclusions is therefore challenging. The binding of RNA also leads to the rigidification of the mobile Edc3 domains (**Fig. 7.2C middle**), as several signals disappear in the scalar NH spectrum. A significant amount of these signals can be attributed to certain residues of the IDR domain with the help of solution-state assignments (provided by Sprangers et al.) of this region (**black crosses, Fig. 7.2C middle**). Interestingly, YjeF_N domain residues also rigidify. A more detailed analysis is precluded due to poor spectral resolution.

YjeF_N stays flexible after the addition of RNA and Dcp1:2

Previously, we observed a significant change in Edc3 mobility upon RNA binding and upon Dcp1:2 addition ²². As part of our investigation into RNA and Dcp1:2 interactions with Edc3, we conducted dipolar and scalar NH experiments of matured Edc3 in the presence of both molecules (**Fig. 7.2D**). The dipolar NH spectrum (**Fig. 7.2D left**) gave a similar result as Edc3 in complex with RNA (**Fig. 7.2C left**) possibly including the reappearance of Edc3 signals that were weak in the presence of RNA alone, pointing towards a stabilized Edc3 conformation that largely agrees with free FL Edc3. For the scalar NH spectrum, we observed signal disappearances in the IDR and the LSm, while only the mobile signals of the YjeF_N domain (**see also Fig. 7.2A, middle panel**) remained. Taken together, the addition of RNA and DCP1:2 leads to the rigidification of LSm and IDR domains in the >100 kDa complex.



The Dcp2 fold is preserved in the matured state

To address the conformation of Dcp2 in matured PBs we compared free solid-phase [$^{13}\text{C}(\text{Met}) : ^{15}\text{N}$] labelled protein in complex with Dcp1 (Fig. 7.33 red) to Dcp1:[$^{13}\text{C}(\text{Met})\text{-}^{15}\text{N}$] Dcp2 in the presence of different binding partners in the matured state (**Fig. 7.3 blue**). The presence of Edc3 leads to the formation of LLPS and subsequent maturation^{22,34}. Again, we employed ^1H -detected dipolar NH and CH ssNMR experiments (**Fig. 7.3**). $^{13}\text{C}(\text{Met})$ labelling allowed us to distinguish the conformational state of the enzymatic site of Dcp2 involved in RNA cleavage. As shown previously in solution¹¹, residues M164 and M221 show significant chemical shift changes upon transition between the open and closed state. While the completely open state is more populated in Dcp2 alone, the closed conformation is prevalent in the case of the Dcp1:2 complex and in the case of Dcp1:2 interacting with Edc1. In the RNA-bound state, an active conformation was previously observed¹¹. As indicated in Fig. 7.3A, there is good agreement between free solid-phase Dcp1:2 protein complex (red) and the matured PB state with Dcp1:2 in the presence of FL Edc3 (blue). Hence, the overall fold of Dcp2 is conserved in the matured phase separate. Note that we observe fewer peaks in the NH dipolar spectrum upon Edc3 addition (**Fig. 7.3A, left**), which may reflect conformational or dynamic changes in a subset of Dcp2 resonances. In the latter case, Dcp1:2 with Edc3 might exist in a more dynamic state.

Utilizing solid-state NMR to investigate mRNA processing bodies

Dcp2 (^{15}N , ^{13}C met) : Dcp1

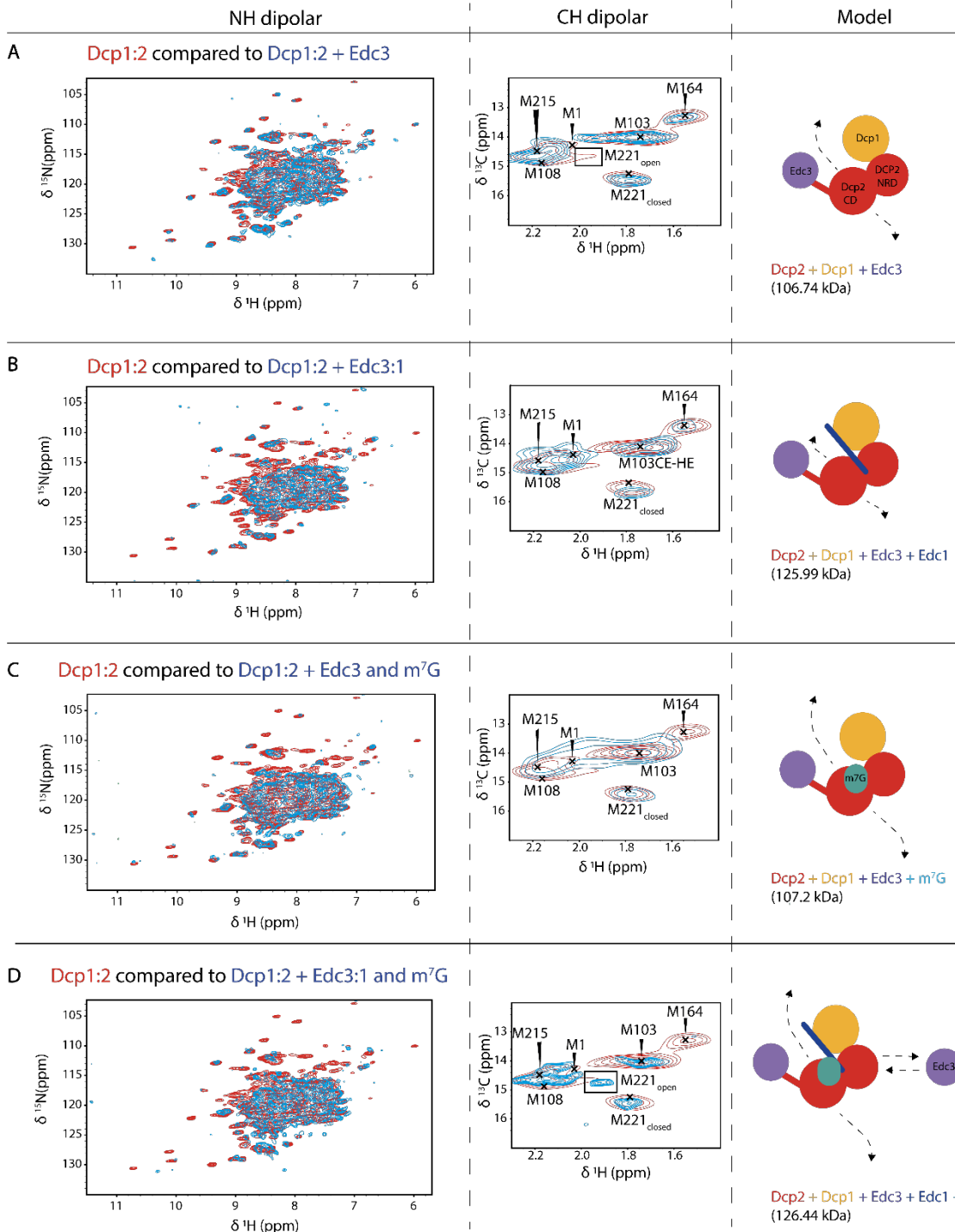


Fig. 7.3: Comparison of $^{13}\text{C}(\text{met})\text{-}^{15}\text{N}$ Dcp2 (in complex with Dcp1) under different conditions (blue spectra) to solid-phase $^{13}\text{C}(\text{met})\text{-}^{15}\text{N}$ Dcp2 (in complex with Dcp1, red spectra). Dipolar (rigid) NH spectra are shown on the left-hand side. The middle panel

Chapter 7

displays results of dipolar (rigid) CH spectra which are overlaid with the Methionine solution-state assignments (provided by Remco Sprangers) of labelled Dcp2 in complex with Dcp1. Models of the measured interactions are shown on the right side. **(A)** Comparison of the solid-phase Dcp1: $^{13}\text{C}(\text{met})\text{-}^{15}\text{N}$ Dcp2 to phase separated Dcp1: $^{13}\text{C}(\text{met})\text{-}^{15}\text{N}$ Dcp2 in complex with Edc3. The box highlights an extra peak in the dipolar CH spectrum. **(B)** Overlay of solid-phase Dcp1: $^{13}\text{C}(\text{met})\text{-}^{15}\text{N}$ Dcp2 and Dcp1: $^{13}\text{C}(\text{met})\text{-}^{15}\text{N}$ Dcp2 in complex with Edc1:3. **(C)** Spectral change upon addition of $m^7\text{G}$ and Edc3 compared to solid-phase Dcp1: $^{13}\text{C}(\text{met})\text{-}^{15}\text{N}$ Dcp2. **(D)** Complex of Dcp1: $^{13}\text{C}(\text{met})\text{-}^{15}\text{N}$ Dcp2 with Edc1:3 and $m^7\text{G}$. The box highlights an additional peak in the dipolar CH-spectrum.

The dipolar Met CH spectrum shows the same peaks for the matured state and the solid-phase protein, indicative of no or minor conformational changes close to the enzymatic pocket of Dcp2. Interestingly, there is an additional peak (black box) in the solid sample, possibly pointing to an additional conformation in our dipolar ssNMR data of the solid-phase protein (**Fig. 7.4A**). Based on a comparison of the CH spectrum to previous CH spectra of Dcp1:2 in solution ¹¹, we tentatively assigned the additional signal to M221 in a different conformation of Dcp2. As a result, the second conformation corresponds to Dcp1:2 in an open conformation in solution, while the assignment represents Dcp1:2 closed in solution ¹¹. As this peak disappears after adding Edc3 the closed conformation might be stabilized by Edc3. Alternatively, the conformational change may locally alter protein dynamics leading to a conformation that is not observable in our dipolar spectra. This notion would be supported by the decrease in the relative intensity of M164 and M221_{open} in the mature state (**Fig. 7.4A**).

Utilizing solid-state NMR to investigate mRNA processing bodies

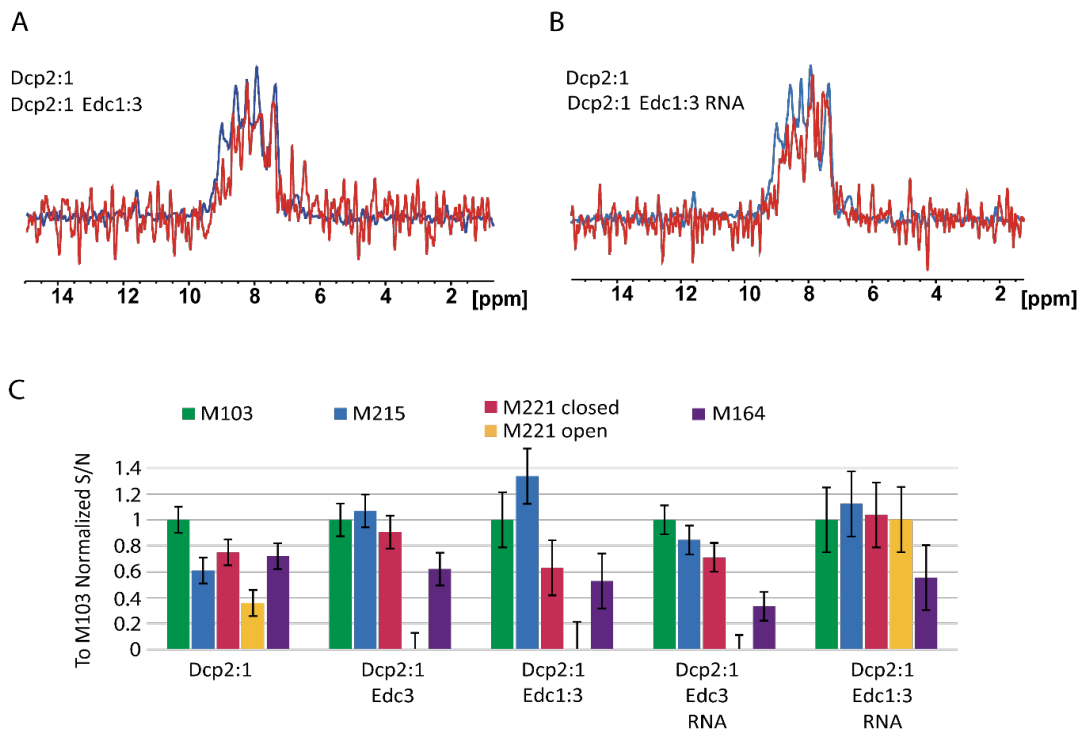


Fig. 7.4: (A) and (B) 1D slices of NH dipolar spectra at ^{15}N value of 120 ppm. (C) To M103 normalized signal-to-noise ratio of methionine signals in the dipolar CH spectrum.

After adding Edc1 to Dcp1:2 and Edc3, the Dcp2 fold seems preserved and the closed confirmation might be populated

Interestingly, the number of observable correlations in the dipolar-NH spectrum of Dcp1:2 Edc1:3 is significantly decreased compared to the Dcp1:2 complex (Fig. 7.3 and 7.4A). This finding may reflect an increase in protein dynamics (which reduces signals in our dipolar spectra) and an increase of conformations present in our ssNMR data. In the latter case, conformational heterogeneity would be increased. The local fold around the labelled Met residues seems to be conserved as the CH spectra show the same correlations (Fig. 7.3B, middle panel). Notably, the intensity distribution seems similar to the one seen for Dcp1:2 and Edc3 (Fig. 7.4C). A more detailed analysis was hindered by the low signal intensity of the large complex (see error on Fig. 7.4C). Nevertheless, we can conclude that the closed state of Dcp2 seems to be more populated in the presence of Edc3 or Edc1:3 complex than in the other subcomplexes.



Dcp1:2 Edc3 with m⁷G might be in the closed state

Adding m⁷G to the Dcp1:2 Edc3 complex leads to less signals in the NH dipolar spectrum compared to Dcp1:2 alone, as well as fewer correlations, while the CH dipolar spectrum shows decreased intensity in M164 compared to the solid phase complex (**Fig. 7.3C**). This points to more structural inhomogeneity compared to the solid-phase sample. However, the CH dipolar spectrum is of limited resolution, which the complex size can partly explain.

Adding m⁷G and Edc1 to Dcp1:2 with Edc3 leads to the stabilization of a more open conformation

The NH spectrum shows a reduction in signal pointing towards more dynamics and more conformations (**Fig. 7.3D left and 7.4B**). There is a strong attenuation of the M164 signal in the CH spectrum, as well as a second peak for M221 (**Fig. 7.3D middle**). This peak is also observed in the solid phase Dcp1:2 form and was assigned to a different, probably active conformation. Hence, the open/active conformation observed in the solid-phase Dcp1:2 might be stabilized in the matured state with both Edc1:3 and m⁷G present.

Discussion

Here we have shown the utility of solid-state NMR (ssNMR) to characterize complex biomolecular systems, i.e., PBs, as large as 126 kDa. By isotopically labelling one of the proteins within the complex and probing rigid and flexible components, our approach allows us to see observe dynamic changes in the processing bodies of *S.pombe*. Furthermore, the combined use of solution and ssNMR enables residue-specific analysis.

Utilizing this approach, our data points to alterations in the PBs central hub enhancer of decapping 3 (Edc3) upon RNA and decapping protein (Dcp1:Dcp2) interaction. When Edc3 interacts with Dcp1:2 and RNA, we observe rigidification of the IDR and

LSm domains. The latter observations are in line with our previous studies that only contained Edc3²². Subsequently, we were able to probe Dcp2 and its activation^{23,26–28}-related states in the mature phase using ssNMR. By introducing [¹³C, ¹⁵N] labelled methionines¹¹, we further observed stabilization of an open/active conformation in the presence of Edc1:3 and m⁷G. The observed dynamics might highlight the importance of the interplay of all these interaction partners for the function of Dcp2 in LLPS. Moreover, these results underline that dynamics are critical in physiological systems but often neglected in structural studies. Further examination of these results would be facilitated by residue-specific assignments of Dcp2 to understand the conformational changes and stabilizations observed in the dipolar NH spectra and may pave the way for the structural study of enzymatic states in the context of LLPS.

Material and Methods

Mutagenesis, Gibson assembly

The genes encoding for Dcp1 and Edc3 were cloned into a modified pET-M11 vector containing an N-terminal, TEV cleavable hexahistidine tag (N-His₆-TEV). The gene encoding for Dcp2 1-270 was generated by fusion at its N-terminus with the maltose binding protein (MBP) via Gibson assembly to enhance the solubility of the protein and it was cloned into a modified pET-M40 vector containing a TEV cleavage site at its N-terminus and a non-cleavable His₆ tag at its C-terminus.

Transformation and protein expression

Edc3, Dcp1 and Dcp2 (residues 1-270) proteins from *S. pombe* were over-expressed in *E. coli* BL21(DE3) Codon PlusRIL cells (Stratagene). To aid purification, Dcp1 and Edc3 proteins contained an N-terminal His₆-TEV tag and Dcp2 1-270 proteins contained a C-terminal His₆ tag and an N-terminal MBP-TEV tag. Thus, pET derived plasmids were transformed into the cells and grown overnight at 37°C on LB agar plates in the presence of chloramphenicol (chl) and kanamycin (kan). Colonies were resuspended in 25 ml LB pre-cultures with kan and chl and grown to an optical



Chapter 7

density OD₆₀₀ of 0.8 -1.0 at 37°C for subsequent inoculation of 50 ml H₂O M9 minimal medium pre-cultures. H₂O M9 pre-cultures were grown at 37°C and centrifuged for 10 minutes at 3500 xg. Pellets were resuspended in 100 µL ¹⁴N or ¹⁵N recycled D₂O pre-culture (60-80 % D₂O) at an OD₆₀₀ of 0.15 and grown overnight at 37°C. Next, 900 mL recycled D₂O M9 medium were added to the pre-culture, cells were grown to an OD₆₀₀ of 0.8 at 37°C and then protein expression over night was induced by addition of 1 mM IPTG and a reduction of temperature to 20°C. For ¹⁵N labelling, ¹⁵NH₄Cl was used as the only nitrogen source and for methionine-ε methyl group labelling, 100 mg/l of [methyl- ¹³CH₃] methionine was added to the cultures 1 h before induction. Cells were harvested 12-18 h after induction by centrifugation at 5000 rpm and 20°C for 20 min and cell pellets were stored at -20°C.

Protein purification

Cell pellets were solubilized in lysis buffer (250 mM NaCl, 25 mM sodium phosphate, pH 7.4, 10 mM imidazole) supplemented with 0.1 % (v/v) Triton X-100, 5 mM MgCl₂, 1 µg/ml Dnase I and 200 µg/ml lysozyme. Cells were lysed by sonication on ice and the lysate was cleared by centrifugation (18000 rpm, 30 min, 4°C) and filtered. The filtered supernatant was applied to a NiNTA-column which was equilibrated in lysis buffer. Purification occurred via a wash step with 5 column volumes of lysis buffer and the subsequent elution of the target protein from the column using elution buffer (250 mM NaCl, 25 mM sodium phosphate, pH 7.4, 300 mM imidazole). The eluted protein was dialysed over night at 4°C against dialysis buffer (125 mM NaCl, 25 mM HEPES, pH 7.3, 0.5 mM EDTA, 1 mM DTT) in the presence of 1 mM DTT and TEV protease to remove the MBP and His6 affinity tags. The His6 tag and the TEV protease were removed from the Dcp1 and Edc3 proteins by a reverse NiNTA column that was equilibrated in lysis buffer and the MBP tag was removed from Dcp2 1-270 by a reverse NiNTA column that was equilibrated in lysis buffer and washed with one column volume 75 % diluted lysis buffer. The protein was then eluted using elution buffer. Dcp1:Dcp2 decapping complexes were formed by combining both

Utilizing solid-state NMR to investigate mRNA processing bodies

proteins in a 2:1 ratio and excess of Dcp1 was removed by and Edc3 was further purified by size exclusion chromatography (Superdex 75; GE Healthcare) in size exclusion buffer (125 mM NaCl, 25 mM HEPES, pH 7.3 and 1 mM DTT).

Fractions containing the Dcp1:Dcp2 complex or Edc3 were combined and concentrated to 200-300 μ l and 500-800 μ M using a spin concentrator. Protein concentrations were determined by absorption measurements at 280 nm using the NanoDrop 2000/2000c (Thermo Scientific) and then protein complexes were formed by combining the labelled protein (Dcp1:Dcp2 or Edc3) with a 1.3-fold molar excess of either the Edc1 peptide (sequence SILYAGPTFTHSPAASNLPITFLHS), and/or 2.5-3-fold molar excess mRNA or m7G and a 1.3-fold molar excess of the unlabelled protein (Dcp1:Dcp2 or Edc3). Phase separation was then induced by adding four volumes of buffer containing no salt (25 mM HEPES pH 7.3, 1 mM DTT), the phase separated protein complex was kept at room temperature for > 1h to form the gel and then the sample was centrifuged for 20 minutes at 16000 xg to collect all gel droplets.

ssNMR experiments

For solid-phase samples, the proteins were lyophilized overnight in water and subsequently rehydrated. Afterwards, they were used to fill 1.3 mm ssNMR rotors. The gel samples were also packed into 1.3 mm rotors. A 1.3 mm triple-resonance $^1\text{H}/\text{X}/\text{Y}$ MAS probe with a proton resonance frequency of 800 MHz was used for the ssNMR experiments. Scalar-based correlation experiments utilized $^1\text{H}^{15}\text{N}$ INEPT transfer. Samples were spun at MAS frequencies of 55, 58 and 60 kHz and the approximate real temperature was 310 K. Cross-polarization (CP) steps with amplitude ramps of 80–100 % and 15 kHz PISSARRO decoupling were employed and hNH and hCH spectra were recorded³⁵. The Bruker TopSpin 3.6.2 software was utilized for spectra processing. Linear prediction in the indirect dimension was utilized. Chemical shift referencing was done by utilizing the water resonance. The spectra were analysed using POKY from NMRFAM-Sparky^{36,37}. In the supplementary table, ssNMR parameters are summarized.



References

1. Bergeron-Sandoval, L.-P., Safaee, N. & Michnick, S. W. Mechanisms and consequences of macromolecular phase separation. *Cell* **165**, 1067–1079 (2016).
2. Wang, B. *et al.* Liquid–liquid phase separation in human health and diseases. *Signal Transduction and Targeted Therapy* **6**, 1–16 (2021).
3. Cho, W.-K. *et al.* Mediator and RNA polymerase II clusters associate in transcription-dependent condensates. *Science* **361**, 412–415 (2018).
4. Gibson, B. A. *et al.* Organization of chromatin by intrinsic and regulated phase separation. *Cell* **179**, 470–484 (2019).
5. Decker, C. J. & Parker, R. P-bodies and stress granules: possible roles in the control of translation and mRNA degradation. *Cold Spring Harbor perspectives in biology* **4**, a012286 (2012).
6. Wang, J. *et al.* A molecular grammar governing the driving forces for phase separation of prion-like RNA binding proteins. *Cell* **174**, 688–699 (2018).
7. Banani, S. F., Lee, H. O., Hyman, A. A. & Rosen, M. K. Biomolecular condensates: organizers of cellular biochemistry. *Nature reviews Molecular cell biology* **18**, 285–298 (2017).
8. Boeynaems, S. *et al.* Protein phase separation: a new phase in cell biology. *Trends in cell biology* **28**, 420–435 (2018).
9. Wu, H. & Fuxreiter, M. The structure and dynamics of higher-order assemblies: amyloids, signalosomes, and granules. *Cell* **165**, 1055–1066 (2016).
10. Murthy, A. C. & Fawzi, N. L. The (un) structural biology of biomolecular liquid-liquid phase separation using NMR spectroscopy. *Journal of Biological Chemistry* **295**, 2375–2384 (2020).
11. Wurm, J. P., Holdermann, I., Overbeck, J. H., Mayer, P. H. & Sprangers, R. Changes in conformational equilibria regulate the activity of the Dcp2 decapping enzyme. *Proceedings of the National Academy of Sciences* **114**, 6034–6039 (2017).
12. Krempl, C. & Sprangers, R. Assessing the applicability of ¹⁹F labeled tryptophan residues to quantify protein dynamics. *Journal of Biomolecular NMR* 1–13 (2023).
13. Baldus, M. Biological solid-state NMR: Integrative across different scientific disciplines. *Journal of Structural Biology: X* **6**, 100075 (2022).
14. Sheth, U. & Parker, R. Decapping and decay of messenger RNA occur in cytoplasmic processing bodies. *Science* **300**, 805–808 (2003).
15. Luo, Y., Na, Z. & Slavoff, S. A. P-bodies: composition, properties, and functions. *Biochemistry* **57**, 2424–2431 (2018).
16. Van Dijk, E. *et al.* Human Dcp2: a catalytically active mRNA decapping enzyme located in specific cytoplasmic structures. *The EMBO journal* **21**, 6915–6924 (2002).
17. Dunckley, T. & Parker, R. The DCP2 protein is required for mRNA decapping in *Saccharomyces cerevisiae* and contains a functional MutT motif. *The EMBO journal* **18**, 5411–5422 (1999).
18. Li, Y. & Kiledjian, M. Regulation of mRNA decapping. *Wiley Interdisciplinary Reviews: RNA* **1**, 253–265 (2010).
19. Kshirsagar, M. & Parker, R. Identification of Edc3p as an enhancer of mRNA decapping in *Saccharomyces cerevisiae*. *Genetics* **166**, 729–739 (2004).
20. Arribas-Layton, M., Wu, D., Lykke-Andersen, J. & Song, H. Structural and functional control of the eukaryotic mRNA decapping machinery. *Biochimica et Biophysica Acta (BBA)-Gene Regulatory Mechanisms* **1829**, 580–589 (2013).

21. Franks, T. M. & Lykke-Andersen, J. The control of mRNA decapping and P-body formation. *Molecular cell* **32**, 605–615 (2008).
22. Damman, R. *et al.* Atomic-level insight into mRNA processing bodies by combining solid and solution-state NMR spectroscopy. *Nature communications* **10**, 1–11 (2019).
23. Fromm, S. A. *et al.* The structural basis of Edc3- and Scd6-mediated activation of the Dcp1: Dcp2 mRNA decapping complex. *The EMBO journal* **31**, 279–290 (2012).
24. Schütz, S., Nöldeke, E. R. & Sprangers, R. A synergistic network of interactions promotes the formation of in vitro processing bodies and protects mRNA against decapping. *Nucleic acids research* **45**, 6911–6922 (2017).
25. Lin, Y., Protter, D. S., Rosen, M. K. & Parker, R. Formation and maturation of phase-separated liquid droplets by RNA-binding proteins. *Molecular cell* **60**, 208–219 (2015).
26. Floor, S. N., Borja, M. S. & Gross, J. D. Interdomain dynamics and coactivation of the mRNA decapping enzyme Dcp2 are mediated by a gatekeeper tryptophan. *Proceedings of the National Academy of Sciences* **109**, 2872–2877 (2012).
27. Mugridge, J. S., Ziemniak, M., Jemielity, J. & Gross, J. D. Structural basis of mRNA-cap recognition by Dcp1–Dcp2. *Nature structural & molecular biology* **23**, 987–994 (2016).
28. Collier, J. mRNA decapping in 3D. *Nature Structural & Molecular Biology* **23**, 954–956 (2016).
29. Valkov, E. *et al.* Structure of the Dcp2–Dcp1 mRNA-decapping complex in the activated conformation. *Nature Structural & Molecular Biology* **23**, 574–579 (2016).
30. Beelman, C. A. *et al.* An essential component of the decapping enzyme required for normal rates of mRNA turnover. *Nature* **382**, 642–646 (1996).
31. Steiger, M., Carr-Schmid, A., Schwartz, D. C., Kiledjian, M. & Parker, R. Analysis of recombinant yeast decapping enzyme. *Rna* **9**, 231–238 (2003).
32. Charenton, C. *et al.* Structure of the active form of Dcp1–Dcp2 decapping enzyme bound to m7GDP and its Edc3 activator. *Nature structural & molecular biology* **23**, 982–986 (2016).
33. Mugridge, J. S., Tibble, R. W., Ziemniak, M., Jemielity, J. & Gross, J. D. Structure of the activated Edc1-Dcp1-Dcp2-Edc3 mRNA decapping complex with substrate analog poised for catalysis. *Nature communications* **9**, 1152 (2018).
34. Fromm, S. A. *et al.* In vitro reconstitution of a cellular phase-transition process that involves the mRNA decapping machinery. *Angewandte Chemie International Edition* **53**, 7354–7359 (2014).
35. Weingarth, M., Bodenhausen, G. & Tekely, P. Low-power decoupling at high spinning frequencies in high static fields. *Journal of Magnetic Resonance* **199**, 238–241 (2009).
36. Lee, W., Rahimi, M., Lee, Y. & Chiu, A. POKY: a software suite for multidimensional NMR and 3D structure calculation of biomolecules. *Bioinformatics* **37**, 3041–3042 (2021).
37. Lee, W., Tonelli, M. & Markley, J. L. NMRFAM-SPARKY: enhanced software for biomolecular NMR spectroscopy. *Bioinformatics* **31**, 1325–1327 (2015).



Supplements:**Supplementary Table:** Overview of the solid-state NMR parameters

Sample	Experiment	Scans	Acquisition time in ms (Direct-/indirect dimension)	Window Function	MAS (kHz)	Figure
Dcp1 :Dcp2	NH dipolar	320	22/9	Qsine (3)	58	3
	CH dipolar	320	23/9	Qsine (2.5)	58	3
Dcp1 :Dcp2 + 1.3 x Edc3 FL	NH dipolar	640	22/9	Qsine (3)	60	3A
	CH dipolar	640	23/9	Qsine (2.5)	60	3A
Dcp1 :Dcp2 + 1.5 x Edc1 + 1.5 x Edc3	NH dipolar	1280	22/9	Qsine (3)	58	3B
	CH dipolar	640	23/9	Qsine (2.5)	58	3B
Dcp1 :Dcp2 + 1.5 x Edc3 + 4 x m ⁷ GDP	NH dipolar	892	22/9	Qsine (3)	60	3C
	CH dipolar	1152	23/9	Qsine (2.5)	60	3C
Dcp1 :Dcp2 + 1.5 x Edc1 + 4 x m ⁷ GDP + 1.2 x Edc3 FL	NH dipolar	512	22/9	Qsine (3)	60	3D
	CH dipolar	1792	23/9	Qsine (2.5)	60	3D
Edc3 FL	NH dipolar	1984	20/7	Qsine (3)	60	2
	NH scalar	576	20/20	Qsine (3)	60	2
Edc3 YjeF_N	NH dipolar	1792	20/7	Qsine (3)	60	2A
	NH scalar	640	20/20	Qsine (3)	60	2A
Edc3 FL + 1.1 x Dcp1:Dcp2	NH dipolar	1984	20/7	Qsine (3)	55	2B
	NH scalar	512	20/20	Qsine (3)	55	2B
Edc3 FL + 2.5 x 30nt RNA	NH dipolar	6528	20/7	Qsine (3)	60	2C
	NH scalar	1248	20/20	Qsine (3)	60	2C
Edc3 FL + 1.1 x Dcp1:Dcp2 + 2.5 x 30nt RNA	NH dipolar	2688	20/7	Qsine (3)	60	2D
	NH scalar	832	20/20	Qsine (3)	60	2D

Chapter 8

Discussion and future perspectives



Discussion and future perspectives

Studying large biomolecular systems is still considered a huge challenge. While cryogenic electron microscopy (cryo-EM) and X-ray crystallography offer an excellent understanding of rigid entities. X-ray crystallography can only give limited information about dynamics and cryo-EM can deliver information about large scale motion and states, but often lacks in atomic-level structural data and internal motion. Classical solution-state nuclear magnetic resonance (NMR) spectroscopy on the other hand requires fast tumbling of molecules and is therefore hindered by molecular size. Through the use of optimized isotope labelling techniques and NMR experiments, the size limit for solution-state NMR can be extended up to the MDa range ^{1,2}. Still, the cell contains many even larger systems such as microtubules (MTs) or condensates that are not amenable by solution-state NMR. Hence, solid-state NMR (ssNMR) has become a valuable tool in overcoming these challenges by providing structural information and molecular dynamics of complex biomolecules in such very large assemblies. In this century, additional advances in this technique like ultra-high field NMR and proton-detected ssNMR led to a drastic improvement in spectral resolution and sensitivity ³⁻⁵. This allowed the investigation of several systems that posed huge obstacles to other structural biology methods⁶ and even the study of proteins in their native environments as cells ⁷ or biomembranes ⁸. Examples of these systems are membrane proteins ⁹, but also liquid-liquid phase separation (LLPS) ¹⁰ or MTs ¹¹. LLPS like mRNA processing bodies (PBs) have been studied extensively, but their dynamic character has been largely neglected by X-ray crystallography hindering the understanding of their formation and enzymatic function in the cell. MTs on the other hand have been investigated to understand their interaction with microtubule-associated proteins (MAPs). However, many of these studies that focus mainly on cryo-EM are complicated by the fact that unrestrained flexibility tends to average out the electron density. Nonetheless, the importance of these interactions has been shown for example at the tubulin carboxy-terminal tails (CTT), whose cleavage leads to decreased binding affinity in several

MAPs and whose extensive post-translational modifications are reported to change cellular functioning.

Chapters 2- 6 presented the process of obtaining residue-specific information on the binding of two MAPs to MTs. They build on previous progress in our lab on the study of these systems by Yanzhang Luo ^{11,12}. In **Chapter 7**, it was shown by ssNMR that it is not always possible to draw a clear picture of complex molecular systems based on their rigid entities. This study builds on the work of Damman et al., who were able to conduct ssNMR on the central hub of these LLPS ¹⁰.

To elucidate the process of sample preparation for ssNMR on MTs-MAP systems **Chapter 2** reported the purification and solution-state NMR characterisation of the microtubule-associated protein 7 (MAP7) microtubule-binding domain (MTBD). This chapter also showed the dynamic and complex behaviour of a MAP in solution, which might be significant for its function in the cell. MAP7 is associated with poor prognosis in several cancers as it was associated with increased metastasis ^{13,14}. Additionally, it has been found to stabilize MTs and to recruit the motor protein kinesin-1 ¹⁵. We showed that the MTBD consists of a long alpha-helix with a flexible hinge. The alpha-helix starts with a helix-capping motif. Aside from this, we assigned the amino-acid sequence of the protein to its solution-state spectra and studied its heterogeneity by size-exclusion chromatography coupled with multi-angle light scattering (sec-MALS), revealing monomer-dimer exchange and aggregation. Most likely, this behaviour is caused by specific residue motifs in the protein. In general, such an NMR characterization of an MAP represents a good workflow prior to the study of protein interactions. Also, it highlights the complexity and diversity of MAPs by characterizing a protein with a distinct structural behaviour. Further studies on the monomer-dimer equilibrium of MAP7 might be of interest, as it could have implications for its binding mechanism on MTs. Due to the fact that overexpression of MAP7 has been associated with several forms of cancer ^{13,14} it may be interesting to investigate concentration-dependent oligomerization. An in-vivo study of the



system might provide a deeper understanding of the biological relevance and possible roles of the system in protein regulation.

A method for producing isotopically labelled MTs for ssNMR is discussed in **Chapter 3**. This procedure allowed the first magic-angle spinning (MAS) high-field ssNMR experiments on human microtubules. The purification builds on the previous protocol for unlabelled tubulin. Despite a small yield, the protocol results in sufficient yield for ssNMR studies, which can record the signals from the CTTs. In light of the fact that CTTs are the site of numerous post-translational modifications (PTMs) and are critical for numerous MAP-MTs interactions, their study is of high interest ^{16,17}. Incorporating these PTMs in future studies might greatly expand our understanding of MTs regulation in health and disease. This additionally provides the possibility to study the modifying enzymes, as changes in the CTTs can now be studied by ssNMR. Moreover, we can look at the binding site on the MTs filament and investigate the binding register of different MAPs on MT. With dynamic-nuclear polarization (DNP) NMR on ¹⁵N labelled MTs and ¹³C labelled MAP, the binding site can be directly observed. Further characterization of the ssNMR spectra, like isotopically labelled MTs, might be necessary to understand the spectroscopically observed changes in depth. It is interesting to note that recent advances in ssNMR hardware are already offering possibilities to further understand these systems. Using 0.7 mm MAS rotors will reduce the sample amount needed and allows spinning at ultra-fast speeds of over 100 kHz. This will enable recording high-resolution proton-detected ssNMR spectra. Additional utilization of 1.2 GHz ultra-high field NMR magnets can further increase sensitivity and resolution.

In **Chapter 4** we further worked on the progress of optimizing the recording of ssNMR by designing a pulse sequence that facilitates the three-dimensional NMR analysis of complex biomolecular systems. By utilizing a ¹³C-¹³C-¹H correlation pulse sequence we were able to distinguish resonances stemming from protein backbone and sidechains that were otherwise overlapping. By conducting these experiments, we were able to record high-resolution spectra of complex molecular systems that

were not deuterated. Further combinations with sequential experiments such as HNC_oCA and HNC_a might allow for full sequential assignments of previously overlapping signals ^{18,19}.

With the optimizations described in the previous chapters, we conducted experiments on MAP7 bound to MTs. The data is presented in **Chapter 5**. We focused our research on the MTBD of the protein that we previously characterised in its free form in solution. Combination of solution- and solid-state NMR with cryo-EM enabled us to observe both strong as well as weak dynamic interactions that contribute to complex formation. The NMR results confirmed and extended, on an atomic level, a previously suggested binding register by cryo-EM. Based on the experiments MAP7 MTBD binds MTs with an alpha-helix that extends C-terminally beyond the protein fold seen in solution. This extension might increase stabilization of the MAP7-MT complex as it spans across tubulin heterodimers. Further experiments focusing on an optimized ratio of MAP7 to MT might increase our understanding of the aggregation process of MAP7 observed in solid-state NMR spectra. This could potentially help obtain improved spectra. Also, studying the $\alpha\beta$ tubulin heterodimer stabilized with the stathmin-like domain ²⁰ with low concentrations of labelled MAP7 in a high salt buffer could be utilised to study the electrostatic interaction in more detail with solution-state NMR, as this set-up might decrease the substantial disappearance of the MAPs signal through binding. Furthermore, our data provide novel insight regarding the MTs C-terminal tails (CTT) binding sites. As previously reported, CTTs bind to a variety of MAPs and are involved in diseases. Due to their flexibility, cryo-EM and crystallography were limited in resolving them. Here we designed peptides with the CTT sequence and observed where they are in contact with MAP7. By selective labelling schemes, it might be possible to probe certain interacting regions of the protein in order to provide additional atomic information. In addition, labelling the CTT peptide might facilitate a deeper understanding of their binding register. The CTTs peptides might also be an excellent starting point to study post-translational modifications (PTMs) and their resulting impact on MTs-MAP interactions ^{16,17}. Furthermore, longer MAP7



constructs might give more insights into the importance of flanking regions and possibly the mechanism of the kinesin-1-MTs interaction promoted by the MAP. Lastly, with this approach further MAP-MTs systems might be studied in the future, allowing us to understand the complex interactions that are fundamental for a cell's function in more detail.

Another demonstration of the power of NMR for the study of MTs MAP interactions was given in **Chapter 6**. Here we presented the interaction of the MAP Tau with MTs. With our detailed analysis, we extend on previous research studying the Tau-MTs interaction well known for its association with Alzheimer's disease (ADs) ²¹⁻²³. We have developed a model, that suggests a zipper-like, fuzzy interaction of the biopolymer with the Tau K32 construct. This construct comprises a proline-rich domain, four repeat domains and a pseudo-repeat domain. According to our findings, the strongest interaction may occur in R3-R', while the P2 region might not be affected. This is in line with the model proposed by El Mammeri et al. ²⁴. Researchers may be able to use these findings to design drugs that alter the Tau-MTs interaction in the case of ADs. We also identified residues on both the MTs and MAP sides that seem to be implicated in the tubulin CTT-Tau interaction. These findings underline the power of the combination of solution- and ssNMR in understanding these complex systems.

Lastly, in **Chapter 7** we analysed the interaction in PB complexes up to a molecular weight of 126 kDa by ssNMR. We investigated the complex behaviour of the enhancer of decapping (Edc3) following up on a previous study by Damman et al. ¹⁰. Our experiments confirmed the previously observed rigidification of the intrinsically disordered region (IDR). We further showed that the decapping proteins 1 and 2 (Dcp1:2) interact with Edc3's N-terminal LSm domain. Additionally, we studied the conformational state of the decapping protein 2 (Dcp2). By selective isotope labelling of the methionines of the protein we found conformational changes previously observed by solution-state NMR and crystallography ²⁵⁻²⁷. We found that our system is rather dynamic in the matured, gel-like phase, with multiple

conformations populated by the whole protein. For both Dcp2 and Edc3 we observed that the overall fold is preserved, which might be critical for the reversibility of LLPS. These findings have significant implications for our understanding of proteins in LLPS, as they highlight the importance of both flexibility as well as structural stability. Additionally, they might provide a starting point for studying the fibrilization of those systems as this process is associated with neurodegenerative diseases. The results may also give us new targets for tackling the formation of aggregates or markers for identifying these diseases.

General conclusions

In recent years there has been huge progress in the field of NMR, enabling us to study more and more complex systems at an atomic level. Advances like higher magnetic fields combined with proton detection and specific labelling techniques allow for the distinction of signals previously overlapping using significantly reduced sample quantities. As a result of the previously described progress, we gained insight into complex, dynamic molecular systems that were otherwise inaccessible.



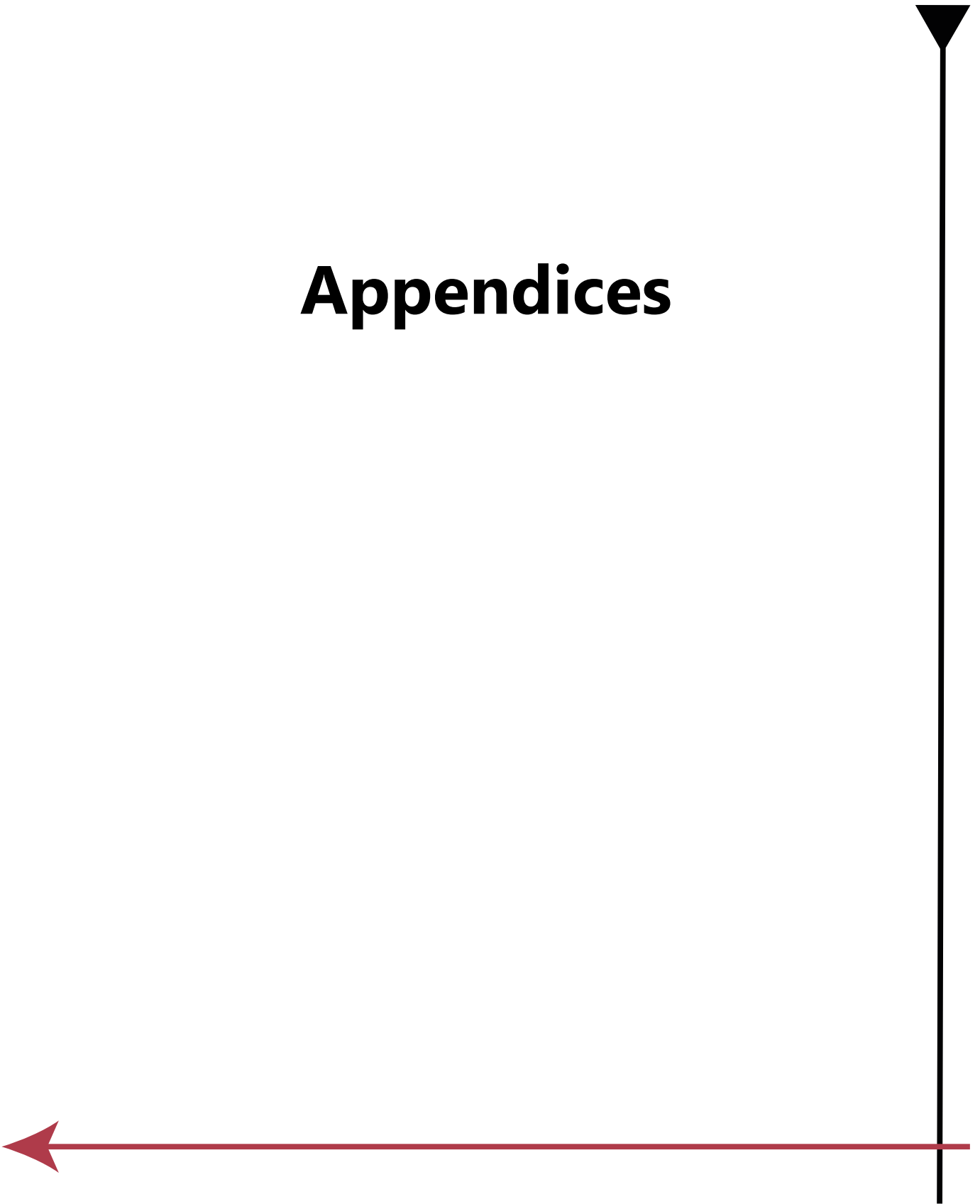
References

1. Mainz, A. *et al.* NMR spectroscopy of soluble protein complexes at one mega-dalton and beyond. *Angewandte Chemie International Edition* **52**, 8746–8751 (2013).
2. Kay, L. E. Solution NMR spectroscopy of supra-molecular systems, why bother? A methyl-TROSY view. *Journal of Magnetic Resonance* **210**, 159–170 (2011).
3. Chevelkov, V., Rehbein, K., Diehl, A. & Reif, B. Ultrahigh resolution in proton solid-state NMR spectroscopy at high levels of deuteration. *Angewandte Chemie International Edition* **45**, 3878–3881 (2006).
4. Vinogradov, E., Madhu, P. K. & Vega, S. Strategies for high-resolution proton spectroscopy in solid-state NMR. *New Techniques in Solid-State NMR* 33–90 (2005).
5. Grant, C. V., Wu, C. H. & Opella, S. J. Probes for high field solid-state NMR of lossy biological samples. *Journal of Magnetic Resonance* **204**, 180–188 (2010).
6. Baldus, M. Biological solid-state NMR: Integrative across different scientific disciplines. *Journal of Structural Biology: X* **6**, 100075 (2022).
7. Narasimhan, S. *et al.* Characterizing proteins in a native bacterial environment using solid-state NMR spectroscopy. *Nature protocols* **16**, 893–918 (2021).
8. Ghassemi, N. *et al.* Solid-state NMR investigations of extracellular matrixes and cell walls of algae, bacteria, fungi, and plants. *Chemical reviews* **122**, 10036–10086 (2021).
9. Ladizhansky, V. Applications of solid-state NMR to membrane proteins. *Biochimica et Biophysica Acta (BBA)-Proteins and Proteomics* **1865**, 1577–1586 (2017).
10. Damman, R. *et al.* Atomic-level insight into mRNA processing bodies by combining solid and solution-state NMR spectroscopy. *Nature communications* **10**, 1–11 (2019).
11. Luo, Y. *et al.* Solid-State NMR Spectroscopy for Studying Microtubules and Microtubule-Associated Proteins. in *Structural Proteomics* 193–201 (Springer, 2021).
12. Luo, Y. *et al.* Direct observation of dynamic protein interactions involving human microtubules using solid-state NMR spectroscopy. *Nature Communications* **11**, 18 (2020).
13. Wang, X., Cao, X., Wu, Y. & Chen, T. MAP7 promotes proliferation and migration of breast cancer cells and reduces the sensitivity of breast cancer cells to paclitaxel. *Journal of Chemotherapy* 1–9 (2022).
14. Blum, C. *et al.* The expression ratio of Map7/B2M is prognostic for survival in patients with stage II colon cancer. *International journal of oncology* **33**, 579–584 (2008).
15. Chaudhary, A. R. *et al.* MAP7 regulates organelle transport by recruiting kinesin-1 to microtubules. *Journal of Biological Chemistry* **294**, 10160–10171 (2019).
16. Gadadhar, S., Bodakuntla, S., Natarajan, K. & Janke, C. The tubulin code at a glance. *Journal of cell science* **130**, 1347–1353 (2017).
17. Janke, C. & Magiera, M. M. The tubulin code and its role in controlling microtubule properties and functions. *Nature Reviews Molecular Cell Biology* **21**, 307–326 (2020).
18. Falk, A. S. & Siemer, A. B. Dynamic domains of amyloid fibrils can be site-specifically assigned with proton detected 3D NMR spectroscopy. *Journal of biomolecular NMR* **66**, 159–162 (2016).
19. Ikura, M., Kay, L. E. & Bax, A. A novel approach for sequential assignment of proton, carbon-13, and nitrogen-15 spectra of larger proteins: heteronuclear triple-resonance three-dimensional NMR spectroscopy. Application to calmodulin. *Biochemistry* **29**, 4659–4667 (1990).
20. Gigant, B. *et al.* The 4 Å X-ray structure of a tubulin: stathmin-like domain complex. *Cell* **102**, 809–816 (2000).
21. Avila, J. Tau phosphorylation and aggregation in Alzheimer's disease pathology. *FEBS letters* **580**, 2922–2927 (2006).

22. Iqbal, K., Liu, F., Gong, C.-X. & Grundke-Iqbal, I. Tau in Alzheimer disease and related tauopathies. *Current Alzheimer Research* **7**, 656–664 (2010).
23. Gao, Y., Tan, L., Yu, J.-T. & Tan, L. Tau in Alzheimer's disease: mechanisms and therapeutic strategies. *Current Alzheimer Research* **15**, 283–300 (2018).
24. El Mammeri, N., Dregni, A. J., Duan, P., Wang, H. K. & Hong, M. Microtubule-binding core of the tau protein. *Science Advances* **8**, eabo4459 (2022).
25. Charenton, C. *et al.* Structure of the active form of Dcp1–Dcp2 decapping enzyme bound to m⁷GDP and its Edc3 activator. *Nature structural & molecular biology* **23**, 982–986 (2016).
26. Krempf, C. & Sprangers, R. Assessing the applicability of ¹⁹F labeled tryptophan residues to quantify protein dynamics. *Journal of Biomolecular NMR* 1–13 (2023).
27. Mugridge, J. S., Tibble, R. W., Ziemniak, M., Jemielity, J. & Gross, J. D. Structure of the activated Edc1-Dcp1-Dcp2-Edc3 mRNA decapping complex with substrate analog poised for catalysis. *Nature communications* **9**, 1152 (2018).



Appendices



English summary

Cells rely on various biomolecular interactions and dynamics to perform their functions. The interacting building blocks range from small molecules with a one-to-one stoichiometry and well-defined binding affinity to complex and dynamic molecular networks such as membrane-less organelles or the cell's cytoskeleton. These systems play a significant role in biological function and the development of diseases such as cancer or neurodegeneration. Thus, understanding their inter- and intra-molecular interactions is crucial. X-ray crystallography and cryogenic-electron microscopy (cryo-EM) enable the atomic investigation of these complexes, by largely probing static states. As a result, insight into the role of dynamics, molecular subspecies or heterogeneity is often limited. Additionally, these structural biology techniques often rely on in-vitro sample preparations, which may lead to an incomplete view. Nuclear magnetic resonance (NMR) spectroscopy, however, is unique, as it can probe at dynamic systems under physiological conditions. Additionally, by utilizing solid-state NMR (ssNMR), it becomes possible to study complexes, as this method is not size limited. This thesis presents a study of complex biomolecular systems by means of NMR. We focused on the system of microtubules (MTs) and their interactions with microtubule-associated proteins (MAPs) as they are essential to cellular processes such as cell division, intracellular transport or cell structure. Moreover, we studied the gel-like phase of mRNA processing bodies (PBs) of *S. Pombe* which are involved in mRNA homeostasis.

Chapter 2 presents the characterization of the microtubule-binding domain (MTBD) of microtubule-associated protein 7 (MAP7). NMR resonance assignment for this protein were obtained in solution and its secondary structure was characterized. We obtained an alpha-helical fold and could define the protein's helicity throughout the sequence. By size-exclusion chromatography coupled with multi-angle light scattering, we further investigated the protein's oligomeric state. Taken together, the data suggest a monomer-dimer equilibrium.

In **Chapter 3** we provided a protocol to isotopically label MTs for ssNMR experiments. Subsequently, we also reported NMR results obtained using dynamic nuclear polarization (DNP) ssNMR.

A novel through-bond hCCH pulse sequence to study complex biomolecular systems was discussed in **Chapter 4**. This sequence is applicable to High-resolution Magic-Angle Spinning ssNMR and uses proton detection. As an example, we applied the sequence to a labelled Tau K32 protein sample in a complex with MTs and the fungal cell wall of *S. commune*.

Building on these results, we examined in **Chapter 5** the interaction of MAP7s MTBD with MTs. Furthermore, we combined this approach with cryo-EM and confirmed our observations with fluorescence anisotropy and solution-state NMR experiments. Combination of these results allowed us to obtain atomic information on the binding of MAP7, which suggests that it forms an elongated alpha-helix upon binding to MTs. By designing peptides compromising tubulin carboxy-terminal tails, we also studied their interaction with MAP7 by solution-state NMR. In full accordance and complementary to previous ssNMR studies on labelled MTs in complex with unlabelled MAP7 ¹ we found that both α - and β -CTTs interact with MAP7 and we were able to pinpoint specific amino-acid stretches in MAP7 that are responsible for this interaction. Together our findings led to a detailed model of the MAP7-MT complex which is formed by both strong as well as weak dynamic protein-protein interactions between MAP7 and the structured and unstructured regions of the MTs.

A similar approach was employed to study the Tau-MTs interaction in **Chapter 6**. SsNMR was used to probe the rigid and flexible regions of the complex, studying MAP and MTs interactions. Thus, we gained information about the Tau binding register that allowed us to extend a model in which Tau interacts with MTs in a zipper-like manner. Moreover, we investigated the tubulin carboxy-terminal tail interaction with the protein, which led to the identification of involved residues in both interaction partners.



Summary

In Chapter 7, we explored another complex and dynamic molecular system that exhibits important dynamics. We conducted CH and NH dipolar- and scalar-ssNMR experiments to investigate protein structures, conformations and dynamics in PBs. Our data shows that in a gel-like state, the overall protein conformations of the enhancer of decapping 3 (Edc3) and the decapping protein 2 (Dcp2) are conserved. We were also able to study dynamic changes upon protein interactions in this state and found that Dcp2 might persist in a dynamic equilibrium of conformations.

To summarize, this thesis presents an approach to studying complex biomolecular systems by solid-state NMR in combination with other methods and highlights the importance of protein dynamics for biomolecular interactions and the formation of complexes.

Reference:

1. Luo, Y. *et al.* Direct observation of dynamic protein interactions involving human microtubules using solid-state NMR spectroscopy. *Nature Communications* **11**, 18 (2020).

Nederlandse Samenvatting

Cellen zijn afhankelijk van verscheidene biomoleculaire interacties en dynamica om hun functies te kunnen uitoefenen. De bouwstenen van de cel hebben veel interacties met elkaar. Deze omvatten alles van kleine moleculen met een één op één stoichiometrie en een goed-gedefinieerde bindings-affiniteit tot complexe en dynamische moleculaire netwerken zoals celorganellen zonder membraan of het cytoskelet van de cel. Deze systemen spelen een belangrijke rol in de biologische functie en de ontwikkeling van ziekten zoals kanker of neurodegeneratie. Hierom is het begrijpen van de inter- en intra- moleculaire interacties cruciaal. Met röntgenkristallografie en cryo-elektronenmicroscopie (cryo-EM) is het mogelijk om grotendeels statische toestanden van deze complexen op atomaire schaal te onderzoeken. Inzicht in de rol van dynamica, moleculaire subpopulaties of heterogeniteit blijft hierdoor veelal beperkt. Bovendien worden de samples voor deze structurele biologische technieken vaak niet onder fysiologische condities, *in vitro*, gemaakt. Nucleaire Magnetische Resonantie (NMR) spectroscopie is uniek omdat het ons in staat stelt om dynamische systemen onder fysiologische omstandigheden te onderzoeken. Verder is het met vaste stof-NMR mogelijk om complexen te bestuderen zonder limitaties voor het formaat van de complexen. Dit proefschrift presenteert een studie naar complexe biomoleculaire systemen door middel van NMR. We hebben ons gericht op het systeem van microtubuli (MT) en hun interacties met microtubuli-geassocieerde eiwitten (MAP's), omdat deze eiwitten essentieel zijn voor cellulaire processen zoals celdeling, intracellulair transport en het behoud van de celstructuur. Bovendien hebben we de gel-achtige fase van mRNA processing bodies (PBs) of *S.Pombe* die betrokken zijn met mRNA homeostase bestudeerd.

Hoofdstuk 2 beschrijft de karakterisering van het microtubuli-bindend domein (MTBD) van microtubuli-geassocieerd eiwit 7 (MAP7). NMR-resonantie toewijzing van dit eiwit werd verkregen met vloeistof-NMR en de secundaire structuur werd gekarakteriseerd. Hieruit verkregen we een alfa-helixvouwing die door de eiwitsequentie kon worden gedefinieerd. Door middel van gelchromatografie, samen



Summary

met multi-angle light scattering onderzochten we de oligomerische toestand van het eiwit. Tezamen suggereren de data een monomeer-dimeer evenwicht.

In **Hoofdstuk 3** beschrijven we een protocol om MT met isotopen te labelen voor vaste stof-NMR experimenten. We rapporteerden ook de NMR-resultaten die verkregen waren met dynamische nucleaire polarisatie (DNP) vaste stof-NMR.

In **Hoofdstuk 4** behandelen we een nieuwe through-bond hCCH pulssequentie om complexe biomoleculaire systemen te bestuderen. Deze sequentie is toepasbaar op hoge-resolutie Magic-Angle Spinning vaste stof-NMR en maakt gebruik van protondetectie. Zo hebben wij deze sequentie onder andere toegepast op een gelabeld Tau K32-eiwitsample in een complex met MT en de celwand van de schimmel *S. commune*.

Voortbouwend op deze resultaten onderzochten we in **Hoofdstuk 5** de interactie van MAP7s MTBD met MT. We combineerden deze aanpak met cryo-EM en bevestigden onze observaties met fluorescentie anisotropie en vloeistof-NMR. De gecombineerde resultaten geven informatie op atomaire schaal en suggereren dat MAP7 een verlengde alfa-helix vormt bij binding aan MT. We ontwierpen peptiden met de sequentie van de c-terminale staart van tubuline. Deze gebruikten we om de interactie met MAP7 in vloeistof-NMR te onderzoeken. In volledige overeenstemming en complementair met eerdere vaste stof-NMR onderzoeken naar gelabelde MT in complex met niet-gelabeld MAP7 vonden we dat zowel de α - en β -C-terminale staarten interacties aangaan met MAP7. We konden specifieke delen van de aminozuurketen in MAP7 aanwijzen die verantwoordelijk zijn voor de interactie. Onze bevindingen leidden naar een gedetailleerd model van het MAP7-MT complex, dat zowel door sterke als zwakke dynamische eiwit-eiwit interacties tussen MAP7 en de gestructureerde en ongestructureerde regio's van de MT wordt gevormd.

Een vergelijkbare aanpak werd gebruikt om de interactie tussen Tau en MT te bestuderen, zoals beschreven in **Hoofdstuk 6**. Vaste stof-NMR werd gebruikt om de rigide en flexibele gebieden van het complex en MAP-MT interacties te onderzoeken. We verkregen informatie over het bindingsregister van Tau waarmee

we een model konden uitbreiden waarin Tau als een rits interacties met MT's aangaat. Bovendien onderzochten we de interactie van de C-terminale staart van tubuline met Tau, wat leidde naar de identificatie van de betrokken aminozuren in beide interactiepartners.

In **Hoofdstuk 7** hebben we een ander complex en dynamisch moleculair systeem onderzocht dat belangrijke dynamiek vertoont. We hebben CH en NH dipolaire and scalaire vaste stof-NMR experimenten uitgevoerd om de eiwitstructuren, conformaties en dynamieken te onderzoeken in PBs. Onze data laten zien dat de eiwit conformaties van de 'enhancer of decapping 3' (Edc3) en van 'decapping protein 2' (Dpc2) in de gel-achtige fase geconserveerd zijn. We konden ook dynamische veranderingen zien wanneer eiwit interacties plaatsvonden in deze gel-achtige fase en we vonden dat Dcp2 mogelijk in een dynamisch evenwicht van meerdere conformaties bestaat.

Samengevat, dit proefschrift presenteert een methode om complexe biomoleculaire systemen te bestuderen met vaste stof-NMR in combinatie met andere methoden en benadrukt het belang van eiwit dynamica in biomoleculaire interacties en in de formatie van complexen.



Acknowledgments

Life is an adventure and a PhD is a journey. But even if I am the narrator of this book, it took way more than me to get it to what it is now. A PhD is first and foremost regarded as an opportunity to gain knowledge, but it is also a time for personal development. Luckily, I had a lot of people that helped me tremendously in all aspects of a PhD. I would now wish to thank you all, all the people that I met along the way and who were and are there for me.

First and foremost, I want to express my gratitude towards my supervisor **Marc** for the opportunity to do my PhD in his research group. Thank you also for the informative and fruitful discussions about our research and for always having the patience to let me figure out experiments.

Next, I want to express my gratitude to all the people from the NMR department with whom I was allowed to work. **Hugo**, I want to thank you for our enjoyable discussions and for looking after me despite the fact that I was not really your responsibility. You gave me a lot of helpful insights and suggestions along the way. You have deep knowledge and I admire how you combine biochemistry and NMR experiments to get the most out of projects. I also want to thank you for making the set-up of solution-state experiments so accessible and for always being willing to help out if it got a bit more complex. Apart from that I really enjoy your personality and heartfelt honesty. **Gert**, I really believe you are a nice person, with quite an enjoyable view on things. Moreover, I want to acknowledge **Markus** for his highly appreciated inputs on recording ssNMR experiments.

Also an immense thank you to **Raymond**. You are not only a technician, but you are also the manager of our lab and you are a very helpful person, always helping out everyone with everything. My deepest respect to you. I wish you all the best, you deserve it. **Geeske** a heartfelt thank you for always being unbelievably supportive. You are a great help to all of the people who spend time in the Bloembergen Gebouw.

Acknowledgments

I am also grateful to all the people I had the privilege of working with. Therefore I also want to thank my collaborators **Mamata** and **Carolyn** from London, who partnered with me through the MAP7 project. I really enjoyed the fruitful discussions we had and I also really liked the rational and calm character of yours. Additionally, I would like to thank **Remco** and **Christina** for the efficient collaboration on the LLPS project. It was by far not always easy, but thanks to you we were able to continue.

Now I want to thank all the members and former members of Marc's ssNMR group with whom I had the honour and pleasure to work with. First and foremost, thank **Anamika**. You have not only been the greatest office mate and co-worker, but also the best friend in the Netherlands that I was actually missing before you appeared. I was looking forward to you coming into the office every day. You have such an honest and open personality that I sometimes really had problems stopping chatting with you at work. Even though a lot of that talking was actually long discussions about our projects. You've taught me to be more true to myself and cope better with all the struggles in life. Let's never give up and stay friends until the end. Additionally, a massive thanks to **Salima**, thank you for helping me so much with ssNMR in my last 1 1/2 years here. It was always handy to know someone was there to help and to double-check, and also to work on your stuff when you were again somewhere super busy on the weekend. I also want to thank you for your jokes, which lightened up the mood of the whole building. Moreover, I want to give gratitude to **Ajit**, you are a funny and open-minded person and it was always a big joy when you shared yummy cakes or Indian desserts with me. **Svetlana** I am grateful for your mature way of helping and I am impressed by your superior level of German.

Other thanks go to **Andre** without whom this NMR community would for certain not work and to **Johann**, who seem to be able to fix just about anything. I also want to appreciate **Adil**, for making dry jokes and being able to say what he thinks. Otherwise, a thank you to **David**, I know we didn't always get along well, but I enjoyed watching you being yourself. Wishing you all the best with the successful life (for whatever that means) as you pursue it. In addition, I would like to thank



Acknowledgments

Michaela. You are a strong person who seems so centred. Also **Julia** I admire how you stand up for the things you want and are not willing to back down.

Now I want to thank those who left the lab some time ago, but who helped me get off to a good start here in Utrecht. So thank you **Yanzhang** (Jon) for giving me your MTs project and a lot of really sound advice, not only scientifically, but also personally. Thanks to you I am able to brush away a lot of trouble with a "so what". **Reinier** thank you for the great pleasure I took in working with you at the beginning of my PhD. You gave me your LLPS project, which turned out to be challenging but nonetheless gave us some interesting results. **Alessandra** (Ale), Ciao Bella!!! You are a ray of sunshine and a person with both feet on the ground, yet you're able to fly. You are a true friend and an inspiration. **Siddartha** (Sid), we were office mates for a long time and I saw you struggling and standing up a lot of times. You are a smart person who is working hard to get what he wants. I am really happy to still have occasional contact with you. And now I want to say a big thank you to **Helena**. Thank you for understanding me and listening to my problems. Thank you for always making me feel smart and capable of everything. I hope our friendship will last, so that we can share funnier, but also sad moments together.

I also had the privilege of supervising a master's student and a postmaster internship. Thank you **Hanneke**, you are a smart and insightful person. You are curious and even though I couldn't always answer all your questions, I hope you will keep asking them. Thank you **Lenette**, you were my first "student" and I was quite intimidated by you. At the beginning of my project, I supervised you and often doubted that I knew more than you did. Being a smart and diligent, but reasonably hardworking person will bring you the things in life that you desire.

A big thank you is also due to all the people who worked or are working in Markus's and Hugo's group. Thank you **Rhythm** for making me laugh so many times, for often enough bringing out the craziness out of me and therefore cheering me up immensely. I enjoyed all the pleasant things we did together at work and also in our free time. Greetings to Nick. Goedendag **Miranda**. I am so happy that our friendship

Acknowledgments

lasted. I admire you for standing tall throughout your life, which sometimes is not as easy as I wish it would be for you. Thanks as well to **Francesca** for bringing a positive mood into the building, staying strong and keeping up a smile. Besides that, thanks to **Maik**, who I often cross early in the morning and who makes the start of my day a bit brighter by joking around. By being a good example of work-life balance, you also helped me leave the building more or less on time. Also a thanks to **Roy** who showed himself to be a greatly reliable person and to **Shadan** for her open mind and personal strength.

From Hugo's group, I want to acknowledge **Andrea** for his great, quite distinguishable humour. Further, I want to give praise to **Vincenzo** for always being ready to help out with his excellent knowledge. I also want to thank you for being a part of the DnD group I had the opportunity to join. You made those events humorous by developing a crazy character. Additionally, I want to thank **Heyi**, I really, really love your ways. How you look at the world is fantastic. You are someone with whom I can talk about everything. With you, I can bring the absurdity of the world to its absurdist point. We all know there is a giant, invisible, rainbow-coloured elephant in the room following me, myself and I. Another former member of the group that I enjoyed and spent a lot of time with is **Ivan**. Thank you for always trying to cheer people up and believing in the good in humans. This is though because people really try to convince you of the opposite all the time. Thank you for feeding me sweets all the time. I think back with a smile about the times when we shared an office.

Now I also want to thank **Alexandre and his research group**. A special thanks to **Rodrigo** for his patience and radiating kindness. Moreover I want to express my gratitude to **Marco** and **Rodrigo**, with whom I had the pleasure to spend a bit more time.

Another thank you to all members of the **International Neighbours Group**. Thank you for all the nice Wednesday evenings (the first Friday of the week) that I was allowed to spend with you people from all over the world, that are funny, open and



Acknowledgments

smart. I had the pleasure of being one of the board members and planning events with amazing and devoted people like **Ali, Kyriacos, Vedran** or **Nazmiye**.

Furthermore, I am grateful for all the memorable weekends I spent playing DnD with Vincenzo, Ulric, **Wouter, Anja, Fatema, Cas, and Ramon**. Thanks to our DM and all of you crazy and creative minds, the quests were a joy.

Im Folgendem will ich meinen Freunden aus Deutschland danken. Erstmal ein riesiges Danke an **Rahel**. Du bist meine beste Freundin seit Grundschulzeiten und wir haben so viel zusammen erlebt und durchgestanden. Danke für die vielen Skype Frühstücke. Danke das wir zusammen dieses Leben leben können und ich weiß, dass ich immer eine beste Freundin haben werde. Die Aggi hat die Rahel liieeeeeeb. Danke auch an all die Freunde, die ich in meinen Jahren in München getroffen habe. Danke **Dinah** und **Eva**. Danke auch an **Marija**, mit dir kann ich stundenlang reden und wandern. Einen speziellen Dank an **Jessica** (Jess), mit dir habe ich Jahre lang zusammen gelebt und du bist für mich das Bild einer starken, unabhängigen Frau, die ihr Leben in der Hand hat. Du bist eine Inspiration und du wirst alles erreichen, was du willst. Dann möchte ich auch **Enikö** (Eni) danken. Du bist eine so energiegelade und lebendige Person. Du hast mich häufig inspiriert und begeistert.

Nun auch ein Dank an meine Familie. Danke **Mama**, dass du immer an mich glaubst, auch wenn ich selber an mir zweifle. Danke **Papa**, dass ich immer deine volle Unterstützung in meiner akademischen Laufbahn habe. Und jetzt ein großes danke an meine Geschwister. Ihr seid mir so wichtig, dass es schwer ist es auszudrücken. **Ansgar**, danke für die stundenlangen Telefonate. Es ist echt manchmal heilsam gewesen, dich in einer ähnlichen Situation zu wissen und zu sehen, dass man auch einfach aufhören kann und was Besseres finden kann. Ansonsten ist es auch gut jemanden zu haben der sich mit MRT auskennt und ein gutes physikalisches wissen mit sich bringt. Ansonsten liebte ich auch all die offenen Gespräche, die wir über quasi alles hatten. Bitte pass auf dich auf. Danke **Arndt**, ich liebe es, mit dir zu diskutieren, manchmal hat es mir wirklich geholfen, die Absurdität meiner eigenen Probleme wieder wahrzunehmen. Vielleicht haben die MRTs deines Gehirns in mir

Acknowledgments

erst das Interesse für NMR geweckt. Liebes Bruderherz **Alexander** (Ali) danke für deinen starken Charakter und den Humor, der einen immer stärker macht. Danke **Erika** (Eri) für deinen kühlen Kopf und deine Hilfsbereitschaft, du hast mich in meinem Leben schon aus so mancher schwierigen Lage gebracht. Außerdem hat deine Weisheit "nicht unterkriegen lassen" mir so manchmal den Kick gegeben weiter zu machen. **Gisela**, ich schaue immer auf zu dir, du bist wirklich eine starke Persönlichkeit die niemals aufgibt und bereit ist zu kämpfen. Ich bin dankbar, dich als älteste Schwester zu haben. Schließlich ein Dank an **meine Oma, meine Omi, Tanten, Onkels, Cousinen, Cousins, Nichten und Neffen und all die Angeheirateten**, eure kleinen Aufmerksamkeiten, die lustigen Telefonate, die sich hin und wieder ergeben und die Treffen, die mich im hier und jetzt leben lassen haben mir sicher geholfen mich immer geborgen und aufgefangen zu fühlen.

Un merci aussi à **la famille de mon petit ami**, j'adorais les weekends avec vous et je vous remercie de me donner autant de motivation pour apprendre le français. Je remercie spécialement **Pascale** tu es une personne avec une intelligence émotionnelle admirable et aussi à **Ulric (père; Kiki)** pour ton humour presque imbattable.

Enfin le plus grand merci à **Ulric** qui m'a aidé dans toutes les façons imaginables et sans qui tout aurait été et serait plus dure. Je ne peux pas imaginer mon PhD sans toi à mes cotes. Tu m'as trouvé juste quand j'ai commencé à travailler à Utrecht. Et tu es vite devenu l'amour dont je ne veux plus me passer. Avec ton humour et ton intelligence immense tu étais là pour me reconforter scientifiquement et mentalement. Tu es toujours si calme et compréhensif, souvent tu avais eu des bonnes idées pour mes projets ou pour me faire sourire après une journée difficile. Merci pour n'avoir jamais douté de moi, même si mon caractère n'est pas toujours facile. Et sache qu'à chaque fois que je monte dans un train je pense encore à: "Und doch, welch Glück, geliebt zu werden! Und lieben, Götter, welch ein Glück!" (Goethe, Willkommen und Abschied, to finish with Goethe what I started with him).

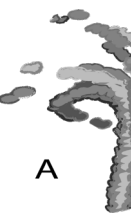


**Danke, Merci, Grazie, Gracias,
ευχαριστώ, धन्यवाद, 謝謝, Спасибо,
Teşekkürler, Köszönöm, Mulțumesc,
Děkuji, Так, благодарам, Bedankt,
شكرًا لك, مرسى**

and thank you all

Curriculum Vitae

Agnes Adler was born on the 23rd of April, 1995 in Pirna, Germany. After growing up in Berlin she did her bachelor's and master's in biochemistry at the technical university of Munich. After that, she started her PhD at Utrecht University in the Netherlands in the group of Prof. Dr. Marc Baldus for solid-state NMR. There she started to work on large biomolecular systems with a special focus on microtubules and their dynamic interactions with microtubule-associated proteins. A major research question was to understand the interactions between microtubule tails and the microtubule-associated proteins MAP7 and MAP Tau, as well as the interaction of these proteins with polymerized microtubule. The work of her PhD is displayed in this thesis.



List of Publications

Bräuning, B., Bertosin, E., Praetorius, F., Ihling, C., Schatt, A., **Adler, A.**, ... Groll, M. (2018). Structure and mechanism of the two-component α -helical pore-forming toxin YaxAB. *Nature communications*, 9(1), 1-14.

Cai, X., Lucini Paioni, A., **Adler, A.**, Yao, R., Zhang, W., Beriashvili, D., ... Liu, Y. (2021). Highly Efficient Trityl-Nitroxide Biradicals for Biomolecular High-Field Dynamic Nuclear Polarization. *Chemistry—A European Journal*, 27(50), 12758-12762.

Luo, Y., Xiang, S., Paioni, A. L., **Adler, A.**, Hooikaas, P. J., Jijumon, A. S., ... Baldus, M. (2021). Solid-State NMR Spectroscopy for Studying Microtubules and Microtubule-Associated Proteins. In *Structural Proteomics* (pp. 193-201). Humana, New York, NY.

Bahri, S., Safeer, A., **Adler, A.**, Smedes, H., van Ingen, H., Baldus, M. ^1H -detected characterization of carbon-carbon networks in highly flexible protonated biomolecules using MAS NMR (2023). *in press*

Adler, A., Kjaer, L., Beugelink, W., Baldus, M., van Ingen, H. Resonance assignments of the microtubule-binding domain of the microtubule-associated protein 7 (MAP7). Accepted: *Biomolecular NMR Assignments* (2023).

Adler, A., Banger, M., Bahri, S., van Ingen, H., Moores, C.A., Baldus M. A structural and dynamic visualization of the interaction between the microtubule-associated protein 7 (MAP7) and microtubules. *submitted*

